

# UNIVERSITÀ DEGLI STUDI DI PADOVA

DIPARTIMENTO DI INGEGNERIA MECCANICA  
SETTORE MATERIALI

SCUOLA DI DOTTORATO DI RICERCA IN  
SCIENZA ED INGEGNERIA DEI MATERIALI  
CICLO XXIV

## **Advanced ceramics from preceramic polymers and fillers**

**Direttore della Scuola:**  
CH.MO PROF. GAETANO GRANOZZI

**Supervisore:**  
CH.MO PROF. PAOLO COLOMBO

**Dottorando:**  
GIULIO PARCIANELLO



*To my family,  
for always supporting me*



*Try not to become a man of success,  
but rather try to become a man of value.*

A. Einstein



# Acknowledgments

My parents surely deserve the first place on this list, for their love and for always supporting me in every decision and every day. Thanks mom and dad.

I owe my deepest gratitude to Prof. Paolo Colombo, for his (really) unlimited kindness, helpfulness, for his guidance, for everything he did for me during these years and for being able to create such a lovely environment to work in. But, above all, because he is a really good person.

A sincere and special thanks goes to Ing. Enrico Bernardo, for always assisting me during these years, for his constant help and all the fruitful discussions we had. Many of the things I wrote here would not have been possible without him, his ideas and the incredible passion he puts into his work.

I'm grateful to Prof. Gary Messing for giving me the opportunity of spending a research period in his group at Penn State University. I like to thank him for always trusting in my ideas, for transmitting me the importance of dedication to work and scientific rigor, and for being an incredible boss.

Finally, it's hard to find the right words to thank all of the guys and girls I've spent the last 3 years (and, in some cases, even more) with. This experience wouldn't have been the same without them and the joyful atmosphere they all contributed to create. I will really miss all of them. I would like to thank Marta, Enrico, Marco, Giovanni, Giovanni, Cekdar, Alessandro, Jlenia, Erika, Michela, Gioia and Laura. A special thanks goes also to Mauro.

I wish them all the best for their careers and for their lives. I hope these true friendships will last in the future.

Thank you guys.



# Abstract

The research work presented in this thesis concerns the synthesis, the characterization and application of ceramic materials synthesized through the controlled pyrolysis of preceramic polymers mixed with fillers of different nature.

The introduction of fillers (passive or active) has been recognized as one of the most effective strategies to decrease, or even totally compensate, the shrinkage that inevitably accompanies the polymer-to-ceramic conversion of preceramic polymers, thus allowing the realization of relatively large ceramic components.

During the present research work, the possibility of synthesizing a wide variety of crystalline ceramics – generally not directly achievable with the standard PDCs route, ranging from silicates (mullite/ $ZrO_2$ , zircon, cordierite, yttrium-silicates, wollastonite) to ceramics in the Si-Al-O-N system – by the controlled pyrolysis of preceramic polymers filled with nano-sized ceramic particles has been extensively explored. Thanks to the presence of a polymeric phase, different shaping technologies were tested for the different ceramics, such as cold pressing, warm-pressing, extrusion assisted by supercritical  $CO_2$ , coating, deposition of thin layers, joining, self-foaming and the use of sacrificial fillers for the generation of highly-controllable porosity.

For each system, the reactions involved during the synthesis process, as well as the properties of the final ceramics, have been studied. Some examples of possible applications are also presented.

The realization of silicates ceramics, in general, was characterized by a relatively simple processing and favorable synthesis characteristics. Possible applications of this class of ceramics include high-temperature components with favorable structural, thermal and/or chemical characteristics (e.g. mullite/ $ZrO_2$ , zircon, cordierite, yttrium-silicates), as well as functional materials such as inorganic phosphors (yttrium-silicates) and biocompatible/bioactive parts for bone tissue engineering (wollastonite).

The successful synthesis at relatively low temperatures of high-purity, sub-micrometric Si-Al-O-N ceramics was also demonstrated, although characterized by a complex reaction system. Sialon ceramics from preceramic polymer-based formulations were successfully applied as sintering aids for  $Si_3N_4$  powders (offering, in principle, improved creep resistance) and as joining media for the joining of sialon substrates. Finally, preliminary results concerning the realization of sialon phosphors for LED applications are reported.



# Riassunto

L'attività di ricerca presentata nella presente tesi ha riguardato la sintesi, la caratterizzazione e le possibili applicazioni di materiali ceramici avanzati, prodotti dalla pirolisi controllata di polimeri preceramici caricati con riempitivi ("fillers") di diversa natura. L'introduzione di fillers (inerti o "attivi") rappresenta sicuramente una delle strategie più adottate per ottenere una efficace riduzione, o addirittura una totale compensazione, del ritiro volumetrico associato alla conversione da polimero a ceramico di tali precursori, in modo da consentire la realizzazione di componenti ceramici integri di dimensioni relativamente grandi.

Durante l'attività svolta, è stata studiata la possibilità di sintetizzare un'ampia varietà di ceramici cristallini – generalmente non ottenibili in modo diretto attraverso la cosiddetta tecnica "PDCs" (Polymer Derived Ceramics), quali silicati (mullite/ $ZrO_2$ , zircono, cordierite, silicati di yttrio e wollastonite) e ceramici nel sistema Si-Al-O-N – attraverso al pirolisi controllata di polimeri preceramici caricati con nano particelle ceramiche.

Grazie alla presenza di una componente polimerica all'interno della miscela di partenza, per la realizzazione dei campioni sono state sfruttate diverse tecnologie di formatura, quali pressatura a freddo, pressatura a caldo, estrusione, rivestimento di substrati, formazione in-situ di pori e l'utilizzo di fillers sacrificali per la creazione di porosità altamente controllabile.

Per ogni sistema ceramico sono state analizzate le reazioni chimico/cristallografiche coinvolte nel processo di sintesi, così come le proprietà dei ceramici finali. Inoltre, vengono presentati alcuni esempi di possibili applicazioni di tali ceramici.

La realizzazione di silicati si è visto essere caratterizzata, in generale, da una semplice processabilità e da caratteristiche di sintesi piuttosto favorevoli. Tali sistemi ceramici possono essere applicati sia come componenti strutturali e/o isolanti per applicazioni ad alta temperatura (mullite/ $ZrO_2$ , zircono, cordierite, silicati di yttrio), sia per applicazioni funzionali come fosfori inorganici (silicati di ittrio) e componenti biocompatibili/bioattivi per impianti ossei (wollastonite).

Infine, è stato possibile sintetizzare ceramici silico-alumino-ossinitruri ("sialon") di elevata purezza e grana sub-micrometrica, anche se attraverso reazioni più complesse, legate alla complessità del sistema ceramico Si-Al-O-N. I ceramici sialon ottenuti attraverso questa nuova metodologia sono stati utilizzati con successo sia come additivi di sinterizzazione per la densificazione di polveri di  $Si_3N_4$ , sia come materiale di giunzione per l'unione di substrati massivi di sialon. Inoltre vengono presentati alcuni risultati preliminari riguardanti la realizzazione di fosfori a base sialon, per applicazioni nel campo dei LED.



# Contents

<b>Abstract</b>	<b>9</b>
<b>Riassunto</b>	<b>11</b>
<b>I Introduction</b>	<b>17</b>
<b>1 PDCs - Polymer Derived Ceramics</b>	<b>19</b>
1.1 Introduction	19
1.2 Preceramic polymers chemistry	20
1.2.1 General aspects	20
1.2.2 Main polymers classes	22
Polysiloxanes	22
Polysilazane	23
Polycarbosilanes	25
Polysilanes	26
1.3 Preceramic polymers processing	26
1.3.1 Shaping	26
1.3.2 Cross-linking	28
1.3.3 Polymer-to-ceramic conversion	28
1.4 Properties of the final ceramics	31
1.4.1 Chemical composition	31
1.4.2 Microstructure	33
1.4.3 Mechanical properties	34
1.4.4 Chemical properties	35
1.4.5 Electromagnetic properties	36
1.4.6 Optical properties	36
<b>2 Preceramic polymers containing fillers</b>	<b>37</b>
2.1 Introduction	37
2.2 Passive fillers	38
2.3 Active fillers	40
2.4 Final considerations	43
<b>II Experimental</b>	<b>53</b>
<b>3 Silicates</b>	<b>55</b>
3.1 Mullite/Zirconia nanocomposites	55
3.1.1 Introduction	55
3.1.2 Experimental procedure	58
3.1.3 Synthesis	59
3.1.4 Characterization	60
3.1.5 Conclusions	67
3.2 Zircon	71
3.2.1 Introduction	71
3.2.2 Experimental procedure	71

3.2.3	Synthesis . . . . .	72
3.2.4	Applications . . . . .	74
	Zircon bulk components . . . . .	74
3.2.5	Conclusions . . . . .	76
3.3	Cordierite . . . . .	81
3.3.1	Introduction . . . . .	81
3.3.2	Experimental procedure . . . . .	81
	Low-porosity samples preparation . . . . .	81
	High-porosity samples preparation . . . . .	82
3.3.3	Synthesis . . . . .	82
3.3.4	Applications . . . . .	83
	Low-porosity cordierite components . . . . .	84
	High-porosity cordierite components . . . . .	86
3.3.5	Conclusions . . . . .	89
3.4	Yttrium silicates . . . . .	93
3.4.1	Introduction . . . . .	93
3.4.2	Experimental procedure . . . . .	96
3.4.3	Synthesis . . . . .	98
3.4.4	Applications . . . . .	99
	Y-disilicate and zircon Environmental Barrier Coatings (EBCs) . . . . .	99
	Red-emitting Y-MS:Eu <sup>3+</sup> . . . . .	101
3.4.5	Conclusions . . . . .	102
3.5	Wollastonite . . . . .	109
3.5.1	Introduction . . . . .	109
3.5.2	Experimental procedure . . . . .	109
3.5.3	Synthesis . . . . .	110
3.5.4	Applications . . . . .	110
	High-porosity wollastonite components . . . . .	110
3.5.5	Conclusions . . . . .	114
<b>4</b>	<b>SiAlON ceramics</b> . . . . .	<b>117</b>
4.1	Introduction . . . . .	117
4.2	SiAlON from silicone-based dispersions . . . . .	124
4.2.1	Experimental procedure . . . . .	124
4.2.2	Synthesis . . . . .	125
	H44/Al <sub>2</sub> O <sub>3</sub> formulations . . . . .	125
	Influence of additives on H44/Al <sub>2</sub> O <sub>3</sub> system evolution . . . . .	131
	Influence of the treatment atmosphere on H44/Al <sub>2</sub> O <sub>3</sub> system evolution . . . . .	135
	Conclusions . . . . .	135
4.3	SiAlON from silazane-based dispersions . . . . .	138
4.3.1	Experimental procedure . . . . .	138
4.3.2	Synthesis . . . . .	138
4.3.3	Conclusions . . . . .	145
4.4	Applications . . . . .	147
4.4.1	Si <sub>3</sub> N <sub>4</sub> composites using polymer-derived sialon as sintering aid . . . . .	147
	Introduction . . . . .	147
	Si <sub>3</sub> N <sub>4</sub> composites preparation . . . . .	148
	Results . . . . .	149
	Conclusions . . . . .	154
4.4.2	Sialon joining with polysiloxane-based formulations . . . . .	155
	Introduction . . . . .	155
	Joining preparation . . . . .	156
	Results . . . . .	158
4.4.3	Sialon phosphors . . . . .	160
	Introduction . . . . .	160
	Phosphors preparation . . . . .	161
	Results . . . . .	161

<b>III Summary, conclusions and future perspectives</b>	<b>169</b>
<b>Appendices</b>	<b>173</b>
<b>A Materials</b>	<b>175</b>
A.1 Polymeric precursors . . . . .	175
A.1.1 Silres MK . . . . .	175
A.1.2 Silres H44 . . . . .	175
A.1.3 Silres H62C . . . . .	175
A.1.4 HTT 1800 and PSZ20 . . . . .	175
A.1.5 NN 120-20 . . . . .	176
A.2 Inorganic powders . . . . .	176
<b>B Materials characterization</b>	<b>179</b>
B.1 X-Ray Diffraction . . . . .	179
B.2 Raman analysis . . . . .	179
B.3 Density measurements . . . . .	179
B.4 SEM - Scanning Electron Microscopy . . . . .	179
B.5 Mechanical characterization . . . . .	180
B.5.1 Flexural strength . . . . .	180
B.5.2 Compressive strength . . . . .	181
B.5.3 Young's modulus . . . . .	181
B.5.4 Hardness . . . . .	182
B.5.5 Indentation toughness . . . . .	182
B.6 Differential Thermal Analysis/Thermogravimetry . . . . .	183
B.7 Photoluminescence . . . . .	183
<b>Curriculum Vitae</b>	<b>185</b>



## **Part I**

# **Introduction**



# Chapter 1

## PDCs - Polymer Derived Ceramics

### 1.1 Introduction

Polymer Derived Ceramics (PDCs), as the name suggests, represents a synthesis route for the realization of ceramic components through the controlled pyrolysis of polymeric precursors. Aspects such as the wide variety of precursors, their easy-handling and simple shaping technologies that could be applied, make PDCs an extremely promising route for the realization of a new class of materials with unique and exceptional properties.

First experiments concerning this new synthesis strategy were made in the early 1960s by Ainger and Herbert<sup>1</sup>, and Chantrell and Popper<sup>2</sup>, concerning the production of non-oxide ceramics starting from molecular precursors. Ten years later, in the early 1970s, the first practical transformation of polyorganosilicon compounds (polysilazanes, polysiloxanes and polycarbosilanes) to ceramic materials was developed by Verbeek, Winter and Mansmann<sup>3-5</sup>, primarily for the manufacturing of small-diameter Si<sub>3</sub>N<sub>4</sub>/SiC ceramic fibers for high temperature applications. Synthesis of SiC materials was further developed by the work of Fritz and Raabe<sup>6</sup>, almost at the same time, the work of Yajima<sup>7,8</sup>. The subsequent so-called Yajima process for the synthesis of SiC is mainly based on the thermolysis process of polycarbosilanes in inert Ar atmosphere.

Silicon-based polymeric precursors demonstrated to be excellent candidates for the realization of many technologically important ceramic components such as fibers, coatings, infiltrated porous media and complex bulk parts. After these discoveries and first successful experiments, the growing interest for this new methodology led to further significant improvements of their chemistry, synthesis, processing and properties. Many different classes of preceramic polymers have been synthesized in the last decades, the most important being polysiloxanes, polysilazanes and polycarbosilanes. With this methodology it was possible to obtain not only binary ceramics such as Si<sub>3</sub>N<sub>4</sub> or SiC, but also more complex compositions in the SiOC and SiCN systems. Increasing the sophistication of the starting precursors could lead to further improvements of the properties of the final ceramics: the introduction of boron atoms inside the starting polymers could produce ceramics in the quaternary SiBCN system. Furthermore, the chemical modification of the starting polymers with precursors of metallic elements like Al, Zr and Ti could provide a further increase of the complexity of the system, for the realization of ceramic components with a wider variety of composition, and with outstanding thermal properties.

The relatively low cost of the precursors, the wide variety of compositions achievable, the characteristic microstructure (which is, in most cases, impossible to be achieved by conven-

tional methods), the unique and exceptional thermo-mechanical and chemical properties of the final ceramics, the possibility of shaping the precursors using well-established, conventional polymer-forming technologies such as Polymer Infiltration Pyrolysis (PIP), injection molding, coating, extrusion, Resin Transfer Molding (RTM), fiber drawing and many others, makes this methodology an extremely promising route for a relatively simple realization of ceramic components.

In the next Sections, the most significant aspects of the PDCs route will be described, with particular attention to the chemistry of preceramic polymers, their processing the properties of the final ceramics.

## 1.2 Preceramic polymers chemistry

### 1.2.1 General aspects

Preceramic polymer could be generally be referred as a class of hybrid materials, consisting of Si-based polymeric chains, and side chain functionalities. A simple and schematic representation of a silicon-based polymer monomeric unit is reported in Fig.1.1.

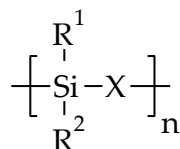


Figure 1.1: General simplified formula of silicon-based preceramic polymers.

Table 1.1: Principal classes of silicon-based preceramic polymers, based on the nature of the X group inside polymers backbone.

X group	Polymer class
O	Polysiloxanes, Polysilsesquioxanes
C	Polycarbosilanes
N	Polysilazanes, Polysilsesquiazanes
B	Polyborosilanes

The main backbone is constituted by silicon atoms bonded to a generic X group, with X=Si, O, NH, CH<sub>2</sub> or N=C=N. The nature of X is the probably the most important variable, since it determines the class of the final polymer: Si-Si backbone defines the polysilanes class, while Si-O, Si-NH, Si-BR, Si-CH<sub>2</sub> and Si-N=C=N define the polysiloxanes, polysilazanes, polyborosilanes, polycarbosilanes and polysilylcarbodiimides, respectively.

R<sup>1</sup> and R<sup>2</sup> instead represent generic side chain functional groups, generally carbon-based (e.g. H, alkyl, aryl, etc.). The nature of these side groups is fundamental in determining the global properties and characteristics of the polymer, especially during their processing before the pyrolysis step. By modifying R groups, properties like solubility, thermal stability and viscosity as a function of the temperature could be easily tailored<sup>9,10</sup>. Moreover, suitable functionalities are necessary to achieve the polymer setting through cross-linking reactions before the pyrolysis step (see Section 1.3.2, the nature of which is strictly related to the nature of the side groups involved (e.g. condensation reactions in the case of -OH functionalities, addition reactions in the case of -vinyl groups). Upon pyrolysis instead, the nature and the quantity of the different side groups is well known to determine the residual carbon content in the final ceramics (if a non-oxidizing atmosphere is used during pyrolysis).

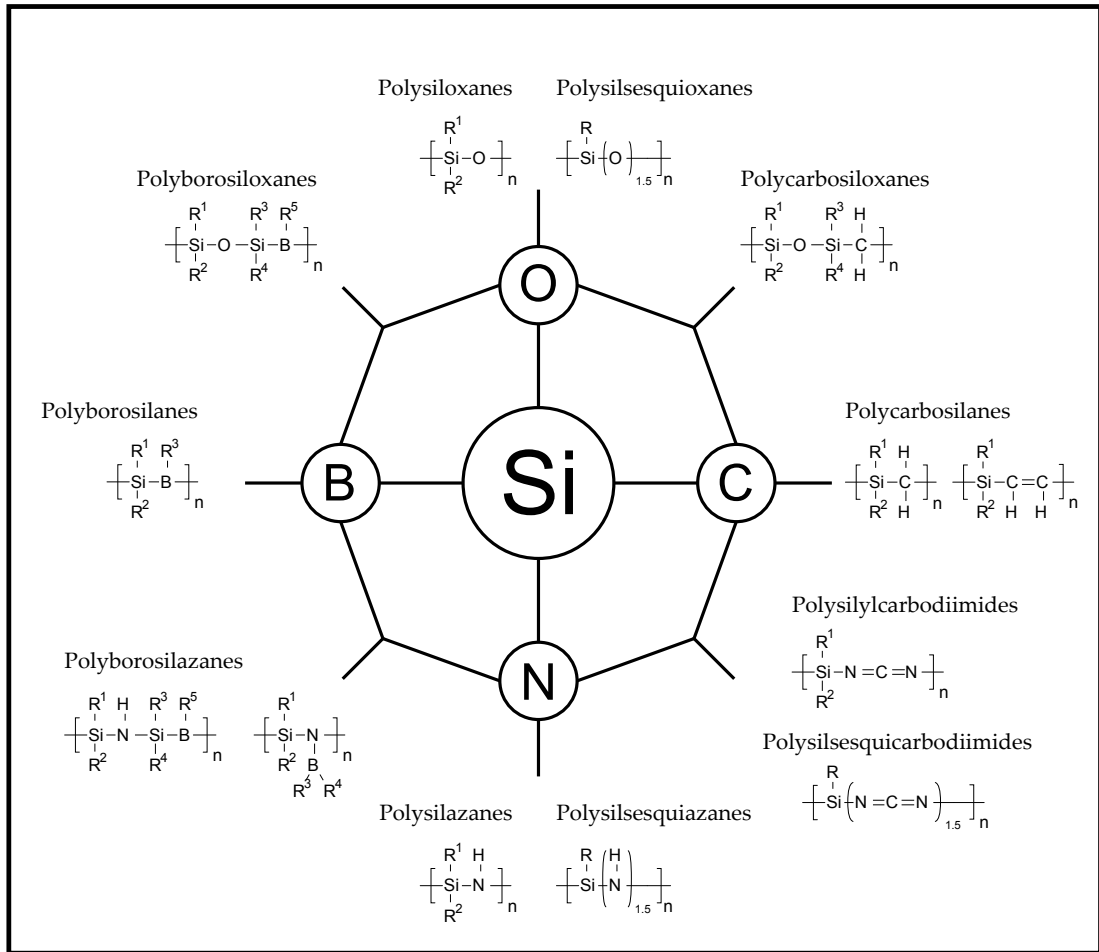


Figure 1.2: Main classes of silicon-based preceramic polymers in the Si-O-C-N-B system<sup>9</sup>.

In principle, since more than one X group could be present at the same time inside the polymer backbone, a wider range of possible polymer compositions must be considered<sup>9,11,12</sup>. As an example, polyborosilazanes are a class of hybrid polymers where both X=B and X=N are present in the main chain. A more comprehensive description and graphical representation of silicon-based preceramic polymers is thus reported in Fig. 1.2, as schematized by Colombo et al.<sup>9</sup>.

Although an extremely wide variety of preceramic polymers is, in principle, achievable, not all the classes of preceramic polymers have become equally "popular" and widespread during the last decades. Beside the mere properties and performances of the final ceramics, other factors must be considered during the selection of a preceramic polymer. The cost of the precursors is, as always, one of the most important parameters of a material or a component, especially under an industrial point of view. Another important factor is represented by the specific handling that every precursor requires, which could be influenced by its chemical durability, thermal stability, toxicity and reactivity towards the atmosphere or other substances, which inevitably influences all the aspects of its processing.

Above all, polysiloxanes represent surely the most studied class of preceramic polymers<sup>13,14</sup> their high thermo-chemical stability and low price make them the preferred choice for the easy realization of silicon oxycarbide glasses with extremely interesting thermo-mechanical properties up to approximately 1200°C.

When higher thermal stability is required, other classes of preceramic polymers should

be chosen, like polysilazane (for temperatures up to approximately 1400°C) or polyboron-silazanes (for temperatures up to approximately 1600°C). The higher performances of these other polymers are accompanied by higher prices of the precursors, more complex synthesis routes, generally higher reactivity towards other substances (above all, moisture and oxygen) and higher toxicity, which often increase processing complexity and hinder their applicability on an industrial scale.

The most important synthesis routes for the production of silicon-based polymers are based on chlorosilanes as starting compounds<sup>9,11,15</sup>. Other synthesis methods have been proposed during the last decades (e.g. sol-gel), but the fact that chlorosilanes are, in many cases, byproducts of the silicone industry, makes this class of precursors very attractive for their low cost, availability, and high purity, which could be easily achieved by distillation<sup>11</sup>. Their general formula is  $R_xSiCl_{4-x}$ , where  $x=0-3$  and  $R$  is a generic side group. Nowadays, the chemistry of organochlorosilanes is very well known, and the reactivity of this class of compounds has been extensively exploited for the synthesis of many different organosilicon polymers such as polysilanes, polycarbosilanes, polyorganosilazanes, polyborosilazanes, polysilylcarbodiimides, polysilsesquioxanes, etc. A more detailed discussion about the synthesis routes of the most important classes of preceramic polymers is reported in the next sections.

## 1.2.2 Main polymers classes

### Polysiloxanes

Polysiloxanes are surely the most important class of preceramic polymers. The main reasons for their widespread utilization are related to their generally low cost (the lowest among all Si-based polymers), their easy and cheap synthesis route, and finally their interesting thermo-chemical stability, which makes this class of precursors very versatile, easy to handle and processable under normal conditions without any particular precaution<sup>16-20</sup>.

Besides their use as preceramic precursors, they are widely available in other more common applications like sealants, lubricants, adhesives and gaskets. They are generally colorless, water resistant, chemical resistant, electrically insulating and stable at high temperatures. Their higher thermal stability, together with relatively high melting and boiling points, make this class of polymers the preferred choice when organic polymers are not applicable. Typical applications are as sealants, coolants in transformers, long lasting motor-insulation, lubricants for bearings, foam-control agent in laundry detergents or as coatings to protect facades and historical monuments.

Polysiloxanes are widely used even in other high-tech fields like aerospace industry, or as protecting materials in the semiconductor industry, or during the processing of products like optical glass fibers, silicon wafers and chips. They are widely used as adhesion promoters in glues, sealants, pigments and paints, but also in the textiles and rubber industry. Moreover, their extremely low reactivity generally makes them non-toxic, and for this reason they can be used also in the personal care products industry, in biomedical applications like breast implants, or even as oral anti-foaming agent (e.g. simethicone) or as food additives.

Thanks to their extremely interesting properties and the continuous development of this class of polymers, polysiloxanes market is expected to further grow and to find new applications, like for example as high oxygen permeable contact lenses, adhesive foams, synthetic fabric, waterproof membranes, process aids, or in lithographic applications<sup>15</sup>.

The most important synthesis route for the realization of polysiloxanes consists on the reaction of chloro(organo)silanes with water, as schematized in Fig. 1.3.

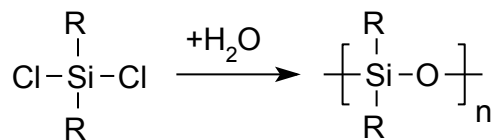


Figure 1.3: Synthesis route to polysiloxanes starting from chlorosilanes<sup>9</sup>.

Other synthesis routes have been proposed for the realization of polysiloxanes. Polycondensation reaction of functionalized linear silanes and ring-opening polymerization of cyclic silaethers lead to the synthesis of silicon-rich polysiloxanes, which combine the properties of polysiloxanes with those of polysilanes.

Besides linear or cyclic polymers, another important subclass are polysilsesquioxanes, characterized by the general formula  $-\text{[RSi-O}_{1.5}]_n-$ . This particular class of siloxanes is characterized by a highly-branched molecular structure, which can have many different possible configurations, such as random, "ladder" or "cage" structure, as reported in Fig. 1.4. Due to their high branching level, this class of polymers is often referred as silicon resins. They are generally solid at room temperature, and characterized by very high ceramic yields upon pyrolysis.

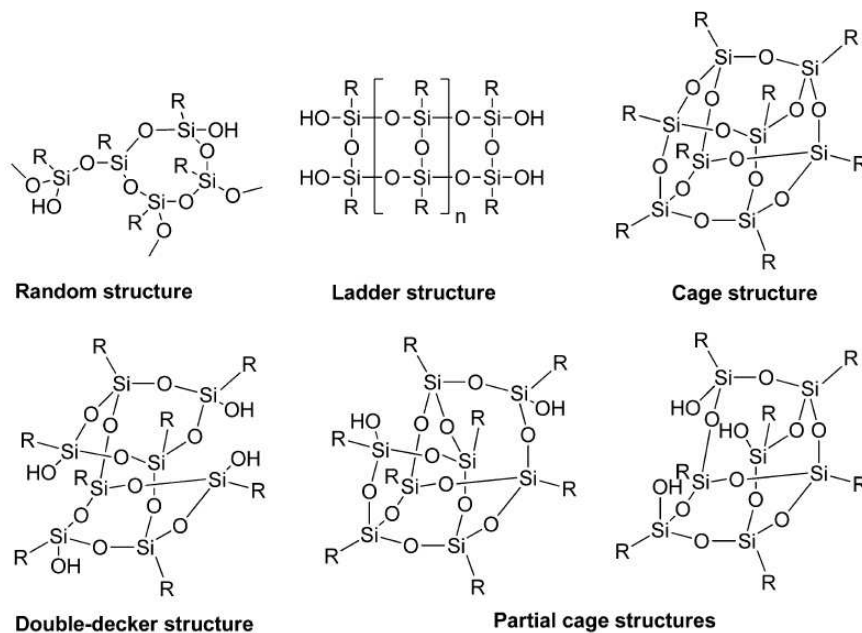


Figure 1.4: Possible structures of polysilsesquioxanes<sup>9</sup>.

Pyrolysis of polysiloxanes in non-oxidizing atmospheres give the formation of a silicon oxycarbide amorphous residue. This amorphous network of both Si-O and Si-C bonds is formed upon pyrolysis at relatively low temperatures, which is impossible to be obtained with more traditional processing techniques. The presence of both covalent bonds is the basis for all the distinguishing properties of PDCs, like enhanced thermal stability and creep, oxidation and corrosion resistance. They are black in aspect, because of the residual "free" carbon present inside the material.

### Polysilazane

Polysilazanes are polymers characterized by a main backbone constituted by alternate silicon and nitrogen atoms. They generally offer enhanced performances both in the poly-

meric and in the pyrolyzed state, if compared to the most widespread polysiloxanes. As polymers, polysilazanes are very versatile materials, and represent an excellent choice when high-temperature stability, corrosion resistance and durability are critical factors<sup>15,21</sup>.

Presently, polysilazanes are commercially available and they are mainly used for the realization of high-temperature SiN or SiCN ceramic coating/components, and especially as coatings in the polymeric state. Polysilazanes have demonstrated to be excellent materials for the realization of protective coatings, thanks to their excellent oxidation and corrosion resistance, UV stability and high hardness. These polymers adhere tenaciously to a wide range of different substrates, including metals, composites, graphite and glass. They have been successfully applied as clear, protective coatings for a lot of different metal alloys (both ferrous and non-ferrous), as clear automotive finishes, thermally durable clear coats, tarnish-resistant clear coats for electrical and plumbing fixtures, industrial, infrastructure and marine coatings, and anti-graffiti coatings for building facades. They have been successfully applied as protective coatings against corrosion in salt environments such as metallic structure in marine water or automobile components, or in industrial applications like pump and engine components, pipelines and tanks; for aerospace applications like structural composites and radome, for electrical insulation, for waterproofing surfaces and for mechanical protection of optical surfaces and indoor flooring.

Other peculiar applications include cements, since they possess properties to combine chemically and/or micro-structurally and/or structurally similar or dissimilar materials including, for example, metals, minerals, ceramics, polymers, natural materials, metal-, ceramic- and polymer-matrix composites, and combinations thereof. They could be used for the realization of hard and soft contact lenses, membranes, clear transparent/translucent bodies in general, photographic films, transparency sheets and packaging for food. They may be used as surface modifiers for compatibilizing inorganic/organic interfaces, or as binders for polymers, mineral, ceramic or metal fillers for the realization of monoliths.

Polysilazanes are generally synthesized by ammonolysis reactions of chlorosilanes with ammonia or other different amines, as schematized in Fig. 1.5.

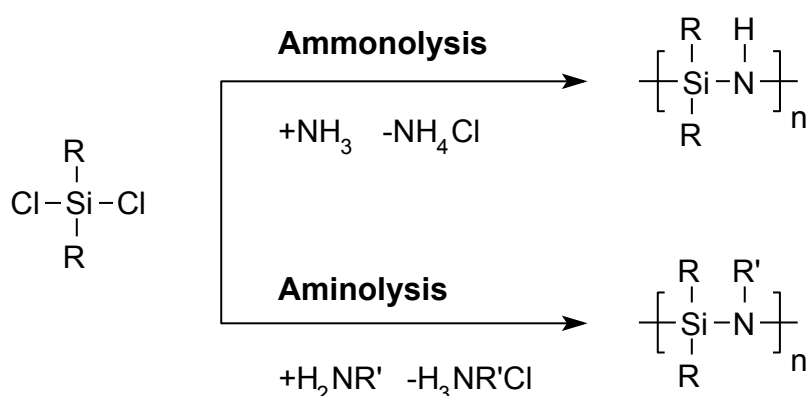


Figure 1.5: Synthesis routes to poly(organo)silazanes starting from chlorosilanes<sup>15</sup>.

The main drawback of this synthesis route is the need of separate the polymeric product from the solid byproducts  $\text{NH}_4\text{Cl}$  and  $\text{H}_3\text{NR}'\text{Cl}$ . The product of the final reaction is generally a mixture of oligomers and low molecular weight polymers, which can easily volatilize and depolymerize, giving low ceramic yields. For this reason, a lot of effort has been devoted to the modification of silazane oligomers into non volatile precursors. Appropriate side-chain groups should be attached to the silicon atoms in order to increase the cross-linking efficiency.

Different organic groups could be attached also to nitrogen atoms, when these polymers are synthesized by ammonolysis with alkylamines. Other strategies have been proposed, such as the use of a KH basic catalyst, the cross-linking in the presence of transition-metal complexes, or the modification of silazane oligomers with urea or isocyanate-containing compounds<sup>9</sup>.

### Polycarbosilanes

Polycarbosilanes represents one of the most interesting and technologically relevant classes of preceramic polymers. The main interests that have led to the synthesis and constant improvement of polycarbosilanes were focused on the realization of precursors for silicon carbide, and this class of silicon-based polymers represented one of the first successful application of the PDCs route, i.e. high-performance SiC fibers (Nicalon™ by Nippon Carbon Co., and Tyranno™ by UBE Industries), by the pioneering work of Verbeek and of Yajima<sup>3-5,7,8</sup>. Like polysilanes, polycarbosilanes can also find applications as functional materials, such as photoresist and semiconductors. Because of their electric conductivity, unsaturated polycarbosilanes could be used in electronic applications such as compact capacitors, electromagnetic shielding of computers, piezoelectric sensors, smart windows (with tunable color and transparency), antistatic coatings, transistors, LEDs, lasers and solar cells<sup>22,23</sup>. Because of their intriguing properties, other more fundamental and theoretical studies have been done on their chemical and electronic structure, to answer important fundamental questions regarding the structure and the properties of compounds and polymers that contain both carbon and silicon in their backbone. In terms of properties, this class of polymers cover the gap between the "classic" biological and petrochemical polymers and the mineralogical and synthesized ceramics.

Polycarbosilanes are often schematized by the following oversimplified formula (Fig. 1.6):

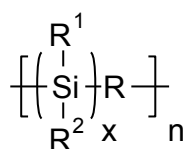


Figure 1.6: General oversimplified representation of polycarbosilanes.

In fact, polycarbosilanes generally show a much more complex structure. Besides the Si-C bond, Si-Si bonds could be present, as well as complex hyperbranched structures, thus modifying both the global Si:C ratio and the final ceramic yield. Many of these different features could be obtained by modifications of the synthesis strategy, but a simple and comprehensive summary of all the different synthesis routes is difficult to be made.

The very first and most famous approach was proposed by Yajima, and is schematized in Fig. 1.7.

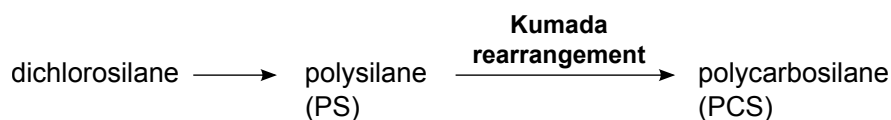


Figure 1.7: Synthesis strategy for polycarbosilanes proposed by Yajima<sup>7,8</sup>, starting from dichlorosilane and polysilane and based on the Kumada rearrangement<sup>24</sup>.

The second step of the Yajima strategy, which represents the PS-to-PCS conversion, is often referred as the "Kumada rearrangement" (due to the work of Kumada<sup>24</sup>). This step is considered to be the most critical in terms of yield and reaction conditions<sup>25</sup>, and consists

of thermally-activated reactions that lead to the cleavage of Si–Si bonds and the formation of Si–C bonds, as schematized in Fig. 1.8 (Kumada rearrangement for polydimethylsilane).

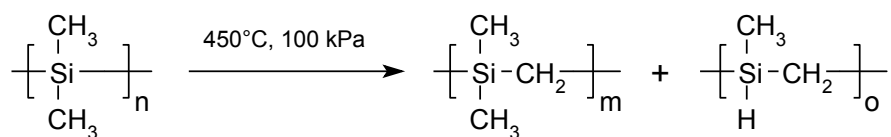


Figure 1.8: Kumada rearrangement for polydimethylsilane<sup>11</sup>.

Other alternative synthesis routes have been proposed for the realization of other types of polycarbosilanes, such as ring-opening polymerization reactions, polycondensation of chloromethylchlorosilanes, hydrosilylation reactions, polycondensation of chlorosilanes with unsaturated hydrocarbons, and many others<sup>25</sup>.

## Polysilanes

Polysilanes are a class of polymers characterized by a one-dimensional silicon backbone and organic side-chain groups. They have been the subject for a lot of investigations<sup>26</sup>, mainly because of their intriguing optoelectronic properties, that originates from the so-called  $\sigma$ -conjugation. Alkylsilanes exhibit unique electronic, physical and chemical properties that distinguish them from the analogous saturated hydrocarbons, and that make this compounds possible candidates for applications in photoconducting and charge-transporting materials.

Polysilanes (as well as polycarbosilanes) are increasingly used as functional materials such as photoresists, semiconductors, hole-transporting materials and as precursors for silicon carbide ceramics.

The typical synthesis reaction for the synthesis of polysilanes is reported in Fig. 1.9. This reaction was proposed for the first time in 1921 by Kipping<sup>27</sup>, and nowadays still remains one of the most common synthesis routes for the production of polysilanes.

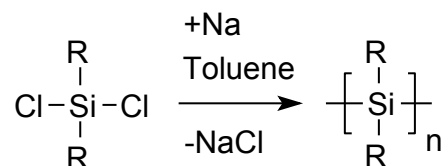


Figure 1.9: Synthesis routes to polysilanes starting from chlorosilanes<sup>9</sup>.

## 1.3 Preceramic polymers processing

### 1.3.1 Shaping

Shaping of preceramic polymer is one of the most advantageous aspects of the PDCs route. If compared with common powder processing routes, having a fully (or partially, in the case of fillers insertion) polymeric system has the potential advantage of an easy fabrication of green compacts with no need for additional binders, that show a suitable mechanical consistency for further handling and, if required, machining (after the cross-linking step). Moreover, the possibility of obtaining a machinable component prior to the polymer-to-ceramic conversion is a remarkable advantage, since it permits a more precise shape control without all the problems related to ceramic brittleness and tool wear<sup>28</sup>. In Fig. 1.10 some shaping technologies for PDCs are reported.

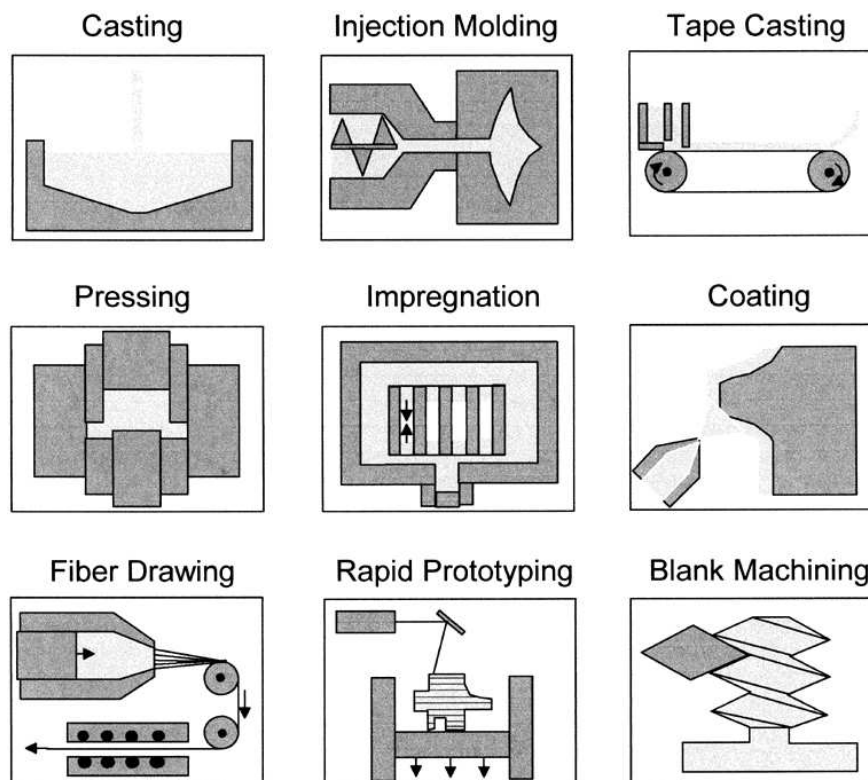


Figure 1.10: Shaping technologies for for polymer derived ceramics manufacturing<sup>11</sup>.

All the common and well-known forming technologies used for plastics could, in principle, be applied to preceramic polymers. Besides the quite standard compaction method by uniaxial, isostatic and warm pressing<sup>29-31</sup>, other possibilities for the shaping of preceramic polymers could include extrusion<sup>32-34</sup>, injection molding<sup>35,36</sup> or coating of substrates by spraying, dip coating, spin coating or chemical vapor deposition (CVD)<sup>37-39</sup>. Coupling the preceramic polymer route with special forming technologies make the realization of some special components – generally not easy if not impossible to achieve with powders processing – possible. Some representative examples include fiber drawing<sup>40,41</sup>, infiltration of pre-formed scaffolds for the realization of ceramic matrix composites (CMCs)<sup>42-44</sup>, ceramic joining/bonding<sup>45-47</sup>, micro-components production through selective curing of substrates by lithographic techniques<sup>48-58</sup>, and easy realization of highly-porous components by direct foaming or other techniques such as sacrificial templates<sup>59</sup>.

Ultra-high performance SiC-based ceramic fibers for polymer, metal or ceramic matrix composites have been produced in the last decades by Nippon Carbon Co. (NICALON™) and by UBE Industries (Tyranno®) through the controlled pyrolysis of polycarbosilane, synthesized in the late '70s by Yajima and coworkers<sup>7,8</sup>. Non-oxide Si-C-N fibers have been successfully produced at ITCF (Denkendorf) from a polycarbosilazane precursor<sup>60</sup>.

Polyacrylonitrile (PAN), although not silicon-based, is another significant example of the application of the PDCs route for the industrial realization of ceramic components. Since first investigation during World War II by Union Carbide Corporation, it has been used extensively for the realization of high-strength carbon fibers for polymer and ceramic matrix composites. Nowadays, the PAN process is the most important production process for carbon fibers<sup>10</sup>.

As a final consideration, it should be pointed out that, although in the last years considerable developments have been made for the obtainment of high-yield preceramic polymers,

only low-dimension products like fibers and coatings, or other special applications, have been successfully applied. The main problem resides in the evolution of the polymeric phase during the pyrolysis step, with the subsequent release of gases, porosity and shrinkage development, that strongly hinders the possibility of obtaining components with dimensions higher than some hundreds of microns. This aspect will be more extensively discussed in Section 1.3.3 and Section 2.

### 1.3.2 Cross-linking

After the shaping process, the cross-linking of the preceramic polymer is of fundamental importance for the obtainment of a material that must result unmeltable during the pyrolysis step at higher temperature, when the polymer converts into the final ceramic material.

Thermal curing in the 150-250°C range represents probably the most common methodology to reach the setting of the polymeric phase, which could be easily achieved if suitable functionalities are present inside the polymer structure, such as –OH, –H or –vinyl groups, that could give condensation or addition reactions. Thermal curing temperatures could be lowered in the presence of an appropriate catalyst or radical initiator, with the further advantage of an increase of the ceramic yield due to a lowering of oligomers evaporation<sup>61,62</sup>.

Depending on the curing mechanism, a release of gaseous by-products could take place during the cross-linking step, e.g. water or ethanol. This release of gases could generate bubbles that could remain trapped inside the polymeric medium; this phenomenon could either be exploited for the realization of porous components by self-foaming processing, or be detrimental if a dense pore-free ceramic is desired.

Other cross-linking strategies could involve the use of UV-radiation (if proper photo-sensitive groups are present),  $\gamma$ -rays, electron-beams, and the use of reactive substances, gases or plasma<sup>54,63–68</sup>. As will be more extensively discussed in Section 1.3.3, polymer cross-linking is also of fundamental importance for the obtainment of high ceramic yields upon pyrolysis: effective cross-linking reactions lead to highly branched/higher molecular weight polymeric molecules, and thus to a lower content of oligomers and low molecular weight chains that could volatilize at higher temperatures, thus increasing the final ceramic yield.

### 1.3.3 Polymer-to-ceramic conversion

The polymer-to-ceramic conversion represents probably the most important phase of the whole processing of preceramic polymers, and is the result of a thermal decomposition process above  $\sim 400^\circ\text{C}$  at which a totally inorganic, non-volatile residue is created.

All organic polymeric compounds used in common powder-processing route (e.g. powder sintering, tape casting), such as binders (e.g. PEG, PVB), dispersants and plasticizers, must undergo a complete removal before the final sintering step, generally carried out by thermal decomposition above  $\sim 400^\circ\text{C}$  in oxidizing or non-oxidizing atmosphere<sup>69</sup>. Unlike common carbon-based compounds, the silicon-based chemistry of preceramic polymers allows instead for the obtainment of a solid ceramic residue after thermal decomposition, which nature and properties will be more extensively discussed in Section 1.4.

The pyrolysis mechanism involved in the polymer-to-ceramic conversion is generally quite complex. This reaction sequence involves structural rearrangements and radical reactions that result in the cleavage of chemical bonds (e.g. Si–H, Si–C and C–H), the release of organic functional groups (e.g.  $\text{CH}_4$ ,  $\text{C}_6\text{H}_6$ ,  $\text{CH}_3\text{NH}_2$ ) and the formation of an inorganic

network<sup>9,11,12,21</sup>. This process could be schematized as a sequence of different distinct rearrangement reactions, each being characterized by its specific temperature range. In the case of polysiloxane resins for example, it has been verified that in the 600–800°C range methane is the main volatile species released, while at higher temperature (600–1100°C) the release of hydrogen is observed<sup>70</sup>.

At temperatures above 400°C, an open-pore channel network is formed that, upon further heating to 800–1000°C, can diminish (transient porosity)<sup>11,12</sup>.

The ceramic yield of a polymer is a fundamental parameter to be considered when working with PDCs. It is defined as the ratio between the mass of the starting polymer and the mass of the ceramic residue upon pyrolysis. The organic-inorganic conversion is terminated at 800–1000°C, and is associated with a weight loss of typically 10–30%. In the last decades, the possibility of increasing the ceramic yield through continuous developments of preceramic polymers chemistry and processing has been of fundamental importance for the obtainment of valuable precursor with potential practical applications<sup>15</sup>.

The total weight loss is the sum of different contributions, each having its characteristic temperature range. The nature of the polymeric precursor and its chemistry are fundamental in determining the final ceramic yield: low molecular weight polymers, as well as the presence of oligomers, could dramatically decrease the ceramic yield upon pyrolysis, due to volatilization and de-polymerization reactions. A proper cross-linking step thus acquires a fundamental importance, not only for the obtainment of an infusible compact, but also to increase the final ceramic yield. Organic side chain groups are as well fundamental in determining both the cross-linking and thermolysis chemistry<sup>15</sup>. Finally, higher branching levels have generally a positive influence on the final ceramic yield. Thermal decomposition during pyrolysis is another fundamental factor, since it represents the step when most of the weight loss is observed, deriving from the cleavage of chemical bonds and release of gaseous byproducts. Finally, dehydrogenation and carbothermal reduction reactions at higher temperatures could give an additional contribution to the global weight loss, although these phenomena are generally less significant<sup>70</sup>. Typical ceramic yields are in the 70–90 wt% range, although higher (even up to ~105 wt%, when reactive atmospheres are used<sup>71</sup>) have been reported. A simplified representation of the weight loss (TG curve) and structural rearrangements of a preceramic polymer (polycarbosilane) during heat treatment in inert (Ar) atmosphere is reported in Fig. 1.11, as schematized by Greil<sup>12</sup>.

The thermal decomposition/rearrangement, that is distinctive of the polymer-to-ceramic conversion, represents also the most important drawback of PDCs. Gases release is inevitably accompanied by the formation of cracks and porosity inside the material, and by a more or less pronounced shrinkage. During the pyrolysis step, an increase in density by a factor of 2–3 is generally observed, passing from the polymeric phase (density ~1 g/cm<sup>3</sup>) to the final ceramic (density of 2.2–2.6 for SiO<sub>2</sub>, 3–3.2 for SiC and Si<sub>3</sub>N<sub>4</sub>)<sup>12</sup>. If the material structural changes could not be relaxed by viscous flow or diffusion processes, the combination of internal tensions, pores and cracks could lately destroy the component integrity, especially when external constraints are present (e.g. coatings). For this reason, an easy and simple conversion of a polymeric compact into a dense, crack-free ceramic compact is in most cases impossible to achieve<sup>12</sup>, even with polymers characterized by high ceramic yields. Few exceptions are represented by components characterized by dimensions below few hundreds micrometers, like fibers, thin films and foams<sup>9</sup>.

A lot of effort has been put in the last 25 years to find viable solution for the scaling up of ceramic components dimensions, to widen the applicability of PDCs especially in the field

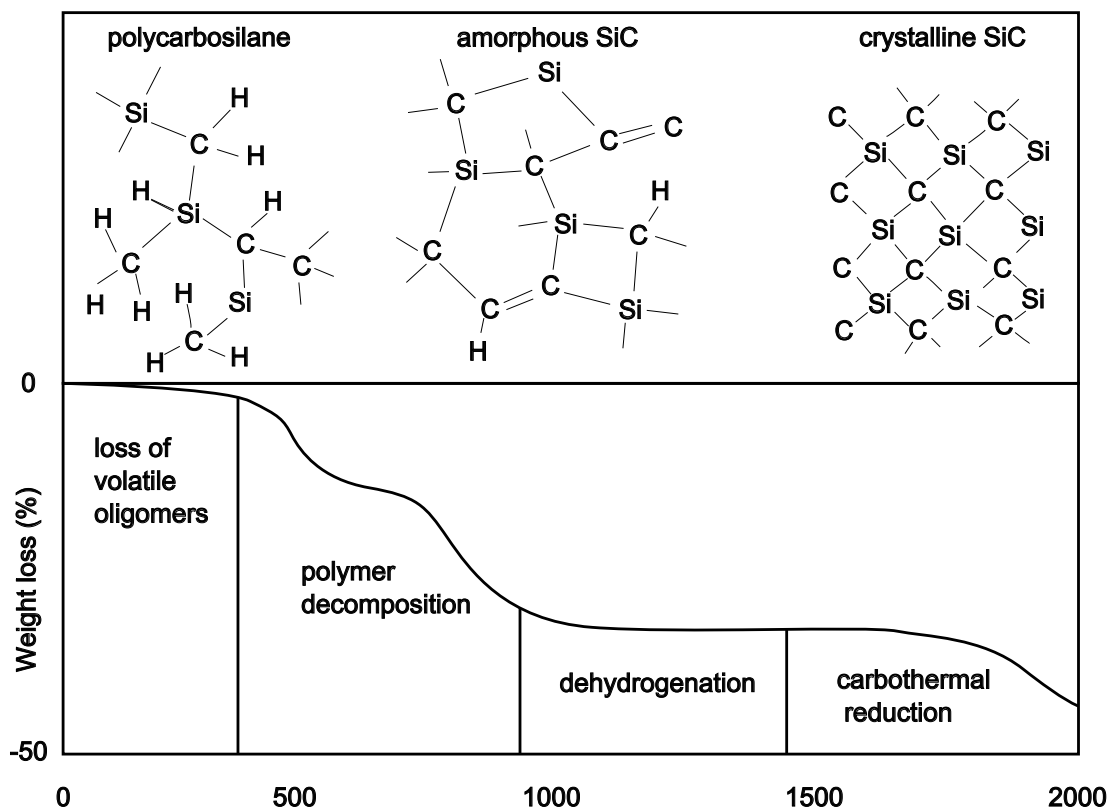


Figure 1.11: Typical structural transformations during thermal decomposition of preceramic polymers (polycarbosilanes)<sup>12</sup>.

of structural ceramics<sup>11,12,72,73</sup>. The introduction of different types of fillers has been so far the most widely explored possibility, and it will be more extensively discussed in Chapter 2, although other possibilities have been proposed, such as the infiltration of scaffolds by a liquid polymer<sup>74</sup> or the compaction of partially pre-cured powders<sup>75,76</sup>.

After the completion of the polymer-to-ceramic conversion, ceramics obtained show an amorphous structure. The amorphous network is constituted by a mixture of covalent bonds, the most important being Si–C, Si–O, Si–N and C–C; other bonds with other atoms like B, Ti, Al or Zr could also be present, depending on the type of precursor used and possible modifications of the polymer made prior to the pyrolysis step. This typical amorphous structure is a distinctive characteristic of polymer-derived-ceramics, which so far has been impossible to be obtained through traditional processing routes (e.g. reactive sintering). This characteristic structure is fundamental in determining the distinguishing properties of PDCs, such as thermal stability, oxidation, creep and chemical resistance<sup>9,11,15</sup>.

At higher temperatures – both during processing or during service – this amorphous structure eventually undergoes further structural rearrangements, that generate both a progressive phase separation and the eventual crystallization of different phases, depending, again, on the nature of the starting precursors, such as SiC, Si<sub>3</sub>N<sub>4</sub>, SiO<sub>2</sub> and carbon (turbostratic or graphitic). If sufficiently high temperatures/times are used, an equilibrium between the above mentioned crystalline phases could be achieved. This devitrification process starts with a progressive redistribution of chemical bonds to give phase separation and crystallization phenomena and, in many cases, the release of gaseous products such as CO, SiO<sub>2</sub>, N<sub>2</sub> and others<sup>9</sup>. This phase separation phenomenon is generally undesired, since most of the beneficial properties of PDCs are connected with the retention of their amorphous structure, and

the nucleation of crystalline phases is often associated with a degradation of their properties.

The type of covalent bonds present inside the ceramic amorphous network – which is directly related with the type of precursor used – is fundamental in determining the characteristic maximum service temperature of the final ceramic before the occurrence of the devitrification process, which could be generally located in the 1000-1800°C range.

SiOC glasses, which are surely the most common type of PDCs, are generally considered to be stable up to ~1200°C. Up to that temperature, creep, oxidation and chemical resistance are maintained. Above 1200°C, properties begin to deteriorate, due to the phase separation/crystallization process that takes place around 1300°C<sup>77,78</sup>.

SiCN amorphous networks instead are able to maintain their properties up to ~1400°C. With regards to oxynitride glasses, the presence of nitrogen atoms have beneficial effects on the viscosity, micro-hardness, elastic modulus and fracture toughness<sup>79</sup> in comparison to pure oxide glasses. This trend could be also observed in the SiOC→SiCN passage.

Moreover, further enhancements of properties could be achieved by the additional presence of boron atoms in SiBCN glasses, which could also increase the crystallization temperature up to about 1600°C. For this reason, SiCN and SiBCN glasses show outstanding properties even at very high temperatures (as high as 1800-2000°C, with respect to some properties<sup>15</sup>), which make them competitive with more traditional nitrides and carbides that are generally characterized by a more complex processing and higher sintering temperatures.

## 1.4 Properties of the final ceramics

### 1.4.1 Chemical composition

The chemical composition of the ceramic after pyrolysis is strictly related to the chemistry of the starting polymeric precursors, as well as to other factors related to treatment conditions (temperature, atmosphere nature and pressure) and the possible insertion of additional additives or modifiers (e.g. fillers, metal alkoxides).

The chemistry of the starting precursors plays probably the most important role in determining the final ceramic composition. Depending on the silicon-based backbone nature and on the side chain groups present, different ceramic systems could be achieved. Polysiloxanes, -silazanes and -carbosilanes, characterized by a Si–O, Si–N and Si–C backbone, respectively, give the formation of amorphous  $\text{Si}_x\text{O}_y\text{C}_z$ ,  $\text{Si}_x\text{C}_y\text{N}_z$  and  $\text{Si}_x\text{C}_y$  ceramics after pyrolysis in inert atmosphere<sup>9</sup> (see Fig. 1.12).

The proportions between the elements in the final amorphous structure depend both on the nature of the polymer backbone (which could, in principle, include any combination of Si–O, Si–C, Si–N and Si–B bonds) and on the nature of the side chain groups. Carbon content, for example, could vary (and thus be easily tailored) by changes of the organic substituents bonded to silicon (e.g. an increase in the phenyl group concentration leads to an increase in the final carbon content).

The pyrolysis atmosphere is as well important in determining the nature of the final ceramics. In general, a pyrolysis process in oxidizing atmosphere leads to the formation of an amorphous silica matrix, regardless of the chemistry of the starting precursors, due to the removal of all the carbon-containing moieties by oxidation reactions, as well as cleavage of Si–C and Si–N bonds of the main chain (less stable than Si–O bond) with a further oxygen intake. Considering the higher synthesis costs of silazanes and carbosilanes if compared to polysiloxanes, pyrolysis of preceramic polymers other than siloxanes in oxidizing atmosphere

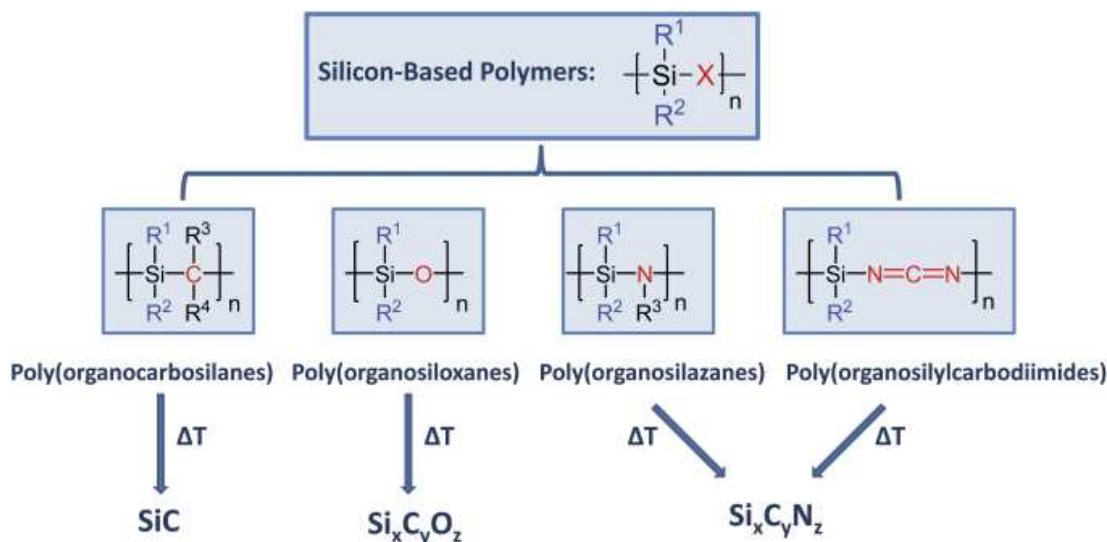


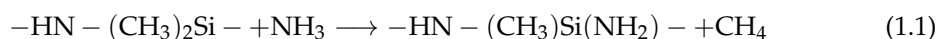
Figure 1.12: Simplified scheme of the influence of the precursor chemistry on the composition of the final ceramic<sup>9</sup>.

are not generally done.

Conversely, non-oxidizing atmospheres are generally preferred because they can produce the most interesting final characteristics. In fact, the retention of an amorphous structure comprising of a mixture of Si–O, Si–N and Si–C covalent bonds represents the key point for properties like high thermal stability (even up to 1800–2000°C), creep, corrosion and oxidation resistance.

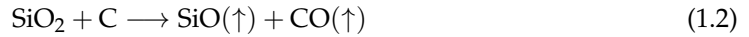
A totally inert atmosphere (e.g. Ar) does not react with the material at any point of the process, and so it has no influence on the final composition of the material. On the contrary, N<sub>2</sub> atmosphere could interact with the evolving materials, increasing the nitrogen content of the final pyrolysis product by nitridation reactions. In this case, N<sub>2</sub> pressure could play an important role, since it has been verified that an increase in N<sub>2</sub> pressure could increase the kinetic of nitridation reactions of both the polymer and, as will be more extensively discussed in Chapter 2, of active fillers introduced to compensate the material shrinkage.

Gaseous NH<sub>3</sub> (pure, or mixed with Ar or N<sub>2</sub>) is also well known to actively react with the preceramic polymers during the polymer-to-ceramic conversion. Ammonolysis reactions are well known to take place in carbon-containing polysilazanes during polymer pyrolysis, with a consequent reduction of final carbon content by substitution of carbon-containing side groups with amine functionality –NH<sub>2</sub><sup>80</sup>. As an example, for a methyl group the global reaction would be



Burns and Chandra<sup>81</sup> demonstrated that the pyrolysis of cross-linked polycarbosilanes, polysilanes and polysilazanes in NH<sub>3</sub> atmosphere yields amorphous Si<sub>3</sub>N<sub>4</sub> powders with a low carbon content, that can crystallize at higher temperatures to give the formation of α-Si<sub>3</sub>N<sub>4</sub>. Other examples regard the nitridation in NH<sub>3</sub> atmosphere of polycarbosilane for the obtainment of silicon nitride and silicon oxynitride fibers<sup>82</sup>. In addition, it has been shown that an NH<sub>3</sub> atmosphere could virtually eliminate the free silicon content in the ceramic deriving from the pyrolysis of perhydropolysilazane (PHPS), and nearly stoichiometric Si<sub>3</sub>N<sub>4</sub> could be produced<sup>21</sup>.

Finally, if pyrolysis is carried out under vacuum, as for example when using hot-press or Spark Plasma Sintering (SPS) equipments, carbothermal reduction reactions are well known to take place, which could lower the final oxygen content. One typical example is silica volatilization, schematized by the reaction



In this case, besides a decrease of the oxygen content, a silica loss is observed as well.

The addition of metal alkoxides together with the preceramic polymers is another effective strategy for the modification of the ceramic composition, by the addition of supplemental metal atoms inside the final amorphous structure. Two significant examples of this possibility have been reported by Ionescu et al.<sup>83</sup> for the realization of SiOC/ZrO<sub>2</sub> nanocomposites, and by Sorarù et al.<sup>84</sup> for the realization of  $\beta'$ -sialon ceramics from a modified polycarbosilane. While in the former authors claim an effective condensation reaction between the Si-OH groups of the silicon resin and zirconium acetylacetonate, thus obtaining a molecular-level dispersion, in the latter instead authors believe that no condensation reactions occur between the Al(O-secBu)<sub>3</sub> (the modifying alkoxide used in the work) and the polycarbosilane chains, and aluminum hydroxide-based particles are physically trapped inside the polycarbosilane chains, thus obtaining a lower homogeneous system.

Finally, the introduction of secondary fillers of different nature (ceramic, metallic) and shape (particles, fibers, whiskers, platelets) could dramatically change the global composition of the final ceramic, which could consist of a relatively simple PDC/filler(s) composite (in the case of inert or active fillers) or of a totally new combination of amorphous and/or crystalline phases, that could not generally be achieved by using pure preceramic polymers (in the case of reactive fillers). Since this topic represents the main subject of the present research work, it would be analyzed and discussed more extensively in Chapter 2 and in Part II.

## 1.4.2 Microstructure

The microstructure of PDCs is strongly influenced by their chemical characteristics and by processing conditions. Chemistry of preceramic polymers is fundamental in determining the type of bonds present in the final ceramics, and the final pyrolysis temperature plays a parallel fundamental role in determining the degree of evolution of the pyrolyzed material. As a general, oversimplified consideration, 3 distinct microstructures could be found in PDCs.

At low temperatures (600–800°C), immediately after the end of the decomposition of the polymeric phase, the microstructure is totally homogeneous and amorphous: a totally random mixture of different covalent bonds (e.g. Si-O, Si-C, Si-N, etc.) could be found (see Fig. 1.13), and they are directly related to the molecular structure of the cross-linked polymer, obviously deprived of all the organic moieties that were removed during the decomposition phase (except for most of the hydrogen)<sup>9,12</sup>. In this phase, excessive carbon (the carbon that is not linked to silicon atoms) is present as carbon clusters (basic structural units, BSU). As a results of all the decomposition reactions and the subsequent release of gaseous products, in this first phase the amorphous ceramic residue is characterized by an open-pore channel network.

By increasing the temperature, the devitrification process begins: as a direct consequence, the previously fully amorphous structure is progressively lost, and the gradual redistribution of chemical bonds generates a progressive phase separation process, with the generation

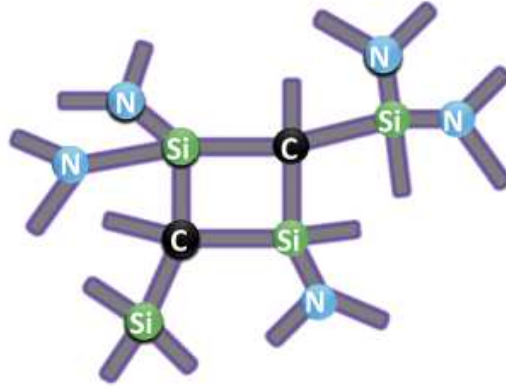


Figure 1.13: Simplified structure of the amorphous network of a polysilazane-derived ceramic, with mixed Si-C and Si-N covalent bonds<sup>9</sup>.

of first crystalline nanodomains (1-3 nm). In Fig. 1.14 an oversimplified model of this microstructure is reported. The porosity previously present can diminish, thanks to viscous flow mechanisms that start to be significant. For this reason, porosity is often defined as "transient". In this phase, although a certain degree of phase separation is achieved, a clear nucleation of crystalline phases has still to be observed. Carbon clusters redistribute as well, to generate a turbostratic ("quasi-graphitic") carbon network, which could further evolve to generate graphitic carbon regions.

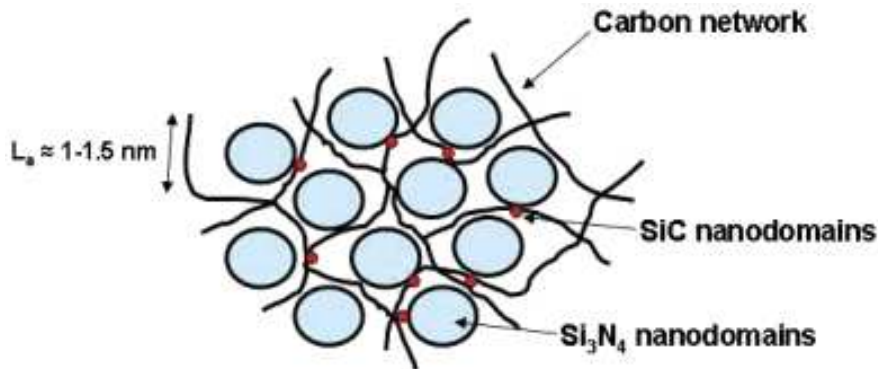


Figure 1.14: Microstructural model for a polysilylcarbodiimide-derived ceramic<sup>9</sup>.

Finally, at high temperatures, the extensive phase separation leads to the formation of crystals of SiC, Si<sub>3</sub>N<sub>4</sub>, SiO<sub>2</sub>, B<sub>4</sub>C, BN, etc., which can further increase their size by a further increase of temperature or of dwell time.

As previously mentioned, the evolution of the amorphous microstructure – characteristic of PDCs pyrolyzed at low temperatures – towards the phase separation and the nucleation of crystalline phases is directly connected with the stability of the amorphous covalent network. Precisely, the type of atoms present plays a fundamental role in determining the temperature range at which first devitrification phenomena are observed.

### 1.4.3 Mechanical properties

Mechanical properties of PDCs are rather difficult to be measured, mainly because of the impossibility of producing sufficiently large bulk components. Some mechanical properties of bulk components have been obtained from samples produced by the pyrolysis of warm-

pressed, partially cross-linked polymer powders<sup>75,76</sup>, or from the casting of a sol-gel solution or a siloxane (for SiOC)<sup>85,86</sup> or a liquid polysilazane (for SiCN), with the realization of small rods<sup>62,87</sup>. Elastic modulus for SiOC is in the 53–113 GPa, while for SiCN is in the 80–155 GPa. They are well below the values for the crystalline counterparts, because of the much more open structure of PDCs network. Densities are in the 1.85–2.35 g/cm<sup>3</sup> range for both SiOC and SiCN systems. Both the elastic modulus and the density generally increase with the increasing treatment temperature<sup>62,85,88</sup>.

Poisson's ratio is generally low, specifically in the 0.21–0.24 range, although even lower values have been reported (e.g. 0.11 for SiOC<sup>89</sup>).

Hardness ranges from 5 to 9 GPa<sup>85,86,89</sup>; toughness is in the 0.56–3 MPa·m<sup>0.5</sup> range<sup>86,88,90–93</sup>.

Creep resistance is surely one of the most attractive mechanical properties of PDCs. Creep is very limited up to 1300°C (SiOC) and 1500°C (SiCN), and it has been proposed that relaxation should be associated with viscous flow involving SiO<sub>2</sub>-rich domains.

Other extensive studies regarded the obtainment of high-performance ceramic fibers (above all, SiC-based fibers). It has been demonstrated, again, that mechanical properties at high temperature are strongly influenced by the presence of oxygen. A reduction of the residual oxygen content was fundamental to increase properties such as creep resistance and high-temperature stability. SiC fibers with a tensile strength and an elastic modulus as high as 6.2 and 440 GPa, respectively, could be produced.

#### 1.4.4 Chemical properties

As verified also for other properties, chemical stability of PDCs is directly related to their microstructure, and the progressive phase separation that is generally observed at high temperatures is, again, fundamental in determining also their chemical behavior.

As a significant demonstrative example concerning their chemical durability characteristics, it has been verified by Sorarù et al.<sup>78</sup> that amorphous silicon oxycarbide (SiOC) obtained both from preceramic polymers (methyl- and methylphenyl-polysiloxanes) and by the sol-gel method show a higher chemical resistance to both strongly basic solutions and HF than pure silica glass, thanks to the presence of Si–C covalent bonds. Moreover, it was demonstrated that siloxane-derived networks show better properties than the sol-gel-derived one. Finally, for temperatures higher than ~1200°C (when phase separation into SiO<sub>2</sub>, SiC and carbon regions inside the amorphous network begins to occur), chemical resistance starts to decrease, since SiO<sub>2</sub> can be more effectively extracted.

Oxidation resistance is another fundamental parameter that has been extensively studied, especially considering that one of the main applications of PDCs is as structural/functional components in high temperature oxidizing environments.

In analogy with the crystalline counterparts (SiC and Si<sub>3</sub>N<sub>4</sub>), polymer derived ceramics generally show a parabolic oxidation regime<sup>94–98</sup>, although generally lower oxidation rates are observed for PDCs, which are generally attributed to the characteristic mixed covalent bonds network of PDCs<sup>99,100</sup>. Oxidation kinetic seems to increase with an increasing amount of "free" residual carbon<sup>9</sup>. Finally, the addition of Al atoms in a SiCN composition was found to be effective in reducing the oxidation rate of the final ceramic, with a stationary parabolic rate observed for t>20 h at 1400°C<sup>101</sup>.

### 1.4.5 Electromagnetic properties

Electrical conductivity  $\sigma$  can vary up to 15 orders of magnitude (from  $10^{-10}$ – $10^{-8}$  to  $1$   $(\Omega \cdot \text{cm})^{-1}$ ), depending on the polymeric precursor, composition, pyrolysis temperature, and atmosphere. For low pyrolysis temperature ( $<600^\circ\text{C}$ ), PDCs can be better described as insulators ( $\sigma < 10^{-10} (\Omega \cdot \text{cm})^{-1}$ ). For amorphous PDCs obtained at pyrolysis temperatures  $>800^\circ\text{C}$ , the conductivity increases with the temperature at which it is measured showing the typical semi-conducting behavior. Metallic-like (electron) conduction with  $\sigma$  as high as  $0.1$ – $1$   $(\Omega \cdot \text{cm})^{-1}$  is found in polysilsesquioxanes-derived SiOC pyrolyzed at high temperatures ( $T > 1400^\circ\text{C}$ ) when a percolation network of  $C_{free}$  is formed. For high-carbon SiOC, such as those obtained from a phenyl-containing polysiloxane, the development of a continuous C network occurs at a lower temperature ( $1100^\circ\text{C}$ ).

The conductivity of PDCs can also be changed by adding filler particles to the preceramic matrix, such as  $\text{MoSi}_2$ <sup>102</sup>, carbon nanotubes<sup>103</sup> or graphene layers, by the formation of an interconnected filler phase.

A rather new finding is the ultrahigh piezoresistivity, i.e. the change of the electrical resistivity due to an applied stress, shown by amorphous PDCs<sup>104</sup>.

The tunable electrical properties, high piezoresistivity, together with the micro fabrication capability and excellent high-temperature thermal and mechanical properties, make the polymer-derived SiCN and SiOC excellent candidate materials for high-temperature sensors and ceramic MEMS for high temperature/corrosive-environment applications<sup>105</sup>, micro glow plugs<sup>26 106</sup> and electrode materials for Li-ion batteries<sup>107 108 109</sup>.

Specific magnetic properties could be imparted to PDCs by the simple introduction of filler with magnetic properties (e.g.  $\alpha$ -iron,  $\text{Fe}_3\text{O}_4$ ,  $\text{Fe}_3\text{Si}$ )<sup>110 111 112</sup> or by the incorporation of metallic iron atoms in the polymer backbone by a chemical modification with organometallic compounds such as ferrocene<sup>113 114</sup>.

### 1.4.6 Optical properties

Very few optical characterizations on PDCs have been carried out during the years, mainly because of their black nature, due to the presence of relatively high amounts of  $sp^2$  hybridized carbon atoms, which form absorbing graphene layers.

However, transparent SiOC glasses were produced by Sorarù et al.<sup>115 116 117</sup> by a careful control of the chemical composition of the starting precursors. The most transparent glasses exhibit an optical absorption edge around  $500$ – $550$  nm, and a broad luminescence band around  $500$  nm, attributable to residual  $sp^2$  carbon clusters. The amount of these clusters is sufficiently high to give an appreciable luminescence, and at the same time sufficiently low not to preclude transparency. In the light of these results, SiOC transparent glasses coped with extra elements such as Eu or Er have been proposed<sup>118 119</sup>. Other examples regards the in-situ formation of Si nanocrystals, which produce a typical luminescence in the  $600$ – $800$  nm range<sup>120</sup>, or C and Au ion irradiation of preceramic polymers<sup>121 122</sup>.

## Chapter 2

# Preceramic polymers containing fillers

### 2.1 Introduction

In Section 1.3.3, the polymer-to-ceramic conversion of preceramic polymers has been discussed. This is probably the most important phase of the whole processing of preceramic polymers: by a pyrolysis process in a selected atmosphere (which could be inert or reactive, oxidizing or non-oxidizing) above  $\sim 400^\circ\text{C}$ , the polymeric component is transformed into a ceramic body by a series of different reactions that progressively eliminate all the organic groups present in the starting precursor and produce a rearrangement of the bonds present to finally generate a fully ceramic component.

It has been mentioned that the polymer-to-ceramic conversion (and, although in a more limited extent, the cross-linking step) is inevitably accompanied by the release of gaseous by-products, which causes a more or less important weight loss (generally not lower than 15%) and a overall shrinkage of the component (10-30% linear shrinkage).

The main problem arises from the fact that, during the pyrolysis process, all the tensions related to the shrinkage of the material and the release of gaseous products could not be relaxed by viscous flow or other mechanisms (although it should be mentioned that some porosity could be eliminated higher temperatures, often referred as "transient" porosity). Cracks (micro and macro) and pores are thus generated in the whole material, that inevitably lead to the destruction of the whole component. This fact represents the fundamental reason why preceramic polymers are not suitable for the realization of relatively large components. The only exceptions are represented by relatively small (few hundreds of microns or less) components, like fibers, coatings or micro-components.

As a direct consequence, a lot of effort has been put during the last years to eliminate (or, at least, to limit) the material shrinkage and the generation of cracks. The most important strategy is surely represented by the introduction of fillers, which is the subject of the present Ph.D. research.

The introduction of secondary fillers has demonstrated to be an extremely effective methodology to limit the global material shrinkage, maintaining at the same time all of the advantages connected to the presence of a polymeric phase, above all, the easy shaping possibilities that polymers could offer. Fillers could be of various nature (ceramic, metallic, polymeric), shape (equiaxed particles, elongate grains, whiskers, platelets, nanotubes, fibers) and dimen-

sions (from nanoparticles to fibers of several centimeters). A further fundamental distinction must also be made between "passive" and "active" fillers, which will be more extensively discussed in Section 2.2 and Section 2.3.

The quantity of fillers introduced is also of fundamental importance, both for passive fillers (since it is directly related with the reduction of global shrinkage) and especially in the case of active fillers.

Of course, the introduction of fillers modifies the properties of the final material, which becomes, in practice, a composite material constituted by a phase deriving from the pyrolysis of a preceramic polymer and one (or more) secondary phase(s) related to the introduction of fillers.

Besides the introduction of fillers, a reduction of shrinkage and cracking have also been achieved by other strategies, such as the direct pyrolysis of specifically-made scaffolds infiltrated by a liquid preceramic polymer<sup>74</sup>, or the warm-pressing of partially cross-linked polymer powders<sup>75,76</sup>.

## 2.2 Passive fillers

Passive fillers represent the most simple solution to effectively reduce shrinkage and formation of cracks in a component obtained by the heat treatment of a preceramic polymer. As the name suggests, passive fillers remain totally inert during the whole processing of the preceramic polymer. They do not undergo any transformation or evolution during the heat treatment and do not react with the ceramic residue of the preceramic polymer, nor with the gaseous by-products released during pyrolysis or the treatment atmosphere. Their only function is to diminish the percentage of the whole volume that evolves during the pyrolysis step, thus reducing the total weight loss, shrinkage and generation of cracks, as well as to favor the escape of gaseous species by the creation of an easier means of escape. A schematic representation of passive fillers action is reported in Fig. 2.1.

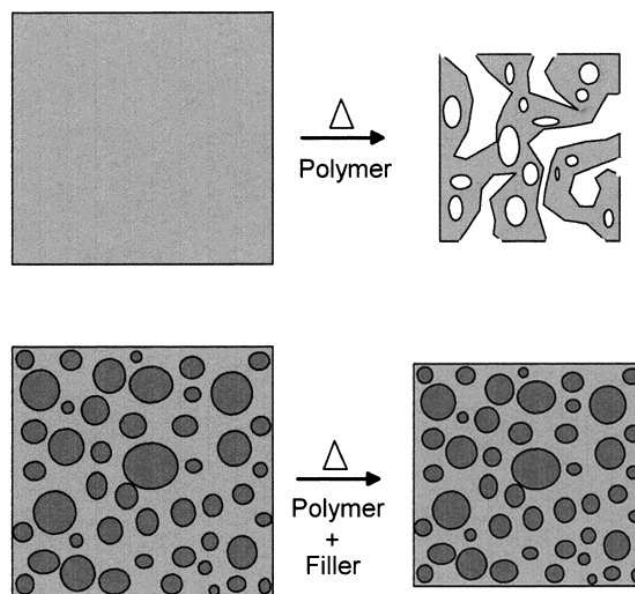


Figure 2.1: Reduction of shrinkage of a PDCs bulk component by the addition of passive fillers.

Typical examples of passive fillers for preceramic polymers are SiC and Si<sub>3</sub>N<sub>4</sub> micro- or nano-powders, but Al<sub>2</sub>O<sub>3</sub>, B<sub>4</sub>C or BN powders has been used as well<sup>11</sup>.

In some cases, when the amount of fillers is predominant over the amount of polymer, the preceramic polymer acts as a low-loss binder that could increase the density of the final part, if compared to analogous parts produced using conventional organic binders, that are completely eliminated after green shaping. The advantageous effects of using preceramic polymers as binders are greatest for powders with the lowest packing densities (ultrafine powders), while a less pronounced effect could be obtained for coarser powders<sup>11</sup>

Preceramic polymers could also be used as sintering aid for pressureless or pressure-aided (e.g. hot-pressing, hot isostatic pressing, spark plasma sintering) sintering of ceramic components. The intergranular phase provided by preceramic polymers, besides acting as a sintering aid during sintering and densification, could also offer enhanced creep resistance at high temperature, due to its higher viscosity (if compared to the intergranular glassy phase that is usually generated when more traditional sintering aids are used, e.g.  $Y_2O_3$ ). In addition, they can provide an improved corrosion resistance and higher mechanical properties. These features are always connected with the characteristic amorphous network of PDCs, which is constituted by a mixture of Si-O, Si-C, Si-N and other covalent bonds (depending on the nature of the starting precursor).

Fillers in general can increase the mechanical properties of the final ceramics. As an example, toughness could be effectively enhanced even at very low (<10 vol%) filler concentrations, thanks to crack-tip bridging phenomena. Generally, the mechanical properties increase with increasing fillers volume fraction up to about 40–50 vol%, followed by a pronounced decrease at higher filler fractions due to enhanced porosity formation (see Fig. 2.2(left)<sup>11</sup>).

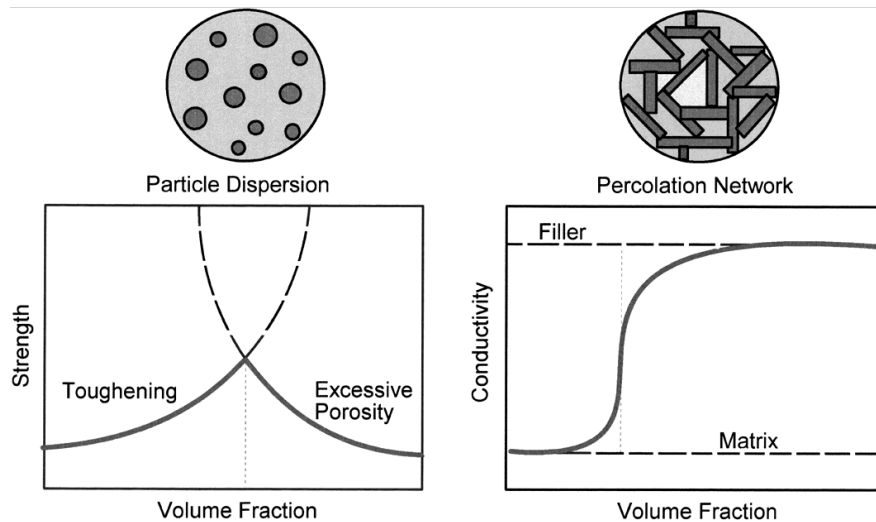


Figure 2.2: Effect of filler loading on the mechanical properties (strength) and field properties (electrical conductivity) of polymer derived ceramics<sup>11</sup>.

The CTE (coefficient of thermal expansion) of the filler phase is also of fundamental importance, since it determines the global CTE of the final composite. A tailorable CTE could be useful in applications such as coatings (e.g. on metals), but it should be noted that a high CTE mismatch between the ceramic residue and the filler(s) could cause the formation of micro-cracks that could have detrimental effects on the final mechanical properties.

Finally, some economic considerations should be done, since the introduction of passive fillers could also represent a way of lowering the cost of the final component.

Some particular fillers, such as  $MoSi_2$ <sup>102</sup>, although still classifiable as “passive”, could impart new specific functional properties to the final ceramic, such as electrical conductivity

or magnetic properties. In these cases the percentage of filler introduced is fundamental: as an example, electrical conductivity does not depend linearly on the percentage of electrically conductive filler introduced, but is subjected to an abrupt increase only when a critical concentration of filler is exceeded. This critical value is often referred as the "percolation threshold", and coincides with the transition from dispersed/isolated particles to an interconnected particles network. Similar results could also be obtained by introducing carbon nanotubes, graphene sheets or carbon nanofibers, to impart electrical conductivity and/or to enhance mechanical properties<sup>103</sup>.

## 2.3 Active fillers

The concept of "active" or "reactive" fillers was introduced in the early 90s, as a result of the work of Prof. Peter Greil and co-workers. It was demonstrated that the use of particular classes of fillers (specifically, but not limited to, metallics and intermetallics) permits the obtainment of a near-net-shape conversion of preceramic polymers into bulk components with extremely limited (or even absent) global shrinkage. Active fillers can increase their volume during pyrolysis by reacting with gaseous species released from the polymer decomposition, or by reacting with the atmosphere of the furnace, thus effectively compensate the polymer shrinkage. A simplified representation of active fillers action is reported in Fig. 2.3 and Fig. 2.4. Fillers progressively evolve during the pyrolysis process, and this reaction, to reduce the global shrinkage, should entail an increase of the filler volume.

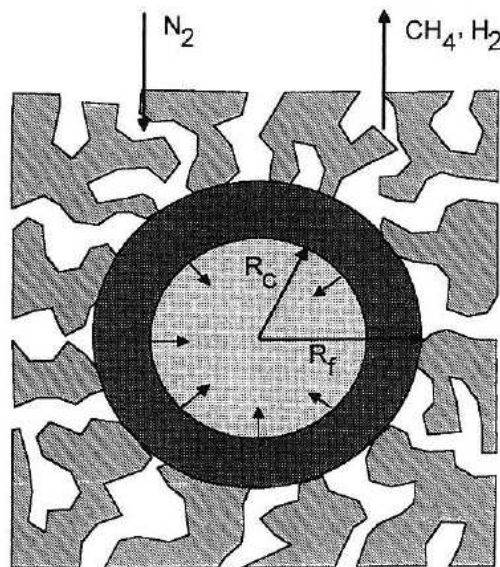


Figure 2.3: Simplified model of filler particle reaction, where  $R_f$  is the starting particle radius and  $R_c$  is unreacted core radius at time  $t$ <sup>12</sup>.

In the case of active fillers, the choice of polymer/fillers combinations could not be done arbitrarily, but must be based on thermodynamic stability criteria, filler expansion characteristics and reaction kinetic limitation (e.g. temperature dependent formation and elimination of transient open porosity, which govern material transport and the reaction process of filler particles)<sup>12</sup>. Linear dimensional changes of less than 0.1% could be obtained with time-temperature controlled pyrolysis of the material, which allow a high precision manu-

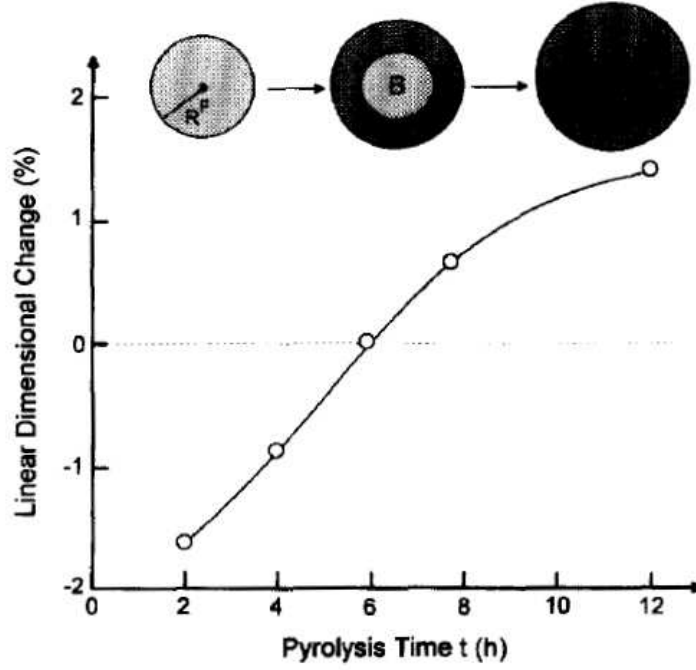


Figure 2.4: Linear dimensional change of polysiloxane/40 vol% boron mixture pyrolyzed at 1480°C in N<sub>2</sub> atmosphere as a function of filler reaction time<sup>72</sup>.

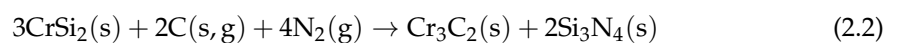
facturing of complex shape components<sup>11</sup>. The resulting material is thus generated by the combination of the preceramic polymer, the active filler introduced, the gaseous by-products deriving from the decomposition of the preceramic polymer, and the treatment atmosphere.

When a precursor is filled with a filler, the following relation represents the total maximum volume change after pyrolysis:

$$\Psi^* = \left(1 - \frac{V_T}{V_T^*}\right) (\alpha\beta - 1) + V_T (\alpha^{TM}\beta^{TM} - 1) \quad (2.1)$$

$\alpha$  represents the ceramic yield of the precursor;  $\beta$  ( $<1$ ) is a density ratio of the precursor, defined as the ratio between the density of the starting polymer and the density of the final ceramic products;  $V_T$  is the filler volume fraction;  $V_T^*$  is a critical filler volume fraction in the starting mixture that determines the maximum particle packing density of the reacted filler phase in the pyrolyzed product;  $\alpha^{TM}$  and  $\beta^{TM}$  describe the mass change of the filler phase and the density ratio in analogy to  $\alpha$  and  $\beta$ . It could be observed that for  $\alpha^{TM}\beta^{TM} > 1$ , a volume expansion of the filler phase could compensate for the polymer shrinkage. Fig. 2.5 shows the normalized linear shrinkage,  $\epsilon^*/\epsilon$ , plotted versus the normalized filler volume fraction,  $V_T/V_T^*$ . With increasing filler expansion characteristics ( $\alpha^{TM}\beta^{TM} > 1$ ), the total linear shrinkage decreases for a given filler volume fraction in the starting mixture. In Tab. 2.1,  $\alpha^{TM}\beta^{TM}$  values for some potential active fillers are reported.

As an example, if CrSi<sub>2</sub> is used as an active filler, at sufficiently high temperatures (around 750°C) it can react with carbon from the ceramic residue of the preceramic polymer (to give the formation of Cr<sub>3</sub>C<sub>2</sub>) and with the nitrogen of the atmosphere (to give the formation of Si<sub>3</sub>N<sub>4</sub>). The global reaction is schematized by the following reaction:



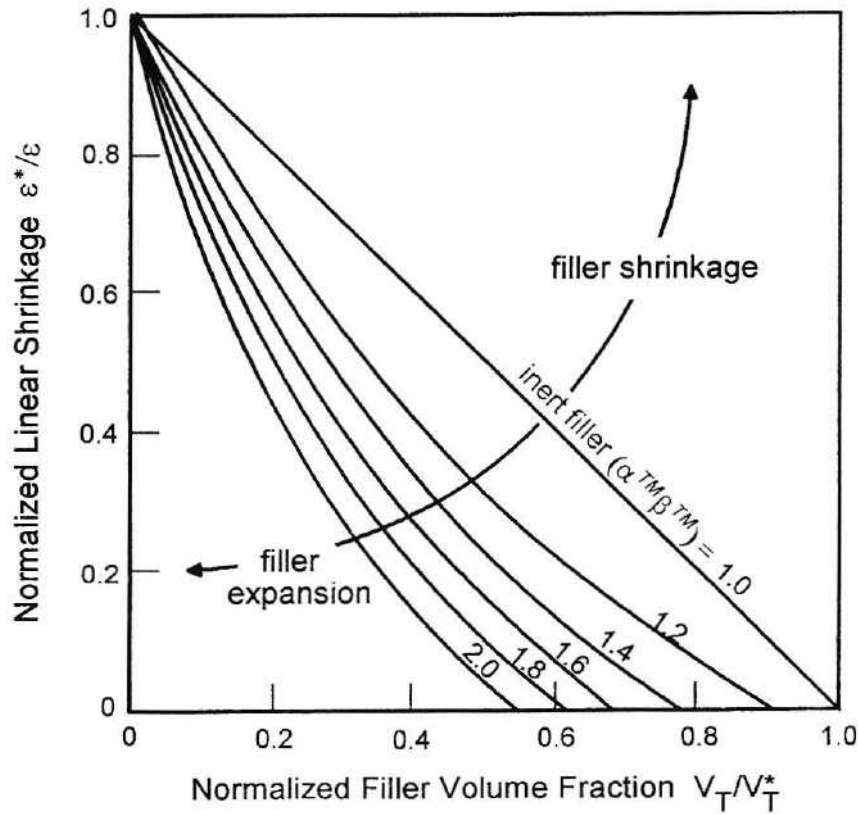


Figure 2.5: Normalized linear shrinkage of polymer-filler systems as a function of normalized filler volume fraction in the starting mixture ( $V_T^*=0.5$  and  $\psi=-0.6$ )

In this case, while the formation of carbides is observed also in argon atmosphere, the formation of  $\text{Si}_3\text{N}_4$  is strictly connected with the nitrogen pressure in the furnace atmosphere. Moreover, the microstructure of the open-pores network (deriving from the pyrolysis of the preceramic polymer) is fundamental as well in determining the reaction of the fillers. For this reason, is generally better to consider the "effective" nitrogen pressure in the open pore channel network, which depends on the nitrogen pressure and the porosity microstructure.

Time is fundamental as well in determining the effectiveness of the active fillers. In fact, the total time required for a complete conversion of a filler particle must consider the diffusion of gaseous reactants through the open porosity surrounding the particle to the surface of the solid, the time of penetration and diffusion of the reactants through the reaction product layer on the particle surface, and finally the time of reaction with the unreacted core at the interface. Based on these considerations and on other thermodynamics parameters, numeric models have been obtained<sup>12</sup>, from which some general trends could be derived. For example, with decreasing particle size, filler reaction time is reduced so that, within a given reaction time, a higher fraction of smaller filler particles is transformed compared to larger particles, and, hence, reduction of overall shrinkage is higher, as described in Fig. 2.6a. A similar tendency should result if the concentration of gaseous reactants increases, as is the case at higher "effective" nitrogen pressures in the pore channel network. With increasing nitrogen pressure, diffusional transport in the porous compact is faster because of a reduction in mean free path length of the gaseous molecules, thus increasing the chemical driving force for filler reaction, and reducing the total shrinkage, as represented in Fig. 2.6b.

Finally, it should also be kept in mind that since the active fillers react with gaseous by-products deriving from the decomposition of the polymeric phase, the final ceramic yield of

Table 2.1: Specific volume changes upon reaction pyrolysis of potential active filler systems<sup>12</sup>

Filler	$\alpha^{TM}\beta^{TM}$		
	Carburization (solid)	Carburization (gaseous)	Nitridation (gaseous)
Ti	0.76 (TiC)	1.14 (TiC)	1.08 (TiN)
V	0.79 (VC)	1.28 (VC)	1.27 (VN)
Cr	0.83 (Cr <sub>3</sub> C <sub>2</sub> )	1.25 (Cr <sub>3</sub> C <sub>2</sub> )	1.5 (CrN)
Zr	0.79 (ZrC)	1.09 (ZrC)	1.03 (ZrN)
Nb	0.85 (NbC)	1.27 (NbC)	1.35 (NbN)
Ta	0.86 (TaC)	1.27 (TaC)	1.25 (TaN)
Mo	0.95 (Mo <sub>2</sub> C)	1.22 (Mo <sub>2</sub> C)	
W	0.84 (WC)	1.32 (WC)	
Al	1.09 c	1.53 (Al <sub>4</sub> C <sub>3</sub> )	1.26 (AlN)
B	0.93 (B <sub>4</sub> C)	1.20 (B <sub>4</sub> C)	2.42 (BN)
Si	0.70 (SiC)	1.07 (SiC)	1.13 (Si <sub>3</sub> N <sub>4</sub> )
MoSi <sub>2</sub>	0.96 (Mo <sub>2</sub> C/SiC)	1.48 (Mo <sub>2</sub> C/SiC)	
CrSi <sub>2</sub>	0.93 (Cr <sub>3</sub> C <sub>2</sub> /SiC)	1.54 (Cr <sub>3</sub> C <sub>2</sub> /SiC)	1.23 (CrN/Si <sub>3</sub> N <sub>4</sub> )
TiSi <sub>2</sub>	0.90 (TiC/SiC)	1.47 (TiC/SiC)	1.53 (TiN/Si <sub>3</sub> N <sub>4</sub> )

the preceramic polymer is then higher than when no active fillers are present.

Although the use of active-filler-controlled pyrolysis of preceramic polymers has proven to be extremely effective in reducing the total amount of porosity in the final ceramics, with consequent improved mechanical properties, it must be said that this technique requires an extremely accurate control of all the pyrolysis conditions, as well as the characteristics of the raw materials. Although theoretical models have been derived for an a priori selection of processing conditions and fillers characteristics, small variations in particle environment, particle distribution and particle physical properties could finally result in significant variations in kinetic variables. For this reason, a trial and error procedure is still generally required to optimize the final properties of the material.

## 2.4 Final considerations

In the previous paragraphs, the main characteristics of passive and active fillers have been described. Both of the strategies has the main objective of reducing the shrinkage and porosity development in polymer derived ceramic components upon pyrolysis, which make the obtainment of relatively large crack-free components virtually impossible.

The introduction of passive fillers is surely the most simple strategy: the "dilution" of the preceramic polymer with a secondary phase which does not evolve during pyrolysis is an effective way to reduce total shrinkage, as well as impart additional features like electrical conductivity or other properties. Passive fillers could be added in relatively large quantities and no special precautions are required.

On the other hand, active fillers demonstrated to be extremely effective for the obtainment of shrinkage-free monoliths: the shrinkage of the preceramic polymer could be totally compensated by the expansion of the active fillers (generally metallic or intermetallic particles) by their reaction with the gaseous by-products produced by the polymer decomposition, as well as from the furnace atmosphere. In this case, an extremely accurate control of the processing conditions (pyrolysis temperature, time and atmosphere), as well as fillers characteristics and amount are essential for the obtainment of the final desired characteristics of the ceramic

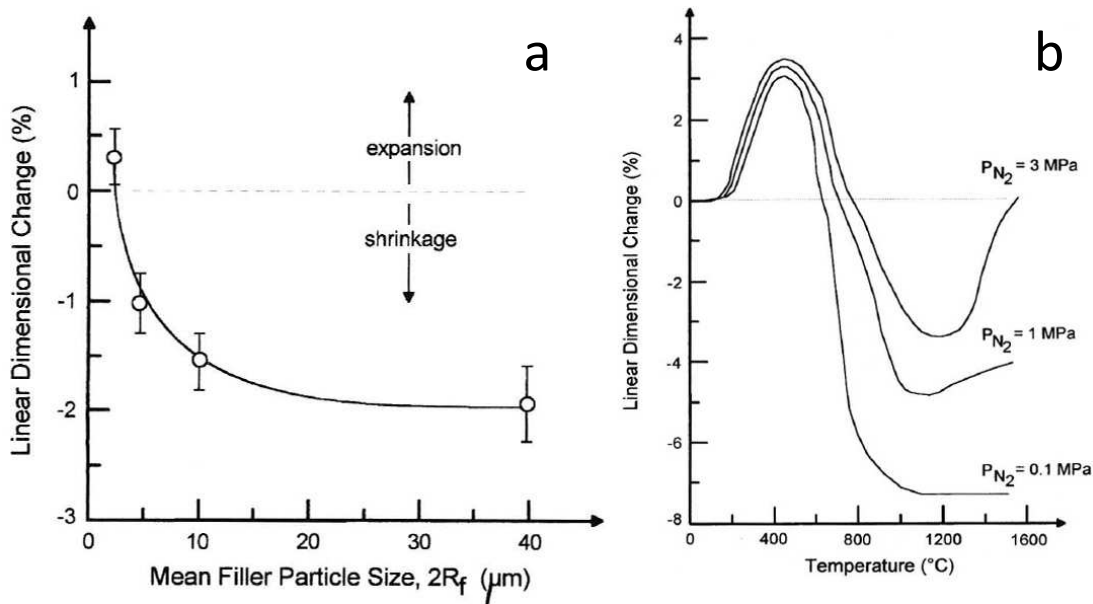


Figure 2.6: Effect of  $\text{CrSi}_2$  filler particle size (a) and of nitrogen pressure (b) on total shrinkage, after pyrolysis at  $1400^{\circ}\text{C}$  in  $\text{N}_2$  atmosphere<sup>12</sup>.

component.

In the case of both passive and active fillers, the ceramic residue is not substantially influenced by the presence of fillers, and the resultant material is in both cases a composite material, comprising of the ceramic residue from the polymer (generally amorphous) and of the filler phase.

Besides these 2 strategies, a relatively new category of fillers has been recently proposed. This new class of fillers are intended to fully or partially react with the ceramic residue of the preceramic polymer, to give the formation of crystalline phase(s) that are generally not directly achievable by the simple pyrolysis of a preceramic polymer. This new strategy can combine the advantages of having a polymeric phase in the raw materials (above all, improved and easier shaping possibilities) with the reduction of shrinkage due to the presence of secondary fillers in the starting mixture and the creation of a highly crystalline material at the end of the heat treatment. In principle, by changing the nature, type and the amount of fillers introduced in the systems, a wide range of ceramic systems can be achieved. This relatively new strategy demonstrated to have extremely promising kinetic characteristics (often comparable to sol-gel derived systems), especially when nano-sized fillers are used, due to both the high reactivity of the amorphous ceramic residue, and to the high specific surface area of the fillers. In addition, nano-grained ceramics could be easily obtained through this methodology, which attracted a lot of interest for their potential improved mechanical characteristics<sup>123-129</sup>. Some first example of this new strategy include the realization of highly pure nano-grained mullite ceramics at temperatures as low as  $1250^{\circ}\text{C}$ <sup>130</sup>, as well as  $\text{SiAlON}$ -based ceramics<sup>73</sup>, cordierite-based ceramics<sup>131</sup> and wollastonite<sup>132</sup>.

In the light of these promising and relatively new results, the present Ph.D. research has been dedicated to a more systematic study of the possibilities that this new strategy could offer. In the following Experimental Chapter, different ceramic systems obtained by preceramic polymers filled with nano-sized particles will be presented. The synthesis characteristics of these materials will be described, as well as some possible potential applications.

## References

- [1] W. Ainger and J. M. Herbert, "The Preparation of Phosphorus-Nitrogen Compounds as Non-Porous Solids"; pp. 168–82 in *Special Ceramics*, Edited by P. Popper. Academic press, New York, 1960.
- [2] P. G. Chantrell and P. Popper, "Inorganic Polymers and Ceramics"; pp. 87–103 in *Special Ceramics*, Edited by P. Popper. Academic Press, New York, 1965.
- [3] Verbeek, "Production of Shaped Articles of Homogeneous Mixtures of Silicon Carbide and Nitride"; *Ger. Offen.*, 2218960 (Bayer AG), November 8, U.S. Patent No. 3853567, 1973.
- [4] W. Verbeek and G. Winter, "Formkoerper aus Siliciumcarbid und Verfahren zu Ihrer Herstellung"; *Ger. Offen.*, 2236078, 1974.
- [5] G. Winter, W. Verbeek, and M. Mansmann, "Formkoerper aus Homogenen Mischungen von Siliciumcarbid und Siliciumnitrid und Verfahren zu Ihrer Herstellung"; *Ger. Offen.*, 2243527, 1974.
- [6] G. Fritz and B. Raabe, "Bildung siliciumorganischer Verbindungen. V. Die Thermische Zersetzung von  $\text{Si}(\text{CH}_3)_4$  und  $\text{Si}(\text{C}_2\text{H}_5)_4$ ," *Z. Anorg. Allg. Chem.*, 286, 149–67 (1956).
- [7] S. Yajima, J. Hayashi, and M. Imori, "Continuous Silicon Carbide Fiber of High Tensile Strength", *Chem. Lett.*, 4 [9] 931–4 (1975).
- [8] S. Yajima, Y. Hasegawa, K. Okamura, and I. Matsuzawa, "Development of High Tensile Strength Silicon Carbide Fibre Using an Organosilicon Polymer Precursor", *Nature (London)*, 273, 525–7 (1978).
- [9] P. Colombo, G. Mera, R. Riedel and G. D. Soraru, "Polymer-Derived Ceramics: 40 Years of Research and Innovation in Advanced Ceramics", *J. Am. Ceram. Soc.*, 1837 1805–1837 (2010).
- [10] W. Krenkel, "Ceramic matrix composites", Springer (2003).
- [11] P. Greil, "Polymer Derived Engineering Ceramics", *Adv. Eng. Mater.*, 2 [6] 339–348 (2000).
- [12] P. Greil, "Active-Filler-Controlled Pyrolysis of Preceramic Polymers", *J. Am. Ceram. Soc.*, 78 [4] 835–848 (1995).
- [13] Abe, Y. and Gunji, T., *Progress in polymer science*, vol. 29 (3), p. 149 (2004).
- [14] Jovanovic, J. D., *Tehnika (Belgrade, Yugoslavia)*, vol. 58, p. 4 (2003).
- [15] R. Riedel, G. Mera, R. Hauser and A. Klönczynski, "Silicon-based polymer-derived ceramics: synthesis, properties and applications - a review", *J. Ceram. Soc. Jpn.*, 114 [6] 425–444 (2006).
- [16] W. J. Noll, *Chemistry and Technology of Silicones*, Academic Press, San Diego, CA, 1968.
- [17] M. Zeldin, "An Overview of Inorganic and Organometallic Polymers"; pp. 151–64 in *Improved Fire- and Smoke Resistant Materials for Commercial Aircraft Interiors*, National Academy Press, Washington D.C., 1995.
- [18] T. C. Kendrick, B. Parbhoo, and J. W. White, "Siloxane Polymers and Copolymers"; pp. 1289–361 in *The Chemistry of Organic Silicon Compounds*, Edited by S. Patai, and Z. Rappoport. John Wiley & Sons, Chichester, 1995.
- [19] R. Corriu, and P. Jutzi (eds). *Tailor-Made Silicon–Oxygen Compounds from Molecules to Materials*, Vieweg & Sohn, Braunschweig/Wiesbaden, Germany, 1996.
- [20] Y. Abe and T. Gunji, "Oligo- and Polysiloxanes", *Progress in Polymer Science*, 29 [3] 149–82 (2004).
- [21] E. Kroke, Y. L. Li, C. Konetschny, E. Lecomte, C. Fasel and R. Riedel, "Silazane derived ceramics and related materials", *Mat. Sci. Eng. R*, 26 [4-6] 97–199 (2000).

- [22] Zeldin, M., Wynne, K. J. and Allcock, H. R., *Inorganic and organometallic polymers*, ACS Symposium series, vol. 360, ACS (1988).
- [23] Zeigler, J. M. and Fearon, F. W. G., *Silicon-based polymer science*, Advances in chemistry series, vol. 144, ACS (1990).
- [24] K. Shiina and M. Kumada, "Thermal Rearrangement of Hexamethyldisilane to Trimethyl(dimethylsilylmethyl)silane", *J. Org. Chem.*, 23, 139–139 (1958).
- [25] M. Birot, J. P. Pillot and J. Dunogues, "Comprehensive chemistry of polycarbosilanes, polysilazanes, and polycarbosilazanes as precursors of ceramics", *Chem. Rev.*, 95 [5] 1443–1477 (1995).
- [26] Miller, R. D. and Michl, J., *Chem. Rev.*, vol. 89, p.1359 (1989) .
- [27] F. S. Kipping, "Organic Derivatives of Silicon. Part XXV. Saturated and Unsaturated Siliconhydrocarbons, Si<sub>4</sub>Ph<sub>8</sub>", *J. Chem. Soc.*, 119, 830–47 (1921).
- [28] R. M. da Rocha, P. Greil, J. C. Bressiani, and A. H. de Almeida Bressiani, "Complex-Shaped Ceramic Composites Obtained by Machining Compact Polymer- Filler Mixtures," *Mater. Res.*, 8, 191–6 (2005).
- [29] R. Haug, M. Weinmann, J. Bill, and F. Aldinger, "Plastic Forming of Pre ceramic Polymers," *J. Eur. Ceram. Soc.*, 19, 1–6 (1999).
- [30] D. Galusek, J. Sedlacek, and R. Riedel, "Al<sub>2</sub>O<sub>3</sub>-SiC Composites Prepared by Warm Pressing and Sintering of an Organosilicon Polymer-Coated Alumina Powder," *J. Eur. Ceram. Soc.*, 27, 2385–92 (2007).
- [31] R. Kumar, Y. Cai, P. Gerstel, G. Rixecker, and F. Aldinger, "Processing, Crystallization and Characterization of Polymer Derived Nano-Crystalline Si-B- C-N Ceramics," *J. Mater. Sci.*, 41, 7088–95 (2006).
- [32] B. C. Mutsuddy, "Use of Organometallic Polymer for Making Ceramic Parts by Plastic Forming Techniques," *Ceram. Inter.*, 13, 41–53 (1987).
- [33] Y.-W. Kim, J.-H. Eom, C. Wang, and C. B. Park, "Processing of Porous Silicon Carbide Ceramics from Carbon-Filled Polysiloxane by Extrusion and Carbothermal Reduction," *J. Am. Ceram. Soc.*, 91, 1361–4 (2008).
- [34] G. Perale, C. Giordano, F. Daniele, M. Masi, P. Colombo, L. Gottardo, and S. Maccagnan, "A Novel Process for the Manufacture of Ceramic Microelectrodes for Biomedical Applications," *Int. J. Appl. Ceram. Technol.*, 5, 37–43 (2008).
- [35] T. Zhang, J. R.G. Evans, and J. Woodthorpe, "Injection Moulding of Silicon Carbide Using an Organic Vehicle Based on a Pre ceramic Polymer," *J. Eur. Ceram. Soc.*, 15, 729–34 (1995).
- [36] S. Walter, D. Suttor, T. Erny, B. Hahn, and P. Greil, "Injection Moulding of Polysiloxane/Filler Mixtures for Oxycarbide Ceramic Composites," *J. Eur. Ceram. Soc.*, 16, 387–93 (1996).
- [37] O. Goerke, E. Feike, T. Heine, A. Trampert, and H. Schubert, "Ceramic Coatings Processed by Spraying of Siloxane Precursors (Polymer-Spraying)," *J. Eur. Ceram. Soc.*, 24, 2141–7 (2004).
- [38] P. Colombo, T. E. Paulson, and C. G. Pantano, "Synthesis of Silicon Carbide Thin Films With Polycarbosilane (PCS)," *J. Am. Ceram. Soc.*, 80, 2333–40 (1997).
- [39] T. P. Smirnova, A. M. Badalian, L. V. Yakovkina, V. V. Kaichev, V. I. Bukhtiyarov, A. N. Shmakov, I. P. Asanov, V. I. Rachlin, and A. N. Fomina, "SiCN Alloys Obtained by Remote Plasma Chemical Vapour Deposition from Novel Precursors," *Thin Solid Films*, 429, 144–51 (2003).

- [40] A. R. Bunsell and A. Piant, "A Review of the Development of Three Generations of Small Diameter Silicon Carbide Fibres," *J. Mater. Sci.*, 41, 823–39 (2006).
- [41] K. Okamura, T. Shimoo, K. Suzuya, and K. Suzuki, "SiC-Based Ceramic Fibers Prepared via Organic-to-Inorganic Conversion Process—A Review," *J. Jpn. Ceram. Soc.*, 114, 445–54 (2006).
- [42] 197K. Satoa, A. Tezuka, O. Funayama, T. Isoda, Y. Terada, S. Kato, and M. Iwata, "Fabrication and Pressure Testing of a Gas-Turbine Component Manufactured by a Pre-ceramic-Polymer-Impregnation Method," *Comp. Sci. Tech.*, 59, 853–9 (1999).
- [43] M. Erdal, S. I. Gu, and S. C. Danforth, "Impregnation Molding of Particle-Filled Pre-ceramic Polymers: Process Modeling," *J. Am. Ceram. Soc.*, 82, 2017–28 (1999).
- [44] I.-K. Sung, S.-B. Yoon, J.-S. Yu, and D.-P. Kim, "Fabrication of Macroporous SiC from Templated Pre-ceramic Polymers," *Chem. Comm.*, 1480–1 (2002).
- [45] P. Colombo, V. Sglavo, E. Pippel, and J. Woltersdorf, "Joining of Reaction-Bonded Silicon Carbide Using a Pre-ceramic Polymer," *J. Mater. Sci.*, 33, 2409–16 (1998).
- [46] C. A. Lewinsohn, P. Colombo, I. Riemanis, and O. Unal, "Stresses Arising During Joining of Ceramics Using Pre-ceramic Polymers," *J. Am. Ceram. Soc.*, 84, 2240–4 (2001).
- [47] C. A. Lewinsohn and S. Elangovan, "Development of Amorphous, Non-Oxide Seals for Solid Oxide Fuel Cells," *Ceram. Eng. Sci. Proc.*, 24 [3] 317–22 (2003).
- [48] T. Hanemann, M. Ade, M. Boerner, G. Molz, M. Schulz, and J. HauXelt, "Microstructuring of Pre-ceramic Polymers," *Adv. Eng. Mater.*, 4, 869–73 (2002).
- [49] M. Schulz, M. Borner, J. HauXelt, and R. Heldele, "Polymer Derived Ceramic Microparts from X-Ray Lithography/Cross-Linking Behavior and Process Optimization," *J. Eur. Ceram. Soc.*, 25, 199–204 (2005).
- [50] H.-J. Lee, T.-H. Yoon, and D.-P. Kim, "Fabrication of Microfluidic Channels Derived from a UV/Thermally Cured Pre-ceramic Polymer via a Soft Lithographic Technique," *Microelect. Eng.*, 84, 2892–5 (2007).
- [51] H. Freimuth, V. Hessel, H. Kolle, M. Lacher, W. Erhfeld, T. Vaahs, and M. Bruck, "Formation of Complex Ceramic Miniaturized Structures by Pyrolysis of Poly(vinylsilazane)," *J. Am. Ceram. Soc.*, 79, 1457–65 (1996).
- [52] H. Yang, P. Deschatelets, S. T. Brittain, and G. M. Whitesides, "Fabrication of High Performance Ceramic Microstructures from a Polymeric Precursor Using Soft Lithography," *Adv. Mater.*, 13, 54–8 (2001).
- [53] Y. Liu, L.-A. Liew, R. Luo, L. An, M. Dunn, V. M. Bright, J. W. Daily, and R. Raj, "Application of Microforging to SiCN MEMS Fabrication," *Sens. Act. A*, 95, 143–51 (2002).
- [54] L.-A. Liew, Y. Liu, R. Luo, T. Cross, L. An, V. M. Bright, M. Dunn, J. W. Daily, and R. Raj, "Fabrication of SiCN MEMS by Photopolymerization of Pre-Ceramic Polymers," *Sens. Act. A*, 95, 143–51 (2002).
- [55] M. J. Pender, K. M. Forsthoefel, and L. G. Sneddon, "Molecular and Polymeric Precursors to Boron Carbide Nanofibers, Nanocylinders, and Nanoporous Ceramics," *Pure Appl. Chem.*, 75, 1287–94 (2003).
- [56] Q.-M. Cheng, L. V. Interrante, M. Lienhard, Q. Shen, and Z. Wu, "Methylene-Bridged Carbosilanes and Polycarbosilanes as Precursors to Silicon Carbide from Ceramic Composites to SiC Nanomaterials," *J. Eur. Ceram. Soc.*, 25, 233–41 (2005).
- [57] H. Termoss, M. Bechelany, B. Toury, A. Brioude, S. Bernard, D. Cornu, and P. Miele, "Shaping Potentialities of Aluminum Nitride Polymeric Precursors Preparation of Thin Coatings and 1D Nanostructures in Liquid Phase," *J. Eur. Ceram. Soc.*, 29, 857–61 (2009).

- [58] T.-H. Yoon, H.-J. Lee, J. Yan, and D.-P. Kim, "Fabrication of SiC Based Ceramic Microstructures from Pre-ceramic Polymers With Sacrificial Templates and Lithographic Techniques—A Review," *J. Jpn. Ceram. Soc.*, 114, 473–9 (2006).
- [59] C. Vakifahmetoglu, I. Menapace, A. Hirsch, L. Biasetto, R. Hauser, R. Riedel and P. Colombo, "Highly porous macro- and micro-cellular ceramics from a polysilazane precursor", *Ceram. Int.*, **35** [8] 3281–3290 (2009).
- [60] B.. Clauss and D.. Schawaller, "Modern Aspects of Ceramic Fiber Development", *Advances in Science and Technology*, **50** 1–8 (2006).
- [61] R. Harshe, C. Balan, and R. Riedel, "Amorphous Si(Al)OC Ceramic from Polysiloxanes: Bulk Ceramic Processing, Crystallization Behavior and Applications," *J. Eur. Ceram. Soc.*, 24, 3471–82 (2004).
- [62] N. Janakiraman and F. Aldinger, "Fabrication and Characterization of Fully Dense Si–C–N Ceramics from a Poly(ureamethylvinyl)Silazane Precursor," *J. Eur. Ceram. Soc.*, 29, 163–73 (2009).
- [63] M. Narisawa, A. Idesaki, S. Kitano, K. Okamura, M. Sugimoto, T. Seguchi, and M. Itoh, "Use of Blended Precursors of Poly(vinylsilane) in Polycarbosilane for Silicon Carbide Fiber Synthesis With Radiation Curing," *J. Am. Ceram. Soc.*, 82, 1045–51 (1999).
- [64] A. Idesaki, M. Sugimoto, S. Tanaka, M. Narisawa, K. Okamura, and M. Itoh, "Synthesis of a Minute SiC Product from Polyvinylsilane With Radiation Curing Part I Radiation Curing of Polyvinylsilane," *J. Mater. Sci.*, 39, 5689–94 (2004).
- [65] A. Idesaki, M. Narisawa, K. Okamura, M. Sugimoto, Y. Morita, T. Seguchi, and M. Itoh, "Application of Electron Beam Curing for Silicon Carbide Fiber Synthesis from Blend Polymer of Polycarbosilane and Polyvinylsilane," *Radiat. Phys. Chem.*, 60, 483–7 (2001).
- [66] D. T. Welna, J. D. Bender, X. Wei, L. G. Sneddon, and H. R. Allcock, "Preparation of Boron-Carbide/Carbon Nanofibers from a Poly(norbornenyldecaborane) Single-Source Precursor via Electrostatic Spinning," *Adv. Mater.*, 17, 859–62 (2005).
- [67] T. A. Pham, P. Kim, M. Kwak, K. Y. Suh, and D.-P. Kim, "Inorganic Polymer Photoresist for Direct Ceramic Patterning by Photolithography," *Chem. Comm.*, 39, 4021–3 (2007).
- [68] M. Schulz, M. Borner, J. Gottert, T. Hanemann, J. Hausselt, and G. Motz, "Cross Linking Behaviour of Pre-ceramic Polymers Effected by UV- and Synchrotron Radiation," *Adv. Eng. Mater.*, 6, 676–80 (2004).
- [69] M. N. Rahaman, "Ceramic processing and sintering", CRC (2003).
- [70] F. I. Hurwitz, P. Heimann, S. C. Farmer and D. M. Hembree, "Characterization of the pyrolytic conversion of polysilsesquioxanes to silicon oxycarbides", *Journal of Materials Science*, **28** [24] 6622–6630 (1993).
- [71] T. Isoda, H. Kaya, H. Nishii, O. Funayama, T. Suzuki and Y. Tashiro, "Perhydropolysilazane precursors to silicon nitride ceramics", *J. Inorg. Organomet. P.*, **2** [1] 151–160 (1992).
- [72] P. Greil, "Near Net Shape Manufacturing of Polymer Derived Ceramics", *J. Eur. Ceram. Soc.*, **132-136** 1981–1984 (1997).
- [73] E. Bernardo, P. Colombo and S. Hampshire, "SiAlON-Based Ceramics from Filled Pre-ceramic Polymers", *J. Am. Ceram. Soc.*, **89** [12] 3839–3842 (2006).
- [74] Available at <http://www.ceramicore.com>.
- [75] R. Riedel, G. Passing, H. Schönfelder, and R. J. Brook, "Synthesis of Dense Silicon-Based Ceramics at Low Temperatures," *Nature* (London), 355, 714–7 (1992).
- [76] G. D. Sorarù, V.M. Sglavo, F. Vulcan, and F. Babonneau, "Fabrication and Characterization of  $\beta'$ -sialon Components from Polymeric Precursors," *Mater. Res. Soc. Symp. Proc.*, 287, 245–50 (1993)..

- [77] G. D. Soraru and D. Suttor, "High temperature stability of sol-gel-derived SiOC glasses", *J. Sol-gel Sci. Techn.*, **14** 69—74 (1999).
- [78] G. D. Soraru, S. Modena, E. Guadagnino, P. Colombo, J. Egan and C. Pantano, "Chemical Durability of Silicon Oxycarbide Glasses", *J. Am. Ceram. Soc.*, **85** [6] 1529–1536 (2002).
- [79] R. E. Loehman, "Oxynitride Glasses"; pp. 119–49 in *Treatise on Materials Science and Technology*, Vol. 26, Glass IV. Edited by M. Tomozawa and R. H. Doremus. Academic Press, New York, 1985.
- [80] D. Galusek, S. Reschke, R. Riedel, W. Drebler, P. Sajgalik, Z. Lenčič and J. Majling, "In-Situ Carbon Content Adjustment in Polysilazane Derived Amorphous SiCN Bulk Ceramics", *Journal of the European Ceramic Society*, **19** [10] 1911–1921 (1999).
- [81] Gary. T. Burns and Grish. Chandra, "Pyrolysis of Preceramic Polymers in Ammonia: Preparation of Silicon Nitride Powders", *J. Am. Ceram. Soc.*, **72** [2] 333–337 (1989).
- [82] K. Okamura, M. Sato and Y. Hasegawa, "Silicon nitride fibers and silicon oxynitride fibers obtained by the nitridation of polycarbosilane", *Ceram. Int.*, **13** [1] 55–61 (1987).
- [83] E. Ionescu, C. Linck, C. Fasel, M. Muller, H. J. Kleebe and R. Riedel, "Polymer-Derived SiOC/ZrO<sub>2</sub> Ceramic Nanocomposites with Excellent High-Temperature Stability", *J. Am. Ceram. Soc.*, **93** [1] 241–250 (2010).
- [84] G. D. Soraru, A. Ravagni, R. Camprostrini and F. Babonneau, "Synthesis and characterization of beta-SiAlON ceramics from organosilicon polymers", *J. Am. Ceram. Soc.*, **74** [9] 2220–2223 (1991).
- [85] G. D. Soraru', E. Dallapiccola, and G. D'Andrea, "Mechanical Characterization of Sol-Gel-Derived Silicon Oxycarbide Glasses," *J. Am. Ceram. Soc.*, **79**, 2074–80 (1996)..
- [86] G. M. Renlund, S. Prochazka, and R. H. Doremus, "Silicon Oxycarbide Glasses: Part II. Structure and Properties," *J. Mater. Res.*, **6**, 2723–34 (1991)..
- [87] S. R. Shah and R. Raj, "Mechanical Properties of a Fully Dense Polymer Derived Ceramic Made by a Novel Pressure Casting Process," *Acta Mater.*, **50**, 4093–103 (2002)..
- [88] 438K. V. Moraes and L. V. Interrante, "Processing, Fracture Toughness, and Vickers Hardness of Allylhydridopolycarbosilane-Derived Silicon Carbide," *J. Am. Ceram. Soc.*, **86**, 342–6 (2003)..
- [89] C. Moysan, R. Riedel, R. Harshe, T. Rouxel, and F. Augereau, "Mechanical Characterization of a Polysiloxane-Derived SiOC Glass," *J. Eur. Ceram. Soc.*, **27**, 397–403 (2007).
- [90] T. Nishimura, R. Haug, J. Bill, G. Thurn, and F. Aldinger, "Mechanical and Thermal Properties of Si–C–N Material from Polyvinylsilazane," *J. Mater. Sci.*, **33**, 5237–41 (1998)..
- [91] A. Bauer, M. Christ, A. Zimmermann, and F. Aldinger, "Fracture Toughness of Amorphous Precursor-Derived Ceramics in the Silicon–Carbon–Nitrogen System," *J. Am. Ceram. Soc.*, **84**, 2203–07 (2001)..
- [92] N. Janakiraman, Z. Burghard, and F. Aldinger, "Fracture Toughness Evaluation of Precursor-Derived Si–C–N Ceramics Using the Crack Opening Displacement Approach," *J. Non-Cryst. Sol.*, **355**, 2102–13 (2009)..
- [93] 439T. Rouxel, J.-C. Sangleb!uf, J.-P. Guin, V. Keryvin, and G. D. Soraru', "Surface Damage Resistance of Gel-Derived Oxycarbide Glasses: Hardness, Toughness and Scratchability," *J. Am. Ceram. Soc.*, **84**, 2220–4 (2001)..
- [94] G. Chollon, "Oxidation Behaviour of Ceramic Fibres from the Si–C–N–O System and Related Sub-Systems," *J. Eur. Ceram. Soc.*, **20**, 1959–74 (2000)..
- [95] S. Modena, G. D. Soraru', Y. Blum, and R. Raj, "Passive Oxidation of an Effluent System: The Case of Polymer-Derived SiCO," *J. Am. Ceram. Soc.*, **88**, 339–45 (2005)..

- [96] L. Bharadwaj, Y. Fan, L. Zhang, D. Jiang, and L. An, "Oxidation Behavior of a Fully Dense Polymer-Derived Amorphous Silicon Carbonitride Ceramic," *J. Am. Ceram. Soc.*, 87, 483–6 (2004)..
- [97] P. Baldus, M. Jansen, and D. Sporn, "Ceramic Fibers for Matrix Composites in High-Temperature Engine Applications," *Science*, 285, 699–703 (1999)..
- [98] S. Bernard, D. Cornu, P. Miele, M. Weinmann, and F. Aldinger, "Polyborosilazane-Derived Ceramic Fibers in the Si-B-C-N Quaternary System for High-Temperature Applications," *Ceram. Eng. Sci. Proc.*, 26, 35–42 (2005)..
- [99] T. Varga, A. Navrotsky, J. L. Moats, R. Michelle Morcos, F. Poli, K. Muller, A. Saha, and R. Raj, "Thermodynamically Stable SixOyCz Polymer-Like Amorphous Ceramics," *J. Am. Ceram. Soc.*, 90, 3213–9 (2007)..
- [100] R. M. Morcos, A. Navrotsky, T. Varga, D. Ahn, A. Saha, F. Poli, K. Muller, and R. Raj, "Thermodynamically Stable SiwCxNyOz Polymer-Like, Amorphous Ceramics Made from Organic Precursors," *J. Am. Ceram. Soc.*, 91 [7] 2391–3 (2008)..
- [101] Y. Wang, Y. Fan, L. Zhang, W. Zhang, and L. An, "Polymer-Derived Si-AlCN Ceramics Resist Oxidation at 1400°C," *Scr. Mater.*, 55, 295–7 (2006)..
- [102] J. Cordelair and P. Greil, "Electrical Characterization of Polymethylsiloxane/MoSi<sub>2</sub>-Derived Composite Ceramics," *J. Am. Ceram. Soc.*, 84, 2256–9 (2001).
- [103] E. Ionescu, A. Francis, and R. Riedel, "Dispersion Assessment and Studies on AC Percolative Conductivity in Polymer-Derived Si-C-N/CNT Ceramic Nanocomposites," *J. Mater. Sci.*, 44, 2055–62 (2009)..
- [104] L. G. Zhang, Y. S. Wang, Y. Wei, W. X. Xu, D. J. Fang, L. Zhai, K. C. Lin, and L. N. An, "A Silicon Carbonitride Ceramic With Anomalously High Piezoresistivity," *J. Am. Ceram. Soc.*, 91 [4] 1346–9 (2008)..
- [105] L.-A. Liew, R. A. Saravanan, V. M. Bright, M. L. Dunn, J. W. Daily, and R. Raj, "Processing and Characterization of Silicon Carbon-Nitride Ceramics: Application of Electrical Properties Towards MEMS Thermal Actuators," *Sens. Act. A: Phys.*, 103 [1–2] 171–81 (2003)..
- [106] L. A. Liew, V. M. Bright, and R. Raj, "A Novel Micro Glow Plug Fabricated from Polymer-Derived Ceramics: In Situ Measurement of High-Temperature Properties and Application to Ultrahigh-Temperature Ignition," *Sensors Actuators A: Phys.*, 104 [3] 246–62 (2003).
- [107] W. Xing, A. M. Wilson, K. Eguchi, G. Zank, and J. R. Dahn, "Pyrolyzed Polysiloxanes for Use as Anode Materials in Lithium-Ion Batteries," *J. Electrochem. Soc.*, 144 [7] 2410–6 (1997)..
- [108] R. Kolb, C. Fasel, V. Liebau-Kunzmann, and R. Riedel, "SiCN/C-Ceramic Composite as Anode Material for Lithium Ion Batteries," *J. Eur. Ceram. Soc.*, 26 [16] 3903–8 (2006)..
- [109] H. Fukui, H. Ohsuka, T. Hino, and K. Kanamura, "Preparation of Microporous Si-O-C Composite Material and Its Lithium Storage Capability," *Chem. Lett.*, 38 [1] 86–7 (2009)..
- [110] L. Biasetto, A. Francis, P. Palade, G. Principi, and P. Colombo, "Polymer-Derived Microcellular SiOC Foams With Magnetic Functionality," *J. Mater. Sci.*, 43, 4119–26 (2008)..
- [111] A. Saha, S. R. Saha, R. Raj, and S. E. Russek, "Polymer-Derived SiCN Composites With Magnetic Properties," *J. Mater. Res.*, 18, 2549–51 (2003)..
- [112] R. Hauser, A. Francis, R. Theismann, and R. Riedel, "Processing and Magnetic Properties of Metal-Containing SiCN Ceramic Micro- and Nano-Composites," *J. Mater. Sci.*, 43, 4042–9 (2008)..
- [113] B.-Z. Tang, R. Petersen, D. A. Foucher, A. J. Lough, N. Coombs, R. Sodhi, and I. Manners, "Novel Ceramic and Organometallic Depolymerization Products from Poly(Ferrocenylsilanes) via Pyrolysis," *J. Chem. Soc., Chem. Commun.*, 523–5 (1993)..

- [114] R. Petersen, D. A. Foucher, B.-Z. Tang, A. J. Lough, N. P. Raju, J. E. Greedan, and I. Manners, "Pyrolysis of Poly(Ferrocenylsilanes) Synthesis and Characterization of Ferromagnetic Transition Metal Containing Ceramics and Molecular Depolymerization Products," *Chem. Mater.*, **7**, 2045–53 (1995)..
- [115] F. Babonneau, G. D. Soraru, G. D'Andrea, S. Dire', and L. Bois, "Silicon- Oxycarbide Glasses from Sol–Gel Precursors," *Mater. Res. Soc. Symp. Proc.*, **271**, 789–94 (1992)..
- [116] G. D. Soraru, "Silicon Oxycarbide Glasses from Gels," *J. Sol–Gel Sci. Technol.*, **2**, 843–8 (1994)..
- [117] G. D. Soraru, G. D'Andrea, R. Campostrini, and F. Babonneau, "Si–O–C Glasses from Gels"; pp. 135–46 in *Sol–Gel Science and Technology*, Edited by E. J. A. Pope, S. Sakka, and L. Klein. Am. Ceram. Soc., Westerville, OH, 1994..
- [118] Y. Zhang, A. Quaranta, and G. D. Soraru, "Synthesis and Luminescent Properties of Novel Eu<sup>2+</sup>-Doped Silicon Oxycarbide Glasses," *Opt. Mater.*, **24**, 601–5 (2004)..
- [119] G. D. Soraru, Y. Zhang, M. Ferrari, L. Zampedri, and R. R. Goncalves, "Novel Er-Doped SiC/SiO<sub>2</sub> Nanocomposites: Synthesis via Polymer Pyrolysis and Their Optical Characterization," *J. Eur. Ceram. Soc.*, **25**, 277–81 (2004)..
- [120] G. D. Soraru, S. Modena, P. Bettotti, G. Das, G. Mariotto, and L. Pavesi, "Si nanocrystals Obtained Through Polymer Pyrolysis," *Appl. Phys. Lett.*, **83**, 749–51 (2003)..
- [121] J. C. Pivin, P. Colombo, and G. D. Soraru, "Comparison of Ion Irradiation Effects in Silicon-Based Preceramic Thin Films," *J. Am. Ceram. Soc.*, **83**, 713–20 (2000)..
- [122] J. C. Pivin, P. Colombo, A. Martucci, G. D. Soraru, E. Pippel, and M. Sendova-Vassileva, "Ion Beam Induced Conversion of Si-Based Polymers and Gels Layers into Ceramics Coatings," *J. Sol–Gel Sci. Technol.*, **26**, 251–5 (2003)..
- [123] K. Niihara, "New design concept of structural ceramics - Ceramic nanocomposites", *J. Ceram. Soc. Jpn.*, **99** [1154] 974–982 (1991).
- [124] M. J. Mayo, "Processing of nanocrystalline ceramics from ultrafine particles", *Int. Mater. Rev.*, **41** [3] 85–115 (1996).
- [125] I. W. Chen and X. H. Wang, "Sintering dense nanocrystalline ceramics without final-stage grain growth", *Nature*, **404** [6774] 168–171 (2000).
- [126] F. Wakai, S. Sakaguchi and Y. Matsuno, "Superplasticity of yttria-stabilized tetragonal ZrO<sub>2</sub> polycrystals", *Adv. Cer. Mat.*, (1986).
- [127] J. Karch and R. Birringer, "Nanocrystalline ceramics: possible candidates for net-shape forming", *Ceram. Int.*, **16** [5] 291–294 (1990).
- [128] J. Karch, R. Birringer and H. Gleiter, "Ceramics Ductile at Low Temperature", *Nature*, **330** [6148] 556–558 (1987).
- [129] J. Binner and B. Vaidhyanathan, "Processing of bulk nanostructured ceramics", *J. Eur. Ceram. Soc.*, **28** [7] 1329–1339 (2008).
- [130] E. Bernardo, P. Colombo, E. Pippel and J. Woltersdorf, "Novel Mullite Synthesis Based on Alumina Nanoparticles and a Preceramic Polymer", *J. Am. Ceram. Soc.*, **89** [5] 1577–1583 (2006).
- [131] I. H. Song, M. J. Kim, H. D. Kim and Y. W. Kim, "Processing of microcellular cordierite ceramics from a preceramic polymer", *Scripta Materialia*, **54** [8] 1521–1525 (2006).
- [132] E. Bernardo, E. Tomasella and P. Colombo, "Development of multiphase bioceramics from a filler-containing preceramic polymer", *Cerami. Int.*, **35** [4] 1415–1421 (2009).



## **Part II**

# **Experimental**



# Chapter 3

## Silicates

### 3.1 Mullite/Zirconia nanocomposites

#### 3.1.1 Introduction

Mullite ( $3\text{Al}_2\text{O}_3 \cdot 2\text{SiO}_2$ ) is an excellent candidate for high temperature structural and electric applications. Properties such as low density, high temperature mechanical properties, high thermal shock resistance, low thermal expansion coefficient, corrosion resistance and high thermal stability make this material very suitable for spacecraft components (e.g. ceramic composite heat shields), aircraft engine parts, ceramic filters and environmental barrier coatings (EBCs) for aircraft engines, powerplant turbines and porous burners<sup>1,2</sup>. Unfortunately, an extensive utilization of this material in engineering applications is often hindered by the very low fracture toughness for mullite ( $2.5 \text{ MPa} \cdot \text{m}^{0.5}$ )<sup>3</sup>. The possibility of increasing the toughness of mullite would in turn improve its mechanical reliability, and dramatically extend its utilization in a wide range of engineering fields.

The toughening mechanism associated to the t→m (tetragonal-to-monoclinic) transformation of zirconia is undoubtedly one of the most effective strategies to increase the toughness of ceramics, and surely one of the most important breakthroughs in the world of ceramics. Before the discovery of this phenomenon in 1975<sup>4</sup>, the general interest on  $\text{ZrO}_2$  ceramics was very limited, especially as a structural or engineering ceramic.  $\text{ZrO}_2$  is characterized by 3 different allotropic forms: monoclinic (stable at lower temperature), tetragonal (stable at intermediate temperatures) and cubic (high-temperature form). In Fig. 3.2 the 3 crystalline  $\text{ZrO}_2$  allotropic forms are reported, while the characteristic temperatures of transformation are reported in Fig. 3.1.

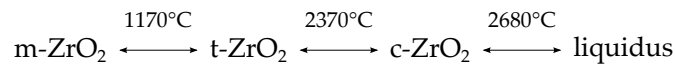


Figure 3.1: Transformation temperatures of  $\text{ZrO}_2$  allotropic forms.

The main limitation on its applicability was represented by the tetragonal-to-monoclinic displacive phase transformation that occurs around  $950^\circ\text{C}$  on cooling in pure  $\text{ZrO}_2$ , which is accompanied by a shear strain of  $\sim 0.16$  and a volume expansion of 4%. As a direct consequence, catastrophic fracture is generally observed for pure- $\text{ZrO}_2$  ceramics, which strongly hinders its reliability in structural components. The discovery that the t→m transformation might be controlled to enhance mechanical properties has constituted a pivotal point in the development of improved engineering ceramics in general and the study of toughening in

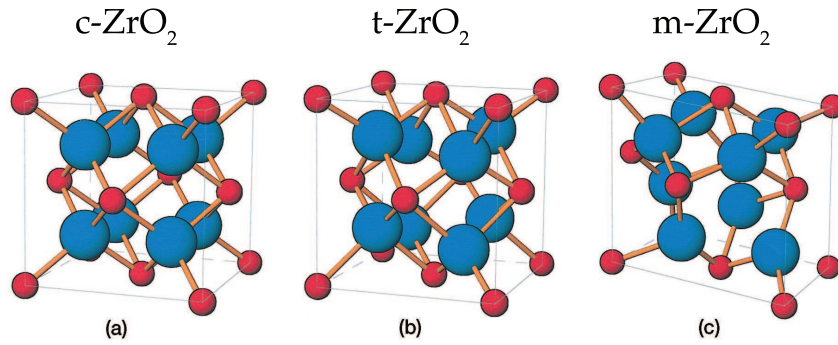


Figure 3.2: Schematic representation of  $\text{ZrO}_2$  allotropic forms: a) cubic, (b) tetragonal and (c) monoclinic.

ceramic systems in particular. This phenomenon has been extensively studied and successfully applied in many different ceramic systems. Above all, the most important examples of the effectiveness of this phenomenon are surely represented by stabilized  $\text{ZrO}_2$  and ZTA (Zirconia-Toughened Alumina)<sup>5</sup>.

The primary fabrication objective for any transformation-toughened ceramic (TTC) material is production and retention of a metastable  $t\text{-ZrO}_2$  phase that transforms to  $m\text{-ZrO}_2$  at/or near room temperature under the influence of any applied stress including a significant shear component. Control of composition, generally with aliovalent cations, and thermal treatment must then produce a  $t$ -phase microstructure with an  $M_s$  temperature ("martensite-start" temperature, at which the  $t \rightarrow m$  transformation occurs) such that spontaneous transformation does not occur on cooling to room temperature. In a ceramic containing a suitable distribution of metastable  $t\text{-ZrO}_2$ , the stress-activated  $t \rightarrow m$  transformation in the stress field of a potentially damaging crack imparts useful toughness to the ceramic through mechanisms associated with the accommodation of the transformation shape change. The volume change accompanying transformation creates a compressive strain field about the crack tip to oppose crack propagation, while the strain energy associated with any net shear component of the transformation strain in the transformation zone contributes an effective increase in the energy of fracture.

In polycrystalline tetragonal zirconia (TZP), suitable additions of the stabilizing oxides  $\text{Y}_2\text{O}_3$  and  $\text{CeO}_2$  to  $\text{ZrO}_2$ , combined with relatively high cooling rates from sintering and solution treatment temperatures, permit metastable  $t\text{-ZrO}_2$  to be retained to room temperature in the form of an equiaxed, fine-grained ( $0.5\text{--}3\ \mu\text{m}$  grain diameter) polycrystalline aggregate. Zirconia-toughened ceramics instead are constituted by dispersed particles of metastable  $t\text{-ZrO}_2$  in a stable ceramic matrix. For this class of ceramics (which comprises the subject of this work, i.e. mullite/zirconia composites), it has been demonstrated that an extremely accurate control of many significant microstructural and compositional aspects (concentration, distribution, particle size of tetragonal zirconia phase, solubility of different oxides in zirconia phases, etc.) is fundamental for the retention of the  $t$ -phase at room temperature, and for its subsequent transformation into the  $m$ -form<sup>6–10</sup>.

All the different models that have been proposed in the last decades to describe this toughening mechanism managed to capture the essence of transformation toughening and to provide a firm foundation for the topic. All the models shared an emphasis on the development of a transformed "process" zone associated with an advancing crack, where it was assumed

that metastable grains or particles of the t-phase could undergo a martensitic transformation in the crack-tip stress field. This continues to be the essential principle underlying the more-recent models and the refinements of the earlier ones. In Fig. 3.3 is reported a schematic representation of the transformation toughening mechanism and the characteristic R-curve behavior of this class of ceramics.

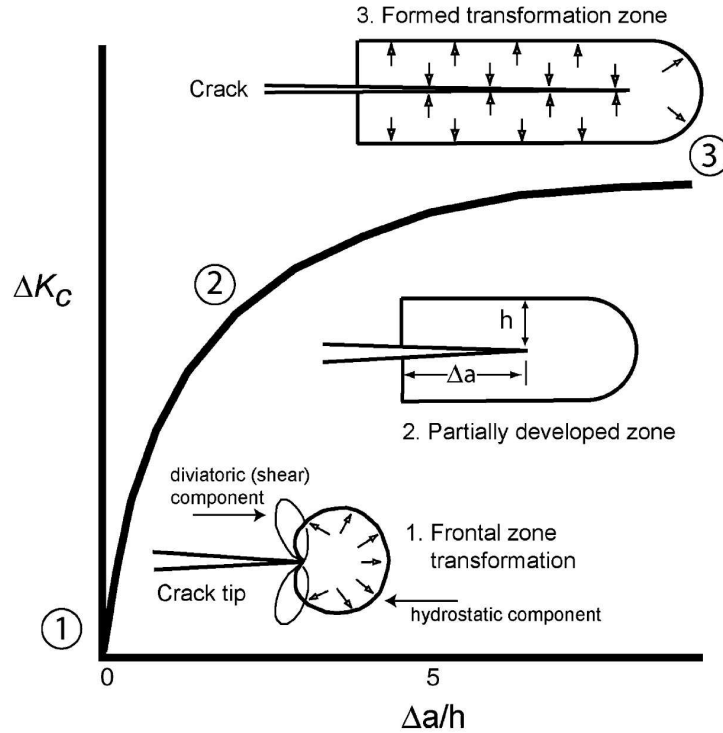


Figure 3.3: Schematic representation of an R-curve behavior of a transformation-toughened ceramic.

In Fig. 3.3,  $\Delta K_C$  represents all the "crack-shielding" contributions to the global toughness of a brittle material, which could be generally described with the relation

$$K_{IC} = K_0 + \Delta K_C \quad (3.1)$$

where  $K_0$  represents the toughness of the matrix.

When little or no R-curve exists, at a critical stress, the crack extends with no additional increase in toughness, and the material generally fails catastrophically. Materials containing extrinsic toughening mechanisms exhibit R-curve behavior when the applied stress is at a value sufficient to propagate the crack but below the fracture stress. Under these circumstances, the process zone and shielding zones are developed, resulting in continually increasing toughness until a saturation level or critical stress intensity is reached, whereupon the crack propagates in an unstable manner, and the material fractures.

Mullite is one of the ceramic matrices that may be toughened by the dispersion of tetragonal zirconia particles, as reported by Schneider<sup>1</sup>. Following the same author, there are many fabrication routes for mullite-zirconia composites, such as sintering of mullite and zirconia powders, reaction sintering of zirconia and mullite precursors, or of  $ZrO_2-Al_2O_3-SiO_2$  mixtures, reaction sintering of zircon and alumina, reaction bonding of aluminum metal, alumina and zircon, crystallization of rapidly quenched melts in the  $ZrO_2-Al_2O_3-SiO_2$  system, and other miscellaneous fabrication methods<sup>1</sup>.

One of the main aims of the present work is exploring the feasibility of an additional route for the fabrication of mullite-zirconia composites, based on the use of a silicone resin (acting as silica source) filled with  $\text{Al}_2\text{O}_3$  and  $\text{ZrO}_2$  nano-particles. Due to the nanometric size of the zirconia reinforcement, the obtained ceramics can be included in the field of bulk nano-structured ceramics and nano-composites, that have attracted a remarkable attention, in the light of their interesting structural characteristics, in the last two decades<sup>11-17</sup>.

As a starting point of the present work, the mullite synthesis route from a preceramic polymer filled with nano-sized  $\gamma\text{-Al}_2\text{O}_3$  proposed by Bernardo et al.<sup>18</sup> was considered. This methodology has been demonstrated to be extremely effective for the obtainment of fine-grained pure mullite phase. This system, as demonstrated by Griggio et al.<sup>19</sup>, is characterized by a remarkable reactivity, comparable even with diphasic sol-gel systems.

### 3.1.2 Experimental procedure

In the main part of this work, a commercial polysilsesquioxane (Silres® MK) was dissolved in isopropanol and mixed with  $\gamma\text{-Al}_2\text{O}_3$  nano-sized powders (AEROXIDE® Alu C) and  $\text{ZrO}_2$  nano-sized powders (VP Zirconium Oxide PH; VP Zirconium Oxide 3-YSZ; TZ-0), thus producing dispersions with 20% solid content. The  $\gamma\text{-Al}_2\text{O}_3$ /polysilsesquioxane weight ratio was kept constant in all the dispersions, and equal to 2.125 (this value was obtained considering both the  $3\text{Al}_2\text{O}_3 \cdot 2\text{SiO}_2$  molar ratio of mullite, and the ceramic yield of the preceramic polymer after heat treatment in air, being 84 wt%).  $\text{ZrO}_2$  nano-sized powders were introduced in the proper quantity to obtain the desired zirconia content in the final composites. Some materials were produced adding  $\text{TiO}_2$  nano-sized powder (VP P90), in an amount of 3 wt% related to the mullite amount after heat treatment.

A first part concerned the synthesis of mullite/20 vol%  $\text{ZrO}_2$  nano-composites using three different starting  $\text{ZrO}_2$  nano-sized powders (Evonik VP-PH, Evonik VP-3YSZ and Tosoh TZ-0), and the respective samples were labeled as MZD20, MZDY20 and MZT20. Based on these preliminary results, more samples with 0, 10, 20 and 30 vol% zirconia were produced using exclusively Evonik VP-PH  $\text{ZrO}_2$  nano-sized powders, which were labeled MZDx, where x is equal to the vol% of zirconia. These new samples were produced with and without the introduction of  $\text{TiO}_2$  as sintering aid; samples containing also  $\text{TiO}_2$  were labeled MZDx\_Ti3.

Other experiments regarded the utilization of chemically-modified oxide powders as starting fillers. This work was made in collaboration with the Department of Material Science and Chemical Engineering of Politecnico di Torino. This methodology<sup>20,21</sup> consisted on a modification of the  $\text{Al}_2\text{O}_3$  powders with inorganic metal salts prior to the realization of the polymer/powders dispersions described before.  $\gamma\text{-Al}_2\text{O}_3$  nanopowders (Aeroxide Alu C) were firstly dispersed in distilled water by ball milling for 3 h (powder/spheres mass ratio of 1:10,  $\alpha$ -alumina spheres with a diameter of 2 mm) and then added with the aqueous solutions of the inorganic metal salts.  $\text{ZrCl}_4$  (0.3 M) aqueous solution was used to yield  $\text{ZrO}_2$ . When  $\text{ZrCl}_4$  is used, pH is less than 1, so a proper amount of tribasic ammonium citrate was added (molar ratio ammonium citrate: $\text{ZrCl}_4$  equal to 2:1), in order to reach a pH of 4.5 and avoid problems of corrosion on the spray-drier steel parts. After homogenization under stirring for 1 hour, the doped suspensions were diluted down to 4 wt% and dried by atomization, in order to avoid segregation of the added salts. After the spray-drying step, powders were finally calcined at 600°C for 1 h. These powders were then dispersed into a Silres MK/isopropyl alcohol solution.

All the dispersions were magnetically stirred for 20 minutes, then ultrasonicated for other

20 minutes, thus obtaining homogeneous and stable dispersions. All the dispersions were dried in oven at 60°C overnight, and the material obtained was first finely ground, then cold-pressed in a cylindrical steel die, without using any binder, thus obtaining specimens with a diameter of 30 mm and thickness of approximately 2 mm. All the samples were thermally cross-linked in oven at 180°C for 6 h, and subsequently heat treated to the final temperature in a muffle furnace in air. All samples without TiO<sub>2</sub> nanopowder were heat treated at 1350°C in air for 1 hour (2°/min heating rate), while all the samples containing TiO<sub>2</sub> underwent a 2-step heat treatment, consisting of a first dwelling at 1200°C for 5 h (2°/min heating rate), and a secondary dwelling at 1350°C for 1 h (2°/min heating rate). After the heat treatment, crack-free monoliths with no significant shape deformation were obtained.

To verify the effectiveness of the transformation toughening mechanism, XRD patterns were also collected after manual grinding of the samples into fine powders, in order to analyze the materials after the creation of an extended crack surface. In order to make the amount of surface of the cracks comparable within all the samples, only the 89–152 μm fraction (100–170 mesh size) was selected for the diffraction analysis.

The volume fractions inferred from Rietveld analysis were taken as a reference for the calculation of the theoretical full density of the samples, by application of the rule of mixtures; mullite, t-ZrO<sub>2</sub> and m-ZrO<sub>2</sub> densities were taken equal to 3.20, 6.10 and 5.68 g/cm<sup>3</sup>, respectively.

### 3.1.3 Synthesis

In Fig. 3.4 are reported the XRD patterns of as-synthesized mullite/20 vol% ZrO<sub>2</sub> nanocomposites produced, as a preliminary study, using three different commercial ZrO<sub>2</sub> nano-sized powders (patterns "a", "b" and "c") and using Al<sub>2</sub>O<sub>3</sub> chemically modified with ZrCl<sub>4</sub> powders (pattern "d"). When commercial ZrO<sub>2</sub> powders were used, only mullite, t-ZrO<sub>2</sub> and m-ZrO<sub>2</sub> were detected. The pyrolysis of a silicone resin at temperatures above 600°C in an oxidative atmosphere led to the formation of a highly reactive amorphous silica matrix, which reacted at higher temperature (>1250°C) with γ-Al<sub>2</sub>O<sub>3</sub> nano-sized particles to give a very pure and fine-grained mullite<sup>18,19</sup>. No evidences of secondary phases formation was found (e.g. zircon formation from the reaction of zirconia with silica). Nanocomposites synthesized using chemically-modified Al<sub>2</sub>O<sub>3</sub> nanopowders (pattern "d" in Fig. 3.4), as could be observed, appear very similar to the other samples, although some differences should be noticed. First of all, although chemical modification was tailored in order to obtain an amount of ZrO<sub>2</sub> in the final composites equal to 20 vol% (as in samples MZD20, MZT20 and MZDY20), Rietveld refinement revealed that a smaller amount of ZrO<sub>2</sub> is present in the final materials (17 vol%). This lower ZrO<sub>2</sub> content should be attributed to the probably poor control on the final doping level when Al<sub>2</sub>O<sub>3</sub> nanopowders are treated with ZrCl<sub>4</sub> solution. In addition, some traces of corundum (α-Al<sub>2</sub>O<sub>3</sub>) were detected in the final materials. Again, the origin of corundum should be probably attributed to the uncertainty over the final stoichiometry of the modified-Al<sub>2</sub>O<sub>3</sub> powders, which in turn creates some uncertainties over the right polysiloxane/Al<sub>2</sub>O<sub>3</sub> ratio to be used.

To summarize, the advantages connected with this alternative procedure include, in principle, a more homogeneous distribution of the toughening phase (ZrO<sub>2</sub>) inside the mullite matrix, a potentially smaller ZrO<sub>2</sub> mean crystallite size (since before the final heat treatment, ZrO<sub>2</sub> phase is still basically amorphous, and crystallizes only at higher temperatures), and a more rapid dispersion procedure (since only one powder component must be added in-

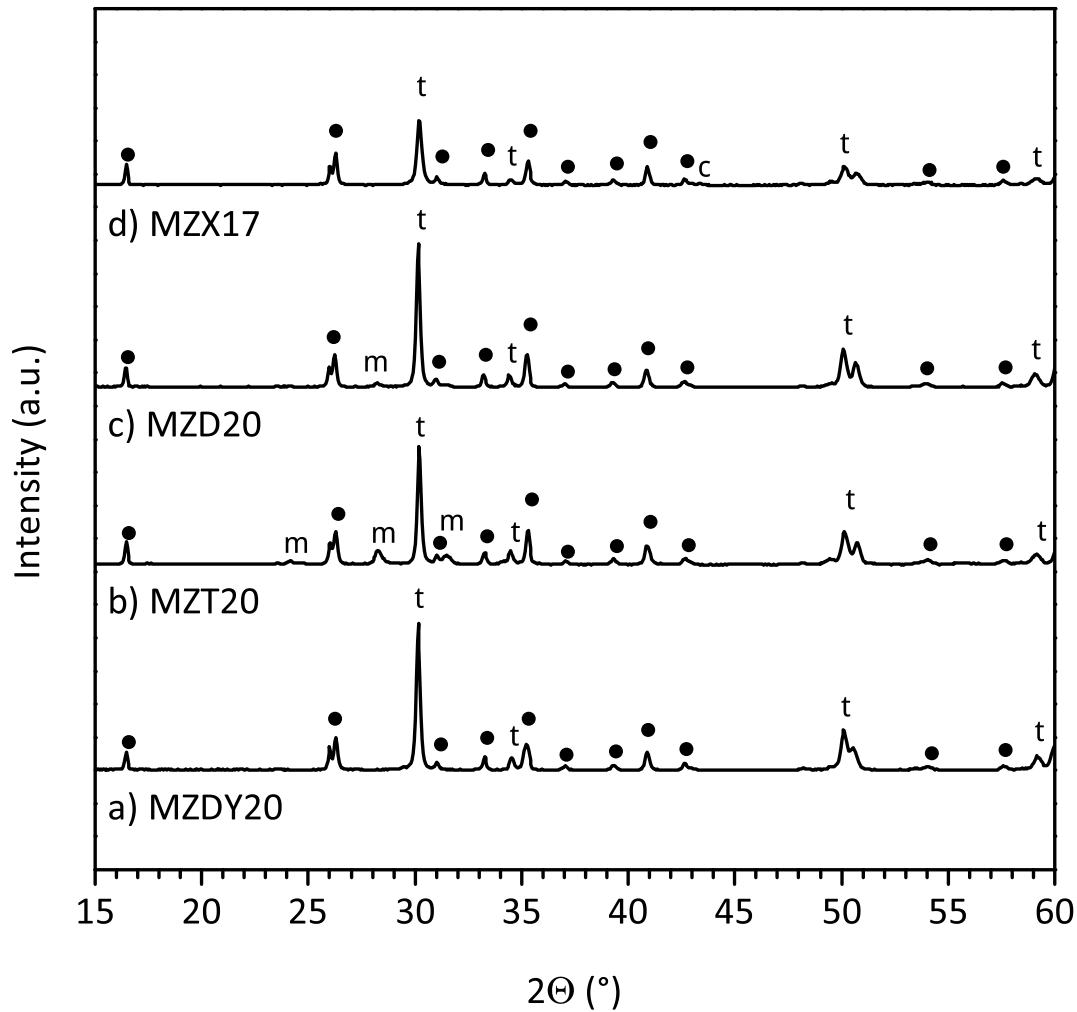


Figure 3.4: XRD patterns of MZD20, MZT20, MZDY20 and MZX17 samples after heat treatment at 1350°C for 1 h. m=m-ZrO<sub>2</sub>, t=t-ZrO<sub>2</sub>, ●=mullite, c=corundum (XRD patterns were normalized on mullite peaks).

side the dispersion). On the contrary, this procedure shows also some drawbacks, which are mainly the additional step of chemical modification of the starting Al<sub>2</sub>O<sub>3</sub> powders, the slightly less accurate control over the composition of the final ceramics (as it was verified in our case), and – as it will be discussed below – the mechanical behavior associated with the microstructural characteristics of the final composites.

### 3.1.4 Characterization

As discussed before, the typical application of mullite-based materials are high-temperature applications, where severe thermal gradients are present and a good thermal shock resistance is fundamental. Mullite could be used as a resistant protective thermal barrier in very demanding applications like space vehicles heat shields. Unfortunately, its very low toughness ( $\sim 2.5 \text{ MPa}\cdot\text{m}^{0.5}$ ) limit its reliability as a possible material for structural components. In the present work, the realization of mullite monoliths with increased toughness has been studied, following the synthesis technique described in the previous section.

In order to better evaluate the mechanical and microstructural behavior of the different composites, XRD analysis on as-prepared and on ground samples were carried out, followed

by Rietveld refinement with special attention to the phase assemblage and the grains dimensions in the final composites.

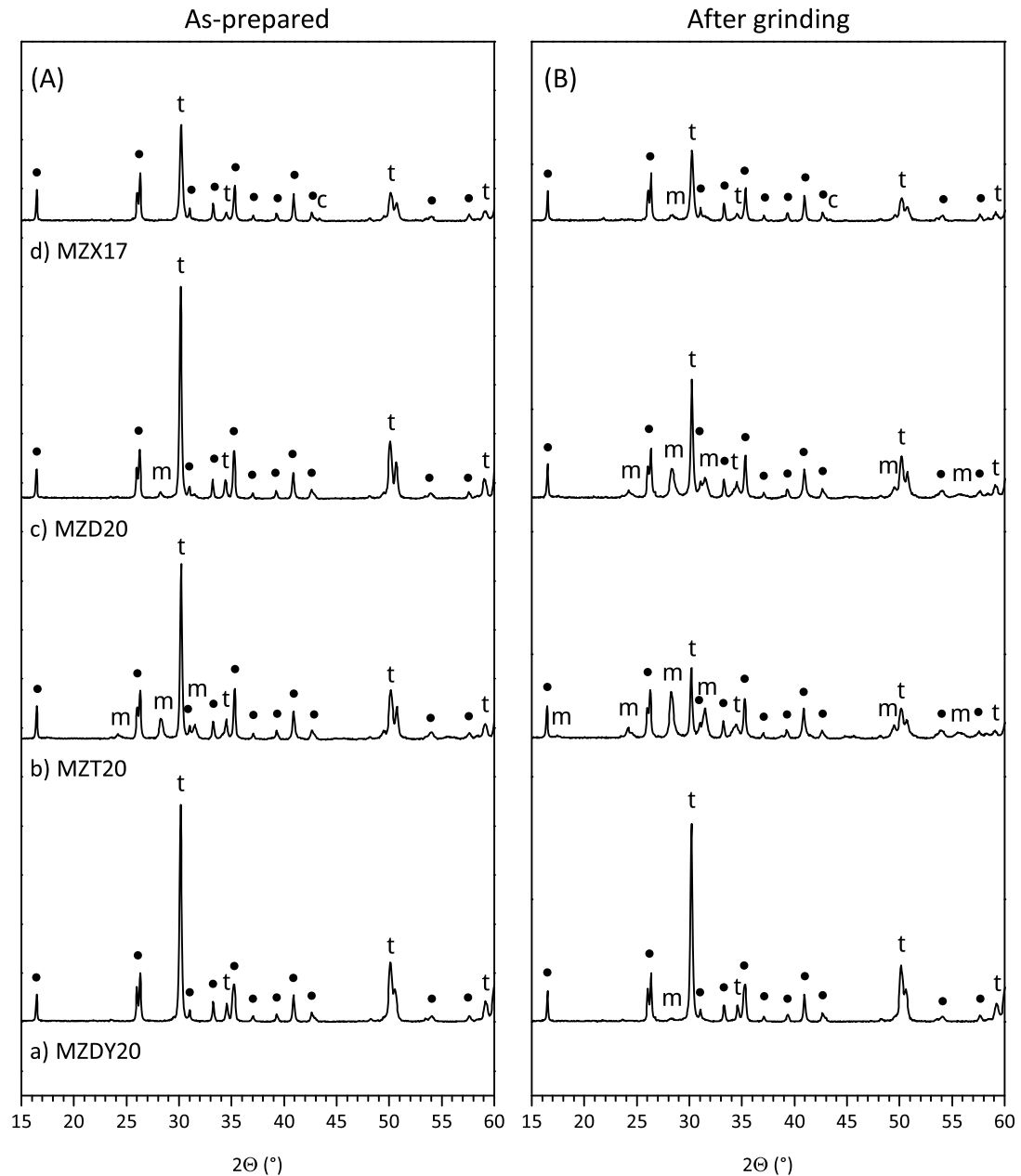


Figure 3.5: XRD patterns of MZDY20, MZT20, MZD20 and MZX17 in the (A) as-prepared and (B) ground state. m=m-ZrO<sub>2</sub>, t=t-ZrO<sub>2</sub>, •=mullite, c=corundum (XRD patterns were normalized on mullite peaks).

Different tetragonal/monoclinic ZrO<sub>2</sub> ratios were found in the 4 samples, and they are correlated with the degree of stabilization of the zirconia particles inside the mullite matrix, in dependence on the type and size of the starting zirconia powders. A total tetragonal phase (t-phase) retention was achieved when using yttria-stabilized powders (MZDY20). More interestingly, a very high t-phase retention was achieved in the other two samples even without the presence of any stabilizing solutes. The MZD20 sample shows a 93% t-phase retention at room temperature, while this value decreased to 69% for MZT20, due to the coarser nature of the initial powders. In sample MZX17 instead, a total t-ZrO<sub>2</sub> retention was achieved, obtain-

Table 3.1: t-ZrO<sub>2</sub> retention (before and after grinding), t-ZrO<sub>2</sub> transformation and indentation toughness values for MZD20, MZT20 and MZDY20 samples.

Sample	t-ZrO <sub>2</sub> retention (%)		Transformed ZrO <sub>2</sub> (%)	Toughness (MPa·m <sup>0.5</sup> )
	as-prepared	after grinding		
MZD20	92	48	48	5.2±0.5
MZT20	69	28	59	4.9±0.6
MZDY20	100	94	6	3.8±0.4
MZX17	100	81	19	3.5±0.8

ing a result basically identical to MZDY20 sample, but without the presence of yttrium oxide as a stabilizing agent for the tetragonal form. In this case, a total tetragonal phase retention must be attributed only to a mechanical constraint effect, which was easily achieved by both a smaller ZrO<sub>2</sub> mean crystallite size (equal to 62 nm) and a lower ZrO<sub>2</sub> content, if compared to other samples (17 vol% vs. 20 vol%).

By collecting XRD patterns of the materials in the ground state (Fig. 3.5(b)), it was possible to obtain important indications on the effectiveness of the transformation toughening mechanism. Tab. 3.1 reports the overall content of t-phase of the nano-composites in the as-prepared state and after grinding; in it, the degree of t→m transformation due to crack formation upon grinding is also reported, inferred from the difference between the above cited contents of t-phase (as an example, if we have 69% t-phase in the as-prepared state for MZT20, and 28% of t-phase after grinding, the difference is 41%, which is the 59% of the initial t-phase content). The highest transformation values of the initial t-ZrO<sub>2</sub> volume that underwent the t→m transformation were obtained for the two un-stabilized samples (48% and 59% for MZD20 and MZT20, respectively), while in sample MZDY20 a very limited fraction of zirconia underwent the t→m transformation (about 6%). Finally, MZX17 show an intermediate behavior between the un-stabilized samples and MZDY20: although a full tetragonal phase retention was achieved (as in yttria-stabilized sample), a more pronounced ability to transform was observed, with a 19% ZrO<sub>2</sub> that underwent the t→m phase transformation.

All these results are in agreement with the fact that the stress required to initiate the t→m transformation is proportional to the degree of stabilization of the zirconia particles, and decreasing the stabilization of the zirconia would also increase the extension of the transformed zone. It has been demonstrated that the global (solute and mechanical) degree of stabilization of zirconia particles depends on (1) zirconia grain dimensions, (2) zirconia content, (3) stabilizing solute content and (4) matrix properties, and is directly related to the M<sub>s</sub> (t→m martensite start transformation) temperature (the more effective the stabilization, the lower the M<sub>s</sub> temperature, and vice versa). While t-phase stabilization tends to increase with decreasing particle size and with increasing concentration of stabilizing agents, the ability to transform shows an opposite trend<sup>6-10</sup>.

The best toughness results (see Tab. 3.1) were obtained by using the two un-stabilized powders (5.2±0.5 and 4.9±0.6 MPa·m<sup>0.5</sup> for MZD20 and MZT20, respectively), while the MZDY20 and MZX17 samples exhibited lower values (3.8±0.4 MPa and 3.5±0.8·m<sup>0.5</sup>, respectively). These data confirm the presence of a very effective transformation-toughening mechanism active in the MZD20 and MZT20 samples, in which a very good combination of t-phase retention and transformation has been reached. The toughness values for the MZD20 and MZT20 samples appear to be very similar, even if their respective t/m ratios are quite different. One likely reason for this could be the very close absolute volume fraction (vol%) of transformed ZrO<sub>2</sub>, inferred from Rietveld refinements, in both samples: the higher t-phase

retention, upon cooling, presented by MZD20 sample compared with MZT20, is counterbalanced by a lower ability to transform. Moreover, the possible presence of microcracks in the MZT20 sample, associated with the formation of a certain quantity of monoclinic  $ZrO_2$  upon cooling, could be taken into consideration as an additional toughening contribute; however, it is well known that the contribution of microcracking is generally much less important than that of the transformation mechanism<sup>6,10</sup>.

On the contrary, the lower toughness values for MZDY20 confirm an excessive t-phase stabilization of the zirconia powders. In MZDY20 sample the additional stabilization contribution of  $Y_2O_3$  was very effective for the obtainment of fully tetragonal zirconia phase, but at the same time it strongly suppressed its ability to transform in the monoclinic form. Finally, MZX17 sample shows an intermediate behaviour: while a full tetragonal retention was achieved, its ability to undergo the t→m transformation was higher than the sample containing yttria-stabilized powders. However, this transformation value is still quite small (19%), if compared to MZD20 and MZT20 (48 and 59%, respectively), and considering also the lower  $ZrO_2$  presence in the final ceramics (17 vol% vs. 20 vol%), the relatively low value of indentation toughness measured could be easily justified.

Based on this preliminary study, further developments and characterization were conducted exclusively on MZDx composites, featuring the most promising balance between t-phase retention and ability to transform. Mechanical properties such as indentation toughness and flexural strength for MZDx and MZDx\_Ti3 composites are shown in Fig. 3.7a and in Fig. 3.7b, respectively, while relative density values are reported in Fig. 3.6. It may be observed that with  $TiO_2$  addition and modification of the thermal treatment it was possible to obtain an increase of density at all  $ZrO_2$  concentrations, probably due to a decrease of the viscosity of amorphous  $SiO_2$  at 1200°C provided by  $TiO_2$ , with a consequent more effective densification process through transient viscous sintering (as reported by other authors<sup>22,23</sup>), before the nucleation of the mullite phase. The effect of  $TiO_2$  was found to be higher for samples with a lower zirconia content, and it decreased at higher  $ZrO_2$  concentrations. In all the samples, residual  $TiO_2$  was always present as rutile phase. Moreover, small quantities (<1 vol%) of residual amorphous phase are believed to be present, according to Rietveld refinement data.

A general remarkable increase of toughness was observed, especially if compared with common mullite/zirconia toughness values reported in literature<sup>3</sup>. In Fig. 3.8 a diagram resuming the toughness range of mullite/ $ZrO_2$  and mullite /SiC composites is reported (as reported by Schneider<sup>3</sup>). As could be noticed, materials developed during the present research not only could be compared to the best analogous mullite/ $ZrO_2$  composite in literature, but also with mullite/SiC composites, which generally show the best toughness properties, thus confirming the good potentiality of the present synthesis strategy for the obtainment of high temperature materials for structural applications. In Fig. 3.9 two examples of Vickers indentations are shown, produced under the same load conditions (50 N for 30 seconds) on the surface of (a) MZD0 and (b) MZD30 samples, where noticeable differences in the cracks generated at the corners between the two samples could be observed.

While for MZDx samples this increase appears to be almost linear with increasing zirconia content, MZDx\_Ti3 series seems to follow a different and more complex behavior. Considering pure-mullite samples (MZD0 and MZD0\_Ti3), the increase of toughness in MZD0\_Ti3 is likely due to the density increment achieved by  $TiO_2$  insertion<sup>24</sup>. On the contrary, in mullite/zirconia nano-composites toughness behavior seems to be quite well related to the volume of transformed zirconia during fracture propagation. Considering that the ability to

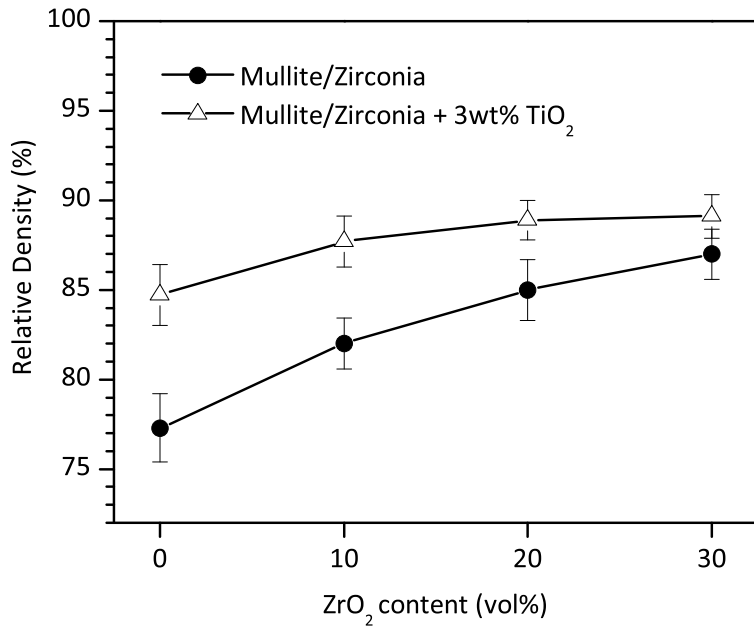


Figure 3.6: Relative density of MZDx and MZDx\_Ti3 samples as function of ZrO<sub>2</sub> content.

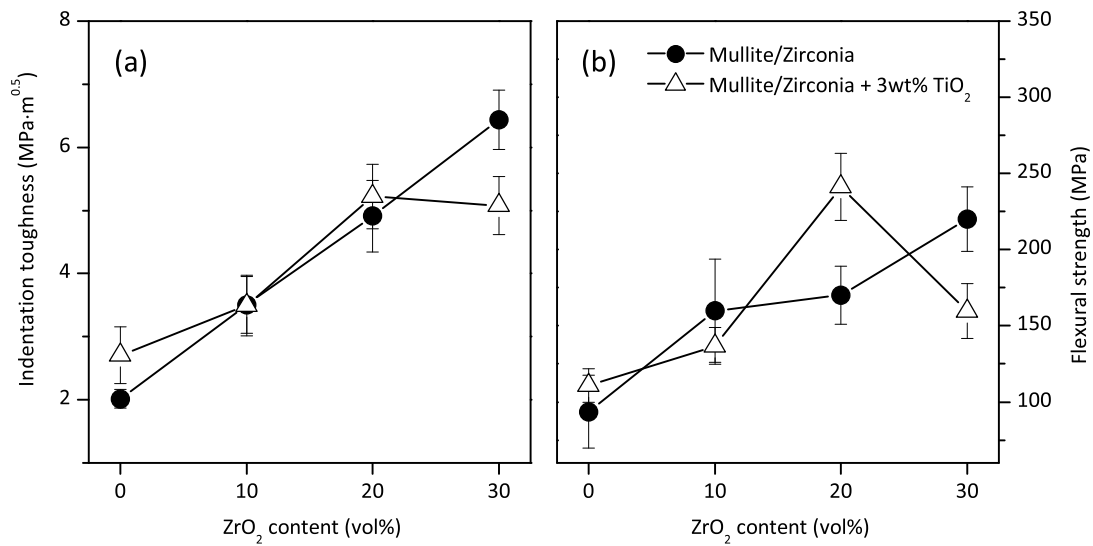


Figure 3.7: Indentation toughness (a) and 4-point flexural strength (b) of MZDx and MZDx\_Ti3 samples as function of ZrO<sub>2</sub> content.

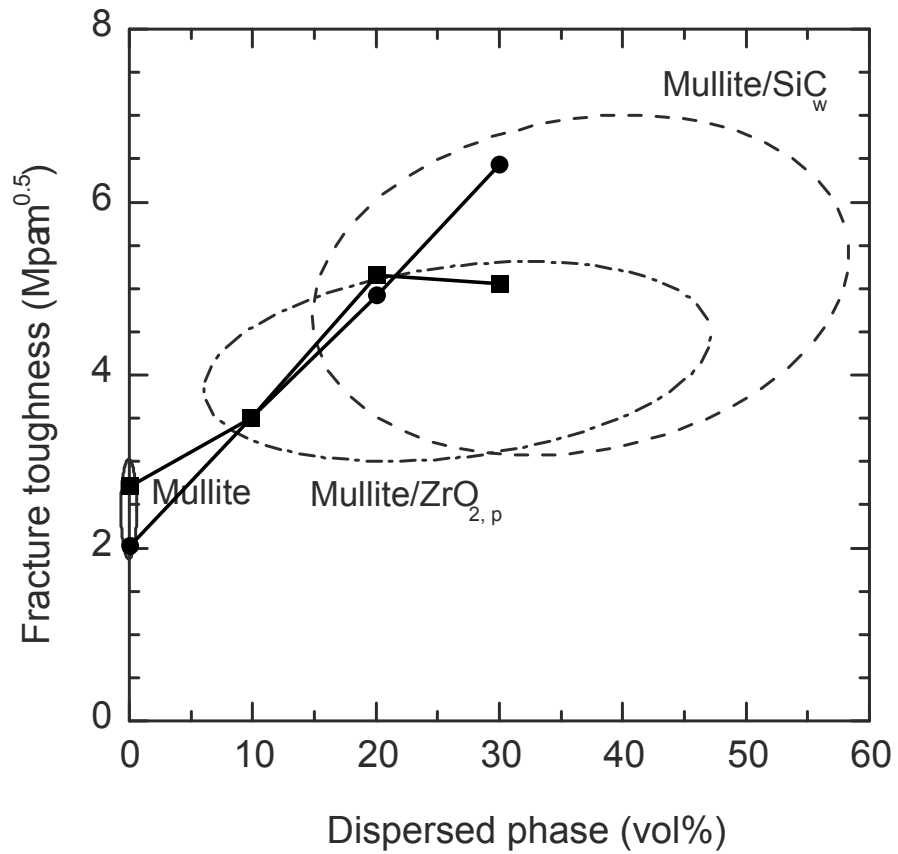


Figure 3.8: Toughness range as a function of the volume fraction of the reinforcing phase for mullite/ $ZrO_2$  particles and mullite/SiC whiskers composites, as reported by Schneider<sup>3</sup>. Superimposed to the original graph, toughness values from Fig. 3.7a are reported.

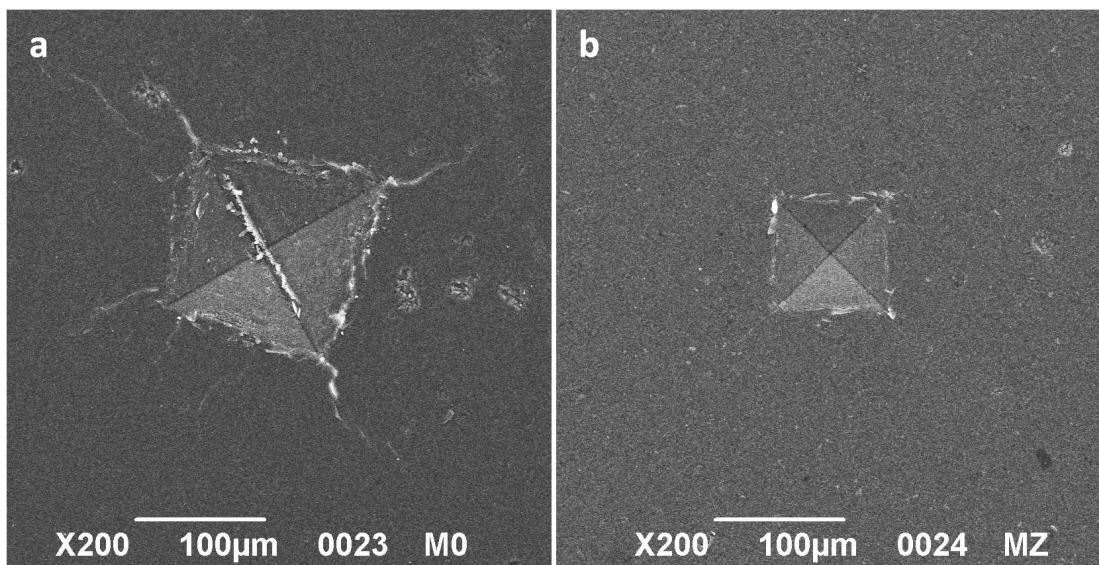


Figure 3.9: Vickers indentations of (a) MZD0 and (b) MZD30 samples using a load of 50 N.

Table 3.2: t-ZrO<sub>2</sub> retention, t-ZrO<sub>2</sub> transformation, grains dimension and Young's modulus of MZDx and MZDx\_Ti3 nano-composites.

Sample	t-ZrO <sub>2</sub> retention (%)	Transformed ZrO <sub>2</sub> (%)	Grains mean dimensions (nm)			Young's Modulus (GPa)
			Mullite	t-ZrO <sub>2</sub>	m-ZrO <sub>2</sub>	
MZD0	/	/	185	/	/	75
MZD10	90	62	181	95	54	140
MZD20	92	48	157	94	41	164
MZD30	55	63	164	75	41	185
MZD0_Ti3	/	/	189	/	/	119
MZD10_Ti3	83	69	166	95	38	145
MZD20_Ti3	85	56	187	102	80	187
MZD30_Ti3	29	57	174	58	47	200

transform does not significantly change after the insertion of TiO<sub>2</sub>, the effective ZrO<sub>2</sub> values are proportional to the t-phase retention (see Tab. 3.2). As a consequence, in the 10-20 vol% range no significant changes in t-phase retention entail no significant changes in toughness values. In the same manner, the strong decrease of t-phase retention of MZD30\_Ti3 sample appears to be connected with its lower toughness value, if compared with MZD30 sample. The fact that t-phase retention decreases abruptly only at higher ZrO<sub>2</sub> content is once more in accordance with results reported in literature about the transformation toughening mechanism<sup>6-10</sup>. It should be observed that the toughness values were probably affected by the residual porosity, since pores can interact with crack propagation and provide some crack blunting<sup>25</sup>. Although further efforts in the toughness characterization are needed (e.g. by applying more reliable SENB or CNB techniques), the increase in toughness, starting from pure mullite, is considered to be noteworthy, since the insertion of ZrO<sub>2</sub> and TiO<sub>2</sub> is always accompanied by a decrease of porosity (see Fig. 3.6).

Flexural strength values showed a general increase with increasing ZrO<sub>2</sub> content for MZDx samples, with values in the 100-220 MPa range. For MZDx\_Ti3 series, the global trend was found to be more complex. TiO<sub>2</sub> presence did not appear to have significant effects at lower ZrO<sub>2</sub> concentrations (0, 10 vol%), while it is possible to observe a good strength increase for 20 vol% nano-composite (241 MPa). For 30 vol% of ZrO<sub>2</sub>, there is an abrupt decrease in strength to 160 MPa, similarly to what described before for toughness. In this case, it is believed that the considerably higher t→m transformation that occurs after heat treatment may produce a certain amount of microcracking, which could be associated with a new family of defects that can have a significant influence on the flexural strength values. Nevertheless, not all the t→m transformation should be associated with microcracking, otherwise a significant decrease in the Young's modulus values (Tab. 3.2) would be expected<sup>9</sup>. Flexural strength results are generally lower than other results previously reported in literature<sup>3</sup>. This could be certainly attributed to the quite high residual porosity, connected to the transformation of the preceramic polymer into a ceramic phase during heat treatment. Effect of porosity on flexural strength has been extensively studied on previous works in literature, and although it appears difficult to find a generally valid model for porosity effect on strength, it is not uncommon to have strength decreases of the order of 20-50% for values of porosity in the 10-25 vol% range<sup>24</sup>.

In Fig. 3.10 SEM images of samples MZD0, MZD20, MZX17 and MZD20\_Ti3 are reported. All images (with the exception of MZD0) were acquired by using back-scattered electrons, to create a more clear contrast between the mullite matrix (which is represented by the gray areas) and the ZrO<sub>2</sub> dispersed phase (associated with the white areas). An homogeneous distribution of the ZrO<sub>2</sub> phase was achieved within the mullite matrix for all the samples. SEM analysis seems to be in good accordance with the mean grain size values obtained from

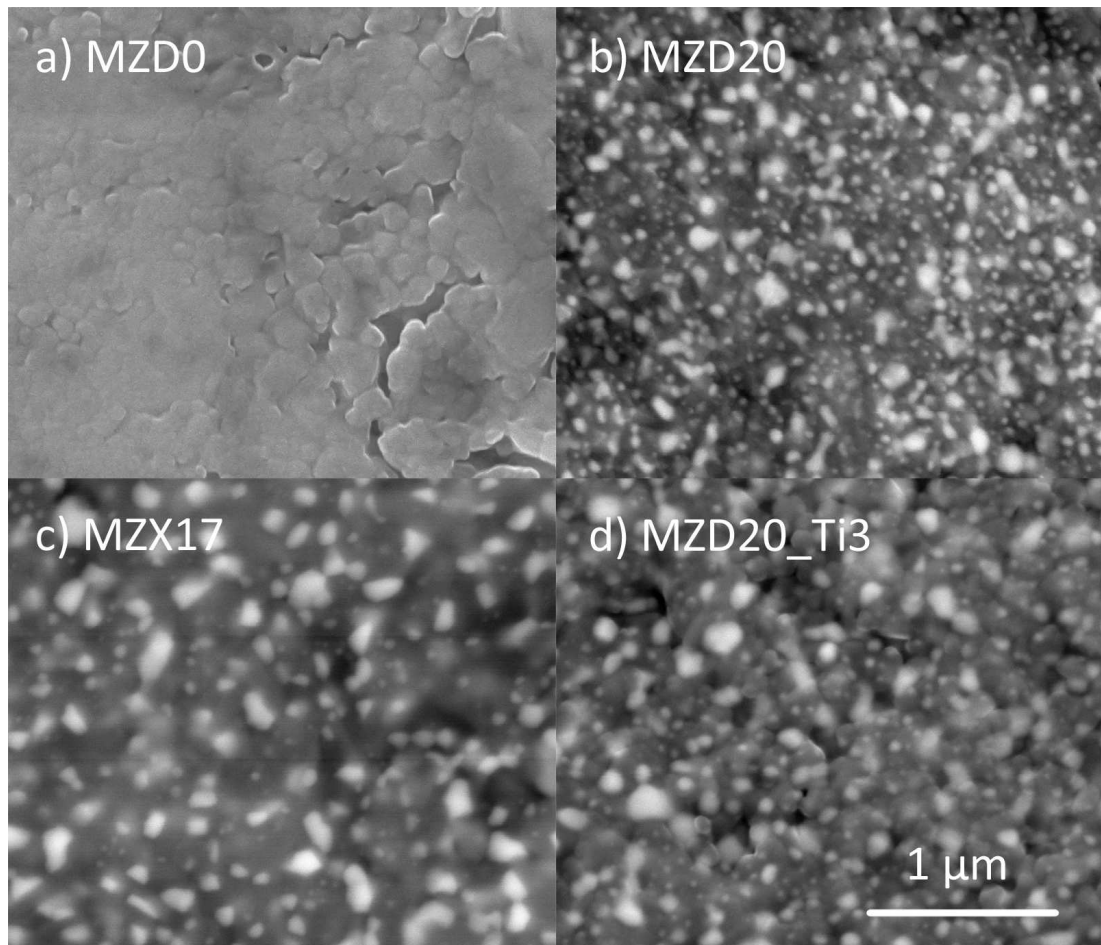


Figure 3.10: Back-scattered electrons (BSE) SEM images of samples a) MZD0 (secondary electrons), b) MZD20, c) MZX17 and d) MZD20\_Ti3 after heat treatment at 1350°C for 1 hr.

Rietveld refinement of XRD patterns (see Tab. 3.2). A certain fraction of smaller (<50 nm)  $ZrO_2$  particles is believed to be placed in intragranular positions, due to a probably reduced pinning effect of  $ZrO_2$  grains on mullite grains. In all the images, evidences of residual porosity could be noticed, confirming the results obtained by relative density measurements (see Fig. 3.6). Cracks and porosity formation should be associated both with the development of the polymeric phase during the pyrolysis step, but also with the subsequent formation of mullite at higher temperatures, which entails a further increase of material density, and thus a further shrinkage of the materials. Tensions are likely generated during both these phases, which could not be totally relaxed by viscous flow or diffusion processes (very limited especially in the case of mullite).

### 3.1.5 Conclusions

A novel method for the production of mullite/zirconia nano-composites has been presented. Oxide nano-particles were found to be useful as both active and passive fillers.  $Al_2O_3$  nano-powders were confirmed to yield highly pure mullite at relatively low temperature, reacting with the  $SiO_2$  residue provided by the silicone resin (active fillers);  $TiO_2$  nano-powders led to improvements in the densification of mullite and  $ZrO_2$ -reinforced mullite matrix composites, reasonably by modifying the viscosity of the  $SiO_2$  provided by the silicone resin (low temperature transient viscous sintering);  $ZrO_2$  nano-powders acted as a passive fillers, since they

did not react with the silicone resin, but they were very effective in modifying functionality, i.e. in controlling fracture propagation by transformation toughening. Due to the nanometric distribution of  $ZrO_2$  in the mullite matrix provided by the  $Al_2O_3$ /silicone reaction, the retention of tetragonal  $ZrO_2$  phase and the associated toughening effect were found to be effective without any need for additional stabilizing solutes (e.g.  $Y_2O_3$ ). Furthermore, an alternative route for the realization of mullite/ $ZrO_2$  nanocomposites by chemically modifying the starting fillers was studied, and first results demonstrated the possibility of obtaining an even more homogeneous distribution of  $ZrO_2$  reinforcing phase inside the mullite matrix, thanks to an "in-situ" nucleation of  $ZrO_2$  nanograins during the pyrolysis/sintering process.

Thanks to a systematic study of the behavior of different  $ZrO_2$  nanoparticles and their influence on the microstructure of the final materials, best conditions were found to achieve the best balance between t-phase retention and its ability to undergo the t→m transformation during the propagation of cracks, which – as confirmed by the present work – is a fundamental aspect of the whole transformation-toughening mechanism. On the basis of the simplicity of the process and the low treatment temperatures, the presented approach is thought to be very favorable to the production of strong monolithic ceramic components, even in the case of complex shapes, that could be obtained by an easy machining of nano-filled silicone components, before heat treatment.

## References

- [1] H. Schneider and S. Kormaneni, "Mullite", 445–455, Wiley-VCH (2005).
- [2] H. Schneider, J. Schreuer and B. Hildmann, "Structure and properties of mullite—A review", *J. Eur. Ceram. Soc.*, **28** [2] 329–344 (2008).
- [3] H. Schneider and S. Kormaneni, "Mullite", 399–402, Wiley-VCH (2005).
- [4] R. C. Garvie, R. H. Hannink and R. T. Pascoe, "Ceramic steel?", *Nature*, (1975).
- [5] R. H. Hannink, P. M. Kelly and B. C. Muddle, "Transformation Toughening in ZrO<sub>2</sub>-Containing Ceramics", *J. Am. Ceram. Soc.*, **83** [3] 461—487 (2000).
- [6] R. H. J. Hannink, P. M. Kelly and B. C. Muddle, "Transformation toughening in zirconia-containing ceramics", *J. Am. Ceram. Soc.*, **83** [3] 461–487 (2000).
- [7] P. F. Becher, K. B. Alexander, A. Bleier, S. B. Waters and W. H. Warwick, "Influence of ZrO<sub>2</sub> Grain Size and Content on the Transformation Response in the Al<sub>2</sub>O<sub>3</sub>-ZrO<sub>2</sub>(12 mol% CeO<sub>2</sub>) System", *J. Am. Ceram. Soc.*, **76** [3] 657–663 (1993).
- [8] A. H. Heuer, N. Claussen, W. M. Kriven and M. Rühle, "Stability of tetragonal ZrO<sub>2</sub> particles in ceramic matrices", *J. Am. Ceram. Soc.*, **65** [12] 642–50 (1982).
- [9] D. J. Green, "Critical Microstructures for Microcracking in Al<sub>2</sub>O<sub>3</sub>-ZrO<sub>2</sub> Composites", *J. Am. Ceram. Soc.*, **65** [12] 610–614 (1982).
- [10] Y. S. Shin, Y. W. Rhee and S. J. L. Kang, "Experimental Evaluation of Toughening Mechanisms in Alumina–Zirconia Composites", *J. Am. Ceram. Soc.*, **82** [5] 1229–1232 (1999).
- [11] K. Niihara, "New design concept of structural ceramics - Ceramic nanocomposites", *J. Ceram. Soc. Jpn.*, **99** [1154] 974–982 (1991).
- [12] M. J. Mayo, "Processing of nanocrystalline ceramics from ultrafine particles", *Int. Mater. Rev.*, **41** [3] 85–115 (1996).
- [13] I. W. Chen and X. H. Wang, "Sintering dense nanocrystalline ceramics without final-stage grain growth", *Nature*, **404** [6774] 168–171 (2000).
- [14] F. Wakai, S. Sakaguchi and Y. Matsuno, "Superplasticity of yttria-stabilized tetragonal ZrO<sub>2</sub> polycrystals", *Adv. Cer. Mat.*, (1986).
- [15] J. Karch and R. Birringer, "Nanocrystalline ceramics: possible candidates for net-shape forming", *Ceram. Int.*, **16** [5] 291–294 (1990).
- [16] J. Karch, R. Birringer and H. Gleiter, "Ceramics Ductile at Low Temperature", *Nature*, **330** [6148] 556–558 (1987).
- [17] J. Binner and B. Vaidhyanathan, "Processing of bulk nanostructured ceramics", *J. Eur. Ceram. Soc.*, **28** [7] 1329–1339 (2008).
- [18] E. Bernardo, P. Colombo, E. Pippel and J. Woltersdorf, "Novel mullite synthesis based on alumina nanoparticles and a preceramic polymer", *J. Am. Ceram. Soc.*, **89** [5] 1577–1583 (2006).
- [19] F. Griggio, E. Bernardo, P. Colombo and G. L. Messing, "Kinetic Studies of Mullite Synthesis from Alumina Nanoparticles and a Preceramic Polymer", *J. Am. Ceram. Soc.*, **91** [8] 2529–2533 (2008).
- [20] P. Palmero, V. Naglieri, J. Chevalier, G. Fantozzi and L. Montanaro, "Alumina-based nanocomposites obtained by doping with inorganic salt solutions: Application to immiscible and reactive systems", *J. Eur. Ceram. Soc.*, **29** [1] 59–66 (2009).
- [21] V. Naglieri, P. Palmero and L. Montanaro, "Preparation and characterization of alumina-doped powders for the design of multi-phasic nano-microcomposites", *J. Therm. Anal. Calorim.*, **97** [1] 231–237 (2009).

- [22] S. H. Hong and G. L. Messing, "Anisotropic Grain Growth in Diphasic-Gel-Derived Titania-Doped Mullite", *J. Am. Ceram. Soc.*, **81** [5] 1269–1277 (1998).
- [23] M. D. Sacks, N. Bozkurt and G. W. Scheiffele, "Fabrication of mullite and mullite-matrix composites by transient viscous sintering of composite powders", *J. Am. Ceram. Soc.*, **74** [10] 2428–2437 (2005).
- [24] R. W. Rice, "Porosity of ceramics", 168–275, CRC (1998).
- [25] Z. Y. Deng, J. She, Y. Inagaki, J. F. Yang, T. Ohji and Y. Tanaka, "Reinforcement by crack-tip blunting in porous ceramics", *J. Eur. Ceram. Soc.*, **24** [7] 2055–2059 (2004).

## 3.2 Zircon

### 3.2.1 Introduction

Zircon (zirconium silicate,  $ZrSiO_4$  or  $ZrO_2 \cdot SiO_2$ ) is a ceramic material which is suitable for multiple applications, although most of them have been rather unexplored so far. The classical application is in the field of refractory materials, where zircon is appreciated mainly for its very low CTE, although the performance is generally lowered by the presence of impurities<sup>1</sup>. More recent high-technology applications are in the nuclear and electronic fields. In fact, zircon has been considered a promising nuclear waste host material<sup>2-4</sup>, owing to the possibility of introducing large amounts (up to 20 wt%) of radionuclide cations inside its crystal structure<sup>4</sup>. Electronic applications are in relation to the possibility to replace  $SiO_2$  in silicon-based MOSFET, thanks to its relatively large dielectric constant, high band gap, high breakdown field, and good thermal stability in contact with silicon<sup>5-7</sup>.

According to several studies in literature, zircon synthesis from  $SiO_2$  and  $ZrO_2$  raw materials is characterized by a very slow kinetic, and achieving high zircon yield through this reaction sintering is possible only at high temperatures (above 1500°C). High synthesis temperatures, however, hinder the applicability: as an example, the hosting of nuclear waste may be compromised, due to the risk of volatilization of some radionuclides, lowering the immobilization efficiency<sup>4</sup>. The possibility of lowering the synthesis temperature of zircon has been explored in several studies, most of them based on the sol-gel route<sup>8-11</sup>, well known to be hardly applicable to the manufacturing of monoliths.

In the recent years, the use of Polymer Derived Ceramics (PDCs) in conjunction with nano-sized particulate fillers has proved to be a straightforward methodology for the realization of advanced ceramic monoliths, featuring a kinetic comparable, if not better, to the sol-gel method. The coupling of the high reactivity of nano-sized particles with that of amorphous silica, provided by the ceramic conversion of silicones, leads to a high phase purity and to an interesting microstructure. In particular, it has been shown the possibility to produce nano-structured ceramics, i.e. fine grained monophase ceramics or ceramic matrix nanocomposites, such as zirconia-toughened mullite<sup>12</sup>.

In this section, the application of the method of nano-sized filled silicones to the manufacturing of zircon ceramics will be discussed. The approach was found to enable the synthesis of crack-free and high purity zircon monoliths at low temperature (1200°C), starting from a silicone and zirconia nano-sized particles, through a careful control of additional secondary fillers and seeds.

### 3.2.2 Experimental procedure

A commercially available polysilsequioxane (Silres MK) was dissolved in isopropyl alcohol under stirring.  $ZrO_2$  nano-sized powders (VP Zirconium Oxide PH) were subsequently dispersed into the solvent/polymer solution, without the addition of any chemical dispersant. A pure  $ZrO_2$ /MK system, where the  $ZrO_2$ /MK weight ratio was kept constant and equal to 1.682, was investigated first. The weight ratio value of 1.682 was calculated by considering both the stoichiometry of zircon ( $SiO_2$  and  $ZrO_2$  in equal molar concentration) and the ceramic yield of the polysiloxane, which is equal to 82 wt%. Although it should be considered that, in some cases, the introduction of secondary fillers could have some influence on the chemical composition of the final ceramic residue (particularly in the case of active fillers), during the present work calculations were made with the assumption that a pure  $SiO_2$  ce-

ramic residue from the polysiloxane(s) is obtained, thus neglecting possible polymer-fillers interactions during the pyrolysis step. This assumption seems to be reasonable, since heat treatments were carried out in oxidative atmosphere and only oxides were used as fillers. In other formulations, TiO<sub>2</sub> nanopowders (VP P90) and/or zircon seeds were also introduced. Considering the possibility that Ti<sup>4+</sup> cations could enter into the zircon crystal lattice by substituting Zr<sup>4+</sup> cations<sup>13</sup>, in all the dispersions containing TiO<sub>2</sub> the original ZrO<sub>2</sub>/MK weight ratio was adjusted according to the relation  $n(\text{SiO}_2)=n(\text{ZrO}_2)+n(\text{TiO}_2)$ , with  $n(x)$ =moles of species  $x$ . Samples were labeled "X-Y", where "X" and "Y" represent the molar TiO<sub>2</sub> and seeds concentrations in the final ceramic, respectively. All the dispersions were homogenized by magnetic stirring for 10 minutes, and then ultrasonicated for 20 minutes to reduce the size of the residual particles agglomerates, thus obtaining homogeneous and stable dispersions. After the evaporation of the solvent in oven at 90°C the material obtained was finely ground in a mortar with a pestle and sieved (75 μm aperture). Powders were uniaxially compacted at room temperature under a pressure of 40 MPa. Pellets with a diameter of 20 mm were subsequently heat treated in air in the 1100-1500°C range for 1 and 4 h (10°Cmin heating rate).

For some samples, part of Silres MK was substituted by another polysiloxane (Silres H62C), which is characterized by a different SiO<sub>2</sub> yield (approx. 58 wt%) and does not releases gaseous products during the curing step. For these samples, a partial pre-curing treatment (250°C 30 min) was necessary before the grinding step.

Phase evolution was investigated by means of X-ray diffraction, coupled with Rietveld refinement. After Rietveld refinement, a zircon yield parameter was calculated with the formula reported below:

$$\text{zircon yield} = \frac{\text{vol}\%_{\text{zircon}}}{(\text{vol}\%_{\text{zircon}} + \text{vol}\%_{\text{m-ZrO}_2} + \text{vol}\%_{\text{t-ZrO}_2})}$$

### 3.2.3 Synthesis

In Fig. 3.11, XRD data for a pure MK/ZrO<sub>2</sub> system are reported as a function of the temperature (1 h soak time). As it can be observed, zircon is virtually absent even at 1500°C as a confirmation of the already reported extremely slow nucleation kinetic, and unreacted ZrO<sub>2</sub> and SiO<sub>2</sub> continue to be the predominant phases. Below 1500°C ZrO<sub>2</sub> is the only crystalline phase, and the SiO<sub>2</sub> component deriving from the pyrolysis of the silicone resin is still present as an amorphous phase. The t-ZrO<sub>2</sub>/m-ZrO<sub>2</sub> ratio first increases up to 1300°C and then decreases until 1500°C the first increase, from one hand, is probably due to the well known mechanical constraint effect of the matrix on the t-ZrO<sub>2</sub> phase; the decrease, on the other hand, could be associated with an progressive increase in the dimension of the ZrO<sub>2</sub> grains, counteracting the mechanical constraint provided by the matrix<sup>14</sup>.

An approximate but rapid evaluation of the kinetic of the system, in the form of MK and ZrO<sub>2</sub> nano-particles, with or without additives, comes from the evolution curves reported in Fig. 3.12. It is evident that the formation of zircon was effectively enhanced by the introduction of small quantities (5 and 10 mol%) of TiO<sub>2</sub> and/or zircon seeds, since the zircon yield is much higher than that from only MK and ZrO<sub>2</sub>, in any condition of concentration of additive, temperature and soak time. Specific features, however, should be noted. First of all TiO<sub>2</sub> may be seen as a key additive, as testified by the evolution curves for samples 5-0 (5% TiO<sub>2</sub>, no seeds) and 10-0 (10% TiO<sub>2</sub>, no seeds), for both 1 and 4 h treatments, shown in Fig. 3.12, and by the XRD patterns as a function of the treatment temperature, at a constant soak

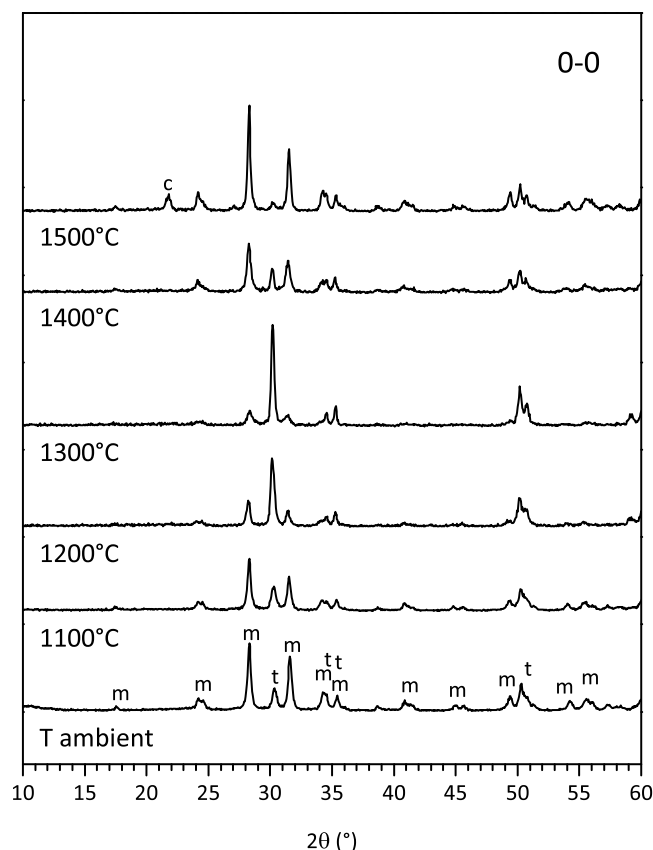


Figure 3.11: XRD patterns as a function of the treatment temperature of 0-0 sample. m=m-ZrO<sub>2</sub>, t=t-ZrO<sub>2</sub>, c=cristobalite.

time of 1 h, for samples 10-0 and 10-10 (10% TiO<sub>2</sub>, 10% seeds), shown in Fig. 3.13.

TiO<sub>2</sub> nanoparticles accomplish their beneficial effect by providing a reduction of the viscosity of the SiO<sub>2</sub> phase (deriving from the pyrolysis of the polymeric phase) before the reaction of the latter with ZrO<sub>2</sub> nanoparticles to give the formation of zircon. The reduction of SiO<sub>2</sub> viscosity by the introduction of Ti<sup>4+</sup> cations, which was also observed in previous works in literature<sup>15,16</sup>, is associated with a breakage of the silica network produced upon pyrolysis, thus leading to a lower network connectivity. The improved mobility of silicon and oxygen ions, upon rupture of siloxanic network, as a triggering event, is also consistent with the observation that silicon and oxygen ions are the mobile species in zircon formation<sup>17</sup>.

If TiO<sub>2</sub> may be seen as an actual catalyst, the sigmoidal curves for samples 5-0 and 10-0 being shifted towards lower temperatures with increasing TiO<sub>2</sub> content, the role of seeds is less clear. The zircon yields were simply shifted up by a constant quantity, below a "critical temperature", 1300°C for 1 h soak time or 1200°C for 4 h, according to the different quantity of seeds added to the starting mixture, compared to the yields for pure Mk and ZrO<sub>2</sub>. The seeds reasonably provided some heterogeneous nucleation, but with a much less marked effect on the temperature for extensive zircon formation than TiO<sub>2</sub>. Interestingly, a synergistic effect of TiO<sub>2</sub> addition and seeding occurs, testified by the high zircon yields for the 5-5 and 10-10 systems even below 1200°C. In the presence of both TiO<sub>2</sub>, after 4 h at 1100°C the effect of seeding starts to be significant already at 1100°C and gives almost phase pure zircon at 1200°C (sample 10-10). The synergy is further illustrated by the DTA analysis reported in Fig. 3.14 whereas for pure MK and ZrO<sub>2</sub> there is no practical evidence of crystallization exothermic peak, the sample with both TiO<sub>2</sub> and seeds shows a well defined peak at about

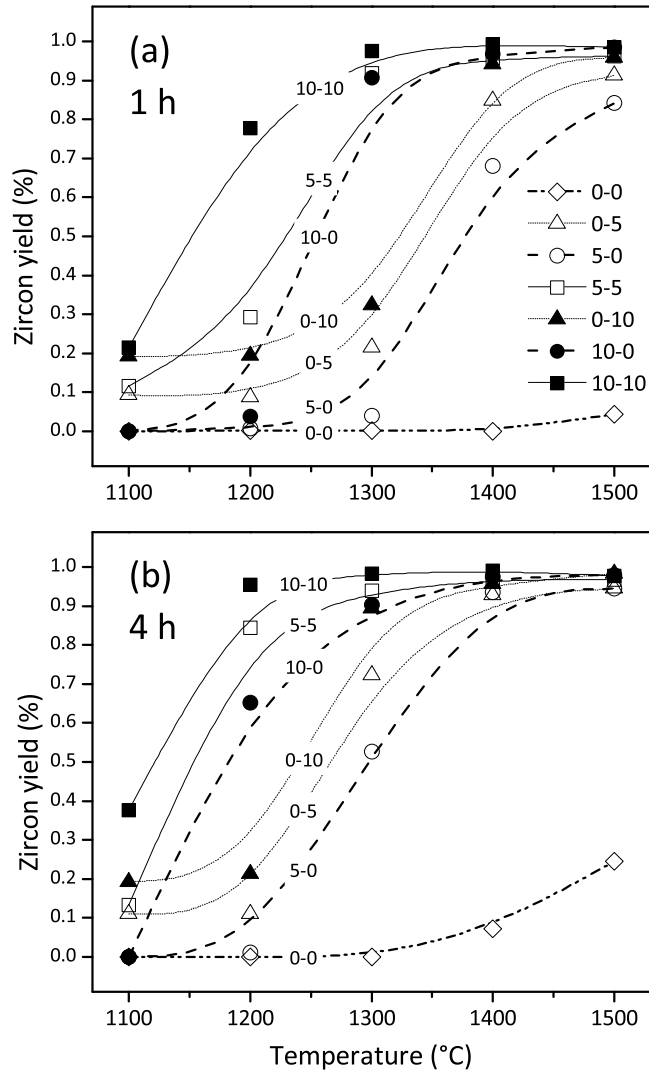


Figure 3.12: Zircon yield as a function of the treatment temperature for all the different systems studied. (a) 1 h soak, (b) 4 h soak.

1320°C (the other peaks are all attributable to the decomposition of the silicone resin, evident also from the weight loss in the thermogravimetric – TG – plot).

### 3.2.4 Applications

#### Zircon bulk components

The phase purity, in the newly developed zircon ceramics, is not accompanied by mechanical consistency. SEM analysis revealed many cracks in all samples, as it could be observed, as an example, for sample 0-0 (Fig. 3.15a,b) and sample 10-10 (Fig. 3.15c,d). Compact regions are separated one from each other, leading to very poor mechanical properties. This effect is very likely to be associated with the lacking compensation of the significant shrinkage and gas release occurring upon polymer decomposition at high temperature<sup>18</sup>. For this system, the effect of fillers does not seem sufficient to compensate the shrinkage upon pyrolysis and crystallization, even in the case of 10-10 sample, where the highest concentration of passive zircon seeds has been introduced.

Besides micro-cracks observable in SEM images, polymer evolution during pyrolysis has

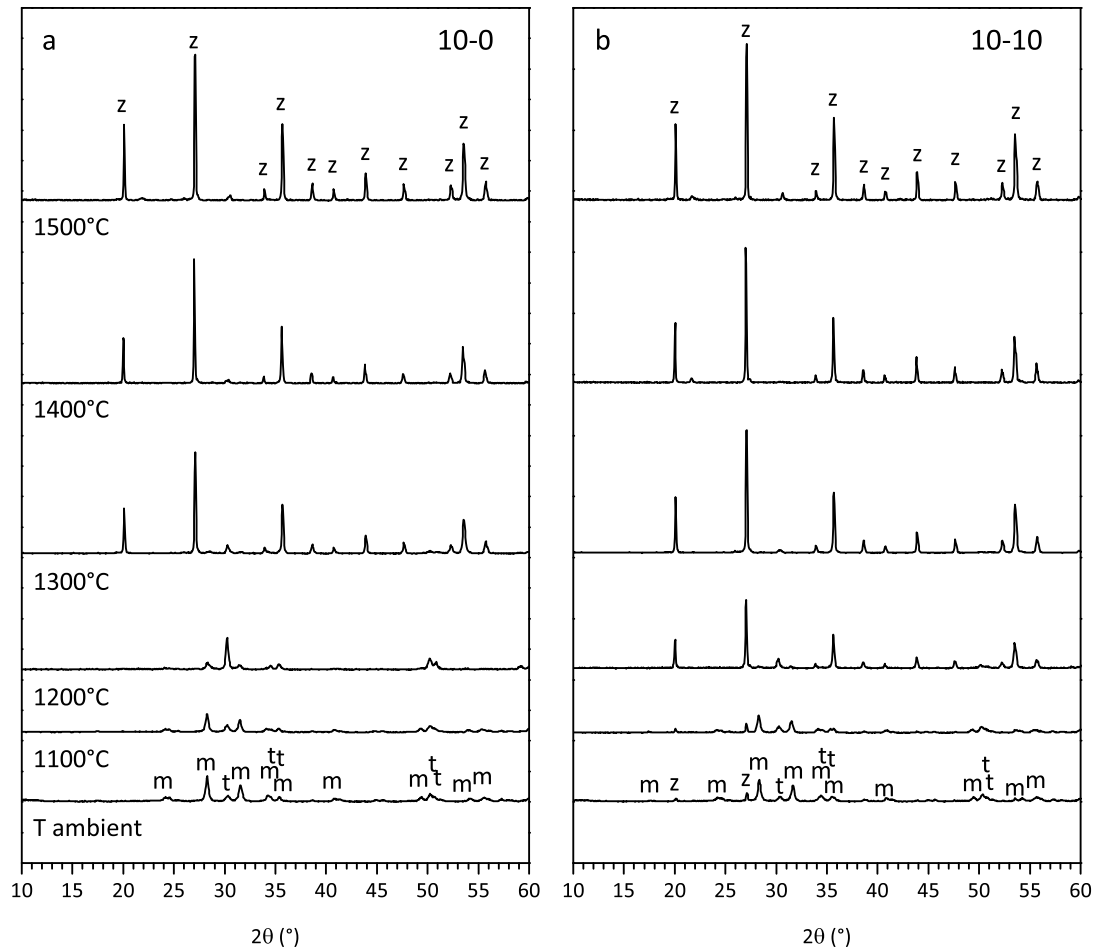


Figure 3.13: XRD patterns as a function of the treatment temperature (1 h soak) of 10-0 (a) and 10-10 (b) samples. m=m-ZrO<sub>2</sub>, t=t-ZrO<sub>2</sub>, z=zircon, c=cristobalite.

also a major influence in the integrity of samples after heat treatment. As could be observed in Fig. 3.16a, visible cracks are present in 10-10 sample (1300°C 1 h), which of course hinders any possible application of this type of ceramics as structural components.

To increase the integrity of the samples, part of Silres MK was replaced with Silres H62C, in order to have an equal SiO<sub>2</sub> contribution from both the polymers. Sample 10-10 was realized with this new formulation (referred as "10-10H"), and a picture of this sample is reported in Fig. 3.16b. No evident macrocracks could be observed in the sample: this result is considered to be noteworthy, especially considering the high temperature increasing rate (10°/min) adopted during the experiments. As shown by Fig. 3.17, the formation of zircon does not seem to be affected by the new source for silica (as a representative example, only patterns for the condition 1300°C/1 h are reported, which are virtually identical).

The new samples, although much improved compared to those from only MK, being visibly not cracked and hard to be powdered, were not actually fully dense, as reported by Tab. 3.3. No significant increase in apparent density and decrease of open porosity could be observed in the 1200-1400°C range, while a certain densification seems to start at 1500°C. Zircon monoliths synthesized at 1500°C showed a biaxial flexural strength equal to 138±19 MPa.

SEM images in Fig. 3.15e,f confirm the presence of residual porosity, but also show, significantly, a much different structure from 0-0 and 10-10 samples. Long cracks are replaced

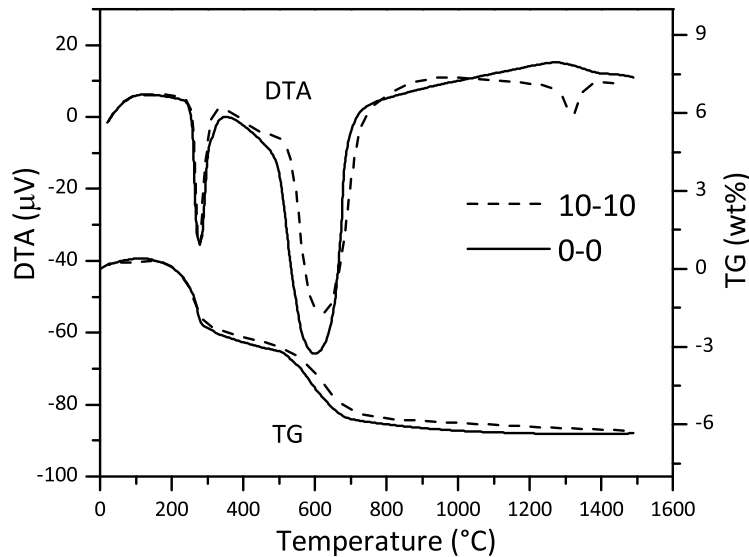


Figure 3.14: DTA/TG analysis of samples 0-0 and 10-10.

by a system of microcracks, likely determining a much lower enweakening effect, owing to crack branching<sup>14</sup>. A clear explanation for this improved samples mechanical consistency is still not very clear. The residual porosity (which is believed to be connected with the powder compaction step, which have still to be optimized) should give an beneficial effect with regard not only to the integrity of the samples after heat treatment, but also to the final properties such as thermal-shock resistance. Another contribute could be connected with the pre-curing step before powders compaction, which can eliminate (at least partially) the contribute of both shrinkage and gaseous products release during cross-linking. In any case, this does not seem to be the only reason. In fact, samples containing only Silres MK which have been pre-cured with the same methodology before compaction (data not shown for seek of brevity) still suffer cracking after heat treatment. Similar results for different ceramic systems (e.g. cordierite ceramics in Section 3.3) suggest that the molecular structure of the starting polymer could influence the characteristics of the amorphous SiO<sub>2</sub> network (i.e. connectivity, number of defects) after pyrolysis, and specific studies (regarding tests with many different weight proportions between MK and H62C) are currently being planned for the future.

A final remark concerns the possible applications of the developed ceramics. The very low synthesis temperature is attractive for the realization of monoliths to be used as refractory components or as dielectrics (e.g. the possibility of shaping in the preceramic state could be interesting, for the manufacturing of electronic micro-components); in addition, considering the low coefficient of thermal expansion, zircon anti-oxidation coatings could be proposed on SiC substrates: the low firing temperature could allow zircon formation without extensive oxidation of the substrate. Results regarding the realization of zircon-based protective coatings will be presented in Section 3.4.4, together with analogous results on Yttrium-disilicate coatings.

### 3.2.5 Conclusions

We may conclude that:

- silicone resins, properly filled with oxide nano-particles, are suitable for the preparation of zircon monoliths, starting from the very low temperature of 1200°C

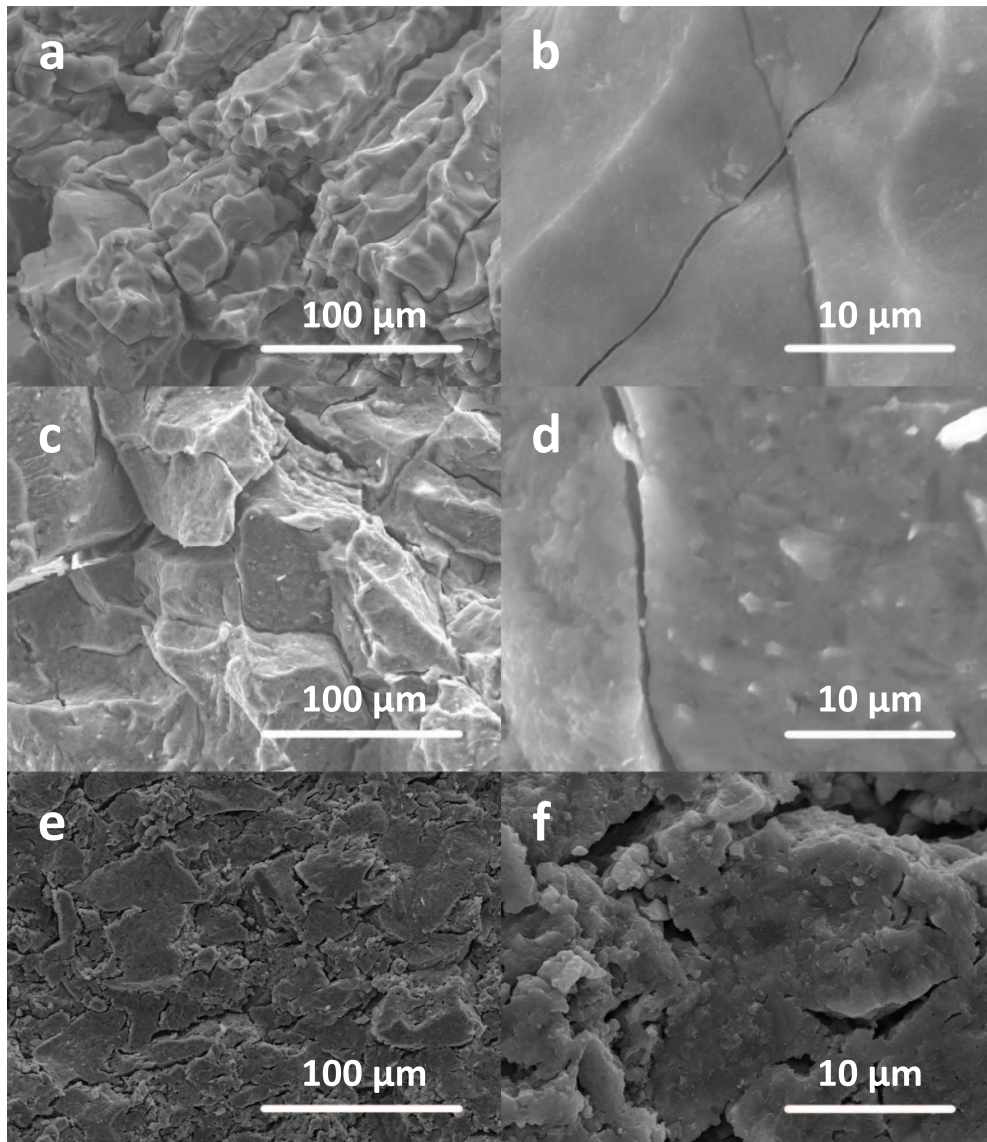


Figure 3.15: SEM images of samples (a,b) 0-0, (c,d) 10-10 and (e,f) 10-10H (1300°C 1 h).

- $\text{TiO}_2$  nano-particles are very effective in promoting low temperature synthesis of zircon, reasonably by operating a decrease in viscosity of the amorphous phase provided by the ceramic conversion of silicones;
- zircon seeds are particularly appreciated in their synergistic effect with  $\text{TiO}_2$ ; an optimum composition comprises 10 mol%  $\text{TiO}_2$  and 10 mol% seeds; variations in the silica source, i.e. changes in the formulation of the starting silicone, do not seem to affect the formation of zircon, rather than the density and integrity of the obtained monoliths;
- the low firing temperature is promising for extending the applications of zircon ceramics.
- the partial substitution of Silres MK with H62C was extremely effective for the realization of crack-free bulk components with interesting values of mechanical strength.

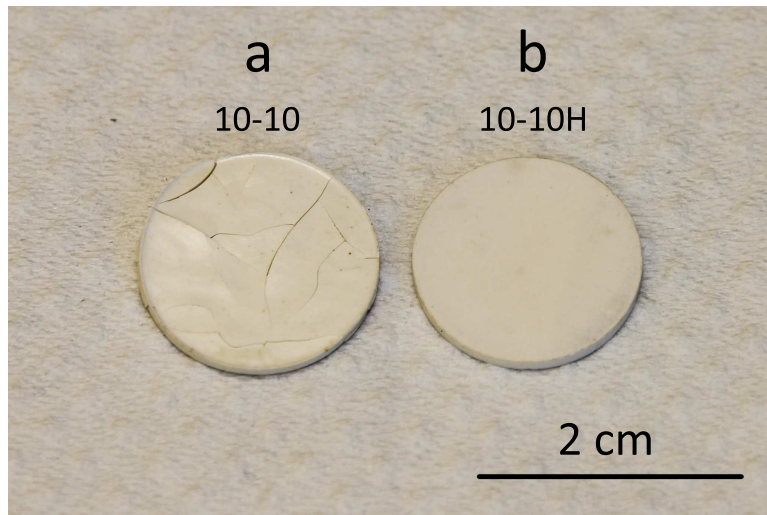


Figure 3.16: a) 10-10 and b) 10-10H samples after heat treatment at 1300°C for 1 h.

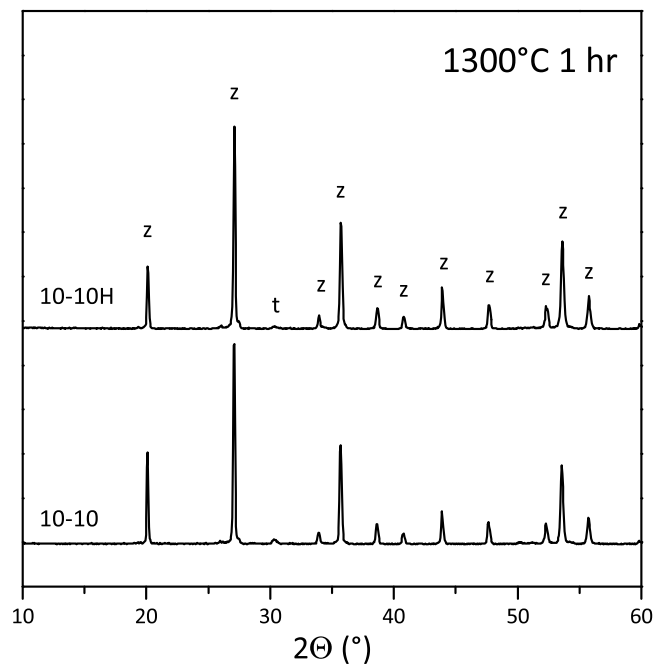


Figure 3.17: XRD patterns of samples 10-10 and 10-10H (1300°C 1 h). z=zircon, t=t-ZrO<sub>2</sub>.

Table 3.3: Bulk and relative density values for sample 10-10H as a function of the treatment temperature. A theoretical density of zircon equal to 4.6 g/cm<sup>3</sup> was considered to calculate relative density values.

Treatment temperature (1 h soak)	Bulk density (g/cm <sup>3</sup> )	Relative density (%)
1200°C	3.74	81
1300°C	3.75	81
1400°C	3.79	83
1500°C	3.97	86

## References

- [1] Y. Kanno, "Thermodynamic and crystallographic discussion of the formation and dissociation of zircon", *J. Mater. Sci.*, **24** [7] 2415–2420 (1989).
- [2] K. E. Sickafus, "Radiation Tolerance of Complex Oxides", *Science*, **289** [5480] 748–751 (2000).
- [3] R. C. Ewing, W. Lutze and W. J. Weber, "Zircon: A host-phase for the disposal of weapons plutonium", *J. Mater. Res.*, **10** [2] 243–246 (1995).
- [4] S. H. Lee, S. Kochawattana, G. L. Messing, J. Q. Dumm, G. Quarles and V. Castillo, "Solid-State Reactive Sintering of Transparent Polycrystalline Nd:YAG Ceramics", *J. Am. Ceram. Soc.*, **89** [6] 1945–1950 (2006).
- [5] R. Puthenkovilakam, E. Carter and J. Chang, "First-principles exploration of alternative gate dielectrics: Electronic structure of ZrO<sub>2</sub>/Si and ZrSiO<sub>4</sub>/Si interfaces", *Phys. Rev. B*, **69** [15] 1–11 (2004).
- [6] R. Shaltaf, T. Rangel, M. Grüning, X. Gonze, G. M. Rignanese and D. Hamann, "Electronic properties of zircon and hafnium from many-body perturbation theory", *Phys. Rev. B*, **79** [19] 1–6 (2009).
- [7] G. D. Wilk, R. M. Wallace and J. M. Anthony, "High-k gate dielectrics: Current status and materials properties considerations", *J. Appl. Phys.*, **89** 5243 (2001).
- [8] C. Veytizou, "Preparation of zircon bodies from amorphous precursor powder synthesized by sol-gel processing", *J. Eur. Ceram. Soc.*, **22** [16] 2901–2909 (2002).
- [9] G. Vilmin, S. Komarneni and R. Roy, "Lowering crystallization temperature of zircon by nanoheterogeneous sol-gel processing", *J. Mater. Sci.*, **22** [10] 3556–3560 (1987).
- [10] S. Ying, H. Xiaoxian and Y. Dongsheng, "Effect of natural zircon powder as seeds on the gel synthesis of zircon powder", *Mater. Lett.*, **21** [1] 79–83 (1994).
- [11] P. Tartaj, C. J. Serna, J. Requena, S. D. E. Aza and F. Guitian, "The formation of zircon from amorphous ZrO<sub>2</sub>-SiO<sub>2</sub> powders", *J. Mater. Sci.*, **31** 6089–6094 (1996).
- [12] G. Parcianello, E. Bernardo and P. Colombo, "Mullite/Zirconia Nanocomposites from a Pre-ceramic Polymer and Nanosized Fillers", *J. Am. Ceram. Soc.*, **94** [5] 1357–1362 (2011).
- [13] C. Du, Q. Yuan and Z. Yang, "Lowering the synthesis temperature of zircon powder by yttria addition", *J. Mater. Sci. Lett.*, **18** [12] 965–966 (1999).
- [14] An Introduction to the Mechanical Properties of Ceramics.
- [15] S. H. Hong and G. L. Messing, "Anisotropic Grain Growth in Diphasic-Gel-Derived Titania-Doped Mullite", *J. Am. Ceram. Soc.*, **77** [5] 1269–1277 (1998).
- [16] M. D. Sacks, N. Bozkurt and G. W. Scheiffele, "Fabrication of Mullite and Mullite-Matrix Composites by Transient Viscous Sintering of Composite Powders", *J. Am. Ceram. Soc.*, **74** [10] 2428–2437 (1991).
- [17] E. C. Cortés, J. A. M. Fuente, J. M. Moreno, C. P. Pérez, E. C. Cordoncillo and J. B. C. Castelló, "Solid-Solution Formation in the Synthesis of Fe-Zircon", *J. Am. Ceram. Soc.*, **87** [4] 612–616 (2004).
- [18] P. Greil, "Active-Filler-Controlled Pyrolysis of Pre-ceramic Polymers", *J. Am. Ceram. Soc.*, **78** [4] 835–848 (1995).



## 3.3 Cordierite

### 3.3.1 Introduction

Cordierite is a Mg-aluminosilicate with the general formula  $2\text{MgO}\cdot 2\text{Al}_2\text{O}_3\cdot 5\text{SiO}_2$ . Its very low CTE (coefficient of thermal expansion, equal to  $2\cdot 10^{-6}\text{K}^{-1}$ ) and its good thermal stability, corrosion resistance and generally low price make this material one of the most used refractories for high temperature (up to approximately  $1250^\circ\text{C}$ ) applications characterized by severe thermal gradients. Cordierite has also been so far the mainstream ceramic for the realization of particulate filters for diesel engines, and finds also application in the catalytic converters field.

Because of the generally inexpensiveness of cordierite ceramics, the synthesis route and the raw materials selection is of fundamental importance. The most important synthesis route for cordierite ceramics is the reactive sintering at high temperature of various combinations of different inorganic powders like oxides, hydroxides, clays, etc.<sup>1</sup>. Homogeneous and high purity cordierite powders could be also synthesized by the sol-gel route<sup>1,2</sup>, although the relatively high prices of the reagents and the solvents needed during the sol-gel process are generally not compatible with the inexpensive nature of the final ceramics.

In this Section, a simple method for the realization of high purity cordierite ceramics with tailorable porosity is presented, starting from a preceramic polymer system, filled with oxides nanopowders.

### 3.3.2 Experimental procedure

To study the synthesis of cordierite form filled-preceramic polymers, Silres MK was used as a silica source. As a first step, silicone resin was dissolved in isopropyl alcohol by magnetic stirring. After this step,  $\text{Al}_2\text{O}_3$  (Evonik Aeroxide Alu C) and MgO (Inframat Advanced Materials) nanopowders were dispersed into the solvent/silicone solution, in the right proportions to give the formation of pure cordierite. Mixtures were homogenized by magnetic stirring and ultrasonication, thus obtaining homogeneous and stable dispersions. After solvent evaporation at  $80^\circ\text{C}$  overnight, the material was pulverized and subsequently heat treated inside an  $\text{Al}_2\text{O}_3$  boat in the  $1000\text{--}1400^\circ\text{C}$  range for 1 h ( $10^\circ/\text{min}$  heating rate). Phase evolution was investigated by means of X-ray diffraction. For low-porosity samples, mechanical strength measurements were carried out using the Ball on 3-balls technique (see Appendix B) on circular samples, thus measuring the biaxial strength, while highly-porous samples were cut down to small bricks, and crushing strength was measured by uniaxial compression.

#### Low-porosity samples preparation

Silres MK or an MK/H62C mixture was mixed together with  $\text{Al}_2\text{O}_3$  and MgO nanopowder. When an MK/H62C mixture was used, MK/H62C ratio was calculated in order to obtain the same  $\text{SiO}_2$  contribute from both polymers. As reported in Appendix A, Silres MK is a solid polysilsesquioxane powder characterized by a 84 wt% silica yield after pyrolysis in oxidative atmosphere. MK can be thermally cross-linked through condensation reactions between the hydroxyl and ethoxy functionalities present inside its molecular structure, with the consequent release of water and other volatile species, i.e. ethanol<sup>3</sup>. H62C instead is a viscous polysiloxane liquid containing methylic, vinylic and phenylic functionalities, characterized by a lower ceramic yield (approximately 58 wt%) if compared to MK, but with a thermal

cross-linking mechanism that does not entail the release of gaseous byproducts. After the homogenization of the dispersions, solvent was removed at 80°C overnight, and the material obtained was finely ground in a mortar with a pestle. When an MK/H62C mixture was used, because of the plastic behavior of the material after drying (due to the lower viscosity of the H62C component), to make the following grinding step possible an additional step at 250°C for 30 min was necessary to induce a partial cross-linking of the polymeric component. After the grinding step, powder was sieved (75 µm mesh) and uniaxially pressed at 40 MPa. Pressed samples were finally heat treated in the 1100-1400°C range for 1 h in air (10°/min heating rate).

### High-porosity samples preparation

Silres MK (or MK/H62C mixture, in the same proportions as for the realization of cordierite low-porosity samples described in the prior section) was mixed together with Al<sub>2</sub>O<sub>3</sub> and MgO nanopowder, using isopropyl alcohol as dispersion medium. After the homogenization step, 50 µm PMMA micro-beads were added in the dispersions and stirred together for 10 min. Dispersions were then dried at 80°C and manually ground in a mortar with a pestle. Finally, powders were warm-pressed uniaxially at 170°C for 5 min (20 MPa load applied). Before the final pyrolysis treatment, PMMA sacrificial micro-beads were removed at 300°C for 2 h in air (1°/min heating rate).

### 3.3.3 Synthesis

A first part of the work regarded the analysis of the synthesis characteristics of cordierite from a filled-preceramic polymer system. In Fig. 3.18 the XRD analysis of the samples after heat treatment in the 1000-1400°C temperature range are reported. Synthesis results were obtained by using only MK resin as a silica precursor, although equivalent result could be obtained by using an MK/H62C mixture (results not reported here for brevity).

At lower temperature, the ceramic material is mostly XRD amorphous: the broad peak in the 18-26° range is mainly associated with the amorphous ceramic residue deriving from the preceramic polymer, which gives an amorphous silica network after pyrolysis in oxidative atmosphere; the presence of small spinel (MgAl<sub>2</sub>O<sub>4</sub>) crystals (which could be deduced from the width of the peaks) could also be observed, likely deriving from the reaction of MgO and Al<sub>2</sub>O<sub>3</sub> nanopowders, as previously described in literature<sup>1</sup>. In the 1100-1200°C range small quantities of Mg-silicates and of Mg-aluminosilicates have also been observed, but the very low intensity of the peaks makes their identification and the evaluation of their evolution not trivial.

The nucleation of cordierite could be clearly observed at 1250°C, together with the nucleation of cristobalite from the amorphous silica residue present at lower temperature. The main diffraction peak of cristobalite is located at 21.8°, and it is superimposed to one of the main cordierite peaks. The nucleation of these two phases must be associated with the exothermic peak at 1253°C that could be observed in the DTA curve reported in Fig. 3.19. Cordierite seems to nucleate directly in the high-temperature α-form, and the presence of intermediate μ-cordierite, a metastable high-quartz solid solution<sup>4</sup>, was not detected, unlike in other works in literature<sup>2,5,6</sup>.

A further increase in the treatment temperature finally leads to the virtually total elimination of the residual secondary phases, the constituents of which are progressively absorbed inside the cordierite structure, which becomes the only phase detectable for temperatures

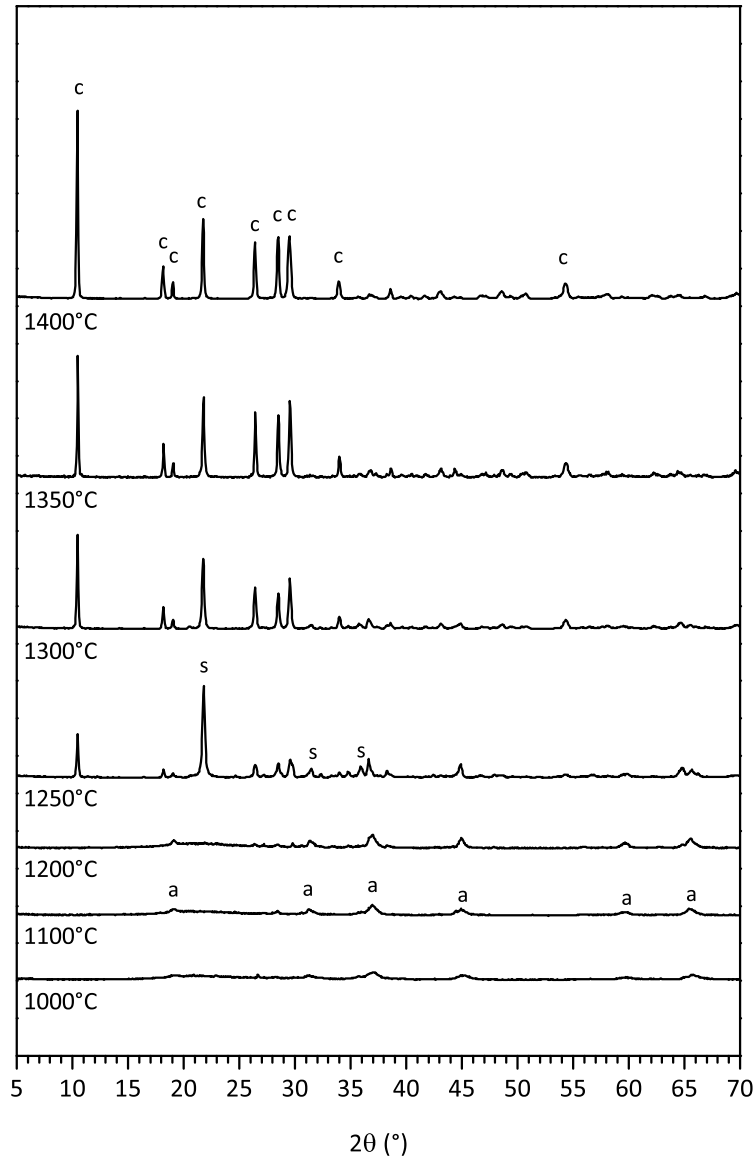


Figure 3.18: XRD patterns of Silres MK filled with  $\text{Al}_2\text{O}_3$  and  $\text{MgO}$  nanopowders and fired in the 1000-1400°C range for 1 h ( $10^\circ/\text{min}$  heating rate). c=cordierite, a=spinel ( $\text{MgAl}_2\text{O}_4$ ), s= $\text{SiO}_2$ .

$\geq 1300^\circ\text{C}$ . The results of the present work regarding cordierite synthesis seem to be comparable with previous observations made on sol-gel-derived cordierite<sup>1</sup>. Enhanced nucleation kinetic seems to be a common feature of many different ceramic systems obtained through the pyrolysis of preceramic polymer filled with nanometric fillers. Fillers with higher specific surface area entail a more intimate mixing of the starting constituent of the final ceramic, thus reducing the mean diffusion path of species involved in the reactions, as so far demonstrated in different works<sup>7-10</sup>.

### 3.3.4 Applications

Based on the synthesis results described in the previous paragraphs, efforts have been put for the realization of pure cordierite ceramics with tailorable porosity, exploiting the shaping possibilities that the PDCs technique can offer. As described in the Experimental procedure section, 2 different types of samples were realized.

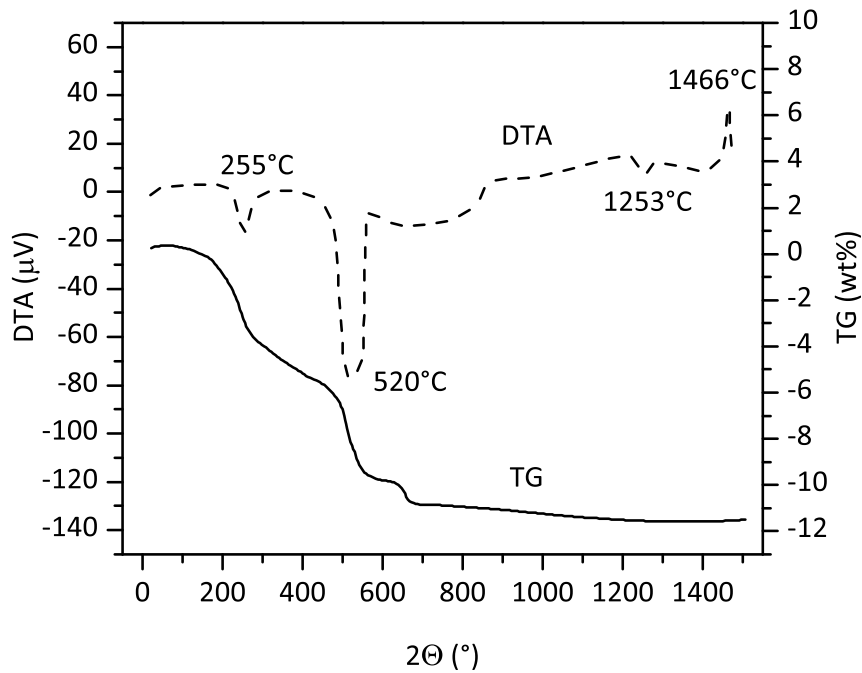


Figure 3.19: DTA/TG curves for an MK/Al<sub>2</sub>O<sub>3</sub>/MgO mixture fired in air.

Low porosity samples were realized by standard uniaxial cold pressing, in order to produce with the PDCs technique cordierite monoliths with values of porosity as low as possible, to realize, in principle, samples with the highest mechanical properties, i.e. mechanical strength.

On the other hand, high-porosity cordierite sample were realized by using PMMA sacrificial micro-beads, coupled with a warm-pressing compaction step: these samples, although characterized in principle by a much lower mechanical resistance, should have the best characteristics for the realization of extremely lightweight samples with extraordinary properties of thermal insulation.

These 2 types of samples are a good representation of the 2 "extremes" that could be produced by the PDCs technique described. In principle, intermediate properties between these two types of samples could be easily realized, thus obtaining sample with a tailorable amount and type of porosity, and thus with tailorable characteristics of thermal insulation, density and mechanical resistance.

Moreover, it should be pointed out that the tailoring of porosity that will be described in the next sections, although applied only to cordierite ceramics, represents an example of shaping methodology that could be, in principle, applied to many other ceramic systems realized through the PDCs technique, such as mullite-based materials, zircon, and many other silicates, for thermal, structural and functional applications.

### Low-porosity cordierite components

Monoliths realized with MK as the only silica source were found to be subjected to cracking upon heat treatment, which off course hinders their applicability. When preceramic polymers are used, reactions like cross-linking and polymer-to-ceramic conversion imply the release of gases and a noticeable shrinkage development, both potential sources of cracks. This evidence is totally analogous to what observed for zircon ceramics in Section 3.2, and is, again, likely due to the fact that the quantity of fillers added to the preceramic polymer is too low to have

a sufficient lowering of the global material shrinkage to avoid the formation of cracks.

The substitution of part of MK with H62C was found to be fundamental for the obtainment of crack-free monoliths. Although the exact mechanism is still not very clear, more factors are believed to contribute to this enhancement of mechanical consistency: 1) the partial substitution of MK for H62C lowers the gas release during polymer cross-linking (due to different cross-linking reactions), thus decreasing the generation of cracks and pores that could extend in the subsequent phases of the heat treatment, 2) the pre-curing step before powder compaction include a certain amount of shrinkage that must not be taken into account in the following treatment, 3) the different precursor nature could generate a silica matrix with different properties, like network connectivity and number of defects, and thus with a different ability to relax structural rearrangements by viscous flow or diffusion processes, and 4) the residual porosity (observable in Fig. 3.20b, which is likely due to a less "efficient" compaction step) could have beneficial effects during the release of gases during the pyrolysis.

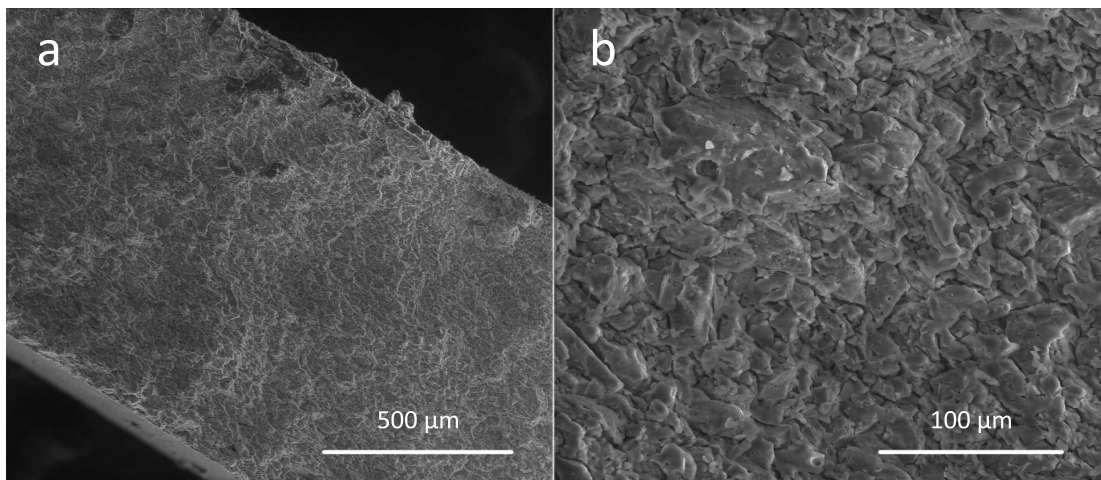


Figure 3.20: a) low magnification and b) high magnification SEM images of a cordierite sample produced from a mixture of MK, H62C,  $\text{Al}_2\text{O}_3$  and MgO nanopowders, after heat treatment at  $1300^\circ\text{C}$  for 1 h.

SEM images of cordierite sample treated at  $1350^\circ\text{C}$  for 1 h are reported in Fig. 3.20 (fracture surface). At a lower magnification level, a quite homogeneous structure could be observed, with no evident big defects such as macro-cracks or pores. At higher magnification instead, the material seems to be constituted by alternated compact regions, partially connected with each other, and micro-voids. This structure should be associated with the pre-curing step and the subsequent compaction phase. Pre-cured powders have a lower ability of producing viscous flow under an applied stress: for this reason, uniaxial pressing process become a less effective method to compact pre-cured powders if compared to un-cured powders, thus producing residual voids that prevent the possibility of obtaining a fully-dense green compact. However, it should be also noted that this lower compaction level could be another favorable factor for the realization of crack-free samples, since the residual pores network in the green state could allow a more efficient and homogeneous elimination of gases during the pyrolysis step, without local pressure accumulation phenomena and the subsequent cracking generation that is typically observed in all PDCs.

In Fig. 3.21 a detail of the cordierite micro-structure could be observed. Dense regions likely represent the original precursor powders that were previously sieved and compacted by uniaxial pressing, which are still clearly separated one from each because of the less efficient mechanism of viscous flow during the compaction step. On average, these regions

are very compact and homogeneous, with the exception of some residual closed porosity (with a mean pore size of 1  $\mu\text{m}$ ) that could be clearly observed.

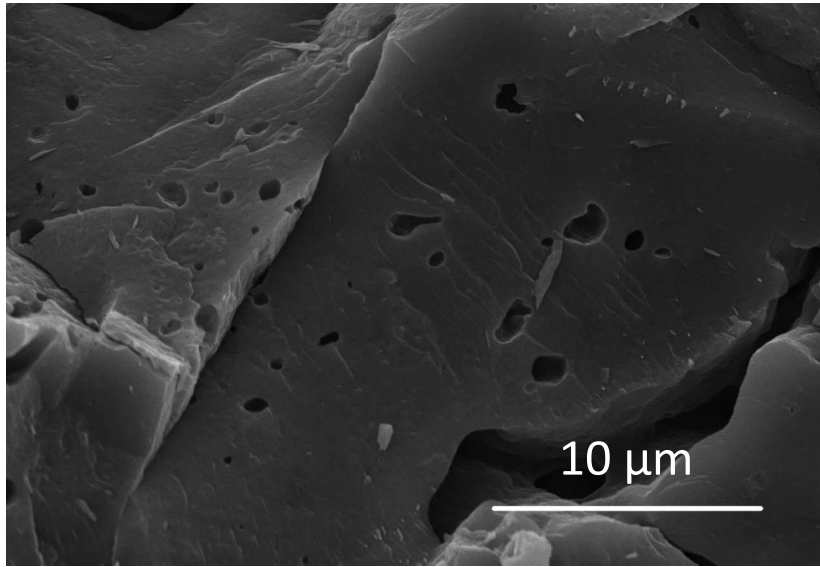


Figure 3.21: High magnification detail of a cordierite sample produced from a mixture of MK, H62C,  $\text{Al}_2\text{O}_3$  and MgO nanopowders, after heat treatment at 1300°C for 1 h.

Density measurements were carried out only on samples heat treated at 1300 and 1400°C. Density for samples treated at lower temperatures were not considered, since pure cordierite ceramics were synthesized only for temperatures  $\geq 1300^\circ\text{C}$ . A slight increase on the density of the samples was observed changing the temperature from 1300 to 1400°C. Density values are reported in Tab. 3.4.

Table 3.4: Bulk and relative density values for cordierite monoliths fired at 1300 and 1400°C for 1 h. A theoretical density of cordierite equal to 2.65  $\text{g}/\text{cm}^3$  was considered to calculate relative density values.

Treatment temperature (1 h soak)	Bulk density ( $\text{g}/\text{cm}^3$ )	Relative density (%)
1300°C	2.01	76
1400°C	2.15	81

Biaxial strength values for low-porosity samples were measured by the Ball on 3-balls test on circular specimens. Values obtained are in the order of 63 MPa for sample treated at 1400°C: these values are comparable to analogous cordierite commercial products<sup>11</sup> with similar density values and obtained by standard powder processing routes, again confirming for the PDCs technique the extremely favorable combination of simple and quite inexpensive processing and the possibility of obtaining near net-shape samples with good mechanical properties (at least comparable to analogous commercial products). Moreover, additional advantages in term of shaping possibilities (e.g. extrusion, injection molding) and specific applications (e.g. coatings, ceramic joining, highly-porous bodies) are possible thanks to the presence of a polymeric phase inside the starting mixture, which are generally not achievable with standard synthesis routes.

### High-porosity cordierite components

As previously observed for highly-porous samples realized from preceramic polymers (by the introduction of sacrificial filler, foaming agents or by self-foaming reactions<sup>12,13</sup>), the

pyrolysis of preceramic polymers, if sufficiently slow heating rates are used, does not show problems related to extensive cracking of the samples, as it is always observed when trying to realize low-porosity monoliths. The reason for this phenomenon is connected with the low thickness of the pores walls (generally ranging from few  $\mu\text{m}$  to few hundreds of  $\mu\text{m}$ ), which enables an efficient polymer pyrolysis and release of gaseous products without the local accumulation of pressure that could generate a more or less extensive cracking, that finally results in the destruction of the sample.

For this reason, contrarily to what observed for low-porosity cordierite samples where no mechanical consistency was achieved (Section 3.3.4), the use of Silres MK as the only silica source allowed the realization of porous cordierite samples with a much more limited (although still visible) presence of cracks.

As a starting point, 2 different concentrations of PMMA micro-beads were tested. Weight ratios of 80/20 and 70/30 (PMMA micro-beads/cordierite preceramic mixture) were selected. SEM images of these 2 samples are reported in Fig. 3.22.

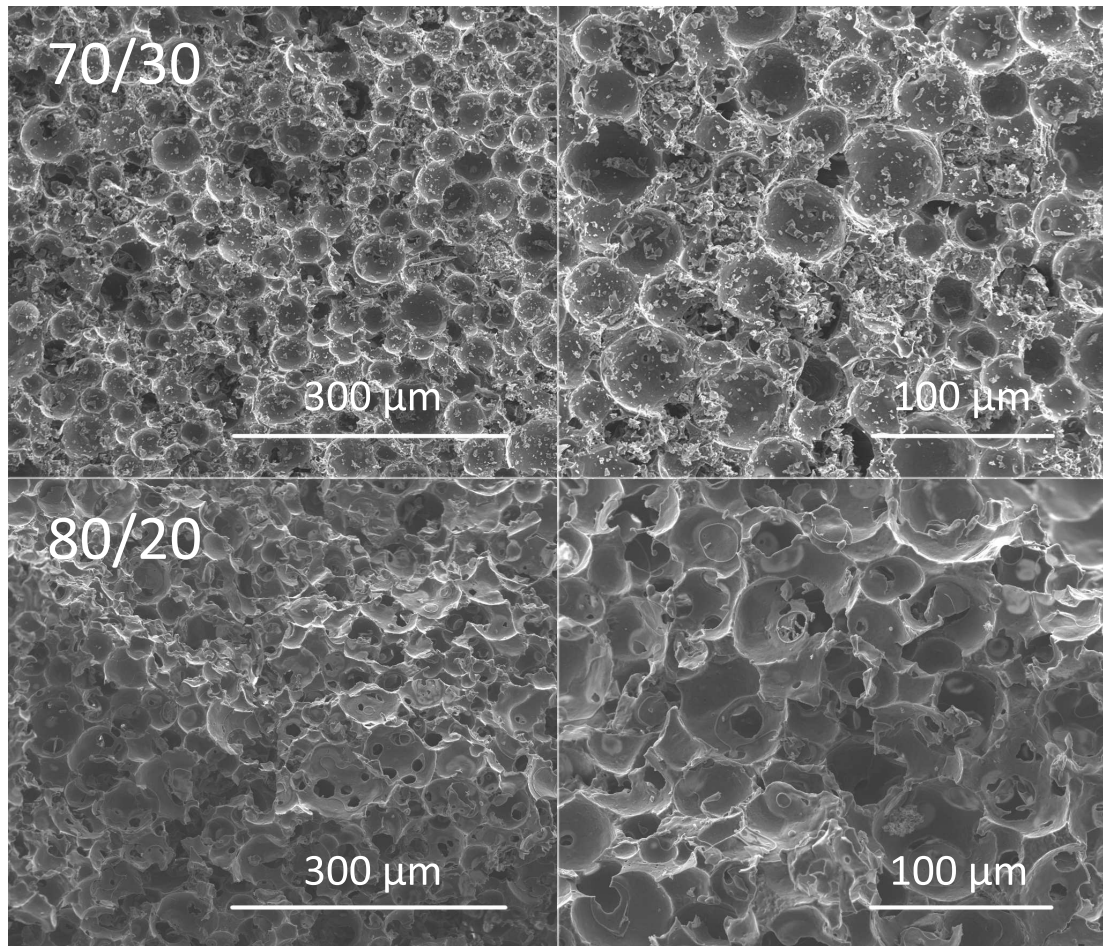


Figure 3.22: SEM images of 70/30 (top) and 80/20 (bottom) highly-porous cordierite samples produced by using PMMA micro-beads as sacrificial fillers (1300°C 1 h). "70/30" and "80/20" refer to the PMMA/cordierite preceramic mixture weight ratio before heat treatment.

As expected, a quite homogeneous pores distribution was achieved inside both the samples, with a mean pore size of approximately  $50 \mu\text{m}$ , which is obviously directly connected with the size distribution of the PMMA sacrificial fillers.

As could be observed, a change of the type of porosity is evident between the two samples: in fact, while 70/30 sample shows a basically closed porosity (no "windows" are present in

the pores walls), 80/20 samples is characterized by a more open porosity (windows in the pores walls are clearly noticeable) and by the presence of more defects – such as cracks and discontinuities – in the walls. These characteristics obviously generate a very low mechanical consistency (sample could be easily cracked and pulverized), which hinders any possible practical application.

With this procedure, dense and continuous struts are produced, as could be observed in some details reported in Fig. 3.23. Moreover, in Fig. 3.23b it could be noted that cordierite grains have a mean dimension in the order of  $0.8\ \mu\text{m}$ , and that, in correspondence of some areas, struts walls are just 1-grain thick.

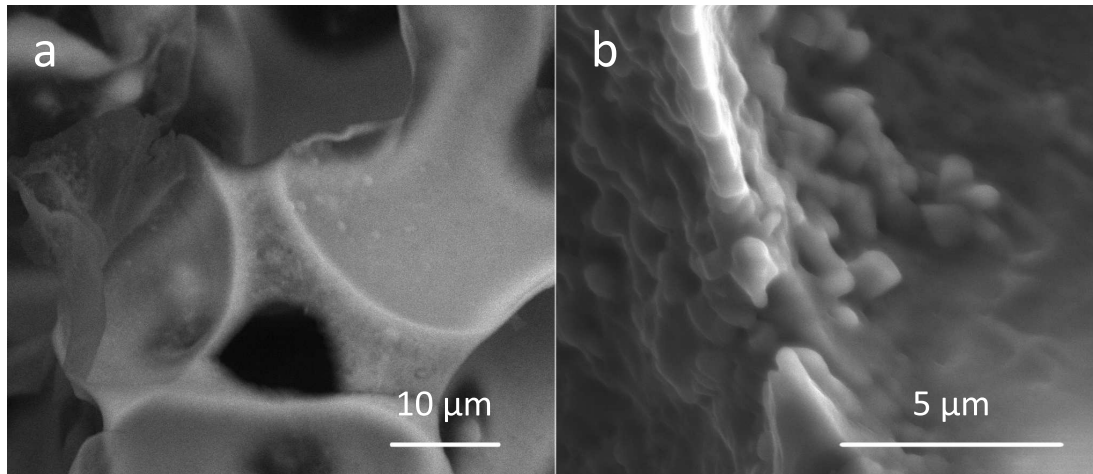


Figure 3.23: Struts details of 70/30 highly-porous cordierite sample produced by using PMMA microbeads as sacrificial fillers ( $1300^{\circ}\text{C}$  1 h).

Based on these first results, a subsequent improvement step involved the substitution of part of Silres MK with Silres H62C, that previously proved to be effective in enhancing the mechanical consistency of both cordierite and zircon monoliths. In addition, an intermediate concentration of PMMA micro-beads was adopted, i.e. 75/25 (PMMA micro-beads/cordierite preceramic mixture). SEM results are reported in Fig. 3.24.

Contrarily to what observed for 80/20 and 70/30 samples obtained by using Silres MK as the only silica source, where some limited sample cracking was observable, the partial substitution of MK for H62C in sample 75/25 produced a more homogeneous sample, with improved mechanical resistance and consistency, where no macro-cracks were observed.

The 75/25 concentration demonstrated to give a good combination of structural homogeneity (especially with regards to the distribution of pores inside the material) and type of porosity. In fact, a mix of closed porosity and some clues for a certain fraction of open pores was found from SEM analysis, which was not present, for example, in 70/30 sample, where a virtually totally closed porosity was present. The level of porosity reached in 75/25 sample probably represents the “threshold” between a material with a totally closed porosity and a material where pores are all interconnected. In principle, this type of sample should show a very good combination of lightness and thermal insulation, while maintaining a sufficient mechanical strength.

Bulk density, relative density and crushing strength values for high-porosity samples are reported in Tab. 3.5. Relative density values are in accordance with previous results on similar foams produced by the pyrolysis of preceramic polymers<sup>12</sup>, but with a higher mechanical strength, associated probably with the crystalline nature of the cordierite foam, if compared

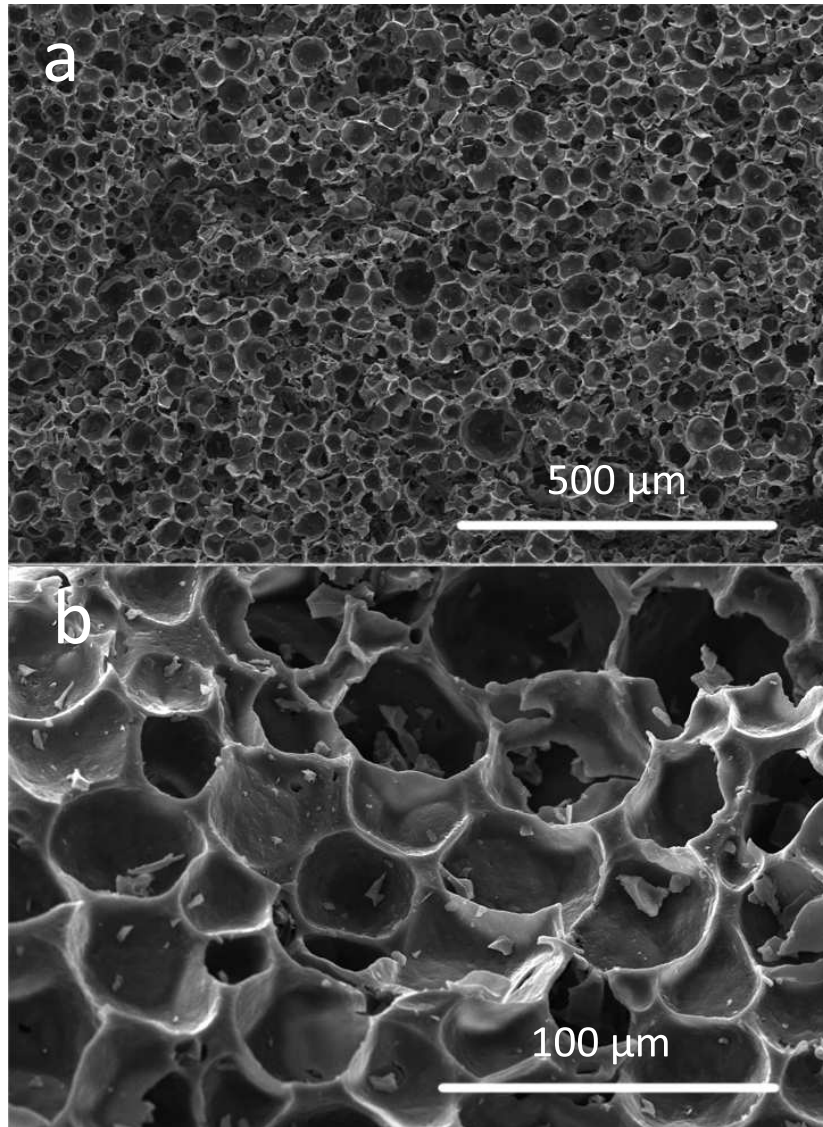


Figure 3.24: a) low magnification and b) high magnification SEM images of a cordierite sample produced from a mixture of MK, H62C, Al<sub>2</sub>O<sub>3</sub> and MgO nanopowders, filled with additional PMMA micro-beads, after heat treatment at 1300°C for 1 h.

with the amorphous structure of the SiOC glass studied in<sup>12</sup>.

In addition, if compared to similar works in literature<sup>14</sup> regarding cordierite ceramics by PDCs technique, present results show many improvements, regarding the micro-structural homogeneity, continuity and integrity (especially at high-porosity levels) and mechanical crushing strength (7.1 MPa with relative density=22.6% for present sample 70/30, vs. 4.8 MPa with relative density=26% of reference<sup>14</sup>). This represents a further confirmation of the extremely high potential of the PDCs technique, and also a demonstration that an accurate selection of the starting materials and a careful control of the processing conditions are fundamental for the obtainment of reliable materials to be applied in specific applications.

### 3.3.5 Conclusions

In this Section, results regarding the synthesis and the shaping of cordierite ceramics starting from mixtures of preceramic polymers and nano-fillers have been presented. Synthesis of cordierite was studied in the 1000-1400°C range: XRD results confirmed the possibility of

Table 3.5: Bulk density, relative density and crushing strength values for highly-porous cordierite monoliths 80/20, 72/25 and 70/30 fired at 1300 for 1 h. A theoretical density of cordierite equal to 2.65 g/cm<sup>3</sup> was considered to calculate relative density values.

Property	Sample 80/20	Sample 75/25	Sample 70/30
Bulk density (g/cm <sup>3</sup> )	0.37±0.01	0.49±0.01	0.60±0.01
Relative density (%)	14.0	18.6	22.6
Crushing strength (MPa)	0.38±0.02	2.8±0.4	7.1±1.6

producing highly-pure cordierite samples with no secondary phases or impurities. Moreover, the nucleation of cordierite was observed for temperatures comparable to those observed for analogous sol-gel derived systems, thus confirming the enhanced nucleation kinetic and reactivity that could be achieved by coupling preceramic polymers and fillers with high specific surface area.

The realization of monoliths with very different levels of porosity have been explored. Near net shape low porosity samples showed a relative density of approximately 80%, with mechanical properties comparable to analogous commercial products. They were easily produced by uniaxial pressing and with very fast (10°/min) heat treatments, which could represent a remarkable advantage in terms of industrial applicability. Highly porous samples were instead realized by the addition of sacrificial fillers (PMMA micro-beads), which allows the realization of monoliths with extremely low relative densities (~18%) and with a highly-controllable size and distribution, as well as type (open or closed) and amount of porosity.

A wide variety of samples with relative density ranging from 18 to 80% could be in principle produced with this technique, in order to achieve the desired combination of thermal and mechanical properties. Moreover, it should be pointed out that this technique could be easily be extended to other ceramic system (some of them studied and described in the present thesis, such as mullite-based materials or zircon ceramics).

## References

- [1] A. Menchi and A. Scian, "Mechanism of cordierite formation obtained by the sol-gel technique", *Mater. Lett.*, **59** [21] 2664–2667 (2005).
- [2] L. Radev, B. Samuneva, I. Mihailova, L. Pavlova and E. Kashchieva, "Sol-gel synthesis and structure of cordierite/tialite glass-ceramics", *Processing and Application of Ceramics*, [3] 125–130 (2009).
- [3] F. Wolff, C. Kugler and H. Münstedt, "Time- and temperature-dependent crosslinking behaviour of a silicone resin", *Rheol. Acta*, (2011).
- [4] W. Storek, R. Muller and G. Kunath-Fandrei, "<sup>27</sup>Al and <sup>29</sup>Si MAS NMR investigations of cordierite glass,[ $\mu$ ]- and [ $\alpha$ ]-cordierite", *Solid State Nucl. Mag.*, **9** [2-4] 227–239 (1997).
- [5] S. P. Hwang and J. M. Wu, "Effect of Composition on Microstructural Development in MgO-Al<sub>2</sub>O<sub>3</sub>-SiO<sub>2</sub> Glass-Ceramics", *J. Am. Ceram. Soc.*, **84** [5] 1108–1112 (2001).
- [6] N. Saito, S. Y. Nishimura, M. Kawano, S. I. Araki, S. Sukenaga, K. Nakashima and T. Yasukouchi, "Fabrication of Nitrogen-Containing Cordierite Ceramics", *J. Am. Ceram. Soc.*, **93** [8] 2257–2263 (2010).
- [7] E. Bernardo, P. Colombo, E. Pippel and J. Woltersdorf, "Novel Mullite Synthesis Based on Alumina Nanoparticles and a Preceramic Polymer", *J. Am. Ceram. Soc.*, **89** [5] 1577–1583 (2006).
- [8] F. Griggio, E. Bernardo, P. Colombo and G. L. Messing, "Kinetic Studies of Mullite Synthesis from Alumina Nanoparticles and a Preceramic Polymer", *J. Am. Ceram. Soc.*, **91** [8] 2529–2533 (2008).
- [9] E. Bernardo, E. Tomasella and P. Colombo, "Development of multiphase bioceramics from a filler-containing preceramic polymer", *Cerami. Int.*, **35** [4] 1415–1421 (2009).
- [10] R. Riedel, L. Toma, C. Fasel and G. Mieke, "Polymer-derived mullite-SiC-based nanocomposites", *J. Eur. Ceram. Soc.*, **29** [14] 3079–3090 (2009).
- [11] ASM Engineering Materials Reference Book, 2nd edition, M. Baucchio, Ed. ASM International, 1994.
- [12] P. Colombo, "Macro- and micro-cellular porous ceramics from preceramic polymers", *Compos. Sci. Technol.*, **63** [16] 2353–2359 (2003).
- [13] C. Vakifahmetoglu, I. Menapace, A. Hirsch, L. Biasetto, R. Hauser, R. Riedel and P. Colombo, "Highly porous macro- and micro-cellular ceramics from a polysilazane precursor", *Ceram. Int.*, **35** [8] 3281–3290 (2009).
- [14] I. H. Song, M. J. Kim, H. D. Kim and Y. W. Kim, "Processing of microcellular cordierite ceramics from a preceramic polymer", *Scripta Materialia*, **54** [8] 1521–1525 (2006).



## 3.4 Yttrium silicates

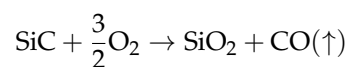
### 3.4.1 Introduction

Yttrium monosilicate,  $Y_2O_3 \cdot SiO_2$  (referred as Y-MS), and yttrium disilicate,  $Y_2O_3 \cdot 2SiO_2$  (referred as Y-DS) are relatively new refractory silicates, and they are subjected to a growing interest for materials suitable for high temperature applications<sup>1</sup>. Y-MS is characterized by 2 different allotropic forms (X1, stable at low temperatures, and X2, stable at higher temperatures), that can undergo displacive transformation<sup>2</sup>. Y-DS instead show a more complex phase diagram, with many different allotropic forms ( $\alpha, \beta, \gamma$ , etc.)<sup>3,4</sup>; all the forms are stable in a certain temperature range, but high temperature polymorphs may be available at room temperature, due to extremely slow transformation kinetics<sup>2</sup>. Both silicates feature high melting points (1775°C for disilicate<sup>5</sup>) and, above all, relatively low CTE and Young's modulus values (20 GPa<sup>6</sup>), leading to a good thermal shock resistance<sup>1</sup>. Moreover, their low volatility in water vapor environment<sup>1</sup>, low oxygen permeability and CTE values close to those of SiC and  $Si_3N_4$  (especially for the disilicate: Y-DS= $4.84 \cdot 10^{-6}K^{-1}$ ; Y-MS= $5-6 \cdot 10^{-6}K^{-1}$ ; SiC= $4.3-5.4 \cdot 10^{-6}K^{-1,2}$ ), make this class of ceramics one of the best candidates for the realization of EBCs to prevent SiC and  $Si_3N_4$  severe corrosion and subsequent recession in combustion environments<sup>1,6,7</sup>.

In the following paragraphs, the synthesis of both Y-MS and Y-DS will be described, starting from mixtures of a silicone resin filled with  $Y_2O_3$  nanoparticles. Some experimental work on the realization of EBCs (Environmental Barrier Coatings) of Y-DS (and zircon) on SiC substrates will be presented, together with some preliminary results about their thermal stability and ability to protect the substrate from oxidation.

The development of Environmental Barrier Coatings (EBCs) on carbides and nitrides has been object of intensive research during the last decades<sup>8-10</sup>. It is well known that carbides and nitrides possess extraordinary thermo-mechanical properties (such as high hardness, mechanical strength, thermal stability and thermal shock resistance) that make them excellent candidates for the realization of structural components for extremely demanding high temperature applications. Beside their high costs of production (mainly related to the necessity of adopting expensive densification technologies such as hot-pressing), their main drawback is represented by their "non-oxide" nature: the presence of Si-C and Si-N bonds – instead of the more stable Si-O bond – make this class of materials susceptible to oxidation at high temperature.

For silicon carbide, 2 different oxidation regimes could be discerned, often referred as "active" and "passive" oxidation<sup>11</sup> (a totally analogous discussion could be made for  $Si_3N_4$  ceramics). The most important factor in determining the oxidation regime is represented by the oxygen partial pressure in the oxidative atmosphere. If oxygen partial pressure is sufficiently high, the passive oxidation regime is active, and a layer of silica builds up on the SiC surface (see Fig. 3.25), as schematized by the following reaction:



In this case, a parabolic oxidation trend is generally observed, as reported in Fig. 3.26.

On the other hand, a low oxygen partial pressure generates an active oxidation regime, which rapidly destroys the material by the formation of volatile species CO and SiO, as

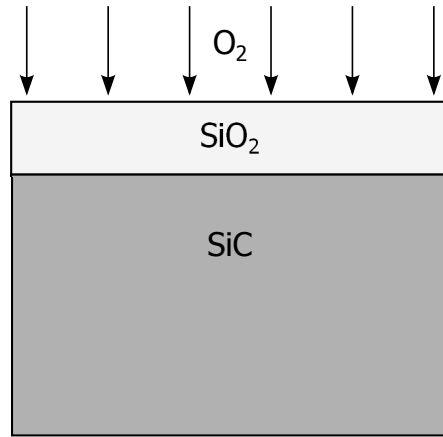


Figure 3.25: Oversimplified representation of the silica layer formation on SiC substrates in a passive oxidation regime.

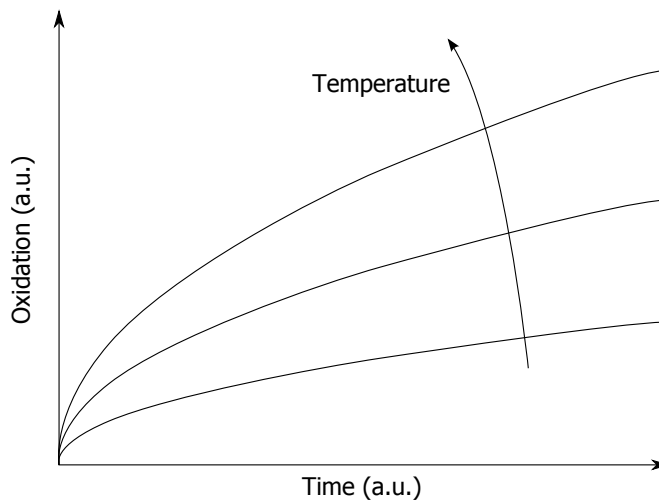


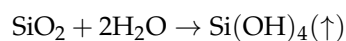
Figure 3.26: Typical parabolic oxidation (passive) kinetic for SiC substrates.

described below:



In this case, a linear oxidation trend is observed, since the oxygen of the atmosphere is always directly in contact with the SiC substrate, and no protective layers could form on its surface.

It must be pointed out that, even in the case of a passive oxidation regime, despite the formation, in principle, of a protective silica layer on SiC surface, the protection provided could not be considered definitive, since different phenomena could progressively damage the continuity of the protective layer (e.g. nucleation of crystalline phases, cracks generated by the different CTE of SiC and SiO<sub>2</sub>). Moreover, in high temperature environments characterized by the presence of high levels of humidity, the recession of the silica protective layer is a well known phenomenon, which occurs following the reaction



From these considerations, it turns out that an effective protection of SiC substrates is necessary to allow the utilization of this class of ceramics for prolonged times in demanding environments. The development of proper protective coatings is of fundamental importance to better exploit the extraordinary thermo-mechanical properties of SiC (and carbides/nitrides

in general) at high temperatures. The realization of oxide-based coatings seems to be a promising approach for the protection of components of advanced machines such as gas turbines.

When a material have to be selected for the protection of a specific substrate, different aspects and parameter should be considered. First of all, the coating material must have suitable properties of chemical resistance in aggressive environments, as well as a low oxygen permeability. Secondly, coating material must possess a CTE as close as possible to the CTE of the substrate, in order to minimize the formation of stresses during the thermal cycling that could cause the generation of ruptures and delaminations. The coating material should be thermally stable, and constituted by phases that are stable at the service temperatures, i.e. do not undergo phase transformations in service. Finally, there should be a high chemical compatibility between the coating material and the substrate, to avoid unwanted reactions at the interface and to provide good adhesion properties.

Based on these considerations, different candidates could be selected for the realization of protective coatings for SiC. Mullite and Y-silicates have been extensively studied during the last years as potential candidates for the realization of protective coatings for SiC, Si<sub>3</sub>N<sub>4</sub> and C/SiC and C/C composites<sup>1,2,6,7,12-15</sup>, mainly because of their oxide-nature, their compatible CTE and their low oxygen permeability. Among the different yttrium-silicates, the disilicate form (Y-DS) is generally preferred for the coating of open-celled SiC foams, due to the lower CTE mismatch with the substrate (if compared to the monosilicate).

Although less studied in previous work, zircon could be a good candidate as well, thanks to its extremely low CTE, its thermal stability and high thermal shock resistance.

Besides this well known application, yttrium silicates have also been tested for the realization of inorganic phosphors, thanks to the possibility of easily substituting Y<sup>3+</sup> cations by other rare-earth trivalent cations (e.g. Eu<sup>3+</sup>), thanks to the compatible cations radius. Inorganic luminescent materials represent an extremely interesting class of substances that have been attracting a lot of attention in the last century. Their first practical applications were developed at the end of the 19th century, with the realization of gas discharges and electron beams in evacuated gas tubes by Geissler and Braun, and the discovery of X-rays by Rontgen<sup>16</sup>. Based on these first results, first luminescent devices were produced few years later, i.e. cathode-ray tubes, fluorescent lamps and X-ray intensifying screens. Research on the cathode-ray tube and on first phosphors led to the development of radar devices during the World War II; other applications included the realization of fluorescent lamps for illumination purposes and X-ray for medical imaging<sup>16</sup>.

In the last decades,unbelievable improvements have been done on both the theoretical and the application aspects regarding luminescent materials. Nowadays, luminescent materials are the basis of all the displays for many different applications (e.g. televisions, radars, electron microscopes), as well as for illumination devices and X-ray intensifiers and scintillators. The continuous research in this field led to noteworthy improvements on devices efficiency and performances, such as reduced mercury adsorption in fluorescent lamps, contrast improvement in displays, and phosphors for LEDs devices.

A lot of research has been done for the synthesis and study on new fluorescent materials: globally, tens of thousands of phosphors have been synthesized and characterized, but factors such as efficiency, emission color, decay time, quenching effects, chemical and physical stability, reproducibility, availability of raw materials, environmental aspects and cost prices dramatically reduced the number of useful materials to around 50<sup>16</sup>.

In the present section, the synthesis of Y-MS:Eu<sup>3+</sup> phosphor from a preceramic polymer

filled with oxide nanoparticles will be presented. Promising results will be discussed in the next paragraphs, although still part of an ongoing work.

### 3.4.2 Experimental procedure

Yttrium-silicates synthesis studies were carried out on polysiloxane/ $Y_2O_3$  nanopowders mixtures. 2 different formulations were produced, were  $Y_2O_3$  nanopowders and silicone resin were mixed in the proper proportions to give the formation of Y-MS and Y-DS. Dispersions were realized in isopropyl alcohol, and homogenized by magnetic stirring and subsequent ultrasonication. Dispersions were then poured inside large glass containers and solvent was removed in oven at  $60^\circ C$  overnight. After solvent evaporation, the material obtained was manually ground and heat treated in air in the  $900\text{--}1500^\circ C$  range for 1 h. The evolution of the phases of the 2 systems was followed by XRD. For the realization of  $\gamma$ -silicate phosphors, Y-MS composition was considered. The formulation used for the synthesis of pure Y-MS was modified, substituting part of  $Y_2O_3$  nanopowders with  $Eu_2O_3$  nanopowders (Cometox Srl, Milan, Italy), in order to obtain the final composition  $Eu_{0.1}Y_{1.9}SiO_5$  (5 mol% of  $Y^{3+}$  substituted by  $Eu^{3+}$ ). Powders were ground and heat treated in the  $1100\text{--}1300^\circ C$  range for 1–3 h. For photoluminescence analysis, powders were finely ground and sieved ( $20\ \mu m$ ) and dispersed in distilled water. The concentration of powders dispersed in water was kept constant for all the samples, and dispersion were homogenized by ultrasonication immediately before each measurements, in order to minimize possible sedimentation effects. Y-DS and zircon-based coating were produced, on the basis of the promising results described in Section 3.4.3 (see below) and 3.2.3. Since the substrates to be coated, the selection process of the coating formulations and the overall processing are essentially identical, experimental procedure and results for both  $\gamma$ -silicates and zircon coatings are discussed together.

Substrates to be protected are Si-SiC open-cell foams (silicon-infiltrated SiC, kindly provided by Erbicol SA, CH), produced by the replica technique from a SiC slurry, and then infiltrated with metallic silicon in order to improve mechanical strength by providing densification at relatively low temperatures. They were approximately  $2 \times 2 \times 2$  cm in size, with a 10 ppi (pores per inch) porosity. Their typical applications regard the field of porous heater and porous burners, for both industrial and house equipments. They offer a wide range of advantages – mainly in terms of combustion efficiency, stability, security and lower emissions of uncombusted hydrocarbons (UHCs) and  $NO_x$  – if compared to traditional free-flame burners.

Because of the peculiar morphology of these substrates, dip-coating technique was selected for the deposition of relatively thick protective layers on the surface of the foams. Coatings were produced by a dipping procedure in  $Y_2O_3$ /polysiloxane-based and  $ZrO_2$ /polysiloxane-based dispersions in isopropyl alcohol. Dip-coating, in principle, should allow an easy access to the whole surface of the foam, thus obtaining an homogeneously distributed deposition of material. On the contrary, common thermal/plasma spray deposition techniques are not suitable, since the inner regions of the foams could not be easily reached by the stream of heated particles.

To obtain dispersions stable during the time-frame of the deposition process, the effects of both solid content and the addition of kaolin were investigated. The optimal solid content of the dispersion was established to have the highest solid content inside the dispersion, but without an excessive increase of viscosity. Washed-kaolin (Carlo Erba) was added as a stabilizing agent. Kaolin demonstrated to be extremely effective as a stabilizing agent. Qualitative

tests were done by measuring the time required to achieve a certain level of sedimentation. From the results of these tests, a concentration of +10 wt% of kaolin (with respect to Silres MK mass) was selected as concentration to be adopted. Analogous results (not reported here for brevity) were also observed for ZrO<sub>2</sub>/polysiloxane dispersion. During the subsequent heat treatments at high temperature, kaolin transforms into metakaolin around 550°C, and subsequently into mullite and amorphous silica around 930°C. Silica generated by the decomposition of kaolin was compensated by the introduction of a proper amount of extra Y<sub>2</sub>O<sub>3</sub> (or ZrO<sub>2</sub>, in the case of zircon coatings), for the formation of an extra amount of Y-DS (or zircon).

The introduction of secondary passive fillers was found to be necessary in order to limit the shrinkage of the coatings during the polymer-to-ceramic conversion. Mullite was introduced in the dispersions as a secondary passive filler for Y-DS coatings, while zircon acted as a secondary passive filler for the realization of zircon coatings. For both systems, a quantity of passive filler equal to 70 wt% was selected. Finally, in the light of the results obtained in Section 3.2.3, in ZrO<sub>2</sub>/polysiloxane dispersions part of MK was substituted for H62C, in order to have an equal amount of silica from both polymers upon pyrolysis, and TiO<sub>2</sub> was added to promote zircon formation at temperature compatible with the stability of the substrates to be coated (below the  $T_m$  of metallic silicon, which is 1414°C).

Final mixtures selected for the realization of Y-DS-based and zircon-based coatings are reported in Tab. 3.6 and Tab. 3.7.

Table 3.6: Formulation for the realization of Y-DS-based coatings on Si-SiC foams.

Component	Content (wt%)
Silres MK	7
Y <sub>2</sub> O <sub>3</sub>	12
Kaolin	1
Mullite	13
Isopropyl alcohol (cc)	67

Table 3.7: Formulation for the realization of zircon-based coatings on Si-SiC foams.

Component	Content (wt%)
Silres MK	3
Silres H62C	5
ZrO <sub>2</sub>	11
Kaolin	2
Zircon	12
TiO <sub>2</sub>	1
Isopropyl alcohol (cc)	66

Dispersions were maintained under magnetic stirring until immediately before the dipping steps, in order to keep a constant dispersion homogeneity. Samples were put directly inside the dispersion, maintained there for approximately 10 seconds and then removed slowly. Immediately after sample extraction, a compressed air stream was used to removed the excess of slurry from the foams, which have a strong tendency to be retained inside due to surface tension effects. For the realization of sufficiently thick and homogeneous depositions, an optimized multi-coating procedure was followed. It consisted of repeated steps of deposition, solvent removal after deposition (made at 60°C for 5 min) and coating stabilization (made at 260°C), in order to cross-link the polymeric phase and to "fix" the coating on the SiC substrates. After this procedure, the final heat treatment was carried out in air with a 2°/min

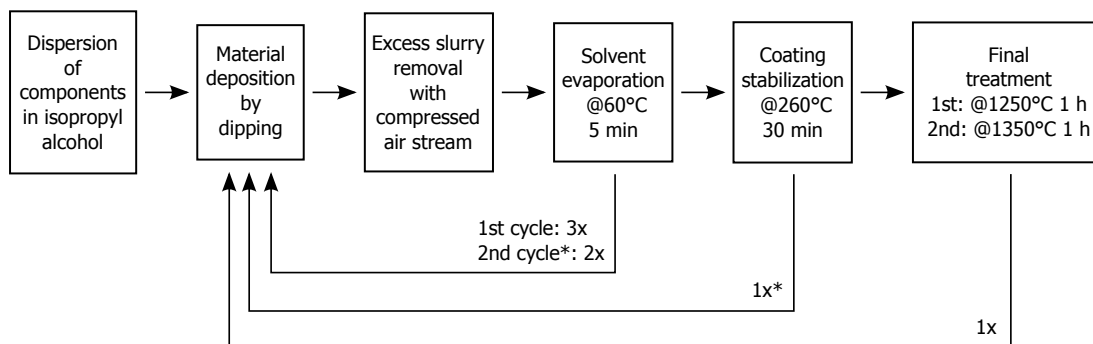


Figure 3.27: Diagram of the procedure of coating/heat treatment followed for the realization of Y-DS and zircon coatings on Si-SiC foams.

heating rate. The overall procedure was repeated twice: the first time, 1250°C was selected as the final treatment temperature, while the second time 1350°C was selected. A scheme of the coating and heat treatment procedure is represented in Fig. 3.27,

### 3.4.3 Synthesis

XRD evolution of both Y-MS and Y-DS is reported in Fig. 3.28. At low temperatures (900°C), the 2 systems are both constituted by amorphous SiO<sub>2</sub> (which could not be easily detected by XRD analysis) and Y<sub>2</sub>O<sub>3</sub>, which is the only crystalline phase that could be detected.

For both systems, the first nucleation of Y-silicate phases is observed from 1000°C, although the evolution of the 2 systems is quite different. As could be observed for the Y-MS in Fig.3.28a, X1 phase forms at 1000°C (the low temperature form of Y-MS), and remains the predominant phase until the X1→X2 transformation takes place between 1200 and 1300°C. This transformation is virtually complete, and the reverse transformation upon cooling is not observed. Some residual Y<sub>2</sub>O<sub>3</sub>, considering the overlapping of peaks, cannot be excluded even at the highest temperatures; however, the pycnometric analysis of powdered samples gave a density of 4.53±0.01 g/cm<sup>3</sup>, very close to the theoretical value for yttrium monosilicate (4.45 g/cm<sup>3</sup>)<sup>17</sup>, therefore suggesting the presence of only a limited content of secondary phases.

In the case of Y-DS instead (Fig.3.28b), a more complex reaction path was observed. Interestingly, similarly to the Y-MS evolution, the first phase to nucleate is the low-temperature form of the monosilicate, i.e. phase X1 at 1000°C. The first disilicate polymorph, i.e. α-yttrium disilicate, appears at 1200°C. The low temperature α-phase is known to be obtained when starting from sol-gel formulations<sup>18,19</sup>: as previously shown for the synthesis of mullite<sup>20,21</sup>, the approach of "nano-filled silicones" is found to yield similar results than sol-gel, but with a much simpler chemistry.

Interestingly, the presence of both monosilicate and disilicate phases was kept even at higher temperatures, after polymorphic transformations: X2 monosilicate replaced X1 monosilicate at 1200-1300°C, while γ-yttrium disilicate replaced α-phase at 1400°C. The development of γ-phase is particularly significant, since this is known as the most stable, and consequently desirable, Y-DS polymorph<sup>4</sup>. Also in this case, due to the similarity of the measured density with the theoretical value expected for Y-DS (4.15±0.01 g/cm<sup>3</sup> compared with 4.04 g/cm<sup>3</sup>)<sup>4</sup>, the content of secondary phases is reputed to be quite limited.

The coexistence of both mono- and di-silicate even at the highest temperature tested could be attributed to the presence of small quantities of residual SiO<sub>2</sub>-rich glassy phase, which could

not be completely react with the Y-MS to give the formation of a fully Y-DS system.

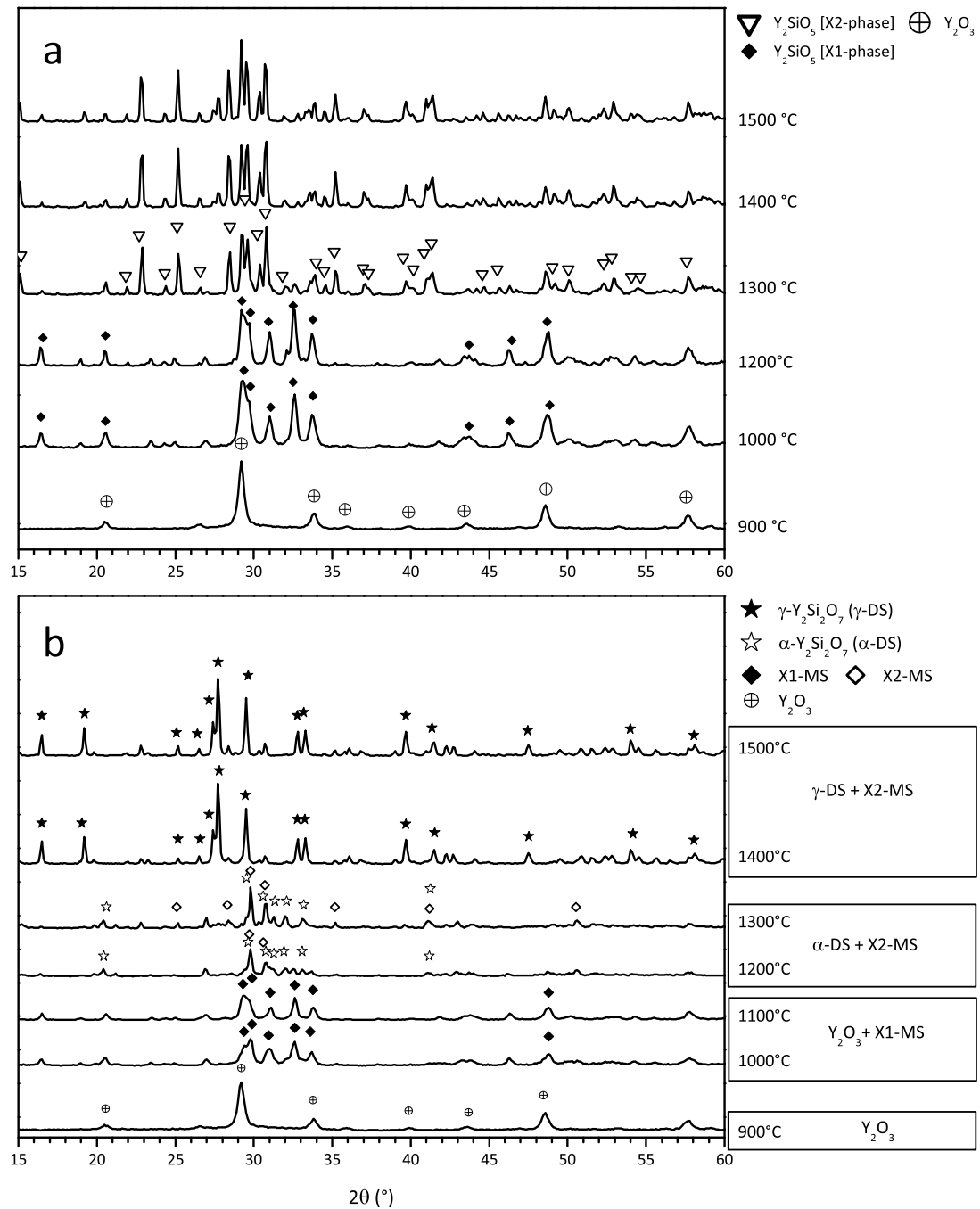


Figure 3.28: XRD patterns as a function of treatment temperature for Y-MS (a) and Y-DS (b).

### 3.4.4 Applications

#### Y-disilicate and zircon Environmental Barrier Coatings (EBCs)

Si-SiC foams after the procedure of material deposition and heat treatment are reported in Fig. 3.29.

Oxidation tests on coated SiC foams consisted in measuring the weight increase of the specimens after oxidation in air at 1200 °C for a period of 5–100 hours<sup>22,23</sup>. Generally, the

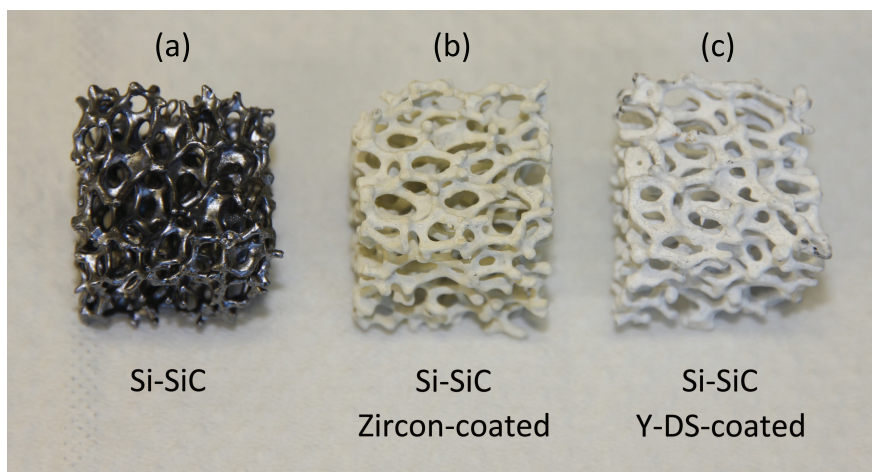
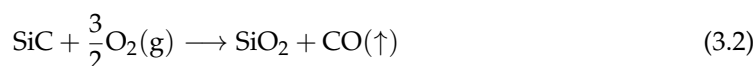


Figure 3.29: From left to right: Si-SiC open-cell foams uncoated, zircon-coated and Y-DS-coated.

higher the weight increase, the higher the oxidation of the substrate, according to reaction 3.2.



First preliminary results (Fig. 3.30) showed a parabolic trend, which is characteristic of this oxidation process, as previously mentioned. Weight increases are in the order of the 0.1-0.5 wt%, and some differences are observable between Y-DS-coated foams and zircon-coated foams. Based on the weight increases after oxidation, Y-DS appears to have a slightly better protective behavior than zircon coating. Unfortunately, a direct comparison with analogous results in literature is difficult to be done, since many different factors could directly modify the results of this type of oxidation test. Besides the characteristics of the coating (materials, thickness, continuity, deposition technique), the morphology of the substrates plays another fundamental role, in particular its specific surface area. The particular morphology of the substrates used during the present work make any comparison with previous works in literature meaningless.

In Fig. 3.31, a picture of all samples after the oxidation tests is reported. A slight change of color of zircon-coated samples with increasing temperature could be observed, while the aspect of the Y-DS coatings remains essentially unchanged.

SEM analysis of the surface and the cross-section of Y-DS- and of zircon-coated Si-SiC substrates are reported in Fig. 3.32 and in Fig. 3.33, respectively. By looking at the SEM images, it is clear that dense, pore-free coatings were not obtained, probably because of the relatively low temperatures that were used for the ceramization, which were not sufficiently high to give an effective sintering and densification of the coatings. It was observed that all the macro-cracks that are clearly visible on the surface of the coatings belong, in most cases, only to the outer (second) layer of the coating, while the first layer deposited (the one directly in contact with the substrate) seems to be more continuous, and thus guarantees a higher protection. This higher continuity should be attributed to the second deposition procedure, which could effectively cover all the cracks that were generated on the first layer upon the first pyrolysis. Anyway, these cracks – although not directly connecting the underlying substrates with the oxidizing atmosphere, but possessing a more tortuous geometry – could strongly limit the protective characteristics of the coating layer, since they represent a preferential path for the oxygen to reach the SiC substrate susceptible to oxidation. From the cross-section

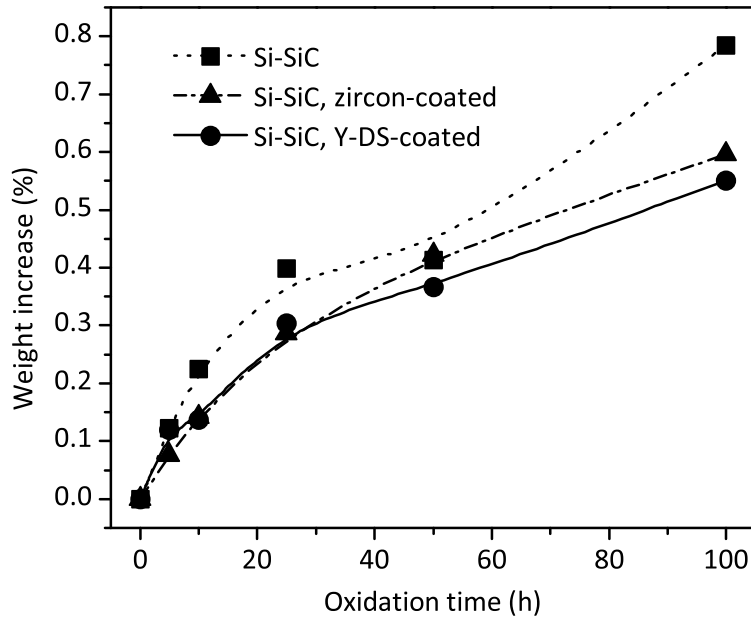


Figure 3.30: Results of oxidation test on Si-SiC foams coated with Y-DS-based and zircon-based EBCs. Oxidation test was carried out at 1200°C in air.

images, no evident delaminations between the substrate and the coatings could be observed, which confirms both the effectiveness of the deposition methodology and the selection of the proper material for the realization of the coatings. On average, coatings are 100µm thick, and they seem to adhere very well to the substrate. By looking at the Y-DS coatings (Fig. 3.32), no significant changes on the layer morphology and continuity can be observed passing from 5 to 100 h of oxidation. Instead, zircon coatings (Fig. 3.33) seems to show a slight change of their morphology: after an oxidation period of 100 h, grains seems to be slightly coarser, which is instead not observable for Y-DS coatings, where the mean grain size seems to remain basically unchanged. This coarsening phenomenon is apparently not accompanied by an increase of continuity and densification. This fact could in part justify the lower protection that zircon-based coatings offered to the SiC substrates, according to the weight increase measurements reported in Fig. 3.30.

### Red-emitting Y-MS:Eu<sup>3+</sup>

XRD results for Y-MS doped with Europium are reported in Fig. 3.34. Again, the X1→X2 transformation is observed changing the firing temperature from 1200 to 1300°C, as previously described in the Synthesis section. No significant changes due to the presence of Eu<sub>2</sub>O<sub>3</sub> could be observed. This fact confirms the very similar behavior of Y<sup>3+</sup> and Eu<sup>3+</sup> cations, because of both their identical valency inside the Y-MS crystal lattice, and their very similar cationic radius (0.93 Å for Y<sup>3+</sup> vs. 0.95 Å for Eu<sup>3+</sup>). No significant changes were observed in XRD analysis for prolonged (3 h) heat treatments.

A better evaluation of the system evolution could be obtained by considering the photoluminescence spectra reported in Fig. 3.35. As could be observed from the excitation spectrum ( $\lambda_{em}=614$  nm), samples could be excited in the near-UV and in the blue-violet region, which make this class of phosphors suitable for LED application, where luminescent media are coupled with a source emitting in the near-UV. The strong emission at 614 nm is related to the  $^5D_0 \rightarrow ^7F_2$  transition of Eu<sup>3+</sup>.

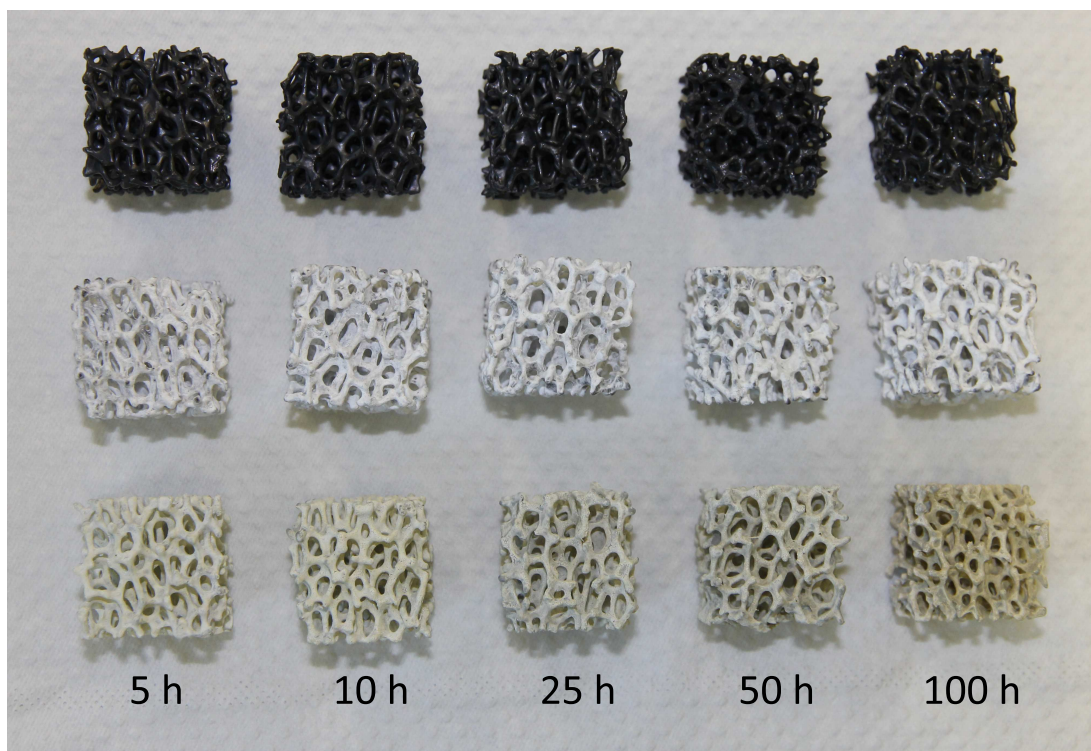


Figure 3.31: Un-coated (top row) and coated (Y-DS middle row, zircon bottom row) Si-SiC foams after the oxidation test in air at 1200°C for 5, 10, 25, 50 and 100 h.

The lowest emission intensity is observed for samples fired at 1000°C (both 1 and 3 h), while a noteworthy increase of the emission intensity is observed by increasing the temperature to 1200 and 1300°C. Although quite similar emission intensity are obtained for all the 1200 and 1300°C sample, it should be noted that samples fired for 3 h show a higher emission intensity than samples fired for 1 h, despite of the firing temperature (1200 or 1300°C). Since the only structural change that is observable is the X1→X2 transformation passing from 1200 to 1300°C, it could be concluded that the specific allotropic form of Y-MS has a little influence on the emission intensity (even if X2 form has been recognized to be the most efficient phase for emission<sup>24</sup>, and that other factors – above all, probably  $\text{Eu}^{3+}$  diffusion inside both the X1 and X2 forms – have a stronger importance in determining the final emission characteristic of the material.

Finally, a photograph of synthesized powders is reported in Fig. 3.36, where a clear red emission could be appreciated ( $\lambda_{em}=614$  nm,  $\lambda_{exc}=400$  nm).

### 3.4.5 Conclusions

In the present work, the synthesis of yttrium-silicates starting from polysiloxane/oxide nanoparticles mixture was described for the first time. Both the monosilicate (Y-MS) and the disilicate (Y-DS) forms were successfully synthesized, achieving good levels of phase purity by using simple processing conditions. 2 possible applications of this class of refractories were tested. The first one regarded the possibility of producing y-silicate coating for SiC-based substrates, as protective layer against oxidation in high temperature environments. Analogous experiments also involved zircon-based protective coatings, in light of successful results discussed in Section 3.2.3. From the preliminary oxidation tests, Y-DS coatings seem to show the better performances in terms of protection against oxidation and stability of

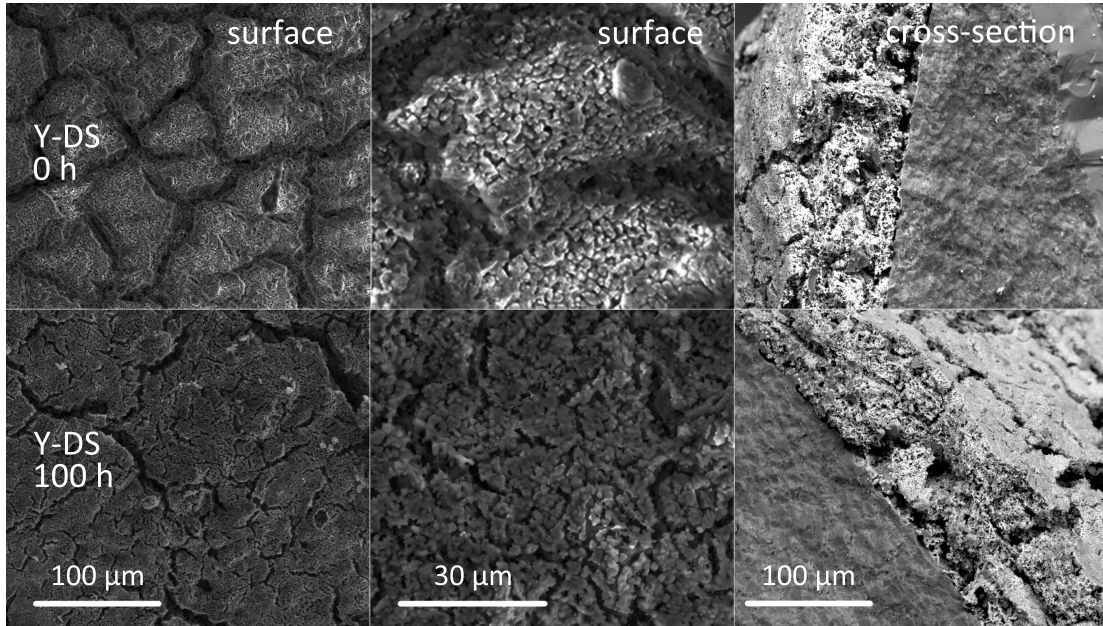


Figure 3.32: SEM images of Y-DS-based coatings, as prepared (0 h) and after oxidation (100 h) in air at 1200°C. First and second columns show the surface of the coatings, while on the third column a cross-section view of the coating (brighter areas) and the Si-SiC substrate (darker areas) is presented.

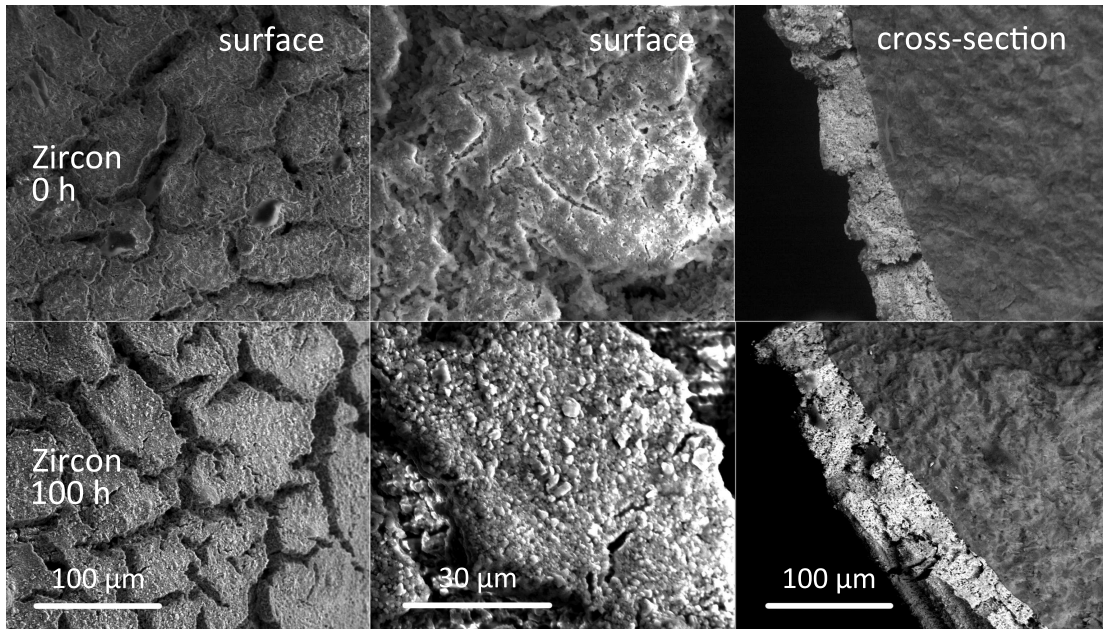


Figure 3.33: SEM images of zircon-based coatings, as prepared (0 h) and after oxidation (100 h) in air at 1200°C. First and second columns show the surface of the coatings, while on the third column a cross-section view of the coating (brighter areas) and the Si-SiC substrate (darker areas) is presented.

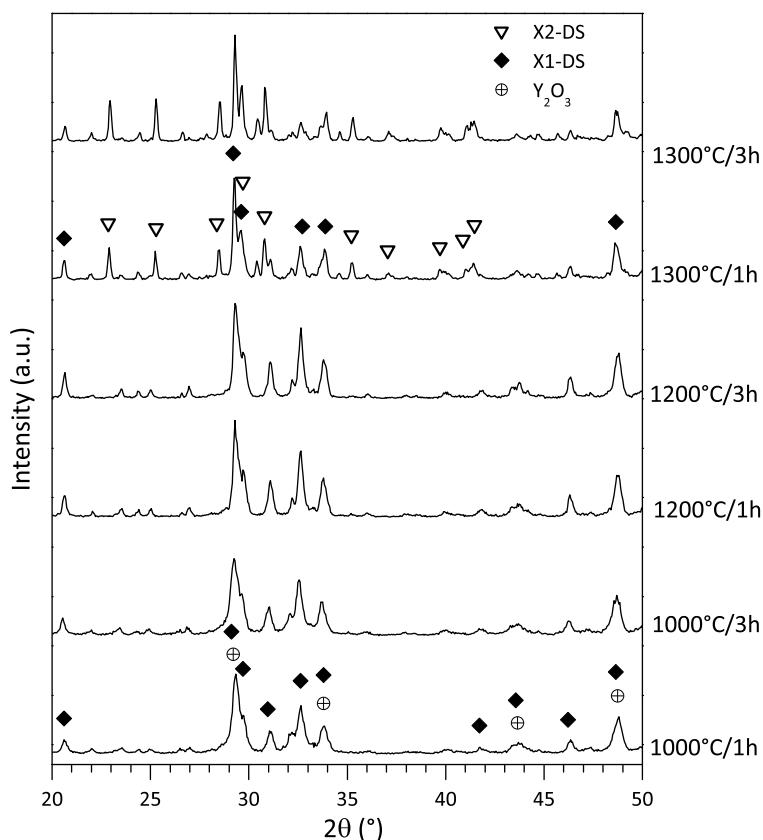


Figure 3.34: XRD patterns of Y-MS:Eu<sup>3+</sup>, with increasing ceramization temperature and time.

the coating, while slightly worse results were obtained with zircon-based coatings. Y-MS system was instead exploited for the realization of red-emitting phosphors, by substituting 5 mol% of Y<sup>3+</sup> with Eu<sup>3+</sup>. Luminescence properties were studied as a function of the synthesis temperature, and the highest emission intensities were observed for sample treated at high temperature (1200–1300°C) for 3 h. These preliminary results are extremely promising, since other trivalent rare earths cation could be, in principle, introduced inside Y-MS crystal lattice, thus obtaining different emission wavelengths with the same host material.

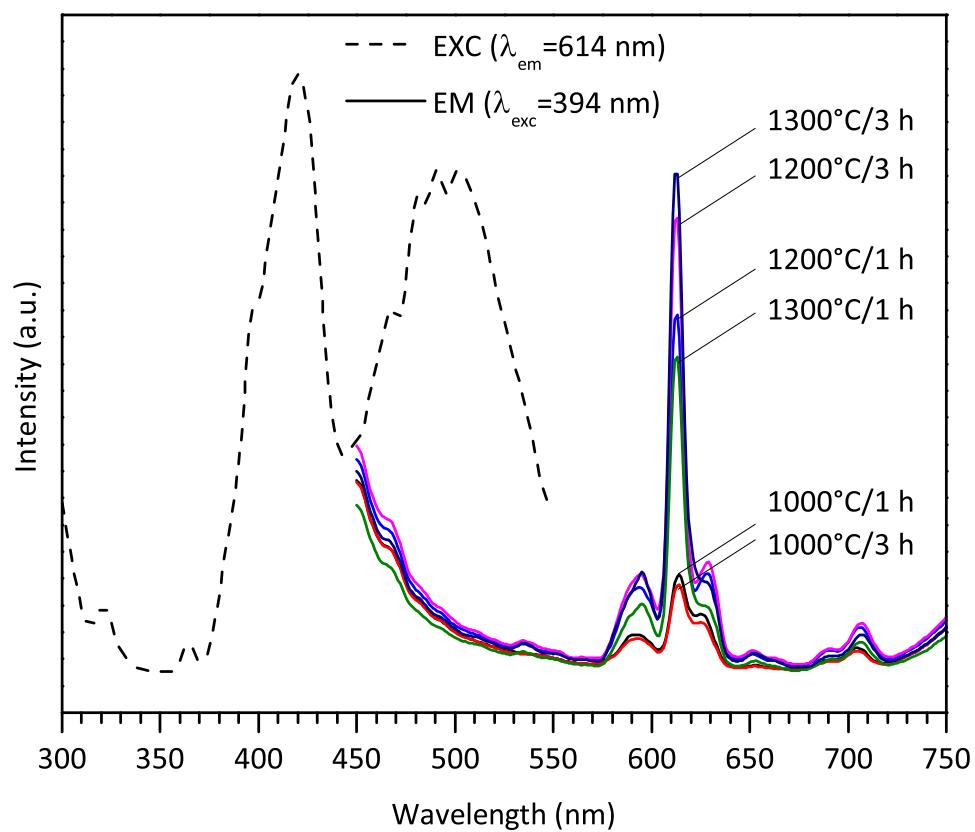


Figure 3.35: Excitation and emission spectra of Y-MS:Eu<sup>3+</sup>, with increasing ceramization temperature and time.

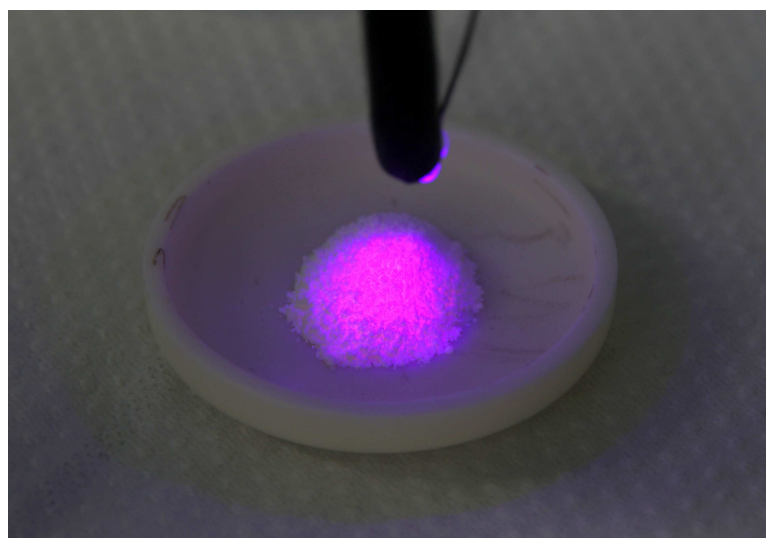


Figure 3.36: Photograph of Red-emitting Eu<sup>3+</sup>:Y-MS powder synthesized at 1300°C for 1 h.  $\lambda_{exc}=400$  nm.

## References

- [1] K. N. Lee, D. S. Fox and N. P. Bansal, "Rare earth silicate environmental barrier coatings for SiC/SiC composites and SiN ceramics", *J. Eur. Ceram. Soc.*, **25** [10] 1705–1715 (2005).
- [2] H. J. Seifert, S. Wagner, O. Fabrichnaya, H. L. Lukas, F. Aldinger, T. Ullmann, M. Schmucker and H. Schneider, "Yttrium Silicate Coatings on Chemical Vapor Deposition-SiC-Precoated C/C-SiC: Thermodynamic Assessment and High-Temperature Investigation", *J. Am. Ceram. Soc.*, **88** [2] 424–430 (2005).
- [3] J. Feslche, "The crystal chemistry of rare-earth silicates", *Struct. Bonding*, **13** 99-101 (1973).
- [4] Z. Sun, Y. Zhou, J. Wang and M. Li, "gamma-Y<sub>2</sub>Si<sub>2</sub>O<sub>7</sub>, a Machinable Silicate Ceramic: Mechanical Properties and Machinability", *J. Am. Ceram. Soc.*, **90** [8] 2535–2541 (2007).
- [5] I. MacLaren, P. A. Trusty and C. B. Ponton, "A transmission electron microscope study of hydrothermally synthesized yttrium disilicate powders", *Acta Mater.*, **47** [3] 779–791 (1999).
- [6] J. D. Webster, M. E. Westwood, F. H. Hayes, R. J. Day, R. Taylor, A. Duran, M. Aparicio, K. Rebstock and W. D. Vogel, "Oxidation protection coatings for C/SiC based on yttrium silicate", *J. Eur. Ceram. Soc.*, **18** [16] 2345–2350 (1998).
- [7] H. Jian-Feng, Z. Xie-Rong, L. He-Jun, X. Xin-Bo, F. Ye-Wei and H. Min, "SiC/yttrium silicate multi-layer coating for oxidation protection of carbon/carbon composites", *J. Mater. Sci.*, **39** [24] 7383–7385 (2004).
- [8] K. N. Lee, "Current status of environmental barrier coatings for Si-Based ceramics", *Surface and Coatings Technology*, **133-134** 1–7 (2000).
- [9] H. Fritze, J. Jojic, T. Witke, C. Rüscher, S. Weber, S. Scherrer, B. Schultrich and G. Borchardt, "Mullite based oxidation protection for SiC-C/C composites in air at temperatures up to 1900 K", *J. Eur. Ceram. Soc.*, **18** 2351–2364 (1998).
- [10] T. Damjanović, C. Argirusis, G. Borchardt, H. Leipner, R. Herbig, G. Tomandl and R. Weiss, "Oxidation protection of C/C-SiC composites by an electrophoretically deposited mullite precursor", *J. Eur. Ceram. Soc.*, **25** [5] 577–587 (2005).
- [11] J. Eck, M. Balat-Pichelin, L. Charpentier, E. Bêche and F. Audubert, "Behavior of SiC at high temperature under helium with low oxygen partial pressure", *J. Eur. Ceram. Soc.*, **28** [15] 2995–3004 (2008).
- [12] T. Morimoto, Y. Ogura, M. Kondo and T. Ueda, "Multilayer coating for carbon-carbon composites", *Carbon*, **33** [4] 351–357 (1995).
- [13] M. Huang, K. Z. Li, H. J. Li and J. F. Huang, "Yttrium silicate coatings for SiC coated C/C composites prepared by atmospheric plasma spraying", *Carbon*, **48** [13] 3975 (2010).
- [14] C. Argirusis, T. Damjanović and G. Borchardt, "Yttrium silicate coating system for oxidation protection of C/C-Si-SiC composites: Electrophoretic deposition and oxygen self-diffusion measurements", *J. Eur. Ceram. Soc.*, **27** [2-3] 1303–1306 (2007).
- [15] X. Zheng, Y. Du, J. Xiao, W. Zhang and L. Zhang, "Double layer oxidation resistant coating for carbon fiber reinforced silicon carbide matrix composites", *Appl. Surf. Sci.*, **255** [7] 4250–4254 (2009).
- [16] C. Feldmann, T. Jüstel, C. R. Ronda and P. J. Schmidt, "Inorganic Luminescent Materials: 100 Years of Research and Application", *Adv. Funct. Mater.*, **13** [7] 511–516 (2003).
- [17] Z. Sun, Y. Zhou, M. Li, "Effect of LiYO<sub>2</sub> on the synthesis and pressureless sintering of Y<sub>2</sub>SiO<sub>5</sub>", *J. Mater. Res.* **23** (2008) 732-736.
- [18] J. S. Moya and M. A. Rodr, "Synthesis of nanocrystalline yttrium disilicate powder by a sol-gel method", *J. Non-Cryst. Solids*, **289** 151–154 (2001).

- [19] J. S. Moya, M. Diaz, C. J. Serna and S. Mello-Castanho, "Formation of Nanocrystalline Yttrium Disilicate Powder by an Oxalate Gel Method", *J. Eur. Ceram. Soc.*, **18** 1381–1384 (1998).
- [20] E. Bernardo, P. Colombo, E. Pippel and J. Woltersdorf, "Novel Mullite Synthesis Based on Alumina Nanoparticles and a Pre ceramic Polymer", *J. Am. Ceram. Soc.*, **89** [5] 1577–1583 (2006).
- [21] F. Griggio, E. Bernardo, P. Colombo and G. L. Messing, "Kinetic Studies of Mullite Synthesis from Alumina Nanoparticles and a Pre ceramic Polymer", *J. Am. Ceram. Soc.*, **91** [8] 2529–2533 (2008).
- [22] H. P. Martin, G. Standke and J. Adler, "A New Oxidation Protection Strategy for Silicon Carbide Foams", *Adv. Eng. Mater.*, **10** [3] 227–234 (2008).
- [23] X. Hou, K. Chou and F. Li, "A new treatment for kinetics of oxidation of silicon carbide", *Ceramics International*, **35** [2] 603–607 (2009).
- [24] X. Qin, Y. Ju, S. Bernhard and N. Yao, "Europium-doped yttrium silicate nanophosphors prepared by flame synthesis", *Mater. Res. Bull.*, **42** [8] 1440–1449 (2007).



## 3.5 Wollastonite

### 3.5.1 Introduction

Wollastonite is among the most established bioceramics. It is composed by an equimolar ratio of calcium oxide and silica, thus giving the chemical composition  $\text{CaO}\cdot\text{SiO}_2$ , or  $\text{CaSiO}_3$ . These bioceramics have recently received great attention as hard tissue repairing material, because they are biocompatible, bioactive and partially biodegradable, and release silicon and calcium ions to the physiological environment, which are able to stimulate the production of bone matrix<sup>1,2</sup>. Different and sometimes quite complex techniques have been proposed during the years for the synthesis of wollastonite, such as sol-gel processing<sup>3</sup>, spark plasma sintering<sup>4-7</sup>, solution combustion processes<sup>8</sup> and devitrification of glass<sup>9,10</sup>. Difficulties in the synthesis of pure wollastonite are mainly connected with its poor solid state sinterability<sup>4</sup>.

The present research activity focused on the possibility of exploiting the potentialities of the polymer-derived-ceramics route as an alternative method for the realization of wollastonite porous monoliths, by pyrolysis in oxidizing atmosphere of silicone resins (acting as a silica source) filled with  $\text{CaCO}_3$  fillers. Results previously published were considered as a starting point for the present work<sup>11</sup>. Further attempts to increase system purity will be described, as well as alternative shaping methodologies (extrusion assisted by supercritical  $\text{CO}_2$ ) for the realization of porous ceramic bodies for bone tissue engineering.

### 3.5.2 Experimental procedure

As a starting point, a synthesis study was carried out by realizing mixtures of silicone resin (Silres MK) and  $\text{CaCO}_3$ , using isopropyl alcohol as dispersing medium. The effect of both micro- $\text{CaCO}_3$  and nano- $\text{CaCO}_3$  fillers were investigated, in order to analyze the "size effect" of the fillers on the general reactivity of the system, which has been demonstrated to be strongly influenced by the characteristics of the filler introduced. To produce the mixtures, silicone resin was supposed to convert, upon pyrolysis in oxidative atmosphere (air), into a pure amorphous silica matrix, which was assumed to completely react with the filler particles to give the formation of the desired phase. Heat treatments were carried out at  $900^\circ\text{C}$ , with a soak time of 1 h. After heat treatment, samples were analyzed by means of XRD (X-ray Diffraction), in order to study the evolution of the phases present.

After the analysis of the synthesis results, an alternative mixing procedure was tested, which could represent a combined mixing/shaping methodology for an industrial application of preceramic polymer-based mixtures. Silres MK was mixed with micro-sized  $\text{CaCO}_3$ , by means of a twin screw extruder (24 mm screw diameter, length/diameter ration=40:1, Thermo Prism Ltd, Stone, United Kingdom). The extrusion process was assisted by supercritical carbon dioxide, kept at a pressure  $>7.4$  MPa and a temperature of  $35^\circ\text{C}$ . Almost cylindrical long rods (length of about 100 mm) with a diameter of about 15 mm were produced by this process. Rod fragments were subjected to heat treatment at  $900^\circ\text{C}$ , for 1 h, with  $2^\circ/\text{min}$  heating rate. Due to their high volatility and the relative high quantities of raw materials needed,  $\text{CaCO}_3$  nanopowders were not used for extrusion experiments, and only micrometric powders were selected. Again, XRD analysis was done on pulverized samples, and results were compared with those obtained by the realization of polymer+fillers dispersions in isopropyl alcohol.

Secondary shaping experiments concerned  $\text{CaCO}_3$ -filled silicone powders, obtained by finely grinding, by means of a ball mill (60 min at 450 rpm), the above mentioned extru-

dates. The obtained powders, sieved to a dimension below 100  $\mu\text{m}$ , were processed by cold pressing, or by warm pressing, with or without addition of PMMA micro-beads having a diameter of 150  $\mu\text{m}$ . The micro-beads, when adopted, were homogeneously mixed with  $\text{CaCO}_3$ -filled silicone powders by a short run (10 min) in ball mill. Processing conditions for all the samples are resumed in Tab. 3.8. Some samples were subjected to a low temperature treatment at 300°C for 1 h, with a heating rate of 1°/min.

### 3.5.3 Synthesis

In Fig. 3.37 the most significant synthesis results are reported. XRD patterns a), b) and c) refer to silicone resin mixed with micro- $\text{CaCO}_3$ , nano- $\text{CaCO}_3$  and micro- $\text{CaCO}_3$  in an extruder, respectively.

By the realization of dispersions using isopropyl alcohol as dispersing medium, when micro- $\text{CaCO}_3$  was used, beside the presence of  $\text{CaSiO}_3$ , di-calcium silicate,  $2\text{CaO}\cdot\text{SiO}_2$  ("larnite", often referred as  $\text{C}_2\text{S}$ ) could be detected after heat treatment (Fig. 3.37a). Nano-sized  $\text{CaCO}_3$  (Fig. 3.37b) instead has beneficial effects on the purity of the system, since  $\text{C}_2\text{S}$  phase is strongly reduced, and a basically pure wollastonite system was achieved. This effect could be apparently attributed to the above mentioned "nano-size effect": powders with smaller size and higher surface area could increase both the homogeneity and the reactivity of the system. However, by looking at patten c) it could be observed that a change in the processing conditions (i.e. mixing of raw materials) a dramatical increase of the phase purity could be achieved as well. This could be justified by considering that the presence of  $\text{C}_2\text{S}$  should be associated not to the presence of micron-sized  $\text{CaCO}_3$  fillers, but instead to possible sedimentation of the micro-fillers that could happen when low-viscosity dispersions are produced. In the case of extrusion, the continuous and vigorous mixing action of the extruder strongly limits this phenomenon, and high-purity wollastonite ceramics could be easily produced after pyrolysis of the extruded materials, even when micron-sized  $\text{CaCO}_3$  is used as  $\text{CaO}$  source.

### 3.5.4 Applications

#### High-porosity wollastonite components

As a first step, experimental work regarded the possibility of obtaining wollastonite monoliths by the direct pyrolysis of extruded rods. Heat treatment at 900°C for 1 h were carried out with an increasing rate of 2°/min. SEM results are reported in Fig. 3.38. In the un-pyrolyzed state (Fig. 3.38a), materials are extremely homogeneous, with no evidents defects such as cracks or macro-pores. Only micro-pores could be observed by SEM analysis, which are likely generated by supercritical  $\text{CO}_2$  introduced during the mixing process. After ceramization (Fig. 3.38b,c), the generation of macro-pores surrounded by a micro-porous matrix is observed: the macro-porosity is likely generated by the coalescence of  $\text{CO}_2$  micro-bubbles, although the additional contribution could be generated by the decomposition of  $\text{CaCO}_3$  at higher temperatures, with the consequent release of additional  $\text{CO}_2$ . Many cracks are generated upon pyrolysis, which strongly limits the mechanical properties of these monoliths.

Extrudates were subsequently pulverized and re-shaped by 2 different methodologies. Before the shaping step, for some samples some PMMA micro-beads were mixed together with the preceramic powders. The processing conditions of samples produce are resumed in Tab. 3.8.

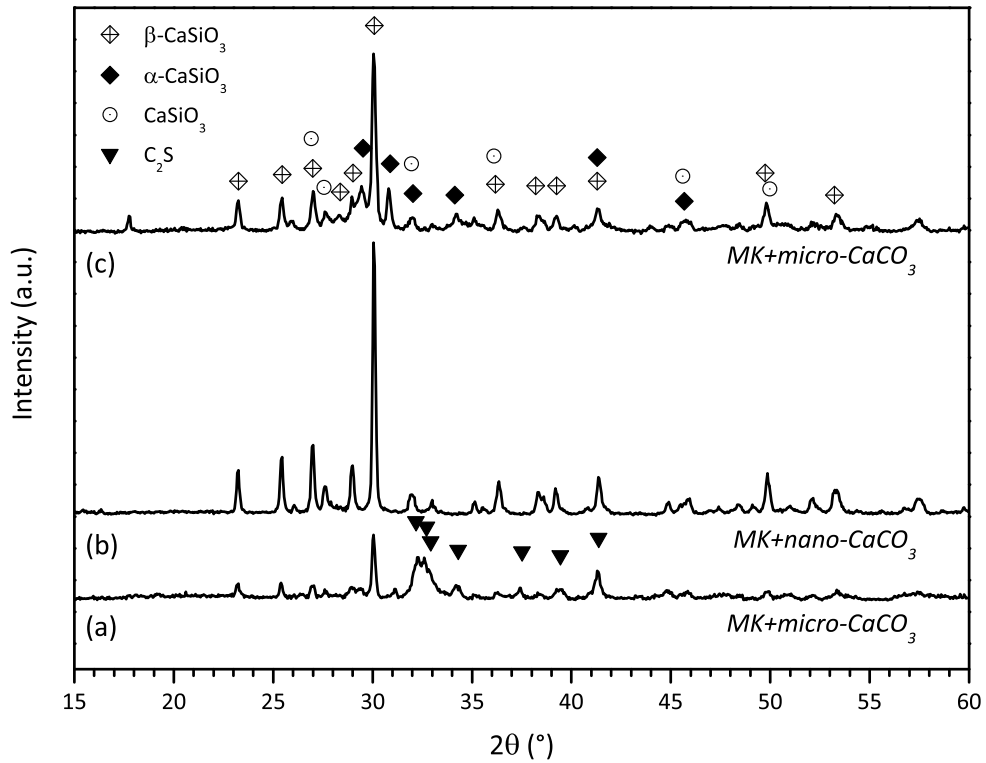


Figure 3.37: XRD patterns of ceramic samples from the heat treatment of MK and CaCO<sub>3</sub> fillers: a) micro-CaCO<sub>3</sub>/MK mixture; b) nano-CaCO<sub>3</sub>/MK mixture; c) micro-CaCO<sub>3</sub>/MK mixture after supercritical CO<sub>2</sub>-assisted extrusion.

Table 3.8: Summary of experimental conditions for the preparation of ceramic foams.

Sample	PMMA content	Shaping conditions			Treatment before ceramization
		Type	Pressure/Time	Temperature	
A	0	Powders distributed in Al mold	/	T <sub>amb</sub>	300°C/1 h
B	20	Powders distributed in Al mold	/	T <sub>amb</sub>	none
D	20	Warm pressing	20 MPa/5 min	170°C	300°C/1 h
E	20	Extended warm pressing	2 MPa/30 min	170°C	300°C/1 h

The first shaping methodology consisted in simply pouring a proper amount of powders inside an aluminum mold (about 2/3 of mold capacity), and in distributing them homogeneously inside the container. After this simple operation, molds were put in the furnace and heat treated at 300°C for 1 h, with an increasing rate of 1°/min. During this step, 2 distinct processes take place on the samples, which consist in a coalescence of the powders (by a progressive lowering of the viscosity of the system as the temperature increases) and the coalescence of the CO<sub>2</sub> micro-bubbles trapped inside the particles. It is reasonable to assume that these two processes are simultaneously active, since they are likely connected with the decrease of viscosity of the system observed during heating. Considering that the T<sub>m</sub> of silicone is approximately 60°C, it is reasonable to assume that first rearrangements start to be active well below 100°C. During this treatment, when present, the PMMA decomposes and is eliminated as well, producing an additional amount of porosity.

After this heat treatment at 300°C, materials were removed from the aluminum molds and subsequently ceramized at 900°C for 1 h. No evident changes in their shape as well as in their pore size, shape and distribution were observed after ceramization, which indicates that the final samples characteristics depend exclusively on the processing conditions at low temperatures, and that no further modifications of the morphology are possible at higher

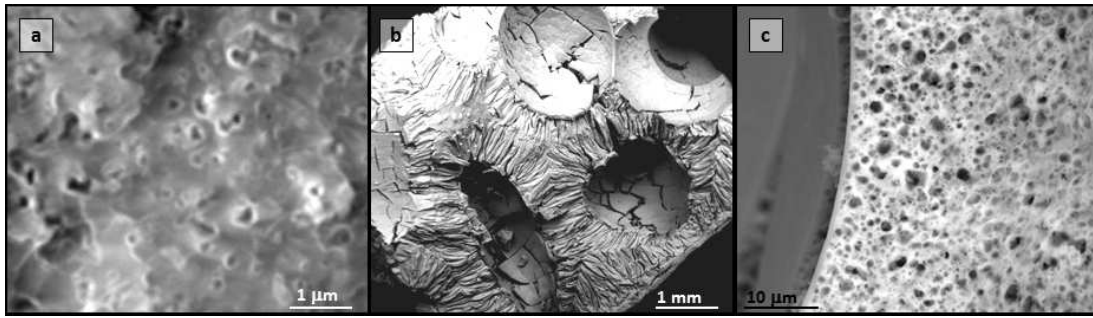


Figure 3.38: Microstructural details of directly ceramized extruded silicone/micro-CaCO<sub>3</sub> mixture: a) cross-section of an as-produced rod (before heat treatment at 900°C); b) low magnification image of the same sample after ceramization; c) high magnification image, after ceramization.

temperatures. Samples before and after ceramization are reported in Fig. 3.39 (without PMMA) and Fig. 3.40 (with PMMA).

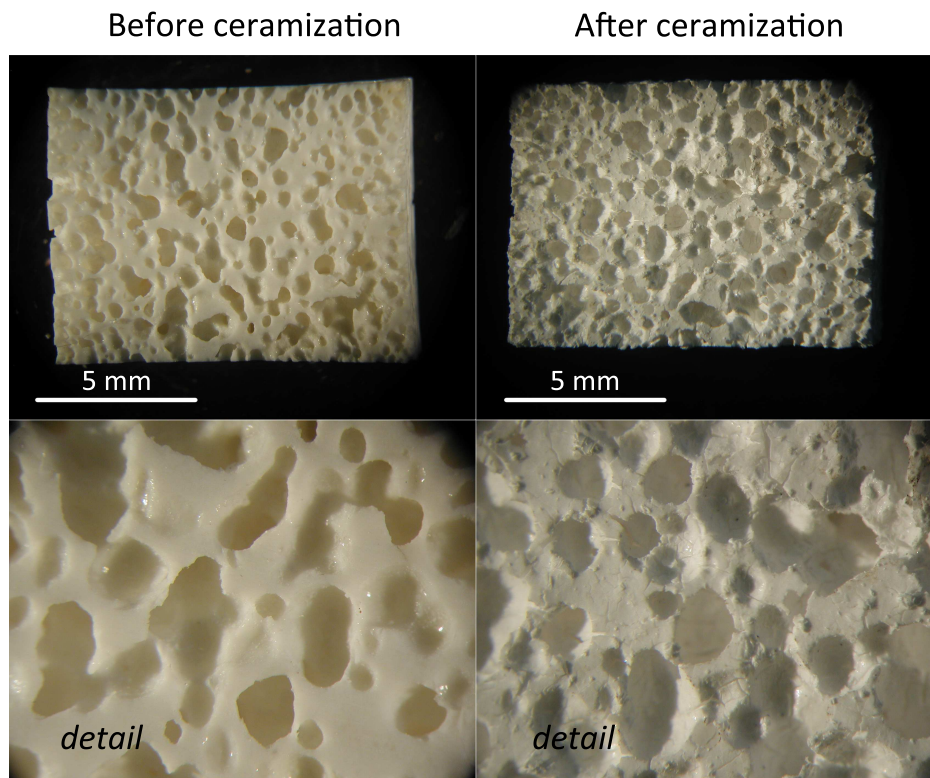


Figure 3.39: Sample A, treated at 300°C (before ceramization) and after ceramization at 900°C.

In both samples, an open porosity was observed, with a good level of interconnections that are beneficial for applications in bone tissue engineering<sup>12,13</sup>. It was observed that the presence of PMMA micro-beads can have beneficial effects in terms of sample integrity: no evident macro and micro-cracks are observed, which are instead present in the sample which does not contain PMMA micro-beads. The presence of additional porosity generated by the elimination of PMMA could have beneficial effects during the pyrolysis step, when gases have to be efficiently released to minimize localized increase of pressure.

Moreover, sample containing PMMA seems to have slightly smaller pores, which could be consistent with a higher viscosity (and, consequently, a lower coarsening of pores) due to the presence of an additional solid filler. Some inhomogeneities of mean pores size could be

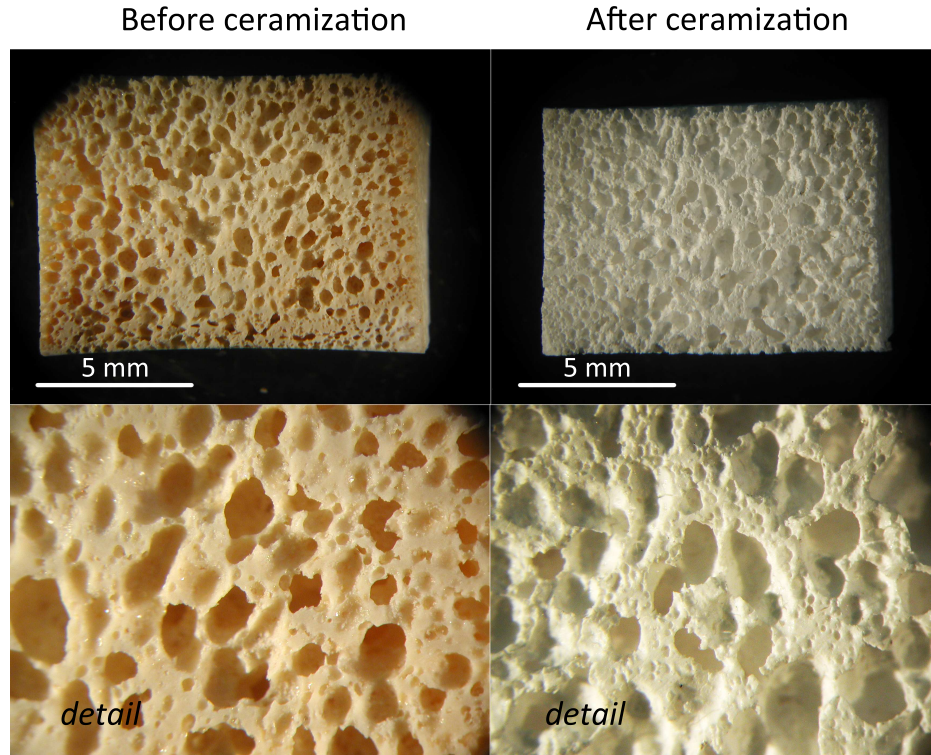


Figure 3.40: Sample B, treated at 300°C (before ceramization) and after ceramization at 900°C.

noted, since pores seem to be slightly bigger in the core of the samples and slightly smaller in the outer regions.

The second shaping methodology (samples C and D) consisted in the compaction of pre-ceramic powders by warm pressing. 2 different warm pressing cycles were tested: while temperature and pressure were kept constant at 170°C and 20 MPa, soak time was varied between 5 (sample C) and 30 (sample D) min. Higher soak times entail a higher level of cross-linking of the polymeric phase, which in turn entail a higher viscosity. Warm-pressed samples were then heat treated at 300°C for 1 h (1°/min), and then ceramized at 900°C for 1 h (2°/min).

Results after ceramization are reported in Fig. 3.41. Also in this case, the generation of porosity is associated with the treatment at low temperatures by the mechanism discussed before, while no significant changes are observed after the ceramization at 900°C. A high level of interconnections is present also in this case, and a more homogeneous distribution of porosity in the sample was observed, with the mean pores size basically constant over all the area of the samples. The main difference between the two samples consists in a smaller pore size for sample D, if compared to sample C. This is, again, consistent with the fact that a higher viscosity during the coalescence of CO<sub>2</sub> bubbles limits their growth.

In Tab. 3.9 the relative density, porosity and crushing strength of the final ceramics are reported. Samples A and B show a basically identical relative density, and thus porosity content. However, crushing strength values are quite different, with strength of sample B being twice the strength of sample A. This different strength should be associated with a higher quantity of crack inside sample A, as previously discussed. Since density values are basically identical, no significant changes are observed by looking at the specific crushing strength values.

Sample C and D show basically identical strength values, which are higher than values

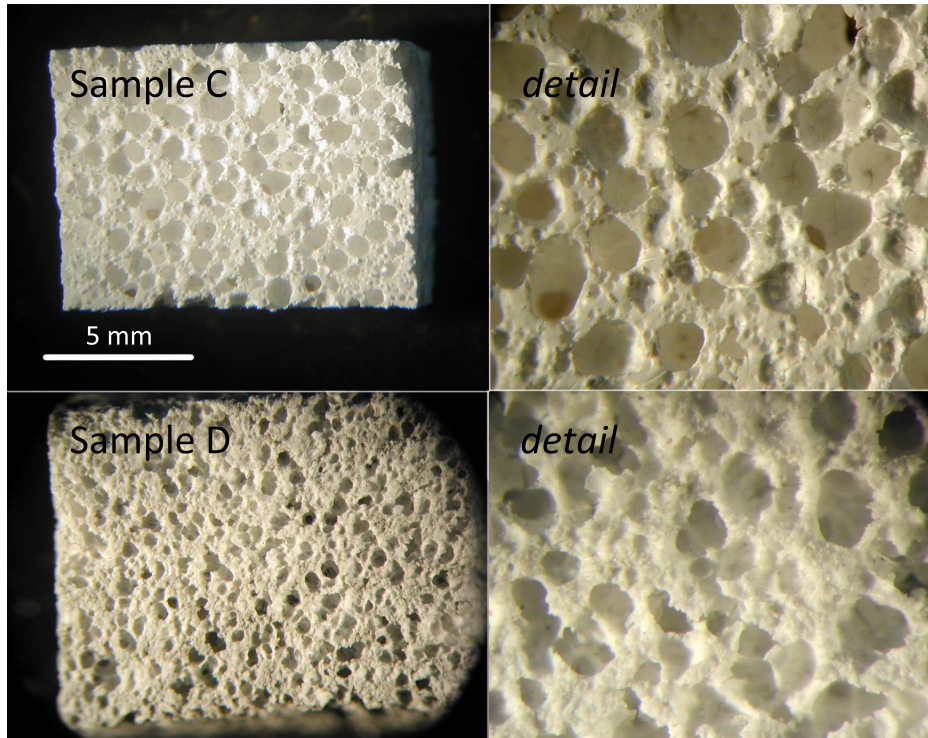


Figure 3.41: Sample C and D after ceramization at 900°C.

obtained for samples A and B. This difference should be directly correlated with the different shaping conditions, and the more regular structure that could be generated. Moreover, sample C show a higher specific crushing strength than sample D, due to its lower density. The strength of samples C and D is high enough for bone tissue applications<sup>5</sup>. If we look at the specific compressive strength (Tab. 3.9), the values are within those of natural cellular materials<sup>6</sup>, even if further improvements are required to approach values of cancellous bone (specific strength above 10 MPa·cm<sup>3</sup>/g). The different structures available depending on the secondary treatment, applied to powdered extrudates, undoubtedly ensures a significant "tunability" of ceramic foams to particular applications. Moreover, infiltration of microporosity with organic polymers and/or drugs could provide both mechanical reinforcement and modulation of bioactivity<sup>7</sup>.

Table 3.9: Density/strength correlation in the investigated ceramic foams.

Sample	Bulk density (g/cm <sup>3</sup> )	Porosity (%)	Crushing strength (MPa)	Specific crushing strength (MPa·cm <sup>3</sup> /g)
A	0.50	80.9	0.45±0.08	0.9
B	0.49	81.3	0.82±0.20	1.67
C	0.52	80.2	1.33±0.44	2.56
D	0.63	76	1.26±0.27	2.00

### 3.5.5 Conclusions

Relatively pure wollastonite ceramics were obtained through the pyrolysis in air at 900°C of polysiloxane/CaCO<sub>3</sub> mixtures. The effect of micro- and nano-CaCO<sub>3</sub> on the phase purity of the final ceramic was investigated: it was observed that, when raw materials are dispersed together in isopropyl alcohol as dispersing medium, best results are obtained by using nano-sized fillers, due to a reduction of sedimentation effects, which are proportional to the mean particle size of the filler. On the other hand, when the mixing of raw materials was carried

out in an extruder (using supercritical CO<sub>2</sub> as solvent), high purity ceramics were obtained even by using micro-CaCO<sub>3</sub>. After heat treatment, extruded rods showed evident micro and macro-cracks, which are detrimental for the final mechanical properties. The extruded material was then pulverized and re-formed by 2 alternative methods, with and without the introduction of PMMA micro-beads as sacrificial fillers. Promising results were obtained in both cases, with the development of an homogeneous porosity characterized by an interconnected network, which represent a promising result for the development of biocompatible and bioactive bone implants.

## References

- [1] P. N. De Aza, F. Guitian and S. De Aza., "Bioactivity of wollastonite ceramics: in vitro evaluation", *Scr. Metall. Mater.* 31, 1001, 1994.
- [2] P. N. De Aza, Z. Luklinska, M. R. Anseau, F. Guitian and S. De Aza., "Morphological studies of pseudowollastonite for biomedical application", *J. Microsc.*, 182, 24, 1996.
- [3] P. Sepulveda, J.R. Jones, L.L. Hench, "Bioactive sol-gel foams for tissue repair", *J. Biomed. Mater. Res.* 59 (2002) 340-348.
- [4] L.H. Long, L.D. Chen, J. Chang, "Low temperature fabrication and characterizations of  $\beta$ -CaSiO<sub>3</sub> ceramics", *Ceram. Int.* 32 (2006) 457-460.
- [5] X. Liu, C. Ding, "Characterization of plasma sprayed wollastonite powder and coatings", *Surf. Coat. Technol.* 153 (2002) 173-177.
- [6] W. Xue, X. Liu, X.B. Zheng, C. Ding, "In vivo evaluation of plasma-sprayed wollastonite coating", *Biomaterials* 26 (2005) 3455-3460.
- [7] W. Xue, C. Ding, "Plasma sprayed wollastonite/TiO<sub>2</sub> composite coatings on titanium alloys", *Biomaterials* 23 (2002) 4065-4077.
- [8] R.P. Sreekanth Chakradhar, B.M. Nagabhushana, G.T. Chandrappa, K.P. Ramesh, J.L. Rao, "Solution combustion derived nanocrystalline macro-porous wollastonite ceramics", *Mater. Chem. Phys.* 95 (2006) 169-175..
- [9] W. Holand, G. Beall, *Glass-ceramic Technology*, The American Ceramic Society, Westerville, OH, 2002.
- [10] M.I. Alemany, P. Velasquez, M.A. de la Casa-Lillo, P.N. De Aza, "Effect of materials' processing methods on the 'in vitro' bioactivity of wollastonite glass-ceramic materials", *J. Non-Cryst. Sol.* 351 (2005) 1716-1726.
- [11] E. Bernardo, E. Tomasella and P. Colombo, "Development of multiphase bioceramics from a filler-containing preceramic polymer", *Cerami. Int.*, 35 [4] 1415-1421 (2009).
- [12] Vitale-Brovarone, C., Verné, E., Robiglio, L., Appendino, P., Bassi, F., Martinasso, G., Muzio, G., and Canuto, R., "Development of glass-ceramic scaffolds for bone tissue engineering: Characterization, proliferation of human osteoblasts and nodule formation", *Acta Biomat.*, 2007, 3, 199-208.
- [13] Sanchez-Sálcedo, S., Arcos, D., Vallet-Regí, M., "Upgrading calcium phosphate scaffolds for tissue engineering applications", *Key Eng Mater.* 2008, 377, 19-42.

# Chapter 4

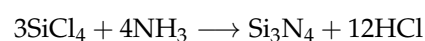
## SiAlON ceramics

### 4.1 Introduction

Sialon ceramics represent an outstanding class of materials for a wide range of high temperature structural applications. Since their discovery, a significant progress has been made concerning the understanding of their crystal structure, their microstructure and the technological aspects and issues regarding their processing. The most important Sialons, i.e.  $\alpha'$ - and  $\beta'$ -sialon, are well known to be isostructural with  $\alpha$ - and  $\beta$ - $\text{Si}_3\text{N}_4$ . Compared to the nitrides, the Sialons generally show slightly lower mechanical properties, but also much higher sinterability, oxidation and corrosion resistance, so that they have been recognized as extremely important and promising ceramics for applications such as cutting tools, metal forming tools, molten metal handling and other high temperature structural parts<sup>1,2</sup>. Moreover, in recent years a great effort has been devoted to secondary, functional or "mixed" (structural and functional) applications, such as phosphors and high strength translucent materials<sup>3-6</sup>.

Sialons were discovered in the early '70s independently by Jack and Wilson in the UK<sup>7</sup> and Osana et al. in Japan, as a consequence of experiments focused on solving the problem of  $\text{Si}_3\text{N}_4$  densification.

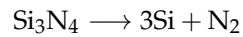
$\text{Si}_3\text{N}_4$  shows excellent mechanical properties, a very low CTE and high chemical resistance, which made  $\text{Si}_3\text{N}_4$ -based ceramics extremely important candidates for high-temperature structural applications. The first example of  $\text{Si}_3\text{N}_4$  components was "Reaction-bonded silicon nitride" (RBSN), obtained through a nitridation treatment of compacted silicon powders in the 1100-1450°C temperature range. The major obstacle against this synthesis route was represented by the high residual porosity that characterized the final ceramics (around 30%), which limited mechanical strength of the final components to about 250 MPa<sup>8</sup>. Alternatively,  $\text{Si}_3\text{N}_4$  could be produced by carbothermal reduction and nitridation of  $\text{SiO}_2$ . Other synthesis routes comprise gaseous-phase reaction of  $\text{SiH}_4$  and  $\text{NH}_3$  (which has some problems over the stoichiometry control) and, above all, reaction between ammonium tetrachloride and ammonia, which could give highly-pure  $\text{Si}_3\text{N}_4$  powders through the following reaction:



In this case, final calcination temperature determines the predominant allotropic form of  $\text{Si}_3\text{N}_4$ :  $\alpha$ - $\text{Si}_3\text{N}_4$  equiaxed grains are produced at 1420°C, while elongated  $\beta$ - $\text{Si}_3\text{N}_4$  whiskers are synthesized for  $T > 1460^\circ\text{C}$ .  $\alpha$ - $\text{Si}_3\text{N}_4$  and  $\beta$ - $\text{Si}_3\text{N}_4$  are both hexagonal, and constituted by  $\text{SN}_4$  tetrahedrons connected by the nitrogen atoms on their vertexes, in such a way that every

nitrogen atom is shared between 3 tetrahedrons. The  $\alpha \rightarrow \beta$  transformation is reconstructive, and is possible when the  $\text{Si}_3\text{N}_4$  is in contact with a liquid phase in the grain boundaries. This phenomenon could be observed at temperatures higher than  $1400^\circ\text{C}$ , and is due to the higher chemical stability of the  $\beta$ -phase, if compared to the  $\alpha$ -phase.

$\text{Si}_3\text{N}_4$  sintering shows intrinsic difficulties, mainly because of the very high Si-N bond energy: this characteristic is the main reason for their outstanding mechanical properties such as mechanical strength and hardness, but represents also their main limitation, since it strongly suppresses diffusion processes. The high treatment temperatures necessary to increase  $\text{Si}_3\text{N}_4$  densification are close to the dissociation temperature of  $\text{Si}_3\text{N}_4$  ( $T > 1850^\circ\text{C}$ ), through the reaction reported below:



An important breakthrough was represented by "Hot-pressed silicon nitride" (HPSN), when it was possible to fully densify  $\text{Si}_3\text{N}_4$  by the addition of  $\text{MgO}$  as sintering aid. The main limitation of HPSN is represented by the extremely limited shaping possibilities that characterize the hot-press technology<sup>8</sup>. Other fundamental improvements – that led to the realization of the first  $\text{Si}_3\text{N}_4$  gas turbines – were achieved by a more deep comprehension of the densification mechanism of  $\text{Si}_3\text{N}_4$  through the insertion of sintering aids, and with the consequent development of the so-called "Sintered silicon nitride" (SSN), "Sintered reaction bonded silicon nitride" (SRBSN), "Hot isostatically pressed silicon nitride" (HIPSIN), and finally solid solutions of  $\text{Si}_3\text{N}_4$  with  $\text{Al}_2\text{O}_3$ , generally referred as "Sialons"<sup>1,8</sup>. Some properties of commercial  $\text{Si}_3\text{N}_4$  products are reported in Tab. 4.1.

To summarize, the main advantages of  $\text{Si}_3\text{N}_4$  ceramics are:

- Relatively low cost and much lower density if compared to super-alloys
- High mechanical strength at high temperatures
- Low friction coefficient and wear resistance
- High chemical resistance
- High thermal shock and fatigue resistance
- Non-wettability by molten metals

These properties make  $\text{Si}_3\text{N}_4$  ceramics suitable for molten metal processing, application as blades for gas turbines, high temperature bearings, and many others demanding high-temperature applications.

Table 4.1: Properties of commercially available  $\text{Si}_3\text{N}_4$  products.

Properties	RBSN	SSN	HIPSIN
Density ( $\text{g}/\text{cm}^3$ )	2.7	3.3	3.3
Young's modulus (GPa)	200	300	300
Modulus of rupture (MPa)	300	900	900
$K_{IC}$	2	6.5	6.5
Weibull modulus	10	13	>20
Hardness (GPa)	9-13	15-18	16-20
Thermal conductivity (W/mK)	10	33	33
Coefficient of thermal expansion	3.1	3.1	3.1

The discovery of an alloy of  $\text{Si}_3\text{N}_4$  with Al and O with similar thermo-mechanical properties and much better densification behavior – good enough to obtain fully dense sample by pressure-less sintering, with the introduction of sintering aid such as  $\text{Y}_2\text{O}_3$  – represented one of the biggest breakthrough of the world of structural ceramics. Since then, considerable progresses have been made concerning the understanding of their crystal structure, their microstructure and all the technological aspects related to their processing.

Among all the different phases present in the Si-Al-O-N system,  $\alpha'$ - and  $\beta'$ -sialon (which are isostructural with  $\alpha$ - and  $\beta$ - $\text{Si}_3\text{N}_4$ , respectively) are surely the most technologically relevant forms. Both  $\alpha'$ - and  $\beta'$ - forms generally show slightly lower mechanical properties (in terms of hardness and strength) than the related  $\alpha$ - and  $\beta$ - $\text{Si}_3\text{N}_4$  forms, but their much higher sinterability, oxidation and corrosion resistance have made them one of the most important and promising ceramics for extremely demanding applications such as cutting tools, metal forming tools, molten metal handling and other high temperature structural parts<sup>1,2</sup>.

Similarly to  $\beta$ - $\text{Si}_3\text{N}_4$ ,  $\beta'$ -sialons generally exhibit very high toughness values (up to 8  $\text{MPa}\cdot\text{m}^{0.5}$ ), thanks to the development of a self-reinforced interlocking microstructures with both equiaxed and elongated grains. The typical microstructure of  $\beta'$ -sialon is reported in Fig. 4.1b.  $\beta'$ -sialon has the general formula  $\text{Si}_{6-z}\text{Al}_z\text{O}_z\text{N}_{8-z}$ , where  $z$  represents the number of Si-N bond replaced by Al-O bonds. This type of substitution does not affect charge neutrality, and thanks to the very close bond lengths (1.74 and 1.75 Å for Si-N and Al-O, respectively), high levels of substitution can be achieved ( $z=0-4.2$ )<sup>9,10</sup>. This fact encouraged the development of production methods alternative to the most common and well established one, i.e. reaction sintering of  $\text{Si}_3\text{N}_4$ ,  $\text{Al}_2\text{O}_3$  and AlN mixtures<sup>11,12</sup>, starting from carbothermal reduction/nitridation (CNR) of  $\text{SiO}_2$  and  $\text{Al}_2\text{O}_3$  mixtures of natural alumino-silicates (e.g. mullite, sillimanite or kaolin)<sup>13</sup>. CNR is also at the basis also of the synthesis of Sialon from other starting materials, such as fly ash and gels (from sol-gel processing)<sup>14,15</sup>.

On the contrary,  $\alpha'$ -sialons are generally characterized by extremely high hardness values. They generally exhibit an equiaxed microstructure, which entails lower toughness values (2-3  $\text{MPa}\cdot\text{m}^{0.5}$ ), although recently the possibility of producing self-reinforced  $\alpha'$ -sialon microstructures, similar to those characteristic of  $\beta'$ -sialons, with  $K_{IC}$  up to  $\sim 7 \text{MPa}\cdot\text{m}^{0.5}$  have been demonstrated. The typical equiaxed microstructure of  $\alpha'$ -sialon is reported in Fig. 4.1a. Their general formula is  $\text{M}_{m/v}\text{Si}_{12-m-n}\text{Al}_{m+n}\text{O}_n\text{N}_{16-n}$ , where  $(m+n)$  Si-N bonds are replaced by  $m$  Al-N bonds and  $n$  Al-O bonds. Since every  $\text{Si-N} \rightarrow \text{Al-N}$  substitution introduces a negative charge inside the crystal lattice,  $m/v$  M atoms ( $v=M$  valency) must be introduced in interstitial positions to re-establish the electroneutrality ( $M=\text{Li, Mg, Ca, Y}$ , and most of the rare-earths series elements).

The complexity of the Si-Al-O-N system, where many important different crystalline phase have been recognized, make the representation of this ceramic system is not trivial. As a starting point, this 4-component system could be represented by the tetrahedron reported in Fig. 4.2.

Assuming that the 4 constituting elements must combine with each other maintaining their accepted valencies ( $\text{Si}^{\text{IV}}$ ,  $\text{Al}^{\text{III}}$ ,  $\text{O}^{\text{II}}$ ,  $\text{N}^{\text{III}}$ ), one degree of freedom could then be eliminated, and it could be demonstrated that all the possible phases are located inside the irregular quadrilateral with  $\text{Si}_3\text{N}_4$ ,  $\text{SiO}_2$ ,  $\text{Al}_2\text{O}_3$  and AlN at its corners (see Fig. 4.2). Finally, this irregular quadrilateral could be "stretched" and transformed into a square with  $\text{Si}_3\text{N}_4$ ,  $3\cdot\text{SiO}_2$ ,  $2\cdot\text{Al}_2\text{O}_3$  and  $4\cdot\text{AlN}$  at its corners, thus obtaining what is for certain the most utilized and reported phase diagram of sialon ceramics (Fig. 4.3).

Inside this diagram,  $\beta'$ -sialon is surely the most technologically relevant phase, although

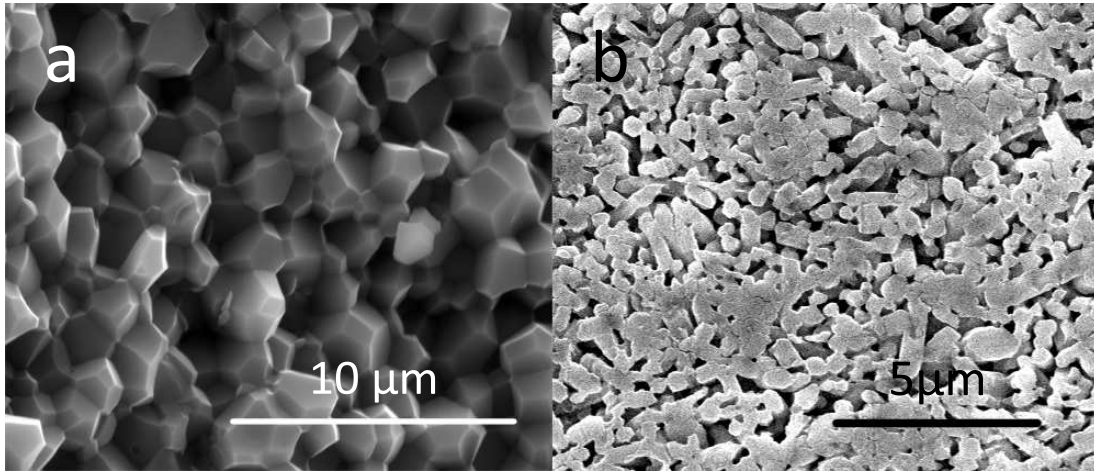


Figure 4.1: a) Y:α'-sialon equiaxed microstructure (hot-pressed at 1800°C for 1 h) and b) β'-sialon microstructure with elongated grains (hot-pressed at 1800°C for 30 min).

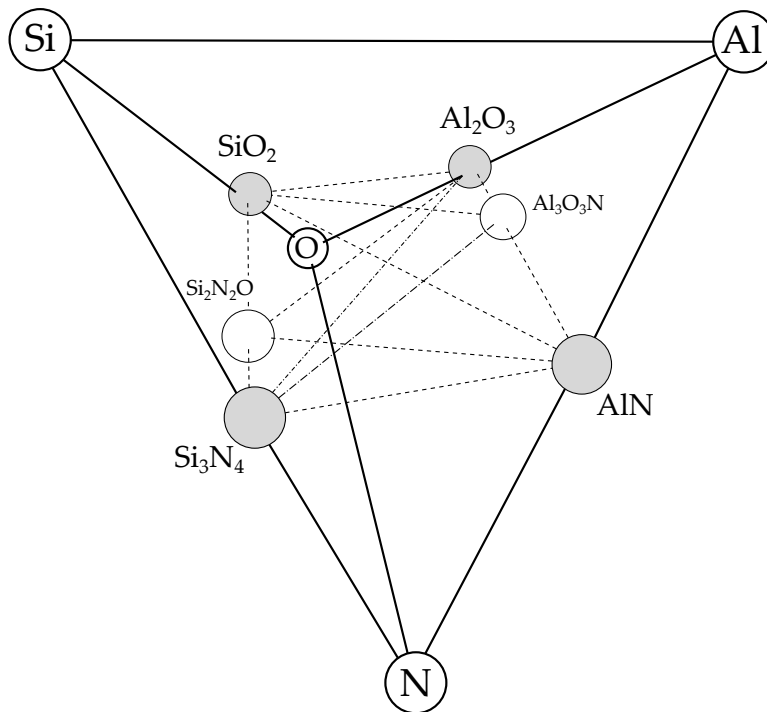


Figure 4.2: Si-Al-O-N system tetrahedron representation<sup>8</sup>.

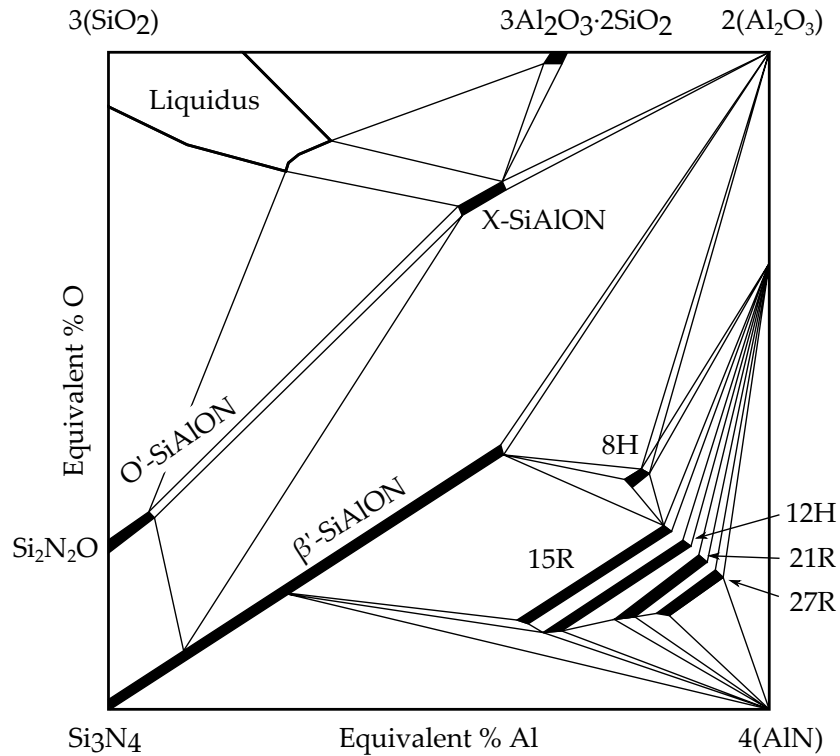


Figure 4.3: Quaternary  $\text{Si}_3\text{N}_4$ -AlN- $\text{Al}_2\text{O}_3$ - system<sup>8</sup>.

other important phases are worth noting, such as X-sialon (general formula  $3(3\text{Al}_2\text{O}_3 \cdot 2\text{SiO}_2) \cdot 2\text{Si}_3\text{N}_4$ , isomorphous to mullite, and for this reason often referred as "nitrogen-mullite"), O'-sialon ( $\text{Si}_{2-x}\text{Al}_x\text{O}_{1+x}\text{N}_{2-x}$ , isostructural with the silicon-oxynitride  $\text{Si}_2\text{N}_2\text{O}$ , with  $x=0-2$ ) and the AlN polytypes, isostructural forms of AlN, generally denoted as 15R (the most frequently observed), 8H, 12H, 21R and 27R. "R" refers to a rhombohedral structure, while "H" refers to an hexagonal structure<sup>8</sup>. O'-sialon, analogously to  $\beta'$ -sialon and  $\beta$ - $\text{Si}_3\text{N}_4$ , presents an acicular microstructure, which could have beneficial effects on the toughness of the ceramic. Its oxidation resistance is higher than other sialon phases, due to the already relatively high oxygen content inside its structure. X-sialon attracts a lower interest, mainly because of its high oxygen content.

Since this diagram was derived from the quaternary Si-Al-O-N system,  $\alpha'$ -sialon phase, which is a 5-elements phase, is absent in Fig. 4.3. Another dimension must be then introduced in the phase diagram in order to take into account the stabilizing element M, thus obtaining what is called the Janecke prism (Fig. 4.4).

Inside the Janecke prism, the plane delimited by  $\text{Si}_3\text{N}_4$ ,  $4/3(\text{AlN} \cdot \text{Al}_2\text{O}_3)$  and  $\text{MN} \cdot 3\text{AlN}$  is what is usually referred as the  $\alpha$ -plane, within which the  $\alpha'$ -sialon stability region lies (Fig. 4.5). Several studies in literature have demonstrated that the  $\alpha$ -stability region is not fixed, but can extend or shrink as a function of both temperature and the stabilizing element M<sup>17</sup>.

Nano-crystalline ceramics have attracted great interest in the last few years, because of their improved mechanical characteristics<sup>18-21</sup>. With traditional powder processing, sub-micron sialon grains are generally not achievable, because their dimensions are limited by the characteristics of the starting raw materials (in particular,  $\text{Si}_3\text{N}_4$ ); an exception being represented by high-energy milling process followed by the novel, but still expensive and not so versatile,

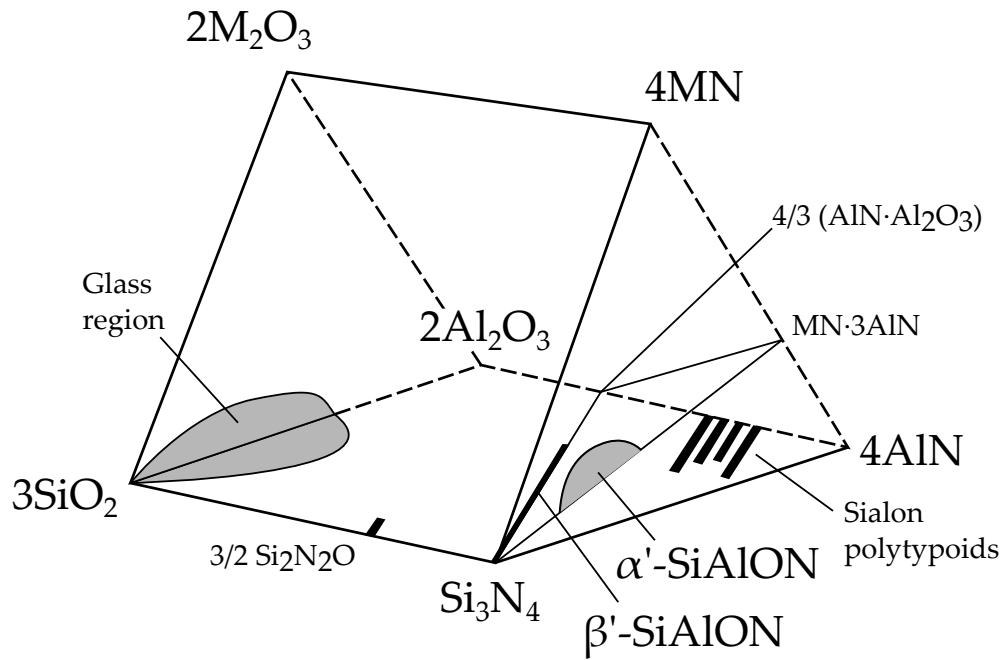


Figure 4.4: Janecke prism representing the 5-elements system M-Si-Al-O-N<sup>16</sup>.

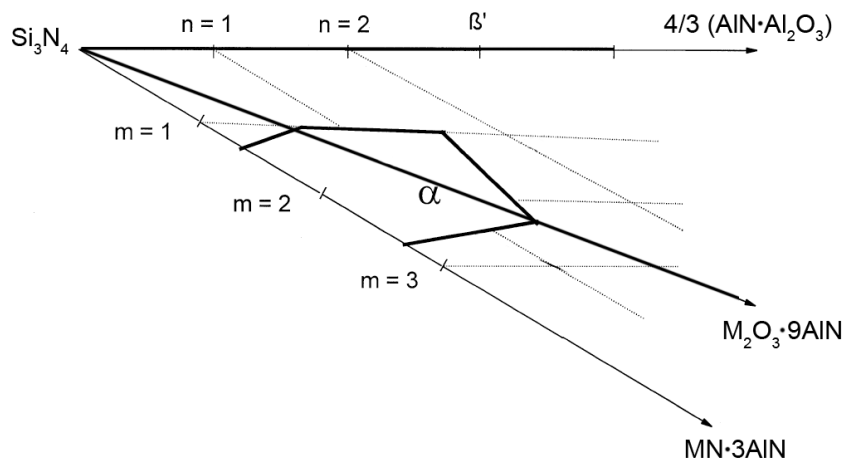


Figure 4.5: Sialon  $\alpha$ -plane and  $\alpha$  stability region.

SPS (Spark Plasma Sintering)<sup>22</sup>. So far, the sol-gel route seemed to be the only method which could provide submicron sialon grains<sup>23</sup>. In addition to sol-gel route, the Polymer Derived Ceramics (PDCs) route has been proven to be an extremely effective and versatile alternative technique for the production of fine-grained ceramics. It is comparable to the sol-gel route in terms of its kinetics, and allows a much simpler processing and shaping because of the polymeric nature of the precursors<sup>24-26</sup>. Very limited research, however, has been dedicated to the production of Sialon ceramics from preceramic polymers. Previous studies<sup>15,27</sup> dealt with chemically modified polymeric precursors, whereas more recent investigation were dedicated to polymers containing micro- and nano-sized filler particles<sup>28-30</sup>.

In the present work, further developments in the preceramic polymers filled with oxide nano-particles approach for the synthesis and the application of sialon ceramics will be presented. In the previous paper on Sialons<sup>28</sup> this approach was applied to the ceramic residue of silicones in nitrogen, possessing a SiOC composition;  $\beta'$ -sialon was effectively obtained, but with a remarkable presence of contaminants, associated to the high oxygen content, which is a common characteristic of many oxygen-rich starting mixtures (which comprises basically all the techniques described above with the exception of powder sintering). At low temperature, the formation of alumino-silicate phases (such as mullite and sillimanite) from the reaction of  $\text{Al}_2\text{O}_3$  with  $\text{SiO}_2$  is firstly observed, when they are not already present in the starting raw materials mixture. A progressive reduction-nitridation of these intermediates then follows when heating in nitrogen gas at temperatures in the range 1400 to 1800°C<sup>14,31</sup>, leading to the formation of the desired  $\beta'$ -sialon phase. At these temperatures, however, undesired reactions like the volatilization of silica ( $\text{SiO}_2 + \text{C} \rightarrow \text{SiO}(\uparrow) + \text{CO}(\uparrow)$ ) are well known to occur<sup>32</sup>, and this could have detrimental effects on the control of the stoichiometry and phase purity of the final ceramic.

Further developments on the siloxane-based system will be presented, in comparison to previous works<sup>28</sup>, by more carefully studying the effects of additives in the starting mixtures, as well as the treatment atmosphere.

Moreover, first results of silazane-based system, which has shown extremely interesting and promising results. The novel approach here presented concerns the use of a ceramic residue rich in Si and N, provided by silazane polymers, reacting with  $\text{Al}_2\text{O}_3$  nano-sized particles. As in the oxygen-rich formulation previously investigated when using silicone preceramic polymers, the C content was found to be essential for the control of the phase purity. Its control was achieved by adjusting the carbothermal reaction with the oxide filler by modifying the temperature and oxide content of the mixture, but also by adding a fully inorganic polymer (perhydropolysilazane, PHPS), not containing carbon-based moieties, which provided, after heat treatment in  $\text{N}_2$ , a ceramic residue in the Si-N system<sup>33</sup>.

## 4.2 SiAlON from silicone-based dispersions

### 4.2.1 Experimental procedure

Polymer selected for these experiments was Silres H44. As reported in the Appendix A, H44 is characterized by both methyl and phenyl side-groups. The presence of organic groups of different nature has a strong influence on the final carbon content on the ceramic residue after pyrolysis when non-oxidizing atmospheres are used. It has been demonstrated in previous studies that, after pyrolysis in inert atmosphere, H44 produces an Si-O-C ceramic residue with atomic proportions reported in Tab.4.2<sup>34</sup>. For comparison purpose, elemental composition of Silres MK (methyl-polysiloxane) is reported. As could be observed, while the atomic proportions between silicon and oxygen are basically equal in the two polymers (since they are mainly related to the chemistry of the main backbone, which is very similar), the carbon content instead is much higher in H44 than in MK, because of the presence in H44 of phenyl groups, which after pyrolysis generate a higher residual carbon content. These elemental compositions were considered for the realization of the different formulations.

Table 4.2: Elemental composition of ceramics residue of Silres MK and Silres H44 after pyrolysis in inert atmosphere at 1000°C<sup>34</sup>.

Materials	Polymer chemistry	Ceramic composition after pyrolysis
Silres MK	methyl polysiloxane	Si <sub>3</sub> O <sub>4.56</sub> C <sub>1.92</sub>
Silres H44	methylphenyl polysiloxane	Si <sub>3</sub> O <sub>4.6</sub> C <sub>8.45</sub>

As a source of Al<sub>2</sub>O<sub>3</sub>, Aeroxide Alu C nanopowders were selected. For formulations designed to give sialon ceramics with a relatively low z-value (z=3), the introduction of some Si<sub>3</sub>N<sub>4</sub> nanopowders (GoodFellow amorphous Si<sub>3</sub>N<sub>4</sub>) was necessary, in order to provide an extra amount of nitrogen-containing phase. For some formulations, Y<sub>2</sub>O<sub>3</sub> nanopowders (Inframat Advanced Materials), carbon black (Carlo Erba) and CaF<sub>2</sub> (Carlo Erba) powders were added. Phenolic resin (Fenotec, Foseco) was also used as an alternative source of carbon: TG/DTA analysis (data not reported here) in inert Argon atmosphere demonstrated that phenolic resin provides a carbon residue with a yield of approximately 48 wt%.

All the components were dispersed in isopropyl alcohol, and homogenized by stirring and ultrasonication. Isopropyl alcohol was selected as dispersing medium due to its ability to both effectively dissolve all the polymers used during the experiments (Silres MK, H44 and phenolic resin) and to create stable fillers dispersions, at least for the timescale used for the preparation of the formulations. For an optimal processing and dispersion of the powders, approximately 10 ml of isopropyl alcohol were used for each gram of powders, and intermediate steps of ultrasonication were applied after the insertion of each component. Some difficulties were found only with the dispersion of Si<sub>3</sub>N<sub>4</sub> nanopowders, likely due to a different surface chemistry. Once homogenized, dispersions were poured into a large glass container and treated at 60°C overnight to completely remove the solvent. After solvent removal, the material obtained was finely ground and compacted by uniaxial pressing at 40 MPa, producing circular-shaped pellets of 20 mm diameter and approximately 2 mm height. Pellets were then heat treated in a tube furnace in N<sub>2</sub> (or, in some cases, in a N<sub>2</sub>/2% H<sub>2</sub> atmosphere). Temperature selected for experiments was 1500°C (boh, vedere alla fine in base ai dati che si inseriscono).

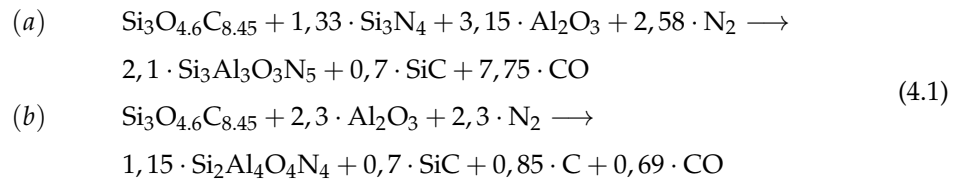
The evolution of all the systems studied was mainly carried out by XRD analysis. As will be observed, because of the general complexity of the phase assemblage in most of the samples,

for a better comprehension and interpretation of XRD results, diffraction peaks in the figures reported were not labeled singularly. Instead, for each XRD pattern, all identified phases are briefly reported on the right side and all the reference patterns used for the identification are reported at the bottom, each one with its ICDD number (also referred as PDF#).

## 4.2.2 Synthesis

### H44/Al<sub>2</sub>O<sub>3</sub> formulations

For the first experiments for the synthesis of β'-sialon samples from preceramic polymers and fillers, 2 different compositions were selected, associated with 2 different z values. As previously discussed in Section 4.1, z value – which indicates the level of substitution of Si–N bonds for Al–O bonds inside the Si<sub>3</sub>N<sub>4</sub> crystal lattice – has a range equal to 0–4.2. For the first experiments, the following hypothetical primary reactions were considered for the formation of β'-sialon with z=3 (Eq.4.1.a) and z=4 (Eq.4.1.b). According to these 2 equations, 2 different samples (labelled as "z3" and "z4") were prepared, with the respective formulations reported in Tab. 4.3.



As could be noticed, in both chemical reactions, the assumption that part of the silicon and of the carbon of the ceramic residue could undergo a partial rearrangement to give the formation of SiC was made. This assumption was made considering that a generic SiOC glass, after pyrolysis in inert atmosphere at sufficiently high temperatures, could undergo a more or less complete phase separation, with the formation of distinct crystalline phases like SiO<sub>2</sub>, SiC and "free" carbon. It was then assumed that the carbon present in the silicon carbide phase would not participate in the reduction reaction to give the formation of carbon monoxide. As described by Sorarù et al.<sup>35</sup>, the composition of a silicon oxycarbide glass could be schematized as

$$\text{Silicon oxycarbide} = \text{SiO}_{2(1-x)}\text{C}_x + y\text{C}_{\text{free}} \tag{4.2}$$

where SiO<sub>2(1-x)</sub>C<sub>x</sub> describes the amorphous silicon oxycarbide network and C<sub>free</sub> the free carbon (carbon that is not bonded to silicon atoms). Moreover, SiO<sub>2(1-x)</sub>C<sub>x</sub> can be rewritten as

$$\text{SiO}_{2(1-x)}\text{C}_x = x\text{SiC} + (1-x)\text{SiO}_2 \tag{4.3}$$

Thus, the amount of SiC considered in Eq. 4.1.a and Eq. 4.1.b was calculated considering Eq. 4.2 and Eq. 4.3, and the elemental composition of the ceramic residue of H44 after pyrolysis reported in Tab. 4.2. As a final remark, it should be said that, although SiC-rich areas are believed to be present in virtually all the materials synthesized (that will be more accurately analyzed in the next paragraphs), it was difficult to clearly identify SiC peaks in XRD patterns, probably because of possible reactions and structural rearrangements involving silicon and carbon that limited its presence in the final materials, its small crystallite size (due to the relatively low treatment temperatures) and, above all, the superimposition of

diffraction peaks of other predominant phases.

Table 4.3: Formulations for z=3 and z=4 sialon compositions, based on Eq. 4.1.

Component	Composition (wt%)	
	z3	z4
H44	37.8	56.8
Al <sub>2</sub> O <sub>3</sub>	39.3	43.2
Si <sub>3</sub> N <sub>4</sub>	22.9	/

As could be observed, z4 composition (which practically represents the solubility limit of aluminum and oxygen inside Si<sub>3</sub>N<sub>4</sub> structure) was selected because in this final composition, no additional starting materials beside the polysiloxane and Al<sub>2</sub>O<sub>3</sub> nanopowders have to be added. Instead, in the case of z3, Si<sub>3</sub>N<sub>4</sub> powder must be added for the obtainment of the right nitrogen content inside the final material. As the source of alumina,  $\gamma$ -Al<sub>2</sub>O<sub>3</sub> nanopowders (Aeroxide Alu C, Evonik Industries) were selected, while amorphous Si<sub>3</sub>N<sub>4</sub> nanopowders (Goodfellow) were selected for z3 sample.

As will be more clearly pointed out during the following discussion, the elimination of oxygen through reduction reactions seems to be the most critical point associated with polysiloxane-based formulations, which makes the synthesis of a pure  $\beta'$ -sialon material not trivial.

Silres H44 was selected for these first experiments, because of its higher residual carbon content after pyrolysis, which is necessary for the reduction of the overall oxygen content (through the formation of CO) and for the subsequent formation of  $\beta'$ -sialon phase. First of all, the oxygen present inside the SiOC ceramic residue should be, in principle, totally removed, and substituted by nitrogen atoms from the atmosphere for the realization of a Si<sub>3</sub>N<sub>4</sub> matrix. Furthermore, also some of the oxygen introduced by the Al<sub>2</sub>O<sub>3</sub> filler should be eliminated. In fact, as discussed in Section 4.1,  $\beta'$ -sialon are generated by substituting Si–N bonds for Al–O bonds. Since Al<sub>2</sub>O<sub>3</sub> is here used as the source for Al–O, an excess of oxygen is thus introduced, since oxygen content in Al<sub>2</sub>O<sub>3</sub> is 50% higher than the stoichiometric quantity required for the formation of  $\beta'$ -sialon.

First results for both z3 and z4 formulations are reported in Fig. 4.6 and Fig. 4.7. For Fig. 4.6, samples were simply placed in an Al<sub>2</sub>O<sub>3</sub> tray during the heat treatments in N<sub>2</sub>, while for Fig. 4.7 samples were placed on a thin layer of graphite distributed on the bottom of the Al<sub>2</sub>O<sub>3</sub> tray, and then slightly covered by some extra graphite. This procedure was necessary in order to provide a more reducing atmosphere during the treatments at high temperature, and to analyze its effect on the composition of the final materials.

2 different behaviors were observed for the 2 different samples. With z3 formulation, X-sialon and mullite are the main phases detected, while  $\beta'$ -phase was observed but at lower concentrations. Moreover, when this sample is placed in a graphite bed, no significant changes in the phase assemblage are observed.

This phase assemblage observed is a good picture of the hypothesized global mechanism for the formation of  $\beta'$ -sialon, which is also confirmed by other works in literature concerning the synthesis of sialon materials by the carbothermal reduction/ nitridation (CNR) of SiO<sub>2</sub> and Al<sub>2</sub>O<sub>3</sub> mixtures of natural alumino-silicates (e.g. mullite, sillimanite or kaolin)<sup>13</sup>, or other starting materials, such as fly ash or gels (from sol-gel processing)<sup>14,23</sup>.

Typically, when oxygen-rich starting mixtures are used, a multi-step reaction sequence towards the formation of sialon phases is observed. At low temperature, the formation of alumino-silicate phases (such as mullite and sillimanite) from the reaction of Al<sub>2</sub>O<sub>3</sub> with

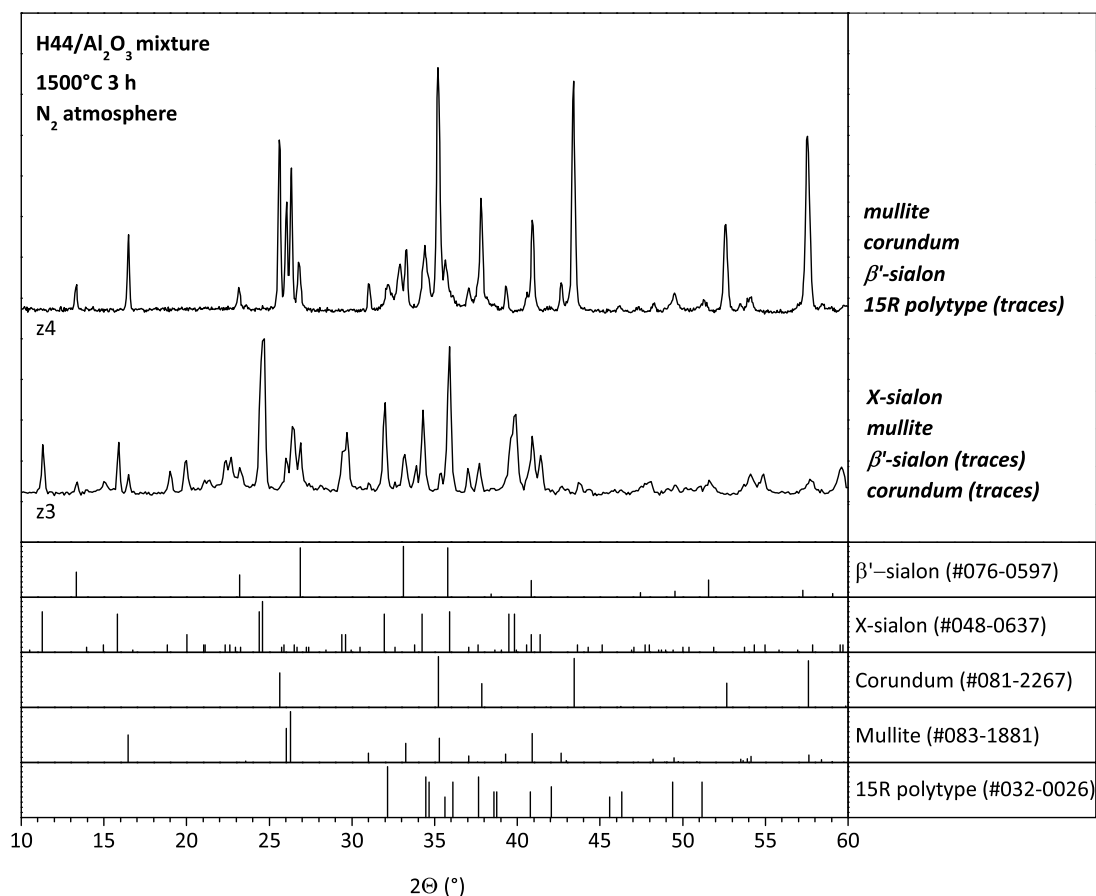


Figure 4.6: XRD patterns of z3 and z4 samples after heat treatment at 1500°C for 3 h in N<sub>2</sub> atmosphere. On the bottom, reference patterns of all the phases identified are reported; on the right, phases detected for each sample are listed.

SiO<sub>2</sub> is firstly observed, when they are not already present in the starting raw materials mixture. A progressive reduction-nitridation of these intermediates then follows when heating in nitrogen gas at temperatures in the 1400-1800°C range<sup>14,31</sup>, leading to the formation of the desired β'-sialon phase.

Apparently, this behavior is present also in the polysiloxane-based mixtures: in the first phases of the treatment, the SiOC ceramic residue reacts with the Al<sub>2</sub>O<sub>3</sub> nanoparticles to give the formation of aluminosilicates, i.e. mullite (3Al<sub>2</sub>O<sub>3</sub>·2SiO<sub>2</sub>). According to previous studies on similar systems based on polysiloxanes filled Al<sub>2</sub>O<sub>3</sub> nanopowders<sup>36,37</sup>, the nucleation of mullite could take place at relatively low temperatures (above 1250°C), even when non-oxidizing atmospheres are used. It is then reasonable to assume that also in the present study mullite is the first phase to nucleate at relatively low temperatures. The nucleation of mullite seems to have a detrimental effect towards the formation of sialon phases: most of the silica and the Al<sub>2</sub>O<sub>3</sub> – which are, respectively in an amorphous and quasi-amorphous state (due to the very small crystallite dimensions of the Al<sub>2</sub>O<sub>3</sub> grains) – quickly undergo a structural rearrangement for the formation of a more stable crystalline phase, which is less “inclined” to undergo the further reactions required for the formation of sialon phases, i.e. oxygen reduction and nitrogen intake from the atmosphere. Subsequently, a carbothermal reduction-nitridation (CRN) process takes place, with a reduction of the global oxygen content of the material (through the reaction of the carbon of the polymer residue with oxygen, with the subsequent formation of CO); at the same time, a progressive nitrogen intake from

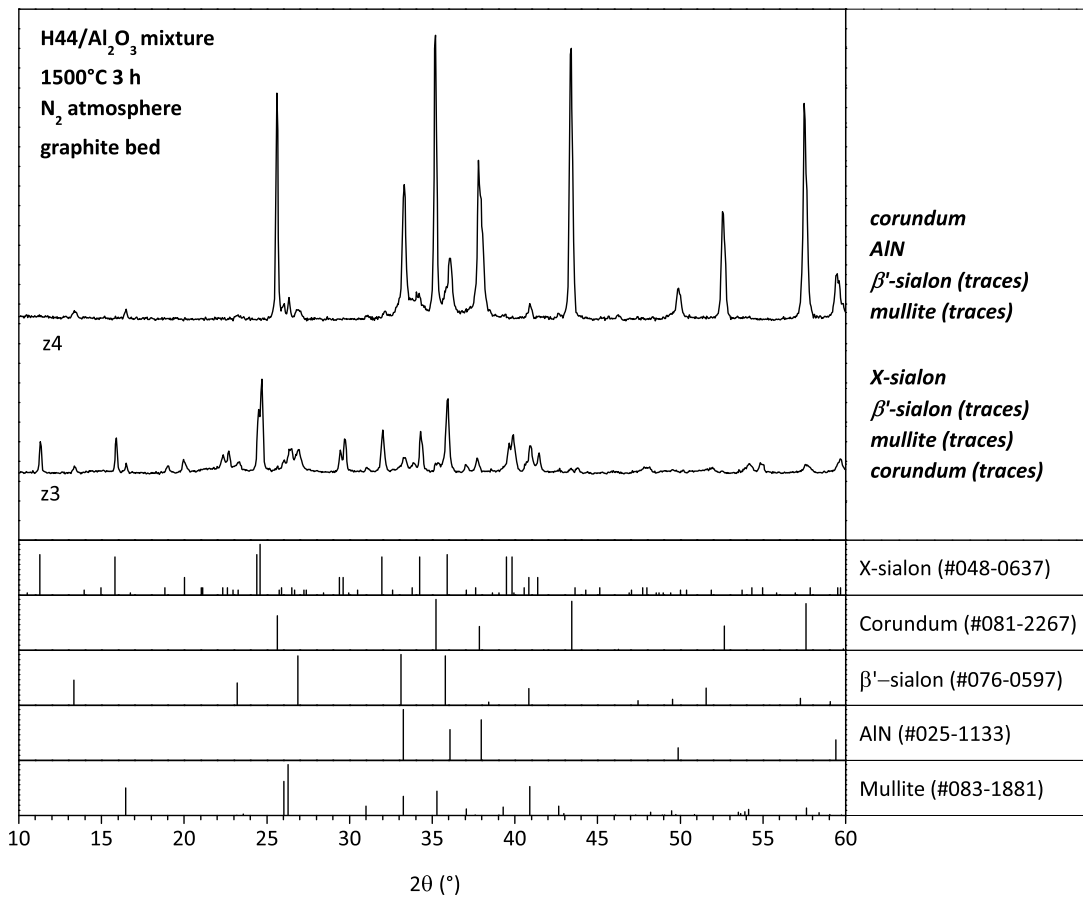


Figure 4.7: FIGURE CAPTION

the atmosphere makes possible the formation of the first nitrogen-containing phase detected, i.e. X-sialon (frequently referred also as "nitrogen-mullite"). At the end of the process, a further nitrogen intake could finally produce the nucleation of  $\beta'$ -sialon. It is then reasonable to assume that in z3 sample, mullite, X-sialon and  $\beta'$ -sialon represent the early, the intermediate and the final stage of the overall process, respectively.

However, it should be pointed out that this phase assemblage is a representation of the *global* material composition, comprising of the outer shell and the inner core, which – as will be shown below – have been demonstrated to differ from each other. In fact, as could be easily observed by optical microscopy of the section of the sample (Fig. 4.9) and XRD analysis (Fig. 4.8), compositional gradients are present inside the sample, which are mainly related to the fact the the only nitrogen source for the formation of nitrogen-containing phases (such as X-sialon and  $\beta'$ -sialon) is the atmosphere inside the tube furnace. Nitrogen must diffuse from the atmosphere inside the samples and, as a direct consequence for relatively short treatments, its presence is lower in the inner core and higher in the outer shell, which thus implies a higher content of  $\beta'$ -sialon in the outer shell and at the same time a higher presence of oxygen-rich, intermediate phases like mullite and X-sialon in the inner core. This hypothesis is confirmed by XRD analysis: in Fig. 4.8 2 patterns of z3 sample are reported, one acquired after grinding in the usual  $\theta$ -2 $\theta$  configuration, and the other acquired before grinding with the incident beam fixed at a  $0.05^\circ$  glancing angle. In the first case, diffraction peaks are obviously related to the global composition of the sample. On the contrary, by using a fixed  $0.05^\circ$  glancing angle, diffraction peaks observed are mainly related the the surface layer of the sample. It could be easily observed that by using a  $0.05^\circ$  glancing angle,

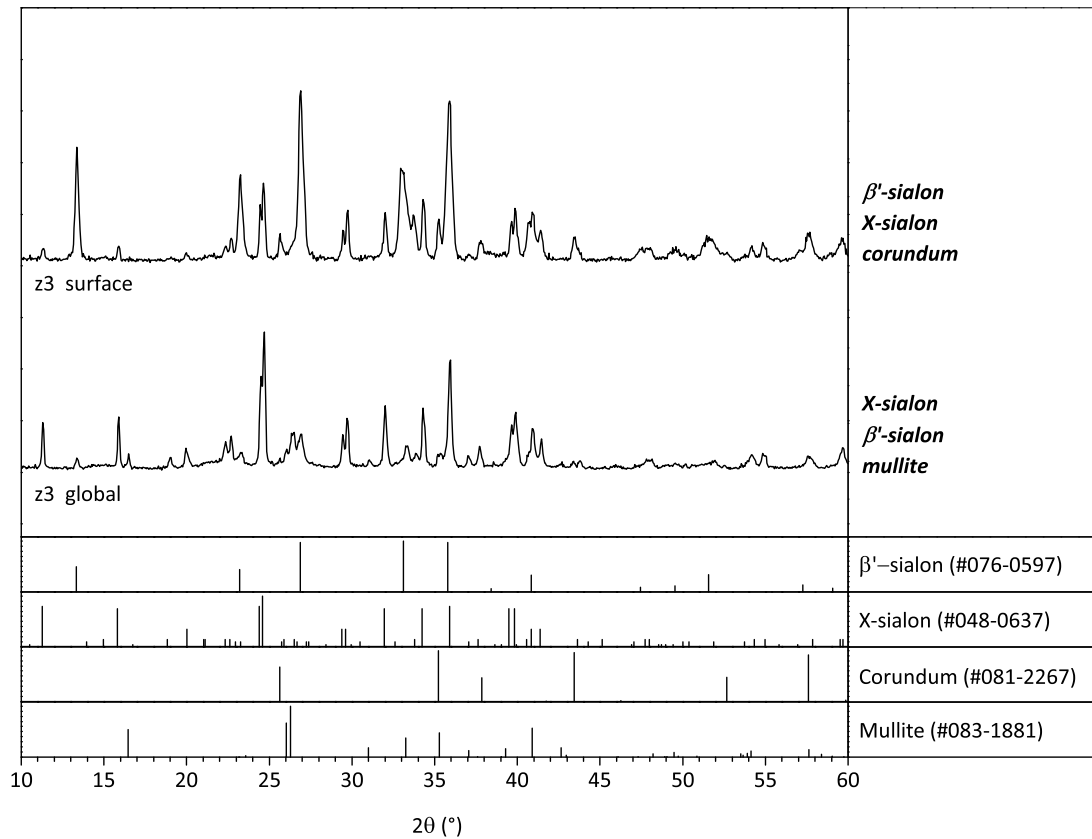
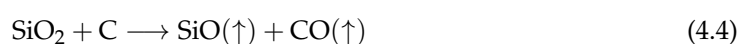


Figure 4.8: XRD patterns of z3 sample. "z3 global" pattern represents the global phase assemblage of the sample, while "z3 surface" is representative of the phase assemblage of the outer layer.

$\beta'$ -sialon is the predominant phase, while with the usual  $\theta$ -2 $\theta$  configuration, additional peaks related to mullite and X-sialon are present with a higher intensity. In the cross-section image (Fig. 4.9), a clear distinction between the darker,  $\beta'$ -sialon rich outer layer and the white, mullite-rich inner core could be easily observed, thus confirming again the compositional gradients issue related with the reaction with the atmosphere.

For z4 formulation, a different behavior was observed. Firstly, when no graphite-bed was used, a slightly different phase assemblage was found if compared to z3 sample. Mullite is still present, confirming the observation that the first reaction to take place in oxygen-rich mixtures is, again, the reaction of silica with  $\text{Al}_2\text{O}_3$  nanoparticles. No traces of X-phase were detected in this sample. A clear explanation for the absence of this intermediate phase (which was instead observed for z3 formulation) is not very clear. The formation of some  $\beta'$ -sialon can also be observed, while remaining crystalline phases detected are corundum and traces of 15R polytype (a Si-Al-O-N phase with the  $\text{SiAl}_4\text{O}_2\text{N}_4$  general composition, based on the AlN structure). The presence of a different phase assemblage, if compared to z3 formulation, could be explained considering that 1) this mixture was formulated in order to have a z-value equal to 4.0, which represents basically the substitution limit of Si-N for Al-O, and 2) a concurrent, secondary reaction takes place during the heat treatments, which must be taken into consideration: the carbothermal reduction of silica, often referred as "silica volatilization".

The silica volatilization process could be briefly schematized by the following possible reactions<sup>38,39</sup>:



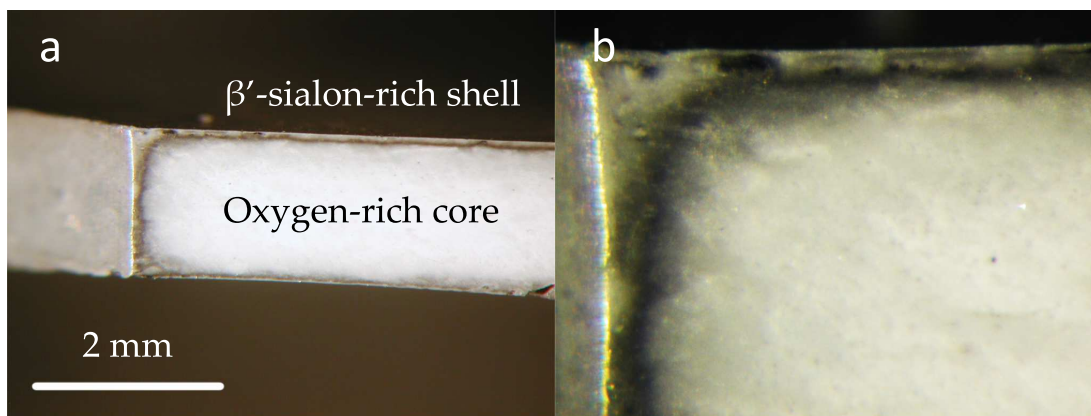


Figure 4.9: a) Optical image of the cross section of sample z3 after heat treatment at 1500°C for 3 h. A distinction between the β'-sialon-rich shell (gray) and the oxygen-rich-core (white) is clearly visible; b) detail at higher magnifications.

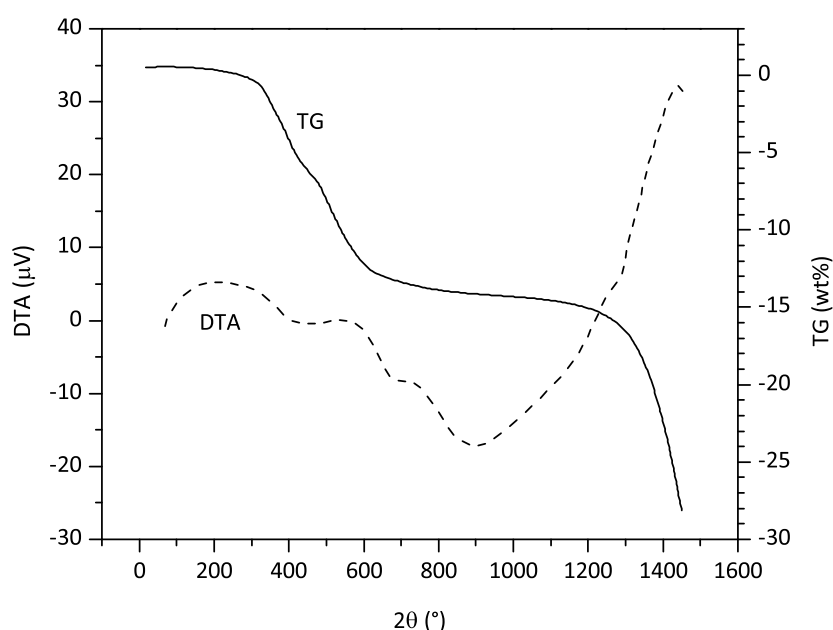
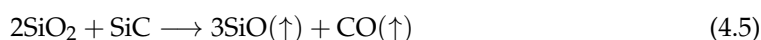


Figure 4.10: TG/DTA analysis of z3 sample in N<sub>2</sub> atmosphere (↑exothermic, ↓endothermic).



In the presence of a non-oxidizing environment, the presence of a reducing agent like carbon (or silicon carbide) could reduce the oxygen content of silica with the subsequent formation of carbon monoxide, which is one of the reactions required for the realization of sialon phases in this type of systems. The main problem associated with the reduction of silica is that the silicon monoxide that forms upon this reaction is a volatile species, and, as a consequence, a progressive loss of SiO<sub>2</sub> is observed. Clues of this ongoing concurrent process have been found both in TG analysis (where a significant weight loss was observed for temperatures higher than approximately 1300°C, see Fig. 4.10) and in the formation nearby the samples of SiC nanowires, due to a further reaction of SiO with the embedding graphite (when used). SiO could also be transported away from the sample by the gas flow, and react with N<sub>2</sub> to form Si<sub>3</sub>N<sub>4</sub> whiskers downstream on cooler parts of furnace<sup>39</sup>. This process eventually changes the global stoichiometry of the material, and strongly limits results reproducibility.

While the effects of this phenomenon in z3 formulation are less noticeable, the stoichiometry-

etry change in z4 sample is quite evident: a lowering of the global silica content corresponds to an increased alumina content, and thus a z-value higher than 4. Since 4 represents the higher limit for Si-N→Al-O substitution, the nucleation of new aluminum-rich phases beside  $\beta'$ -sialon are expected. This is verified by the presence of both corundum (the more stable allotropic form of  $\text{Al}_2\text{O}_3$ ,  $\alpha\text{-Al}_2\text{O}_3$ ) and 15R polytype.

This stoichiometry change is even more evident by looking at Fig. 4.7, where a graphite embedding powder was used. In this case the presence of a more reducing atmosphere seems to push silica volatilization process almost to its completion: main crystalline phases detected are corundum and AlN (totally silicon-free phases), and only traces of  $\beta'$ -sialon and mullite are detected.

Based on these first results, z4 formulation were discarded, since the yield of the desired sialon phases was too low, and the proximity to the upper limit of the existence range of  $\beta'$ -sialon demonstrated to be disadvantageous when the concurrent process of silica volatilization is active.

### **Influence of additives on H44/ $\text{Al}_2\text{O}_3$ system evolution**

A new series of experiments was carried out, starting from first results of z3 formulation, in order to improve different critical aspects that characterized first experiments, compositional homogeneity and phase assemblage above all. Different combinations of  $\text{Y}_2\text{O}_3$ , carbon black and  $\text{CaF}_2$  were used.

$\text{Y}_2\text{O}_3$  was selected to promote densification as well as system homogeneity.  $\text{Y}_2\text{O}_3$  is a well-known sintering aid used for sialon ceramics. It has been verified in many works in literature that, in the case of synthesis of  $\beta'$ -sialon by common powder processing, small amounts of  $\text{Y}_2\text{O}_3$  added in the starting formulation (in the 1-3 wt% range) are able to provide an intergranular glassy phase in the 2-6 vol% range. Even with only 1 wt%  $\text{Y}_2\text{O}_3$  added, 2 to 3 vol% of glassy phase could be found in the final materials (depending on the z-value). It has been shown that the added  $\text{Y}_2\text{O}_3$  reacts with the  $\text{SiO}_2$  present and also with some if the initially added  $\text{Al}_2\text{O}_3$ , which explains why even small additions of an oxide like  $\text{Y}_2\text{O}_3$  can initiate the formation of considerably greater amounts of glassy phase. For applications at low or medium temperatures, a small addition of sintering aid has a positive influence on the fracture toughness<sup>40</sup>. The glassy grain boundary phase that forms is a preferred crack path, and crack branching occurs, thereby increasing the fracture energy. For example, the room-temperature toughness of a  $\beta'$ -sialon ceramic is significantly increased by the addition of 1 wt%  $\text{Y}_2\text{O}_3$ . These results are in accordance with the findings of Tanaka et al.<sup>41</sup> who have found that the fracture toughness is greatly dependent on the grain-boundary properties. When the grain-boundary bonding is sufficiently strong, e.g. in the absence of a glassy grain-boundary phase, cracks propagate transgranularly in the material and the toughness is low. Instead, hot hardness and creep resistance are negatively influenced by the addition of even small (1 wt%) amounts of  $\text{Y}_2\text{O}_3$ <sup>1</sup>.

$\text{CaF}_2$  instead was selected as a nitridation aid. Evidences for an enhanced nitridation process in the presence of  $\text{CaF}_2$  were reported in references<sup>42,43</sup>. The mechanism of  $\text{CaF}_2$  is related to an enhanced break of the Si-O bond, which at the same time could become available for the formation of Si-N bond by a nitrogen intake from the atmosphere. The same effect was also observed with other fluorines (e.g.  $\text{BaF}_2$ ) or chlorines (e.g.  $\text{CaCl}_2$ ,  $\text{BaCl}_2$ )<sup>42</sup>.

Compositions with an over-stoichiometric carbon content were also tested, since it has been demonstrated<sup>13,44</sup> that often the needed carbon content is usually 5-10% higher than

the stoichiometric amount. It is believed that some of the excess carbon is necessary to compensate for the impurities in the carbon and nitrogen.

All the different formulations are reported in Tab. 4.4. Additives additions were equal to +3 wt%  $Y_2O_3$  and +4 wt%  $CaF_2$ , based on the total weight of  $H44+Al_2O_3+Si_3N_4$ . For carbon instead, +10 mol% was calculated with respect to the carbon content of the ceramic residue of H44 reported in Tab. 4.2.

Table 4.4: Formulations produced with the addition of  $Y_2O_3$ , carbon and  $CaF_2$ .

Component	Composition (wt%)			
	z3	z3y	z3yc10	z3yc10caf2
H44	37.8	36.7	36.2	34.9
$Al_2O_3$	39.3	38.2	37.7	36.3
$Si_3N_4$	22.9	22.2	21.9	21.1
$Y_2O_3$	/	2.9	2.9	2.8
Carbon	/	/	1.3	1.2
$CaF_2$	/	/	/	3.7

In Fig. 4.11 and Fig. 4.12 results for the same H44/ $Al_2O_3$  mixture with  $z=3$  are reported, as a function of the additives inserted to enhance system evolution to the desired  $\beta'$ -phase. Again, parallel experiments were carried out on the same samples with (Fig. 4.12) and without (Fig. 4.11) graphite as embedding powder. To simplify discussion, samples treated in a graphite bed will be labelled as "sample\_g" (e.g. z3y\_g, z3yc10\_g, etc.).

Significant differences were observed between samples treated with and without a graphite embedding powder, and also between the different formulations tested in this series of experiments. Although some points are still not very clear and a precise interpretation of the entire mechanism is still quite complicated, some evidences have been summarized in the next paragraphs.

First of all, the insertion of  $Y_2O_3$  (samples z3y and z3y\_g) apparently does not have many significant beneficial effects towards a better phase evolution, except for a slight increase of  $\beta'$ -sialon presence in both samples treated with and without embedding graphite. Moreover, in both samples a slight increase of corundum presence is observed, more pronounced in z3y sample. Finally, mullite traces of z3\_g were completely eliminated in z3y\_g, while mullite concentration in z3y sample remains essentially unchanged if compared with sample z3.

$Y_2O_3$  could likely react with some  $SiO_2$  and/or  $Al_2O_3$  at lower temperatures (as reported by Ekstrom<sup>1</sup> to create a certain amount of liquid phase<sup>1</sup> that could enhance system densification and transportation phenomena. This fact seems to be well confirmed by further optical analysis, that are reported in Fig. 4.13. In this picture, cross-section images of z3 and z3y samples are reported. The clear distinction between the grayish outer layer and white inner core of z3 sample is not present in z3y sample. Moreover, z3y sample is much more compact than z3 sample, thanks to the probable formation during the heat treatment of a certain quantity of liquid phase (provided by the presence of  $Y_2O_3$ ), that could give a better densification through liquid phase sintering.

The fact that no significant improvements in phase purity are observed means that reactions like reduction and nitridation, necessary for system development, do not strictly rely on transportation phenomena, but on the presence of different types of additives, such as reducing agents and nitridating agents (as will be shown in the next paragraphs).

The introduction of some extra carbon inside the material has instead a noteworthy effect on system evolution, which was completely different between z3yc10 and z3yc10\_g samples.

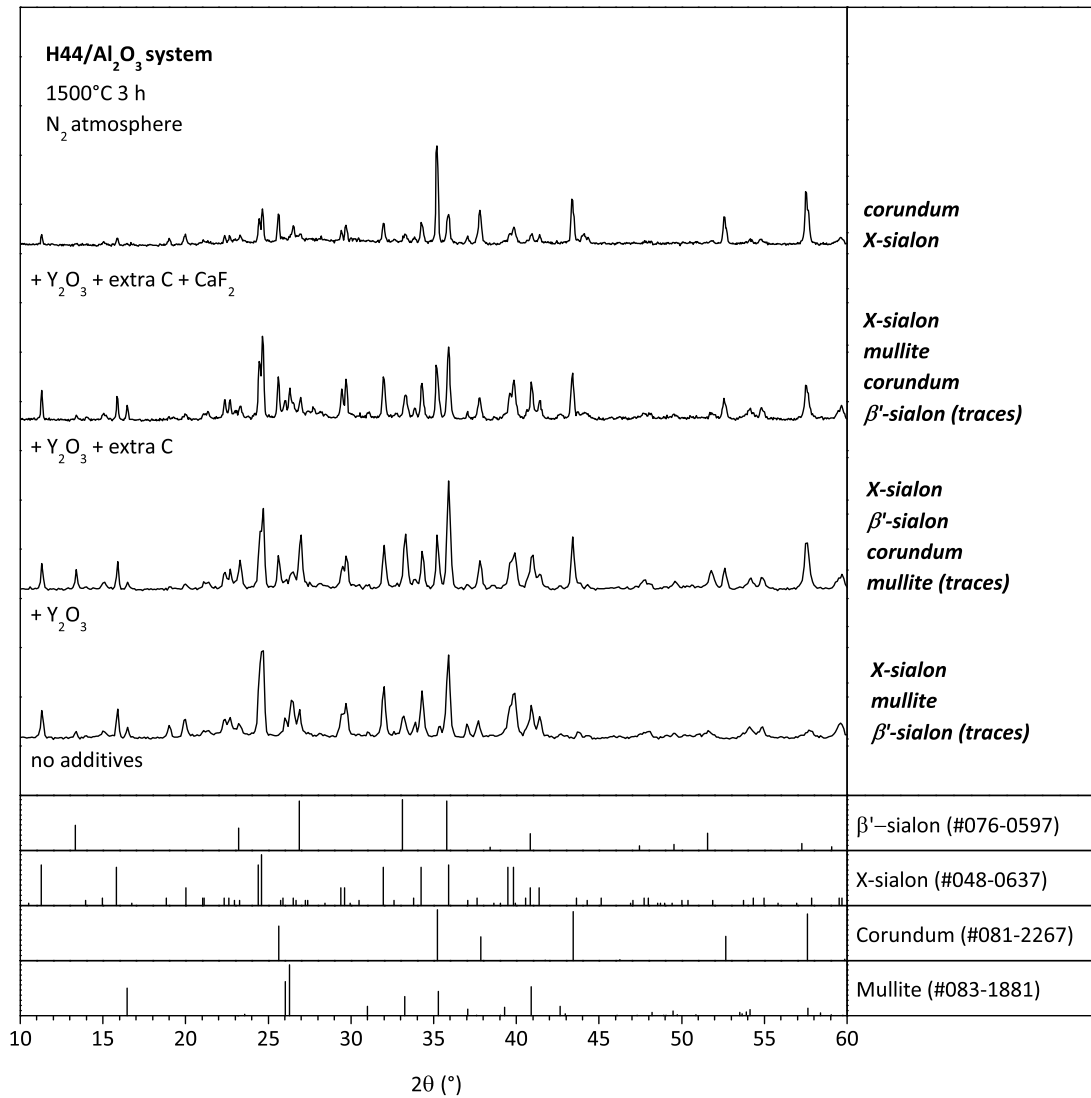


Figure 4.11: XRD results of Silres H44/Al<sub>2</sub>O<sub>3</sub> mixtures, with different combinations of additives (description on the left) inserted to improved system evolution. XRD results refers to pellets heat treated at 1500°C for 3 h in N<sub>2</sub> atmosphere. On the right side, a list of the detected phases is reported.

By looking at the z3y→z3yc10 passage, the most significant difference is the strong reduction of β'-sialon concentration, which is basically absent in z3yc10 sample. X-sialon and corundum presence remain essentially unchanged, while a certain mullite increase is observed.

Instead, by looking at the z3y<sub>g</sub>→z3yc10<sub>g</sub> passage, a totally different behavior is observed: β'-sialon concentration, as well as corundum presence, are strongly increased, while X-sialon is almost completely eliminated. This is probably the most significant step towards the desired system evolution: the elimination of X-sialon and the contemporary increase of β'-sialon are clues for both an effective reduction mechanism, and also a more effective nitridation of the material. The main drawback of this step is the formation of conspicuous quantities of Al<sub>2</sub>O<sub>3</sub>, which should be probably associated with the X-to-β conversion. This fact is also supported by analogous evidence in literature, concerning the nitridation of alumino-silicates<sup>39,45</sup>. Moreover, the presence of residual Al<sub>2</sub>O<sub>3</sub> is believed also to be connected to silica volatilization phenomenon described before, and likely to a still incomplete Al<sub>2</sub>O<sub>3</sub> dissolution inside the β'-sialon structure, due to the relatively low treatment temperatures.

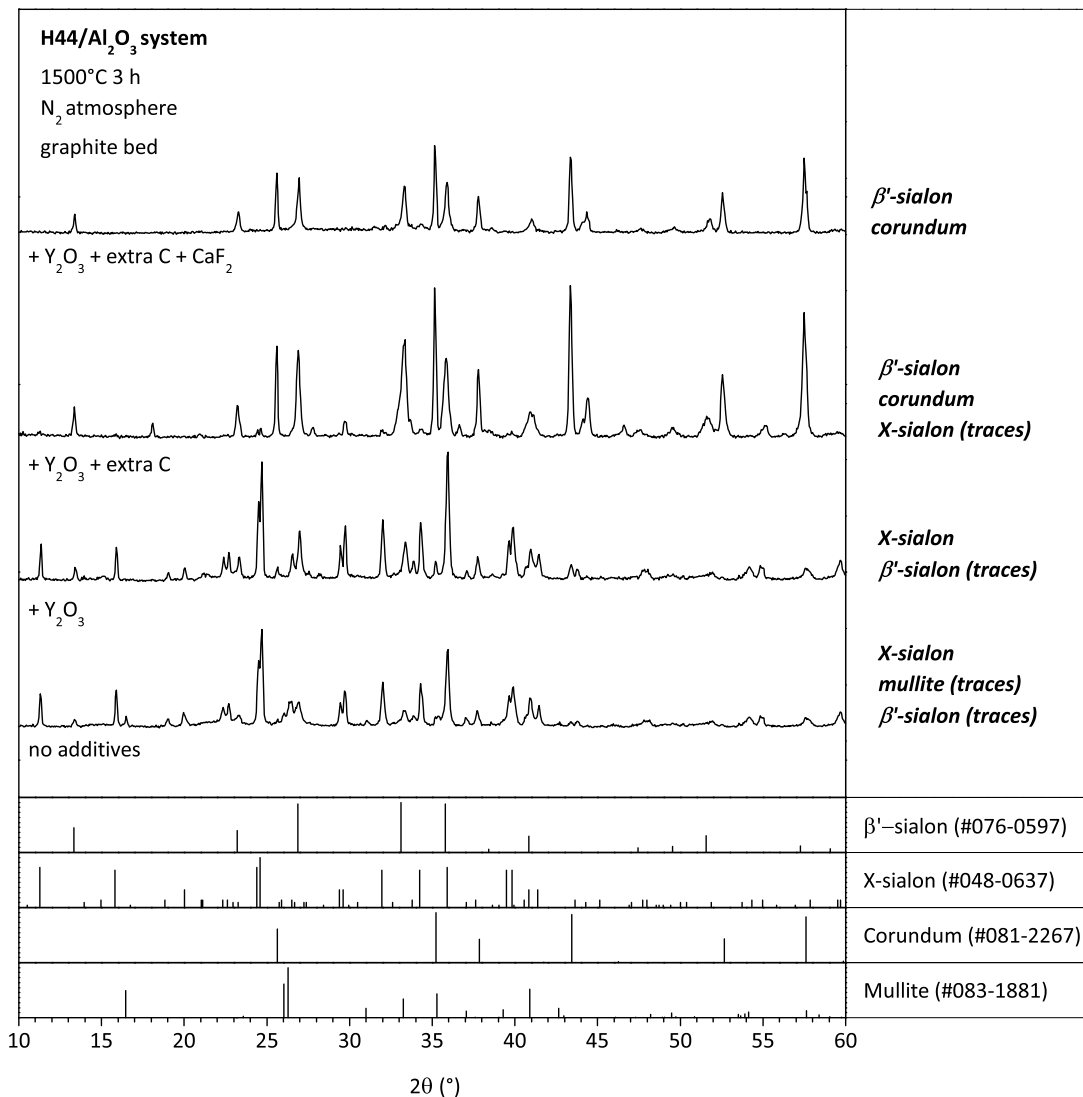


Figure 4.12: XRD results of Silres H44/Al<sub>2</sub>O<sub>3</sub> mixtures, with different combinations of additives (description on the left) inserted to improved system evolution. XRD results refers to pellets heat treated at 1500°C for 3 h in N<sub>2</sub> atmosphere with graphite embedding powder. On the right side, a list of the detected phases is reported.

A justification for the different behavior depending on the presence of a graphite bed is hard to be found, but it seems that the simple introduction of some extra carbon, if not supported by a more reducing atmosphere, could not have any beneficial effect on system reduction and nitridation.

Finally, the introduction of CaF<sub>2</sub> was analyzed, and two similar effects were observed for both z3yc10caf2 and z3yc10caf2\_g samples. When no graphite bed is used, the global effect consists in a reduction of X-sialon and mullite presence, with at the same time an increase of corundum and no formation of β'-sialon. As expected, CaF<sub>2</sub> presence has a strong influence on silica-rich phases: Si-O bond break is enhanced, but without an increase at the same time of nitrogen content. On the contrary, a further silica loss seems to take place, with the subsequent depletion of Al<sub>2</sub>O<sub>3</sub> from the alumino-silicates X-sialon and mullite. This same observation is valid for z3yc10caf2\_g sample, where a total elimination of X-sialon is observed, even though its presence was quite low in z3yc10\_g sample.

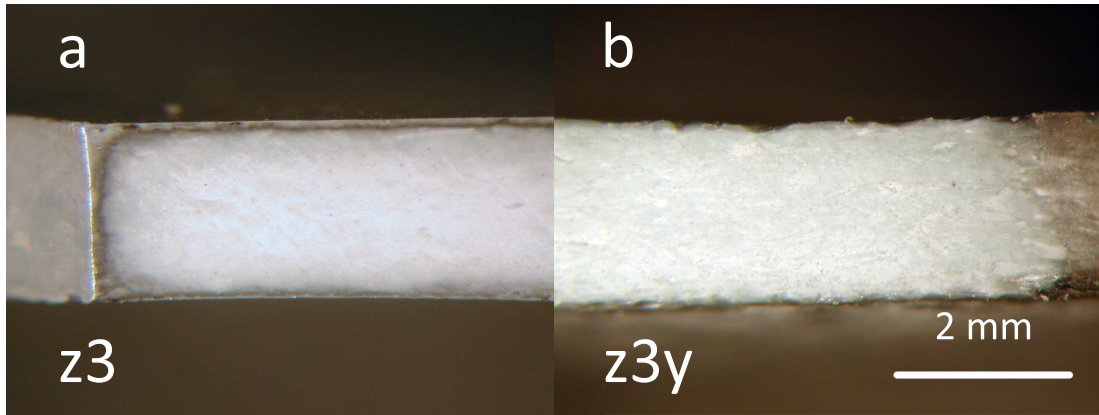


Figure 4.13: Optical image of the cross section of sample z3 and z3y after heat treatment at 1500°C for 3 h.

### Influence of the treatment atmosphere on H44/Al<sub>2</sub>O<sub>3</sub> system evolution

Reducing atmospheres (as in the case of N<sub>2</sub>/2% H<sub>2</sub>) were found to be extremely effective to reduce the final content of oxygen-rich phases such as X-sialon, and to obtain higher quantities of β'-sialon.

XRD analysis of an H44/Al<sub>2</sub>O<sub>3</sub> mixture are reported in Fig. 4.14, where results for z3 sample are presented after heat treatment in N<sub>2</sub> and in N<sub>2</sub>/H<sub>2</sub> 2% atmosphere for 3 h at 1500°C. As could be observed, treatment atmosphere seems to be crucial for both the reactions of reduction and nitridation: phases identified are only β'-sialon and residual Al<sub>2</sub>O<sub>3</sub> (corundum). These results are basically identical to previously described z3yc10CaF<sub>2</sub>\_g sample, which represented the best result in terms of phase purity and system evolution towards the formation of β'-sialon. The use of a slightly reducing atmosphere leads to much faster reactions, even when no additives are introduced inside the starting mixture.

The presence of residual Al<sub>2</sub>O<sub>3</sub> is likely due, again, to the concurrent silica volatilization reaction, and probably to a still incomplete dissolution of Al<sub>2</sub>O<sub>3</sub> inside the sialon phase, due to the relatively low treatment temperature set for the experiment.

As would be described in Section 4.4, the realization of ceramic joining between commercial sialon substrates was carried out by using N<sub>2</sub>/H<sub>2</sub> 2% atmosphere, since results obtained with these process parameter are undoubtedly the most promising, when polysiloxane-based mixtures are used.

### Conclusions

As a concluding remark on synthesis of sialon from siloxanes-based systems, the obtainment of phase purity in the final ceramics, as briefly resumed before, is not trivial. As will be shown in the next paragraphs, a much improved system purity and control could be obtained from silazanes-based systems. It should be noted however that siloxanes-based systems are characterized by a much simpler processing, due to the higher chemical stability of the precursors, that finally leads to an easier and wider applicability of this type of systems (some example are reported at the end of the chapter).

Concerning the synthesis of sialon ceramics from siloxane-based mixture, some experimental evidences have been found, that could be resumed in the following points:

- The reaction path towards the formation of β'-sialon is a complex multi-step reaction system. In the first phases of the treatment, the SiOC ceramic residue reacts

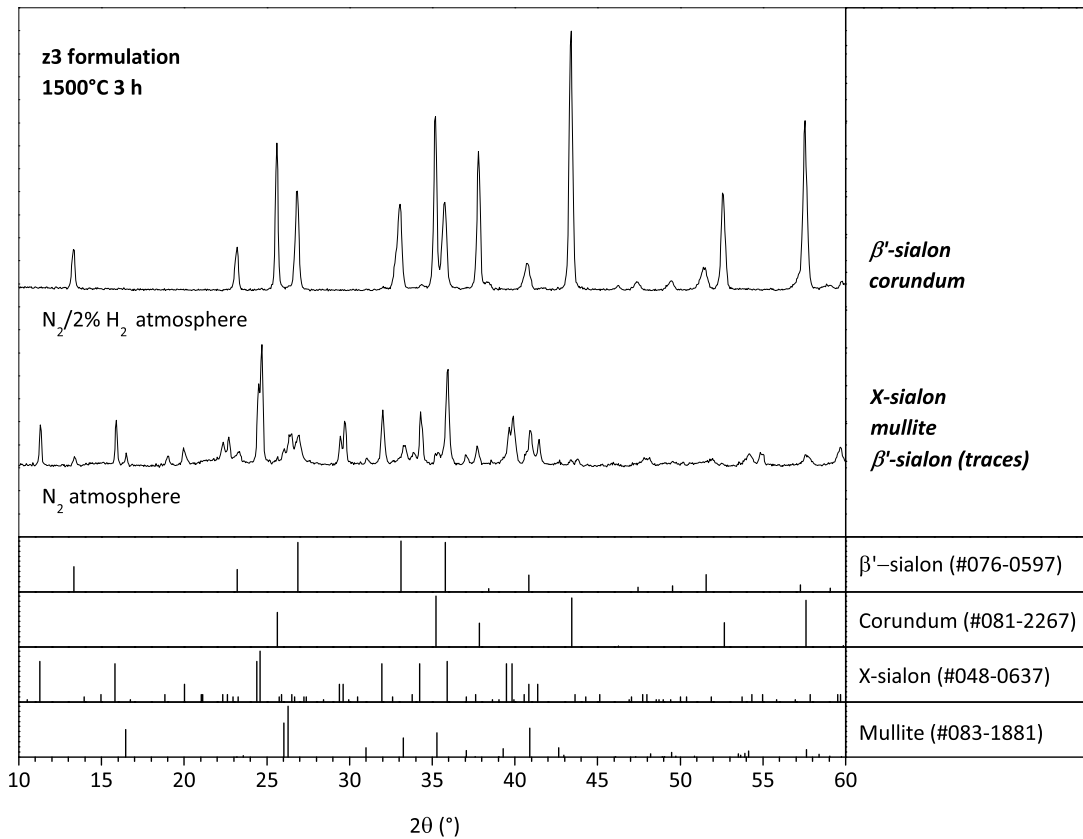


Figure 4.14: Influence of the treatment atmosphere on the evolution of the z3 formulation.

with the  $\text{Al}_2\text{O}_3$  nanoparticles to give the formation of aluminosilicates such as mullite ( $3\text{Al}_2\text{O}_3 \cdot 2\text{SiO}_2$ ). Subsequently, a carbothermal reduction-nitridation (CRN) process takes place, with a reduction of the global oxygen content of the material (through the reaction of the carbon of the polymer residue with oxygen, with the subsequent formation of CO); at the same time, a progressive nitrogen intake from the atmosphere makes possible the formation of the first nitrogen-containing phase, i.e. X-sialon (frequently referred also as "nitrogen-mullite"). At the end of the process, a further nitrogen intake could finally produce the nucleation of  $\beta'$ -sialon.

- Besides this primary reaction, other concurrent processes are believed to take place, the most important being silica volatilization. This process eventually changes the global stoichiometry of the material towards more  $\text{Al}_2\text{O}_3$ -rich compositions, and is believed to be the origin of residual  $\text{Al}_2\text{O}_3$  (observed in most of the samples), which strongly limits results reproducibility. Clues of this ongoing concurrent process have been found both in TG analysis (where a significant weight loss was observed for temperatures higher than  $1300^\circ\text{C}$ ) and in the formation nearby the samples of SiC/Si<sub>3</sub>N<sub>4</sub> nanowires spongy structures, due to a further reaction of SiO with the embedding graphite (when used) or with the  $\text{N}_2$  atmosphere.
- System evolution for pure polysiloxane/ $\text{Al}_2\text{O}_3$  mixtures is extremely slow, and clues for  $\beta'$ -sialon formation can only be detected on the surface of the samples, while in the inner core oxygen-rich phases such as mullite and X-sialon are predominant.
- The introduction of different additives ( $\text{Y}_2\text{O}_3$ , extra carbon,  $\text{CaF}_2$ ) demonstrated to be extremely effective for an increased system homogeneity and a more effective reduction

of oxygen content and nitridation from the atmosphere. Best results showed a final composition which comprised of  $\beta'$ -sialon and some residual  $\text{Al}_2\text{O}_3$  (likely due to silica volatilization).

- Slightly reducing atmosphere ( $\text{N}_2/\text{H}_2$  2%) demonstrated to be extremely effective for a full system development towards, again, a  $\beta'$ -sialon/ $\text{Al}_2\text{O}_3$  final composition, without the need for any additional additive, confirming again that oxygen reduction is probably the crucial point for the synthesis of sialon ceramics from oxygen-rich starting mixtures.

## 4.3 SiAlON from silazane-based dispersions

### 4.3.1 Experimental procedure

Commercially available polysilazane (Ceraset PSZ20, KiON Defense Technologies Inc., Huntingdon Valley, PA, USA), perhydropolysilazane (NN120-20, Clariant, USA) and  $\gamma$ - $\text{Al}_2\text{O}_3$  nano-sized powder (Aeroxide Alu C, Evonik Industries AG, Essen, Germany) were used in the experiments. Either a single preceramic polymer or a mixture of the two liquid precursors was dissolved in n-hexane, and then mixed with a selected amount of  $\text{Al}_2\text{O}_3$  powder. The solid content of the dispersions was kept constant at approximately 40 wt%, and the weight ratio (W) between the polymer component and the ceramic powders was varied between 1.2 and 3.0.

When a mixture of the two precursors was used, silazane/alumina weight ratio was kept constant at a value of 3.0 and PHS:PSZ weight proportion was varied between 0:100, 50:50, 75:25 and 100:0. After desiccation in oven at 200°C overnight, the  $\text{Al}_2\text{O}_3$  powder was removed from the oven and immediately inserted under flowing  $\text{N}_2$  in a sealed glass container, to avoid adsorption of moisture. The silazane(s)/n-hexane solution was produced aside in a beaker, homogenized under stirring, and then injected into the container with the  $\text{Al}_2\text{O}_3$  powder. Homogeneous dispersions were easily obtained by magnetically stirring for 5 minutes and ultrasonication for other 5 minutes. The polysilazane(s) component was found to be very effective for the dispersion of the hydrophilic  $\text{Al}_2\text{O}_3$  nano-sized powders into the highly hydrophobic solvent, without the need for any additional dispersant. The suspensions resulted stable for at least 1 h. The dispersions were then poured into an aluminum container and cured at 300°C for 1 h in  $\text{N}_2$ , in order to cross-link the preceramic polymers. It should be noted that the separation of the curing step from the subsequent pyrolysis step is, in principle, not strictly necessary, and was required only because of the low melting point of the aluminum trays. After the curing step, samples were pyrolyzed in flowing  $\text{N}_2$  (99.99% pure) for 1 h in the 1300-1600°C temperature range (10°/min heating rate) in a tube furnace. Before inserting the samples into the alumina tube,  $\text{N}_2$  was flown for 30 min at 200°C, in order to reduce the humidity content inside the tube. For comparison purpose, some pure PSZ20 samples were also produced in the same experimental conditions. In this case, the first dissolution in n-hexane was not necessary, and polysilazane was directly cured.

Microstructural investigations on the pyrolyzed samples were conducted by means of X-Ray Diffraction (XRD) analysis and by scanning electron microscopy (SEM). A semi-automatic phase identification was performed by using the Match! program package, supported by crystallographic database PDF-2. DTA/TG analysis and Raman spectra were also collected.

### 4.3.2 Synthesis

In Fig. 4.15 XRD data for pure PSZ20 polysilazane treated in  $\text{N}_2$  at different treatment temperatures are reported. Polysilazane residue was XRD amorphous when heated at 1300°C (1 h). At 1400°C (1 h)  $\alpha$ - $\text{Si}_3\text{N}_4$  started to crystallize, and at 1600° additional  $\beta$ - $\text{Si}_3\text{N}_4$  and SiC peaks appear superimposed to an halo still observable in the 32.6-40° range, indicating the presence of a residual amorphous phase. This is in accordance with previous literature<sup>46</sup>.

The situation changed dramatically with the addition of oxide nanofillers, as shown by Fig. 4.16, with important differences based on the weight ratio W, ranging from 1.2 (a) to 3.0 (d). The different weight balances were formulated considering a ceramic yield of PSZ20 of about 70 wt%<sup>47</sup>, a proportion among the elements constituting the ceramic residue of the

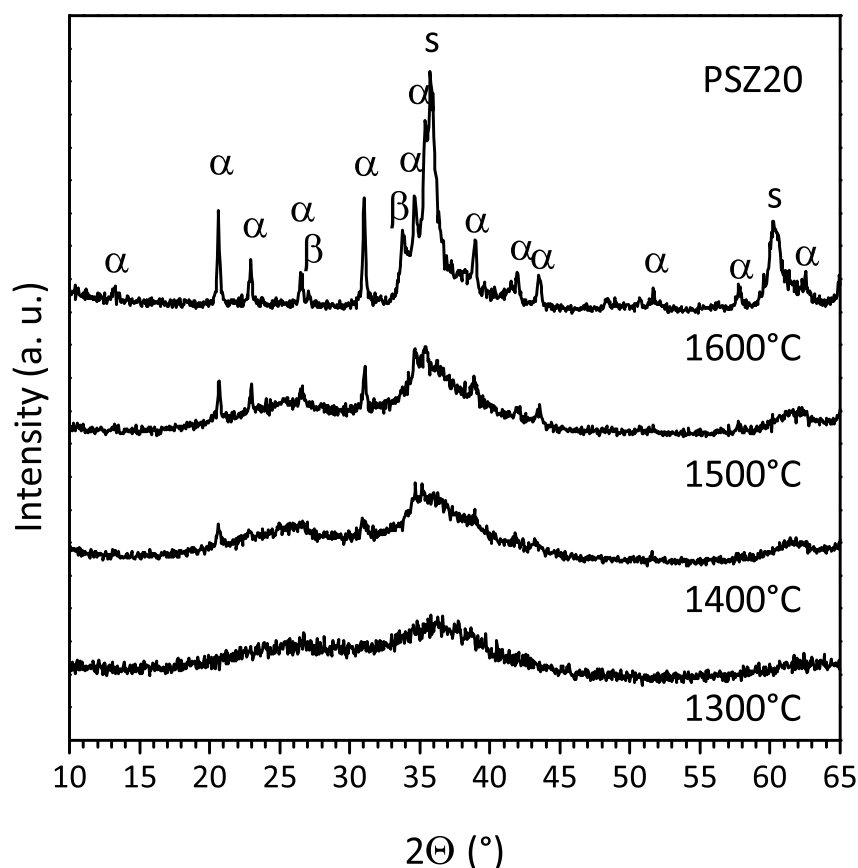


Figure 4.15: XRD patterns of PSZ20 polysilazane as a function of the treatment temperature (1 h soak,  $N_2$  atmosphere).  $\alpha = \alpha\text{-Si}_3\text{N}_4$ ,  $\beta = \beta\text{-Si}_3\text{N}_4$ ,  $s = \text{SiC}$ .

silazane of  $\text{Si/C/N/O} = 1/0.66/0.6/0.03$ <sup>48</sup>, and of different amounts of Si, Al, O and N atoms in the final ceramic, as summarized in Tab. 4.5;  $\beta'$ -sialon with decreasing  $z$  value were expected starting from a composition equal to  $\text{Si}_3\text{Al}_3\text{O}_3\text{N}_5$  ( $z=3$ ) corresponding to  $W=1.2$ . The C present in the silazane pyrolysis residue would remove the excess of oxygen, associated to the incorporation of alumina filler, in the final ceramic, but some residual C could remain present. It is reasonable to assume that some nitrogen could also be incorporated into the system from the atmosphere: to support this hypothesis, as a representative example, the formulation with a PSZ/ $\text{Al}_2\text{O}_3$  ratio equal to 3.0 was pyrolyzed at  $1500^\circ\text{C}$  in Ar atmosphere, and compared to the same formulation pyrolyzed in flowing  $N_2$ . It is evident from Fig. 4.17 that pyrolysis in Ar atmosphere produces a higher amount of oxygen-rich phases ( $O'$ -sialon and X-sialon), which are not present in the sample pyrolyzed in  $N_2$ . Without the presence of nitrogen, the evolution of the system does not proceed towards a ceramic including  $\beta'$ -sialon as the only nitrogen-containing phase. This finding confirms the hypothesized reaction of nitrogen intake from the atmosphere, which could progressively convert oxygen-rich, intermediate phases into the more nitrogen-rich  $\beta'$ -form. Moreover, the slight and progressive weight increase at high temperatures observable from the TG analysis (see Fig. 4.18) represents an additional confirmation of this hypothesis.

The nature of the samples remained essentially amorphous below approximately  $1300^\circ\text{C}$ . The broad peak centered at  $\sim 45.5^\circ$  is related to the  $\gamma\text{-Al}_2\text{O}_3$  nanosized particles, which were embedded in the amorphous Si-C-N phase deriving from the polysilazane. At  $1300^\circ\text{C}$ , a partial atomic rearrangement lead to the formation of  $O'$ -sialon crystallites, while at  $1400^\circ\text{C}$

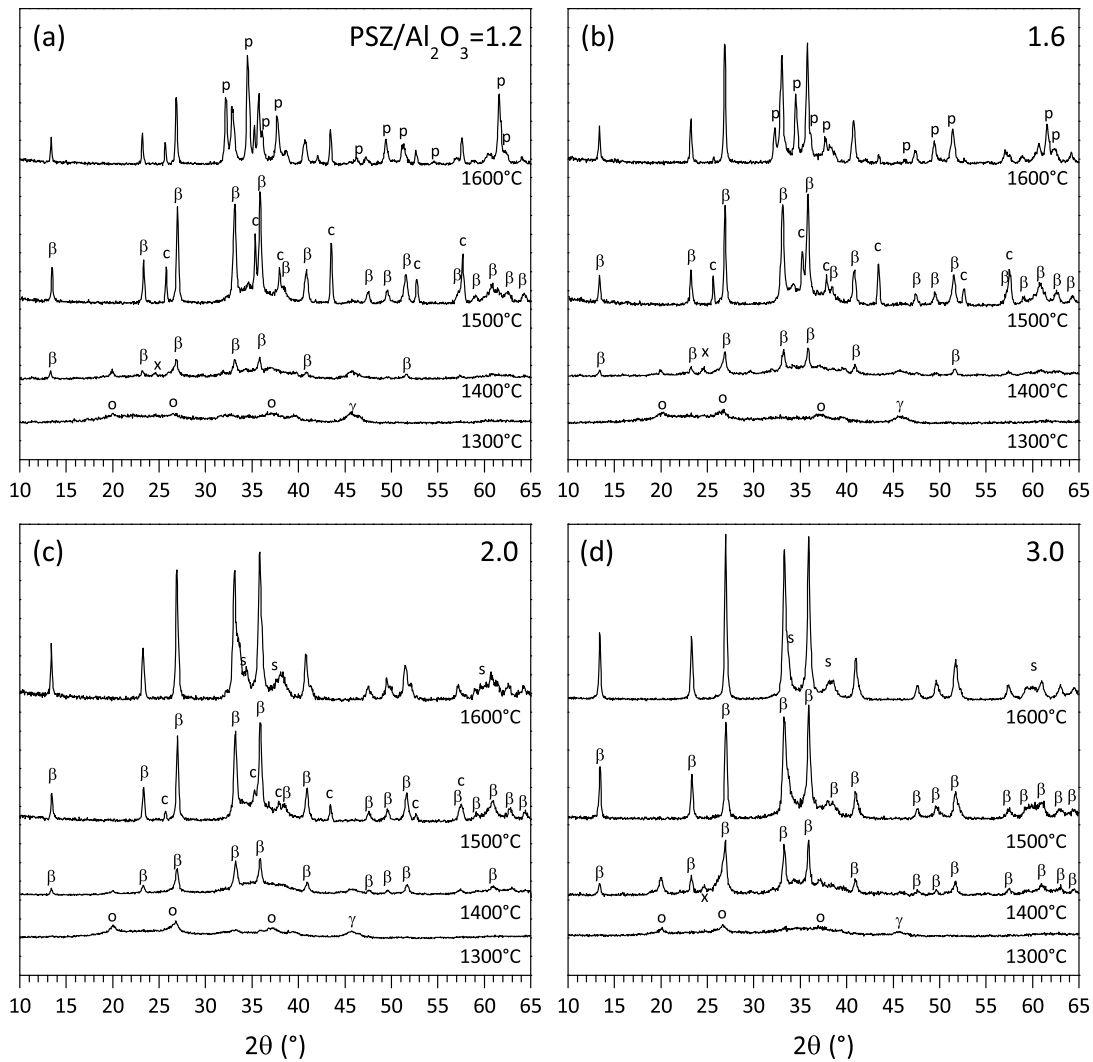


Figure 4.16: XRD results of PSZ/Al<sub>2</sub>O<sub>3</sub> mixtures as a function of PSZ/Al<sub>2</sub>O<sub>3</sub> weight ratio and treatment temperature.  $\beta$ = $\beta'$ -sialon,  $x$ =X-sialon,  $o$ =O'-sialon,  $\gamma$ = $\gamma$ -Al<sub>2</sub>O<sub>3</sub>,  $c$ =corundum,  $s$ =SiC,  $p$ =15R polytype

the first nucleation of  $\beta'$ -sialon phase was observed.  $\beta'$ -sialon nucleation can be associated to the exothermic peak at  $\sim 1430^\circ\text{C}$  in the DTA curve (Fig. 4.18). Since DTA/TG analysis was carried out on pre-cured powders, the typical cross-linking exothermic peak around  $300^\circ\text{C}$  is absent in Fig. 4.18. It should be pointed out that at  $1300^\circ\text{C}$  the silazane-derived ceramic residue, although still essentially amorphous (as demonstrated in Fig. 4.15), could have already undergone a partial phase-separation<sup>46</sup>, leading to coexisting amorphous silicon nitride-rich and silicon carbide-rich regions. For this reason, it is reasonable to assume that the very first reaction yielding the formation of the initial sialon phase (O'-sialon) more specifically involves Al<sub>2</sub>O<sub>3</sub> nanopowders and the silicon nitride-rich amorphous regions of the silazane ceramic residue.

The possible reaction mechanism thus entails: 1) a partial reaction of the SiCN matrix (or, more likely, of its silicon nitride-rich regions), at  $1300^\circ\text{C}$ , with some  $\gamma$ -Al<sub>2</sub>O<sub>3</sub> to give the formation of O'-phase crystallites, 2) the nucleation of  $\beta'$ -sialon nuclei at  $\sim 1400^\circ\text{C}$ , which quickly become the predominant crystalline phase, and at the same time the disappearance of the O'-phase (as frequently observed in literature<sup>31</sup>), and 3) the growth of  $\beta'$ -sialon nuclei with the progressive elimination of the residual  $\gamma$ -Al<sub>2</sub>O<sub>3</sub> via a reaction with the constituents (Si, C and N) of the SiCN matrix and the nitrogen firing gas.

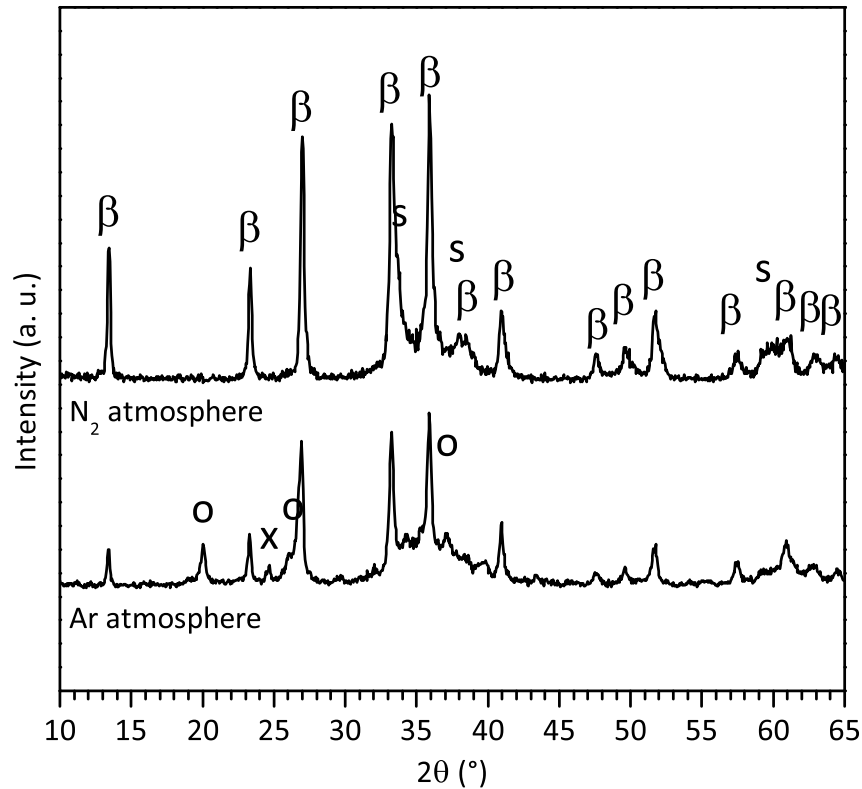


Figure 4.17: XRD results of PSZ/ $\text{Al}_2\text{O}_3=3.0$  composition, pyrolyzed at  $1500^\circ\text{C}$  for 1 h in  $\text{N}_2$  (top) and Ar (bottom) atmosphere.  $\beta=\beta'$ -sialon,  $x=X$ -sialon,  $o=O'$ -sialon,  $s=\text{SiC}$ .

W	Ceramic residue				Filler		Expected Sialon phase	By-products
	Si	C	N	O	Al	O		
1.2	1	0.66	0.6	0.03	1.0	1.5	$\text{SiAlON}_{1.67}$ [ $\text{Si}_3\text{Al}_3\text{O}_3\text{N}_5$ ( $z=3$ )]	0.53 CO + 0.13 C
1.6	1	0.66	0.6	0.03	0.8	1.2	$\text{SiAl}_{0.8}\text{O}_{0.8}\text{N}_{1.6}$ [ $\text{Si}_{3.33}\text{Al}_{2.67}\text{O}_{2.67}\text{N}_{5.33}$ ( $z=2.67$ )]	0.43 CO + 0.23 C
2	1	0.66	0.6	0.03	0.6	0.9	$\text{SiAl}_{0.6}\text{O}_{0.6}\text{N}_{1.53}$ [ $\text{Si}_{3.75}\text{Al}_{2.25}\text{O}_{2.25}\text{N}_{5.75}$ ( $z=2.25$ )]	0.33 CO + 0.33 C
3	1	0.66	0.6	0.03	0.4	0.6	$\text{SiAl}_{0.4}\text{O}_{0.4}\text{N}_{1.46}$ [ $\text{Si}_{4.29}\text{Al}_{1.71}\text{O}_{1.71}\text{N}_{6.29}$ ( $z=1.71$ )]	0.23 CO + 0.43 C

Table 4.5: Estimated atomic amounts corresponding to different polymer/filler ratios.

The formation of the  $O'$ -phase is interesting if we consider the probable proportion among elements in the ceramic residue of PSZ20<sup>46</sup>; in fact,  $O'$ -phase, deriving from the replacement of Si-N bonds with Al-O bonds in the structure of silicon oxynitride ( $\text{Si}_2\text{N}_2\text{O}$ ) features a relatively low N/Si ratio, as in the ceramic residue of PSZ20, and a relatively high oxygen content; the Al content, in addition, is much lower, compared to oxygen, than in the alumina filler (the general formula of  $O'$ -sialon is  $\text{Si}_{2-x}\text{Al}_x\text{O}_{1+x}\text{N}_{2-x}$ , with  $0 < x \leq 0.3$ ). This means that some oxygen contamination occurred during the overall processing, so that the preliminary estimations reported in Tab. 4.5 had to be revised.

Other observations contrasting with the preliminary estimations concern the presence of residual  $\text{Al}_2\text{O}_3$  content for low W values (see Fig. 4.16a-b at  $1500^\circ\text{C}$ ), undergoing transformation from the transitional  $\gamma$  form to the  $\alpha$  form, more stable at high temperatures, and some changes in the z value of developed  $\beta'$ -sialon with increasing temperature. The corundum contamination is likely associated to incomplete incorporation of Al and O, at the temperature of  $1500^\circ\text{C}$  when  $\beta'$ -sialon formed with the expected z value equal to 3 (the most probable phase, according to the semi-automatic phase identification provided by the Match! program package is  $\text{Si}_3\text{Al}_3\text{O}_3\text{N}_5$ , PDF#079-0483), as shown by the high magnification detail of XRD pattern of Fig. 4.19 (left). At  $1600^\circ\text{C}$  corundum decreased, due to progressive interaction at

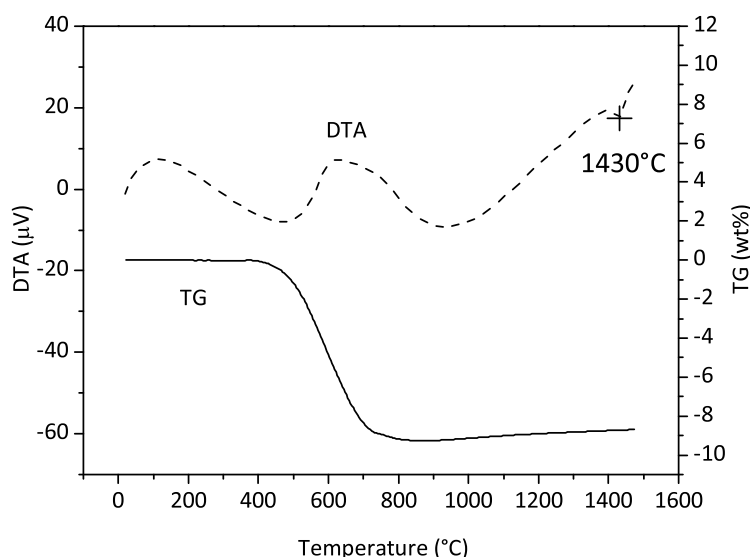


Figure 4.18: DTA/TG analysis of PSZ/Al<sub>2</sub>O<sub>3</sub>=3.0 mixture up to 1500°C. Exothermic peak at 1430°C is related to the formation of β'-sialon.

the interface of Al<sub>2</sub>O<sub>3</sub> residues with the amorphous phase still present (see the broad hump in the 32-39° range), but the XRD peaks associated to the β'-sialon phase appear to have split into two separate peaks. This indicates that besides the expected β'-sialon phase with  $z=3$ , also another β'-sialon phase, with  $z=4$ , is present. Additionally, peaks associated to the 15R sialon polytype (SiAl<sub>4</sub>O<sub>2</sub>N<sub>4</sub>, PDF#042-0160) are visible. In our opinion, such phenomenology is consistent with the formation of volatile SiO together with CO, determining a Si deficiency in the amorphous intergranular phase. The 15R phase has already been reported to form from a Si-depleted (C-rich) amorphous matrix provided by a polycarbosilane, aimed at yielding SiC matrix composites with Al<sub>2</sub>O<sub>3</sub> as secondary phase<sup>49</sup>.

The overall reaction system is very complex and at this stage of the investigations cannot yet be discussed in full detail. In any case, the low temperature oxygen contamination and the Si depletion are key points. Fig. 4.16c and d show that with higher W the phase purity had a significant improvement. Oxygen contaminations were likely compensated by the increased "excess carbon" available according to Tab. 4.5. However, the final phase balance does not simply comprise a single phase β'-sialon: as illustrated by Fig. 4.19 (right), for W=2, the splitting of β'-sialon is still present at 1600°C. More precisely β'-sialon with  $z=2$ , close to the expected value (Si<sub>4</sub>Al<sub>2</sub>O<sub>2</sub>N<sub>6</sub>, PDF#076-0599), alone at 1500°C, at 1600°C is accompanied by a β'-sialon with  $z$  even below 1 (the observed peaks are just at the middle between those of Si<sub>5</sub>AlON<sub>7</sub>,  $z=1$ , PDF# 077-0755, and β-Si<sub>3</sub>N<sub>4</sub>, PDF#083-0701). A likely origin of this splitting is an interfacial reaction among the C-containing amorphous phase and the firstly developed β'-sialon grains (SiAlON<sub>(high-z)</sub>+N<sub>2</sub> (atmosphere)+Si-N-C (matrix)→ SiAlON<sub>(low-z)</sub>+CO(↑)).

The presence of C in the ceramic residue up to high temperatures is testified by the detection of SiC crystallites (PDF#029-1126) in Fig. 4.16d (1600°C) (the phase is supposed to be nano-sized due to the remarkable width of its main peaks), attributable to the crystallization of the remaining amorphous phase. Moreover, residual "free" carbon was also detected by micro-Raman analysis (Fig. 4.21a). The broad peak centered at 1330 cm<sup>-1</sup> can be attributed to the carbon D band. D band originates from the breathing mode of aromatic rings of aromatic rings of a disordered graphite structure<sup>50</sup>. Peak centered at 1600 cm<sup>-1</sup> is generated by the convolution of both graphitic G band (centered at 1580 cm<sup>-1</sup>, often observed in ceramic

residues from preceramic polymers) and D' band ( $1620\text{ cm}^{-1}$ )<sup>51</sup>. A second-order D peak (2D) could also be observed around  $2660\text{ cm}^{-1}$ . Despite their low intensity, other minor peaks located in the  $700\text{-}1000\text{ cm}^{-1}$  region should be attributed to both Si-C ( $\sim 780$  and  $\sim 960\text{ cm}^{-1}$ , labeled with "s") and Si-N bonds<sup>52</sup> present in the material.

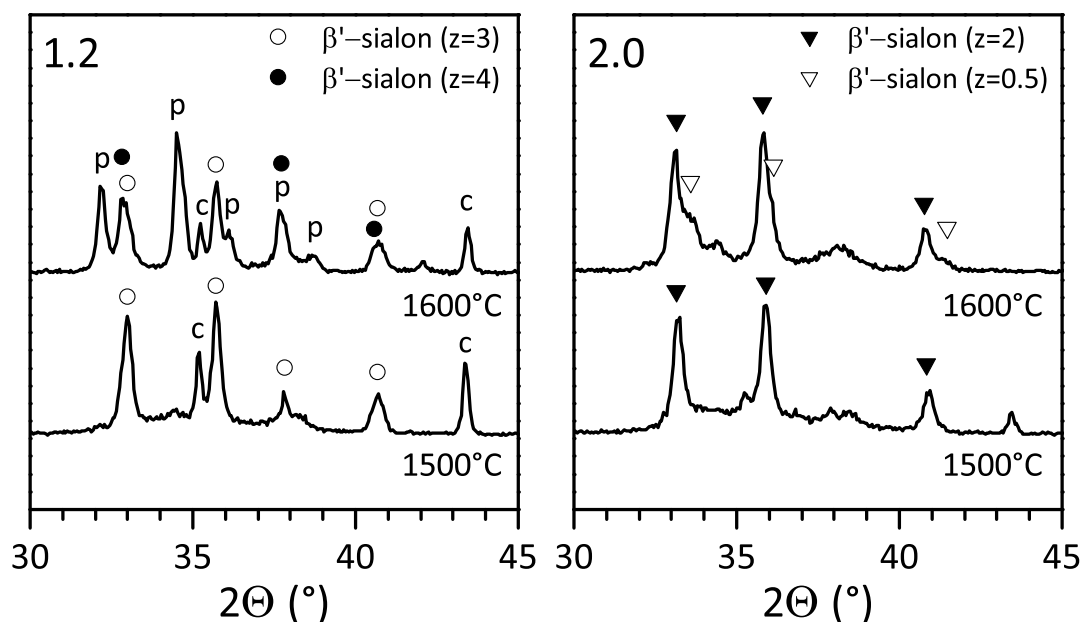


Figure 4.19: Details of selected XRD patterns. c=corundum, p=15R polytype.

In summary, when using a carbon-containing silazane (PSZ20) and nano-sized alumina, it was not possible to obtain phase pure  $\beta'$ -sialon ceramics. Best results were obtained with samples with  $W \geq 2$ , which possessed the least amount of secondary phases, i.e. very fine SiC crystallites.

In order to improve the purity of the phase, a different (non carbon-containing) silazane was used. The addition of PHPS to the dispersion was found to be a very effective way to lower the residual secondary phases in the final materials, and to obtain phase-pure sialon ceramics, as illustrated by the XRD patterns in Fig. 4.20.

When part of the PSZ was substituted with PHPS, the best results were obtained with the 75:25 PHPS:PSZ formulation, for which a virtually complete elimination of SiC crystallites was achieved for a heat treatment at  $1500^\circ\text{C}$  (1 h). A significant lowering of the residual carbon content for the 75:25 formulation was also confirmed by micro-Raman analysis (Fig. 4.21b): all the bands associated to "free" carbon (D, G, D' and 2D, that were clearly visible for 0:100 specimen) are virtually absent for this sample. Some low-intensity peaks are still present in the  $700\text{-}1000\text{ cm}^{-1}$  region, indicating the presence of traces of SiC in the final material. However, silicon carbide quantity should be extremely low, since no peaks attributable to this phase were found in the relative diffraction pattern. The 50:50 sample still showed the presence of an amorphous phase, whilst in the 100:0 sample the amorphous phase disappeared, but secondary oxygen-rich phases were present (O' and X-sialon). This confirms the hypothesis that some of the carbon deriving from the PSZ is necessary for the removal of the excess oxygen deriving both from the alumina and from the moisture contamination of the silazanes. No splitting of characteristic  $\beta'$ -sialon peaks was observed for these samples.

The 75:25 formulation (the one leading to the most phase pure and well crystallized  $\beta'$ -sialon at  $1500^\circ\text{C}$ ) was then tested back at lower temperatures. As it can be observed in Fig.

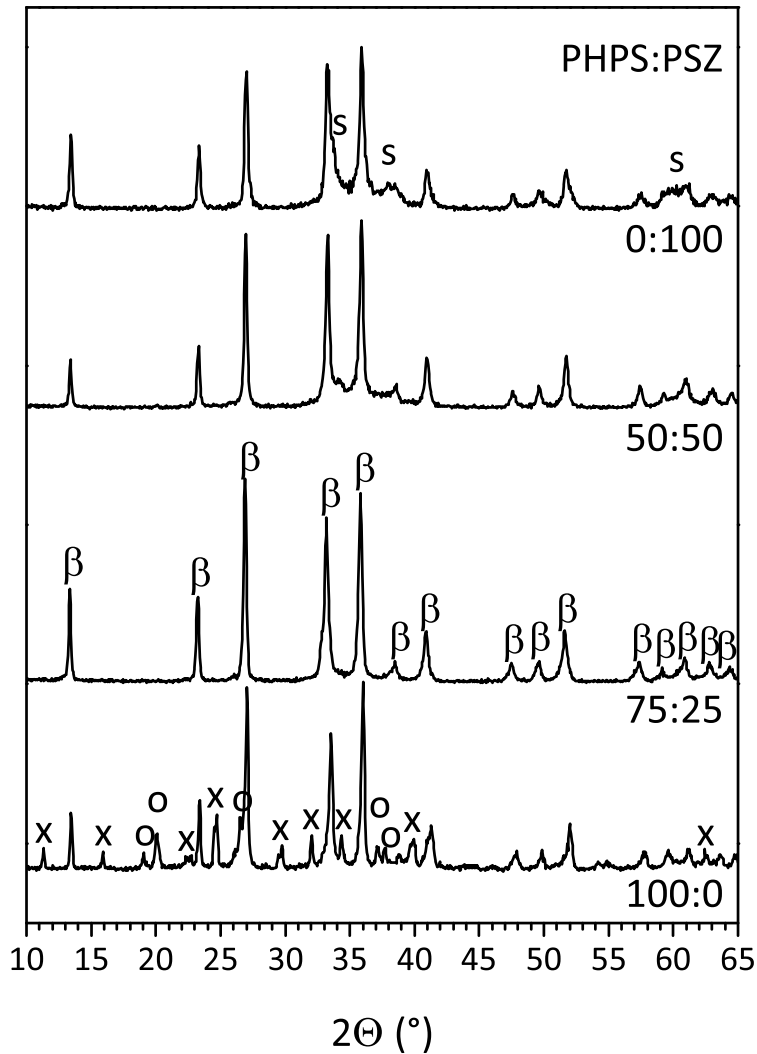


Figure 4.20: XRD results as a function of PHPS:PSZ weight ratio (polysilazanes/ $\text{Al}_2\text{O}_3$  weight ratio equal to 3.0). All samples were heat treated at  $1500^\circ\text{C}$  for 60 min in  $\text{N}_2$ .  $\beta = \beta'$ -sialon,  $x = \text{X}$ -sialon,  $o = \text{O}'$ -sialon

4.22,  $\beta'$ -sialon peaks were already present after a heat treatment at  $1300^\circ\text{C}$ , together with  $\text{O}'$ -sialon (which is again readily converted to the  $\beta'$ -phase at higher temperatures), some unreacted  $\gamma\text{-Al}_2\text{O}_3$  and some metallic silicon. Small quantities of X-sialon are also detected at  $1400^\circ\text{C}$ , but they finally completely converted into the  $\beta'$ -phase at  $1500^\circ\text{C}$ . The decrease in the temperature necessary for the formation of  $\beta'$ -sialon was probably due to the presence of free silicon, which in pure PHPS was found to promote the precipitation of crystalline  $\text{Si}_3\text{N}_4$  from amorphous silicon nitride at relatively low temperatures<sup>53</sup>.

The final ceramic consisted in pure  $\beta'$ -sialon with nano-sized grains with a dimension of approximately 100-200 nm, as shown by SEM investigations on the produced powders (see Fig. 4.23a); for comparison purposes, Fig. 4.23b illustrates the situation when only PSZ20 was used together with  $\gamma\text{-Al}_2\text{O}_3$ , leading to much coarser crystals.

A final remark concerns the possible applications of the proposed approach, that will be the object of future investigations. Highly pure nano-grained  $\beta'$ -sialon powders are undoubtedly attractive for secondary densification treatments, consisting of conventional hot-pressing or SPS. In addition to the production of pure  $\beta'$ -sialon ceramics, we expect that the addition of the preceramic mixture to  $\text{SiC}$  or  $\text{Si}_3\text{N}_4$  powders would lead to  $\text{SiC}$  or  $\text{Si}_3\text{N}_4$  grains sur-

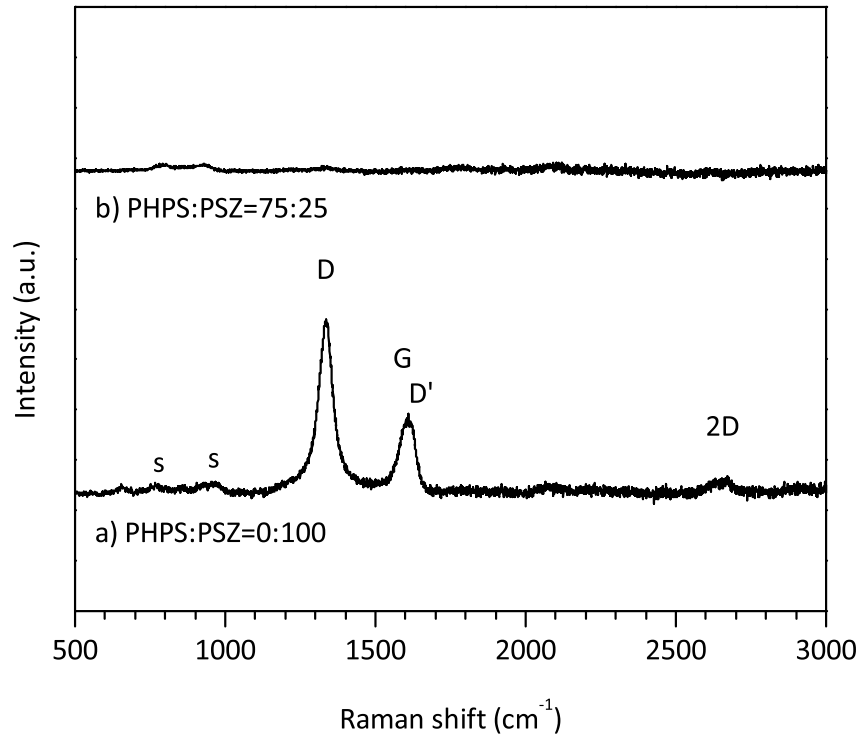


Figure 4.21: Results of micro-Raman analysis for samples with PHPS:PSZ=75:25 and PHPS:PSZ=0:100 weight ratios (polysilazanes/ $\text{Al}_2\text{O}_3$  weight ratio equal to 3.0), after heat treatment for 1 h at 1500°C in  $\text{N}_2$ .

rounded by a highly crystalline and consequently creep resistant sialon phase, in analogy with recent experiments about a polymer-derived intergranular phase with a SiAlOC composition<sup>50</sup>. It should be noted that, in the case of these “sialon-bonded” ceramics, the use of hot-pressing would not be necessary if, for instance, porous components are fabricated, to be used for applications requiring high temperature filters. Finally, pure sialon powders doped with rare earth cations are very attractive as luminescent materials for LED devices<sup>5</sup>, and are currently under investigation.

### 4.3.3 Conclusions

In the present work, a new method for the realization of nano-grained  $\beta'$ -sialon ceramics was presented, based on a simple mixing/dispersion procedure using commercial polysilazane(s) and  $\text{Al}_2\text{O}_3$  nanopowders, followed by a single pyrolysis step in nitrogen atmosphere at relatively low temperatures. The influence of the starting formulation and the heat treatment on the final phase assemblage was investigated, and high purity nano-grained  $\beta'$ -sialon ceramics were obtained from a mixture of appropriate composition of polysilazanes and  $\text{Al}_2\text{O}_3$  nanopowders. A strong influence of the composition of the silazanes on the phase purity of the resulting ceramic was observed, and all secondary phases were eliminated when employing a mixture of two silazanes, one of which did not contain any carbon.

Sub-micrometric sialon grains were generally produced. The highly reactive nature of the ceramic residue generated by the polymeric component allowed also for lower processing temperatures than those generally adopted with powder processing, and in some samples  $\beta'$ -sialon grains already formed after a heat treatment at 1300°C (1 h).

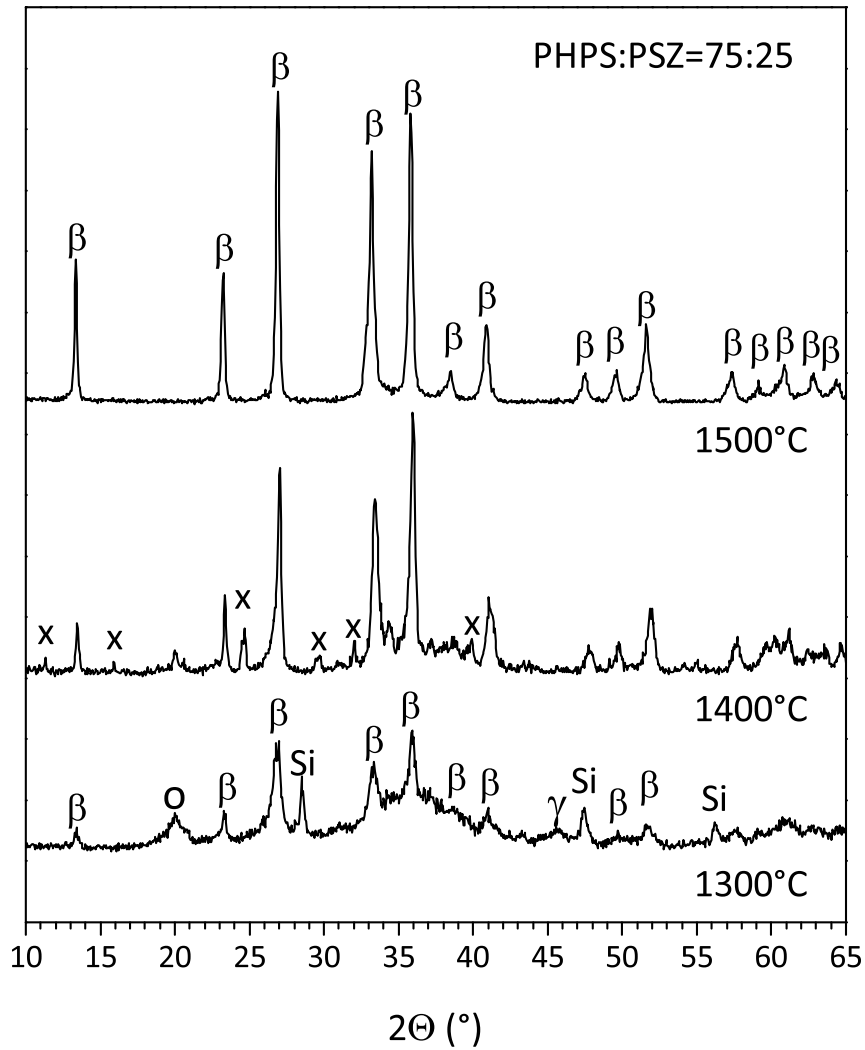


Figure 4.22: XRD results as a function of temperature (1 h soak,  $N_2$  atmosphere) for sample with PHPS:PSZ=75:25 weight ratio (polysilazanes/ $Al_2O_3$  weight ratio equal to 3.0).  $\beta$ = $\beta'$ -sialon, x=X-sialon, o=O'-sialon,  $\gamma$ = $\gamma$ - $Al_2O_3$ , Si=silicon.

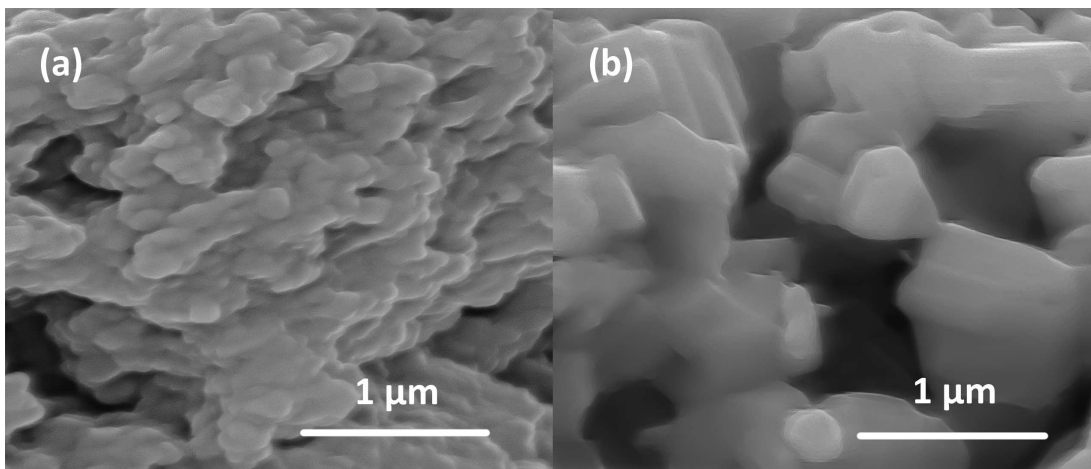


Figure 4.23: FE-SEM image of samples with PSZ/ $Al_2O_3$ =3.0, after heat treatment at 1500°C for 60 min in  $N_2$ . a) PHPS:PSZ=75:25, b) PHPS:PSZ=0:100.

## 4.4 Applications

### 4.4.1 Si<sub>3</sub>N<sub>4</sub> composites using polymer-derived sialon as sintering aid

#### Introduction

The Polymer Derived Ceramics technique have been extensively studied during the last decades, and many improvements have been done regarding the study of their chemistry, their properties and the mechanism of the polymer-to-ceramic conversion that takes place during their pyrolysis. Although many efforts have been put to improve their properties and to increase the ceramic yield of this class of precursors, ceramics from preceramic polymers still suffer from the shrinkage that generates during the pyrolysis step and during the devit-rification mechanism that takes place at high temperature, which in practice strongly limits their applicability to ceramic components of just few hundreds of micrometers (e.g. fibers, coatings, microcomponents). The scaling up of the dimensions of components produced from pure preceramic polymers is practically impossible, and this is the reason why a lot of re-search has been done during the last years on the possibility of introducing passive and/or active fillers to reduce and/or compensate this shrinkage, for the realization of big dense ceramic components.

A special case of the association of preceramic polymers with fillers is represented by the use of relatively limited quantity of preceramic polymers as intergranular binding phase for inorganic powders, such as SiC and Si<sub>3</sub>N<sub>4</sub>. SiC and Si<sub>3</sub>N<sub>4</sub> show outstanding thermal and mechanical properties, thanks to the strongly covalent nature of the Si–C and Si–N bonds, respectively. The main drawback of carbides and nitrides is their extremely poor sinterabil-ity, and expensive densification techniques like Hot-Pressing (HP) or Spark Plasma Sintering (SPS) are required to obtain dense and mechanically reliable components. In some cases, the introduction of sintering aids (e.g. Re<sub>2</sub>O<sub>3</sub>, Al<sub>2</sub>O<sub>3</sub>, MgO) was proven to be effective in enhanc-ing the densification reactions through the formation of intergranular liquid phase during the final sintering. As a direct consequence, the use of sintering aids strongly deteriorates high temperature creep resistance<sup>1</sup>.

The unique amorphous nature of PDCs, which in general is constituted by a mixture of Si–O, Si–C, Si–N covalent bonds (depending on the nature of the precursor used), make preceramic polymers potential candidates for the realization of a continuous amorphous in-tergranular phase for SiC and Si<sub>3</sub>N<sub>4</sub> powders, which on one hand could promote the densi-fication of the material during sintering through viscous flow, and on the other hand could offer a better creep resistance at high temperature thanks to the presence of strong covalent bonds inside their amorphous structure<sup>24,54</sup>.

With the present work, an attempt to further improve the high temperature characteristics of the intergranular phase was made, starting from preceramic polymer+nano-sized fillers mixtures studied in Sections 4.2 and 4.3. Ideally, the use of this type of precursors (that gener-ate a highly crystalline, sialon-based structure) could potentially show advantages in terms of both densification at relatively low temperatures (when a fraction of amorphous phase is still present) and improved creep resistance at high temperature, thanks to the nucleation of crystalline phases in the last moments of the sintering process.

In the next paragraphs, first results on the use of preceramic polymer/fillers mixtures as intergranular/sintering phase are reported. These results were made in collaboration with Prof. Z. Lences and his collaborators of the Institute of Inorganic Chemistry of the University of Bratislava, Slovakia.

### Si<sub>3</sub>N<sub>4</sub> composites preparation

A commercial Si<sub>3</sub>N<sub>4</sub> powder (SN-E10, Ube Industries, Japan, mostly  $\alpha$ -phase) was selected for the realization of the mixtures. As a sintering aid, 2 different preceramic-polymer-based mixtures were selected. First formulation (referred as "Powder A") consisted of a polysiloxane-based mixtures (very similar to formulation "z3yc10" developed in Section 4.2.2), while parallel experiments were conducted using a polysilazane-based mixture (referred as "Powder B"), deriving from studies reported in Section 4.3.2. The 2 different binding phase formulations are reported in Tab. 4.6 (polysiloxane-based) and Tab. 4.7 (polysilazane-based). After mixing and curing in N<sub>2</sub> at 300°C for 1 h, Powder B was immediately pre-pyrolized at 600°C for 30 min in N<sub>2</sub>, because of the high moisture sensitivity of the polysilazane.

Table 4.6: Powder A: polysiloxane-based formulation used as a sintering aid for Si<sub>3</sub>N<sub>4</sub> powders.

Component	wt%
H44	35.7
Al <sub>2</sub> O <sub>3</sub>	37.1
Si <sub>3</sub> N <sub>4</sub>	21.6
Carbon	1.1
Y <sub>2</sub> O <sub>3</sub>	4.4

Table 4.7: Powder B: polysilazane-based formulation used as a sintering aid for Si<sub>3</sub>N<sub>4</sub> powders.

Component	wt%
HTT 1800	67
Al <sub>2</sub> O <sub>3</sub>	33

Prior to the mixing phase with Si<sub>3</sub>N<sub>4</sub> powders, powder A and powder B were put inside an agate container and pulverized in a planetary mill for 30 min. 18 wt% of precursor was added to  $\alpha$ -Si<sub>3</sub>N<sub>4</sub> powders. Due to the limited amount of precursors, the powders were homogenized in an agate mortar, in dry state. The only exceptions are represented by samples SN18A-3M and SN18B-7M: in this case, powders were ball-milled in a planetary mill (Si<sub>3</sub>N<sub>4</sub> pot) with Si<sub>3</sub>N<sub>4</sub> balls for 60 min in hexane (milling conditions: 230 rpm; 3 min milling + 6 min stop, for a total time of milling of 60 min). Suspension was then dried in a rotary evaporator (40°C, 205 mbar) and powder was further dried in a vacuum drier (80°C, 200 mbar) for 12 h. Soft agglomerates were finally crushed in agate mortar prior to the compaction step. From the powders realized, circular pellets with a diameter of 12 mm were produced by uniaxial pressing, with a pressure of 100 MPa.

Densification experiments were then carried out in a graphite resistance furnace with a load of 30 MPa. The load was applied at 1120°C during heating and released at 1300°C during cooling. Nitrogen gas inlet started at 300°C. Gas pressure in the furnace was adjusted to 1.05 bar during the whole experiment (small overpressure).

In Tab. 4.8 is reported a list of all the samples produced for the densification tests. "SN18X" was used as a generic label, where "X" the type of the sintering aid (e.g. SN-18A represents a composite with 72 wt% of Si<sub>3</sub>N<sub>4</sub> powders and 18 wt% of powder A). Intermediate dwells at 1300 and 1420°C were selected, based on the shrinkage curves of powders A and B. The only exception is represented by SN18B-6, for which no intermediate dwells were adopted. Temperature increasing rate was varied as follows: 30°/min until 700°C 20°/min until 1300°C 15°/min until 1420°C and 10°/min until the final densification temperature. Cooling was then carried out at 15°/min until 1000°C and at 20°/min down to room temperature.

Table 4.8: Treatment conditions for  $\text{Si}_3\text{N}_4$  powders densified with powder A or powder B (samples "SN18X, with X=type of the sintering aid) and for powder A (SNPA) and powder B (SNPB).  $T_E$  and  $T_P$  represents the temperature on Eurotherm controller and on pyrometer Ircon (starts at 1100°C), respectively;  $\Delta m$  represents the weight loss during the hot-press step;  $\rho$  the density of the samples after hot-pressing.

Sample	$T_E$ (°C)	$T_P$ (°C)	dwel (min)	$\Delta m$ (%)	$\rho$ (g/cm <sup>3</sup> )
SN-18A-1	1300/1420/1500	1420/1520/1600	30/30/15	-6.01	3.12
SN-18A-2	1300/1420/1600	1420/1520/1755	30/30/2	-6.35	3.11
SN-18A-3M	1300/1420/1500	1420/1520/1600	30/30/15	-6.14	3.12
SN-18B-1	1300/1420/1500	1420/1520/1600	30/30/15	-3.76	2.33
SN-18B-2	1300/1420/1500	1420/1520/1600	30/30/60	-3.69	2.49
SN-18B-3	1300/1420/1550	1420/1520/1650	30/30/30	-4.04	2.71
SN-18B-4	1300/1420/1600	1420/1520/1700	30/30/30	-4.18	2.87
SN-18B-5	1300/1420/1650	1420/1520/1750	30/30/30	-5.54	2.85
SN-18B-6	1600	1700	30	-3.90	2.97
SN-18B-7M	1300/1420/1600	1420/1520/1700	30/30/30	-5.04	3.09
SNPA	1300/1420/1500	1420/1520/1600	30/30/15	-25.19	2.43
SNPB	1300/1420/1500	1420/1520/1600	30/30/15	-13.68	2.48

## Results

In Fig. 4.24 the XRD pattern of the silicon nitride powders to be densified is reported. As could be observed,  $\text{Si}_3\text{N}_4$  is present mostly in the  $\alpha$ -form (approximately 95%), probably connected to the synthesis method adopted.

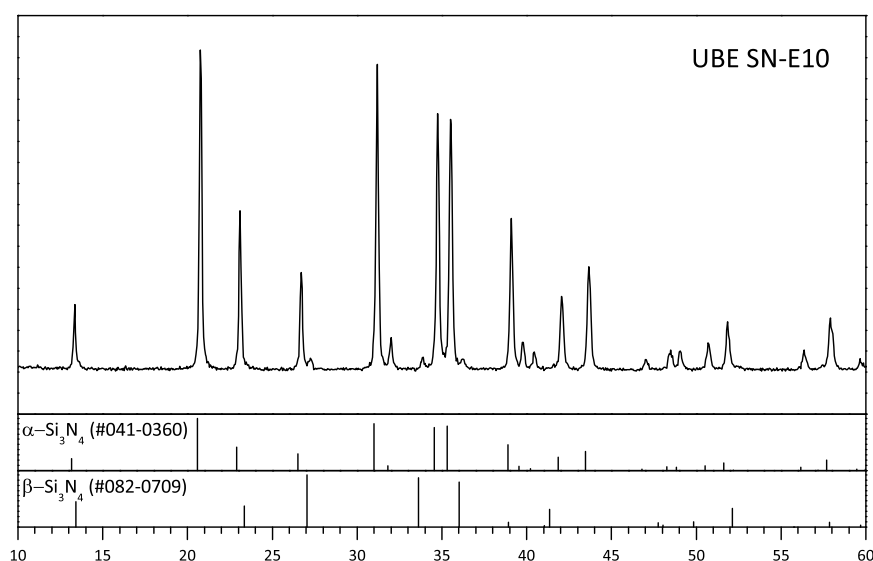


Figure 4.24: XRD pattern of  $\text{Si}_3\text{N}_4$  nanopowders SN-E10 (UBE Industries).

A previously discussed in Sections 4.2 and 4.3, the pyrolysis in nitrogen atmosphere of precursor powder A and powder B produced a material constituted by  $\beta'$ -sialon and  $\text{Al}_2\text{O}_3$  (powder A) and  $\beta'$ -sialon and some amorphous SiC (powder B). Analogous densification experiments were carried out by hot-pressing with the precursor powders alone, in order to evaluate the possibility for variations of the final composition. XRD patterns of HPed (Hot-Pressed) powder A (SNPA) and powder B (SNPB) are reported in Fig. 4.25 (for treatment conditions, see Tab. 4.8).

As could be observed, a totally different phase assemblage from what obtained in Sections

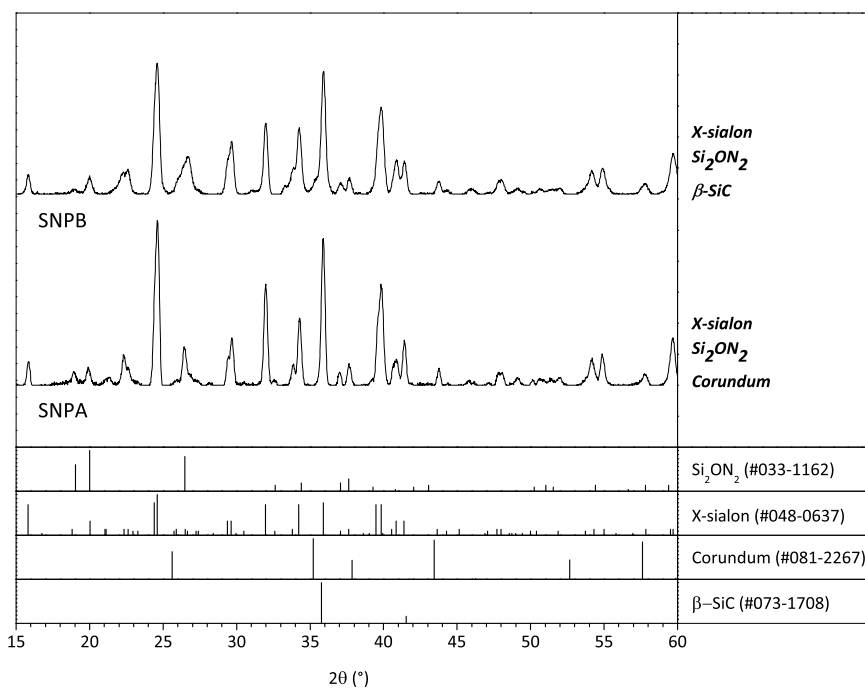


Figure 4.25: XRD pattern of SNPA and SNPB after hot-pressing at 1600°C for 15 min in N<sub>2</sub> atmosphere.

4.2 and 4.3 is present: both the ceramics are constituted by a mixture of X-sialon and Si<sub>2</sub>ON<sub>2</sub>, plus some residual corundum (in the case of powder A) and some SiC (in the case of powder B), while β'-sialon is totally absent in both the samples. The presence of these 2 oxygen rich phases could be justified by the different treatment conditions adopted. In the case of an hot-pressing treatment, powders are introduced inside a graphite dye and closely packed. Although hot-pressing treatments were carried out in nitrogen atmosphere, it appears that the powders in the graphite dye are "sealed" and isolated from the treatment atmosphere, which strongly hinders the nitrogen intake process for both the materials, that upon heat treatment show a much lower quantity of nitrogen-rich phases like β'-sialon. The presence of low quantities of residual corundum in SNPA are in accordance with previous results, and also the presence of small quantities of SiC in SNPB sample again confirms the observation (previously made in Section 4.3) regarding the possibility of having some residual SiC (in an amorphous or crystalline form, depending on the sintering temperature) deriving from the pyrolysis of the polysilazane matrix.

As could be noted in Fig. 4.26 (XRD pattern of SN18A series) and in Fig. 4.27 (XRD pattern of SN18B series), this different phase assemblage eventually have some influence on the phase assemblage of the final composites. In fact, in both the series of samples produced, O'-sialon and X-sialon have been identified. A certain influence of the oxygen contamination of the Si<sub>3</sub>N<sub>4</sub> powders (present in the Si<sub>3</sub>N<sub>4</sub> surface as SiO<sub>2</sub>) should be taken into account, and could give an additional contribution to the formation of these two oxygen-rich phases.

Densification test results are reported in Fig. 4.28, where bulk density values are reported for each sample.

As a starting point, the same heat treatment was carried out at the maximum temperature of 1600°C. 2 different densification behaviors were observed, connected to the different type of precursor used as a sintering aid. When polysiloxane-based precursor was used, a very fast and effective densification was readily achieved after the first treatment (SN18A-1), and at the final sintering temperature no further shrinkage was observed, due to a basically complete

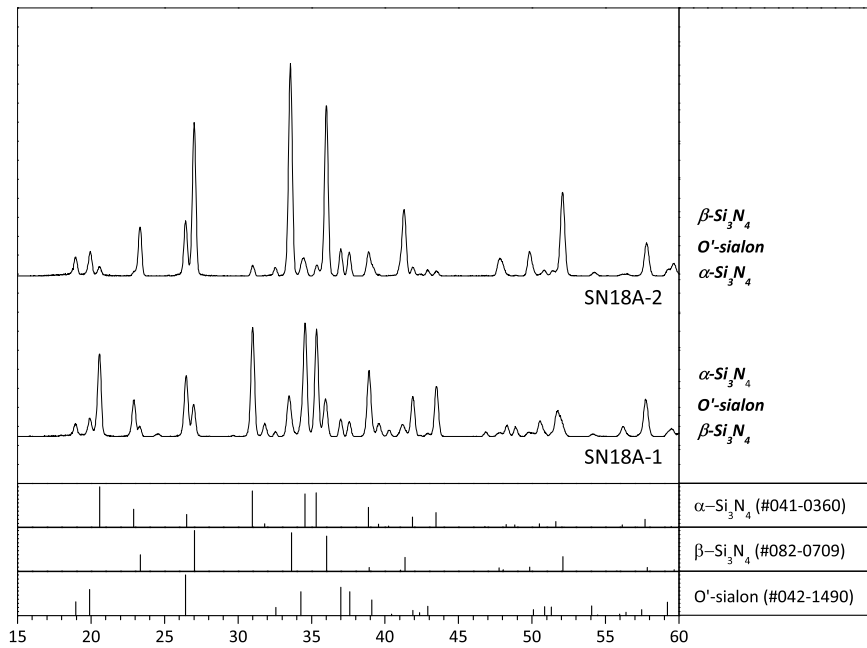


Figure 4.26: XRD pattern of SN18A series. \*(Note: SN18A-3 pattern not available.)

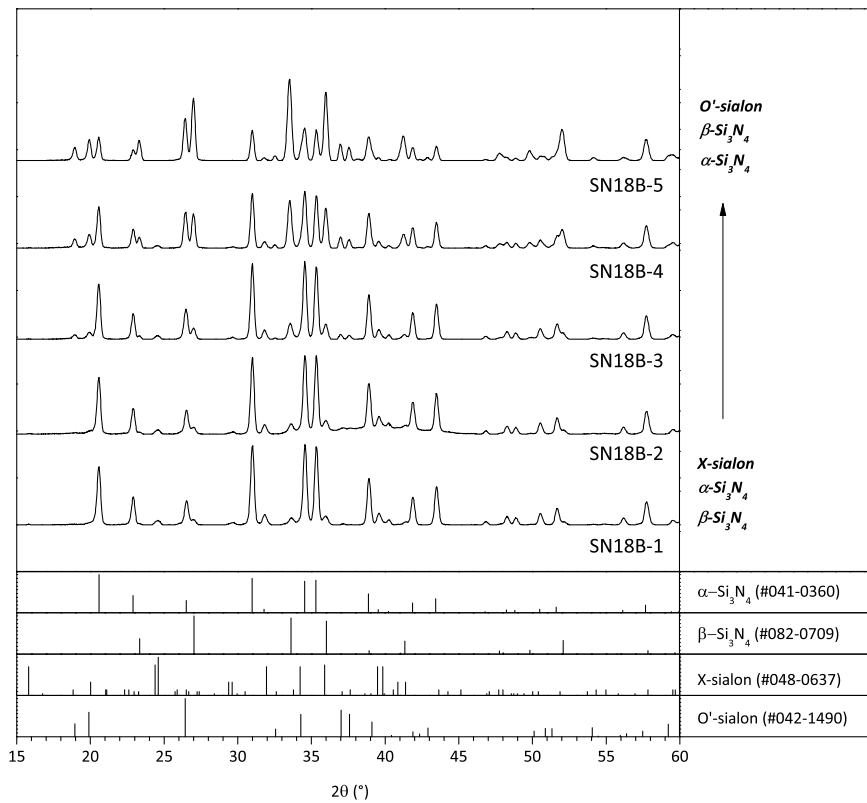


Figure 4.27: XRD pattern of SN18B series. \*(Note: SN18B-6 and SN18B-7 patterns not available.)

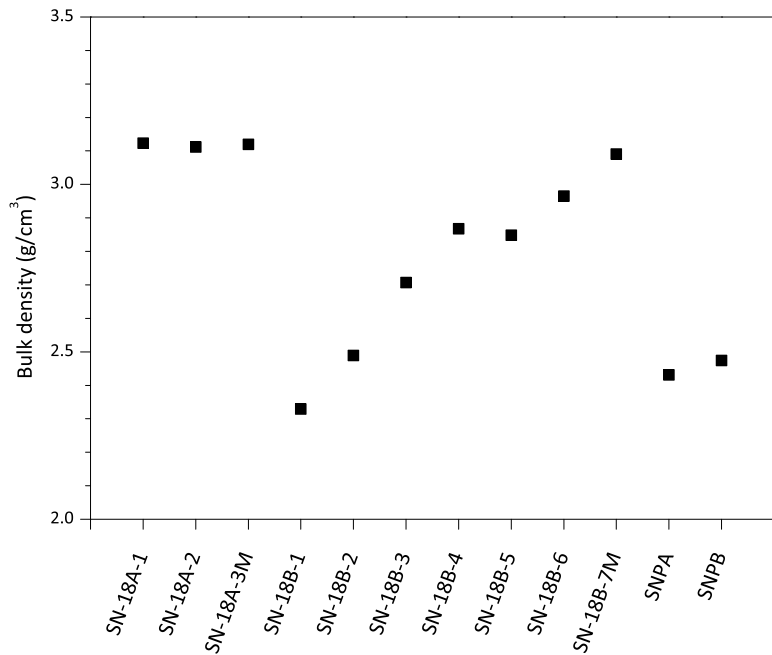


Figure 4.28: Bulk density values for series SN18A, SN18B, and for sintered powders SNPA and SNAPB.

densification process (final density 3.123 g/cm<sup>3</sup>). On the contrary, a much lower density was measured for sample SN18B-1 (2.329 g/cm<sup>3</sup>), which could indicate both an incomplete densification process and/or the presence of higher quantities of residual amorphous phase in the final ceramics. A possible explanation for this slower densification is probably connected with the different nature of the ceramic residue that could be obtained from the 2 different preceramic polymers: in fact, while the higher oxygen content of the polysiloxane-derived ceramic could generate a lower viscosity and likely a higher reactivity towards other phases present (to readily give the formation of crystalline phases), the stronger covalent bonding inside the polysilazane-derived matrix – generated by the massive presence of strongly covalent Si–N and Si–C bonds – could have the opposite effect, producing a higher viscosity network and retaining its amorphous nature (at least of part of it) up to high temperature, testified by the presence of quasi-amorphous SiC, as described in Section 4.3 and also detected in sample SNAPB.

As a consequence of these results, one more sample was produced with powder A (SN18A-2), which was sintered at a higher temperature (1750°C) in order to achieve a complete crystallization (especially of the intergranular phase) and to observe the high-temperature behavior of the final composites. No significant changes of the final density were observed, which probably implies that a basically complete system evolution was already achieved at 1600°C. The only significant change regards the phase assemblage: as expected, a higher  $\beta$ -Si<sub>3</sub>N<sub>4</sub>/ $\alpha$ -Si<sub>3</sub>N<sub>4</sub> ratio was observed, due to the progressive transformation of the  $\alpha$ -form (equiaxed and more stable at low temperatures) into the  $\beta$ -form (elongated and more stable at high temperatures), which in principle entails a higher toughness and a lower hardness. Both these hypotheses find confirmation in Fig. 4.29 and in Fig. 4.30, where toughness and hardness values are reported. Indentation toughness increases from 5.1 to 5.5 MPa·m<sup>0.5</sup>, while hardness values decreases from 18.7 to 17.1 GPa.

Finally, SN18A-B3M (produced by ball milling of the starting powders) showed a more

homogeneous microstructure if compared to B-1 and B-2 samples. Its properties are basically identical to B-1 sample, since the maximum sintering temperature adopted was 1600°C in both cases.

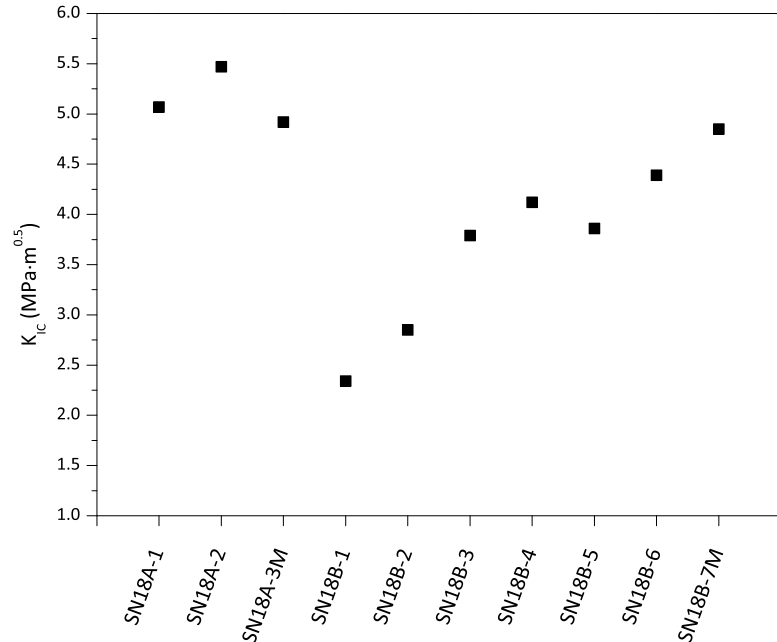


Figure 4.29: Fracture toughness values for series SN18A and SN18B (indentation toughness values based on Shetty's relationship).

Further densification experiments were done on SN18B samples, changing the experimental conditions as reported in Tab. 4.8. Both an increase in the dwell time at the final temperature of 1600°C (30 to 60 min), as well as an increase in the final sintering temperature led to a drastic increase of the density of the samples, which changed from 2.32 to 2.85 g/cm<sup>3</sup>.

A further densification for sample SN18B6 was observed (2.97 g/cm<sup>3</sup>) by changing the heating rate: all the intermediate dwells were removed and powders were directly brought to the final sintering temperature at a relatively high speed (20°/min). Probably, removing the intermediate steps and thus going faster through the "crystallization path" could reduce the gradual increase of viscosity of the system and the reduction of the liquid phase present.

Finally, best results (3.09 g/cm<sup>3</sup>) were obtained with sample SN18B-7M, which is analogous to sample SN18B4, but in this case powders were ball-milled in planetary mill. Apparently, the higher system homogeneity and intimate mixing that could be achieved by this procedure is fundamental for the obtainment of a more effective densification of the sample, which reached almost the same density value of samples obtained by using powder A as sintering aid.

For SN18B series, the increase of density of the samples is quite accordingly followed by an increase of hardness and toughness. Passing from B1 to B7M sample, hardness changes from 5 to 16 GPa, thanks probably to an increased crystallization of the system with a lower quantity of residual amorphous phase.

Toughness increases instead from 2.2 to 4.4 MPa·m<sup>0.5</sup>, probably because, again, of an increased crystallization of the intergranular phase, which should in principle have beneficial effects on the global toughness, as well as on creep resistance at high temperature.

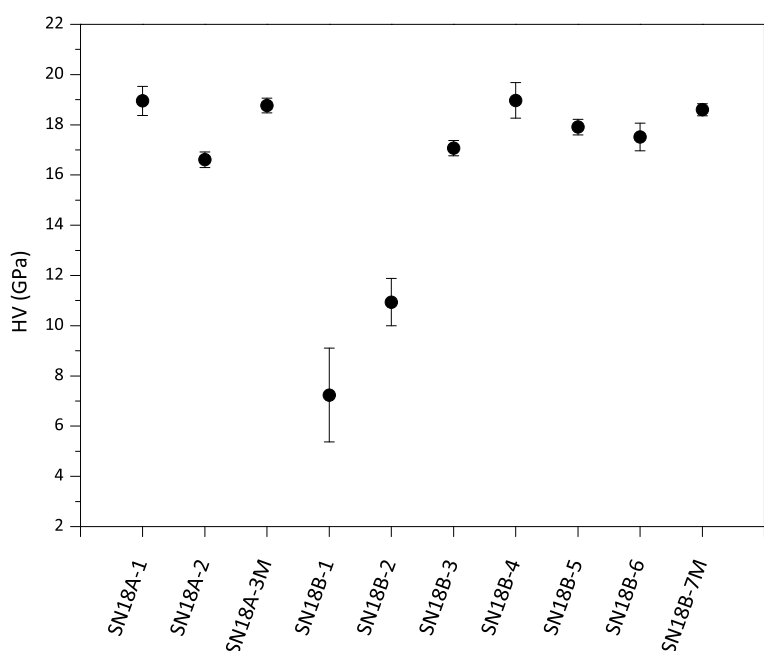


Figure 4.30: Vickers hardness values for series SN18A and SN18B.

## Conclusions

The use of preceramic polymers filled with nanopowders as sialon precursors showed extremely promising results as a potential candidate as  $\text{Si}_3\text{N}_4$  sintering aid. Advantageous aspects of materials synthesized should be found in the potentially high mechanical characteristics, especially regarding toughness, hardness and creep resistance at high temperatures.

Interesting toughness and hardness values were obtained with both sintering powders: best toughness values are approximately  $5 \text{ MPa}\cdot\text{m}^{0.5}$ , while best hardness values are approximately 19 GPa. These values are extremely promising, and represent a big improvement if compared to analogous results in literature<sup>50</sup> concerning the use of preceramic polymers as sintering aid for silicon nitride powders.

Although good results were obtained with both the precursors, some important differences between a polysiloxane-based (A) and a polysilazane-based (B) sintering aid were observed, that could be resumed in the following points:

- Polysiloxane-based powder gives a higher densification rate and a much improved crystallization at relatively low temperatures than polysilazane-based powder. This different behavior is probably associated with the different chemical bonds present inside the ceramic residue that generates upon pyrolysis: while Si–O and Si–C are the main bonds generated by the pyrolysis of polysiloxanes, the replacement of Si–O bonds by more strongly covalent Si–N bonds in polysilazanes gives probably a glassy phase characterized by a higher viscosity, which is less inclined to both crystallize and react with other phases present, to give the formation of crystalline phases. For this reason, higher densification temperatures and longer holding times are required to reach a full system densification/crystallization when using powder B.
- Slightly higher toughness values were obtained by using powder A, especially for samples densified at  $1750^\circ\text{C}$ , also thanks to a partial  $\alpha\text{-Si}_3\text{N}_4 \rightarrow \beta\text{-Si}_3\text{N}_4$  conversion, which

implies the formation of elongated grains that generate an interlocking microstructure.

- Hardness values are basically equivalent between A and B series, although it should be pointed out that when high sintering temperature are applied, B series seems to have a higher potential than A series, as could be observed by looking at its hardness values. A possible explanation for this phenomenon could be found in the nucleation of SiC crystallites when powder B is used.
- Finally, a general consideration about the handling and the cost of the sintering powders should be done: polysilazane-base system show a more complicated handling procedure, due to their high moisture sensitivity, and are generally characterized by higher prices. These aspects slightly hinder their applicability and more widespread utilization, if compared to polysiloxane-based sintering aids.

#### 4.4.2 Sialon joining with polysiloxane-based formulations

##### Introduction

The interest in joining one piece of ceramic to another, whether it is to the same ceramic material or a different one, is usually with a view to producing a more complex shaped ceramic component out of simple starting shapes.

The joining of engineering ceramics, even to themselves, is not an easy problem to solve. This is because of their strong ionic or covalent bonding and the low self diffusivity of the constituent atoms or ions. These characteristics, which are the basis for most of the attractive properties of ceramics, including strength and chemical inertness, makes them relatively difficult to join.

There are a surprisingly large number of ways of joining ceramics both to themselves and to metals. Ideally it would be beneficial to perform any diffusion bonding without any interlayer, in order to create the 'perfect' invisible interface, i.e. one which is pore-free and defect-free when observed by optical microscopy or scanning electron microscopy. However, this is often difficult because of problems in promoting sufficient interdiffusion across the interface in engineering ceramics. For this reason, many different methods have been proposed during the years. These range from mechanical attachment (such as bolting, screw threads and shrink fitting), to chemical methods, which are usually further sub-divided into solid-state and liquid-state joining methods. However, there are several processes which do not fit neatly into these relatively restrictive definitions (or a combination of two or more), and instead it may therefore be more useful to consider a spectrum of joining processes ranging continuously from mechanical to liquid phase. Of course, each joining technique has its specific temperature capability.

A natural extension to the use of glass or glass-ceramic interlayers to achieve ceramic-ceramic bonding is to induce in the region between two ceramic surfaces a chemical reaction which helps to produce a highly refractory chemical bond between the surfaces. In this "class" of techniques, the use of preceramic polymer is a possible and attractive possibility to couple an easy joint realization, through the deposition of a polymeric layer, with the obtainment of a thermally stable ceramic upon pyrolysis. Colombo et al.<sup>286</sup> have used methyl-hydroxyl-siloxane as an interlayer in the joining of silicon carbide (Reaction Bonded Silicon Carbide, RBSC) itself. The technique was easy to implement using simple application procedures of the viscous resin to RBSC, followed by curing at 200°C and then conversion to amorphous silicon oxycarbide at 800-1200°C.

During the present work, the possibility of exploiting the advantages of preceramic polymers to obtain a ceramic interlayer with the same characteristic (composition, microstructure) of the substrate materials has been explored, in connection to the materials synthesis results exposed in Section 4.2.

### Joining preparation

Sialon substrate were kindly provided by International Syalons (Newcastle, UK) in the forms of small blocks of dimensions of 1.2x1.2x0.8 mm. XRD analysis of the substrates (reported in Fig. 4.31) revealed a pure  $\beta'$ -sialon composition, without the presence of any other secondary phase.  $z$ -value of  $\beta'$ -sialon was estimated to be lower than 1.0, since the position of the peaks was found to be intermediate between  $\beta'$ -sialon with  $z=1.0$  (PDF#077-0075) and  $\beta$ - $\text{Si}_3\text{N}_4$  (PDF#083-0701) (corresponding to  $z=0$ ).  $\text{Y}_2\text{O}_3$  was used as sintering aid, although exact concentration is not known.

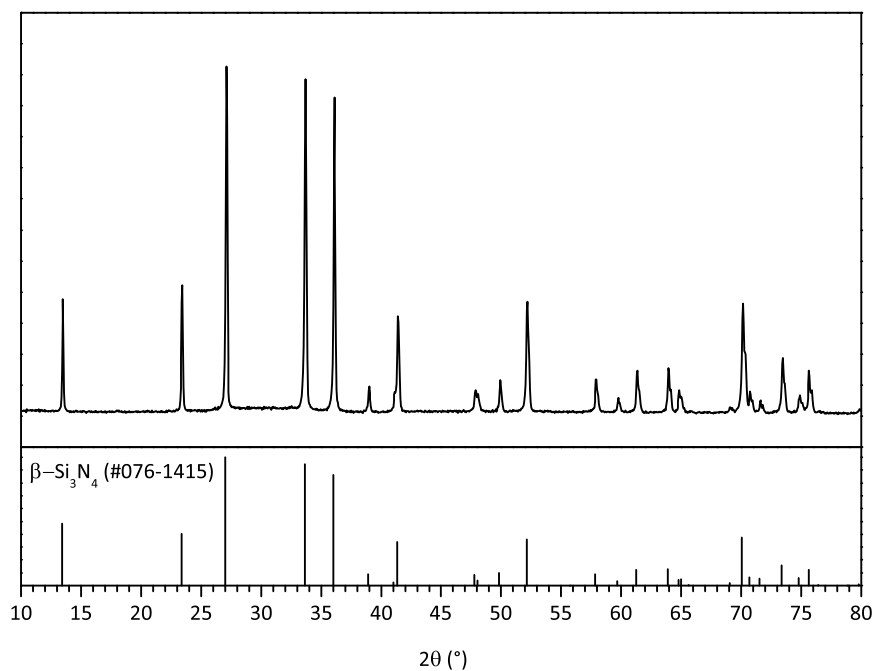


Figure 4.31: XRD pattern of sialon substrates to be joined during experiments.

To select the preceramic formulation, results of Section 4.2.2 were considered. Formulation z3y was selected as precursor for the joining media, and  $\text{N}_2/\text{H}_2$  2% was selected as the treatment atmosphere, due to the promising results obtained with z3 sample. Formulation z3y (which contains some  $\text{Y}_2\text{O}_3$ ) was selected instead of z3, since the presence of small amounts of sintering aid demonstrated to be effective for a better materials densification through liquid-phase sintering. The residual  $\text{Al}_2\text{O}_3$  that characterizes this class of formulations, which originates from silica volatilization, could be potentially absorbed (at least partially) inside the substrate material, because if its low  $z$ -value, and thus have an additional positive influence on the overall joining process.

Composition for the joining media is reported in Tab. 4.4. After the preparation of the dispersion, solvent was completely removed by heating in oven at  $60^\circ\text{C}$ . Material was then finely ground in a mortar with a pestle, and then isopropyl alcohol was added drop-wise to the powders and mixed by grinding with the pestle, until a homogeneous, thick paste was obtained. Substrates were carefully cleaned in acetone by ultrasonication prior to paste

deposition. Paste was homogeneously distributed on one of the two sialon substrates by using a small brush, thus creating a homogeneous layer of paste of approximately 200  $\mu\text{m}$ . After the deposition of the material, substrates were put together (slightly shifted), and a high pressure was applied perpendicular to the joined face by clamping the samples. Excess material was squeezed out and removed, and pieces were then put in oven (still clamped) at 80°C for 3 h, in order to both remove the residual solvent and to favor the flow of the polymer (which has a  $T_g$  in the 45-60°C range). Finally, pieces were positioned in the graphite fixture reported in Fig. 4.32, and the whole piece was put inside the tube furnace for the final heat treatment. This fixture was designed to host the pieces to be joined, and to lock them in a fixed position (but without the application of any pressure). In principle, a certain pressure perpendicular to the joint region should build up at high temperatures, due to the CTE mismatch between the sialon pieces and the surrounding graphite: the thermal expansion of sialon is lower than the thermal expansion of graphite, and at high temperatures a compressive force is generated, which should have, in principle, beneficial effects on the joining process.

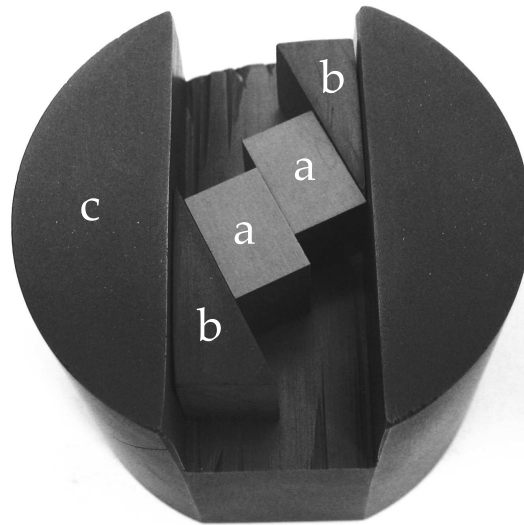


Figure 4.32: Graphite fixture used during the joining experiments. a=sialon substrates, b=graphite wedges used to lock the substrates to be joined, c=main graphite fixture.

The heat treatment pattern was constituted by a dwell at 1550°C for 3 h, with an increasing rate of 2°/min and a controlled decreasing rate of 10°/min. A constant flow of N<sub>2</sub>/H<sub>2</sub> 2% atmosphere was kept during the entire treatment.

After heat treatment, joined samples were ground perpendicularly to the joint plane with abrasive papers, thus removing approximately 500-1000  $\mu\text{m}$  of material. Surface was then polished, and optical and chemical analysis were carried out.

## Results

In Fig. 4.33 an optical image of the joint region after heat treatment is reported. No macro-defects could be observed in the sample, such as detachments or macro voids in the joint region due to material loss. The two faces to be joined adhere one on each other very homogeneously through all the joint region, although it is believed that the pressure generated during the heat treatment was not homogeneously distributed through the all surface. Load gradients are believed to develop because of unavoidable geometrical imperfections present both in the sialon substrates (minor imperfections) and, most of all, in the graphite fixture. A good morphological continuity across the joint line could be observed in Fig. 4.33, especially in those areas where a higher load was believed to be present. Joint region is believed to be approximately 30  $\mu\text{m}$  thick.

The same region was analyzed by electron microscopy, and images are reported in Fig. 4.34. In order to have an estimate of the material composition around the joint region, chemical analysis were carried out by an EDS apparatus attached to the SEM. A chemical mapping of the most relevant elements (silicon, aluminum and yttrium) was made, to obtain some data regarding both the chemical composition of the joint region, and, most important, about the chemical homogeneity across the joint region. Results are reported in Fig. 4.35. As could be observed, besides a good morphological continuity in most of the joint line, clues for a complete chemical integration could also be found in some areas, while in other areas chemical gradients are present. No evidences of major yttrium gradients are generally observable, probably due to an effective flow mechanism during the heat treatment, both from the joining material to the substrates, and viceversa. It could be noted instead that the joint region shows a generally higher aluminum content than the substrates, while a lower silicon concentration could be observed as well. This observation could be in accordance with previous findings (discussed in Section 4.2.2) regarding the silica volatilization process: this secondary reaction could generate both a decrease in the silicon content, and at the same time a build-up of the aluminum concentration (which is present, as demonstrated before, as  $\alpha\text{-Al}_2\text{O}_3$ ). Anyway, some clues for a complete integration are indicated in Fig. 4.35, where the concentration gradients of silicon and aluminum are minimized, and almost eliminated.

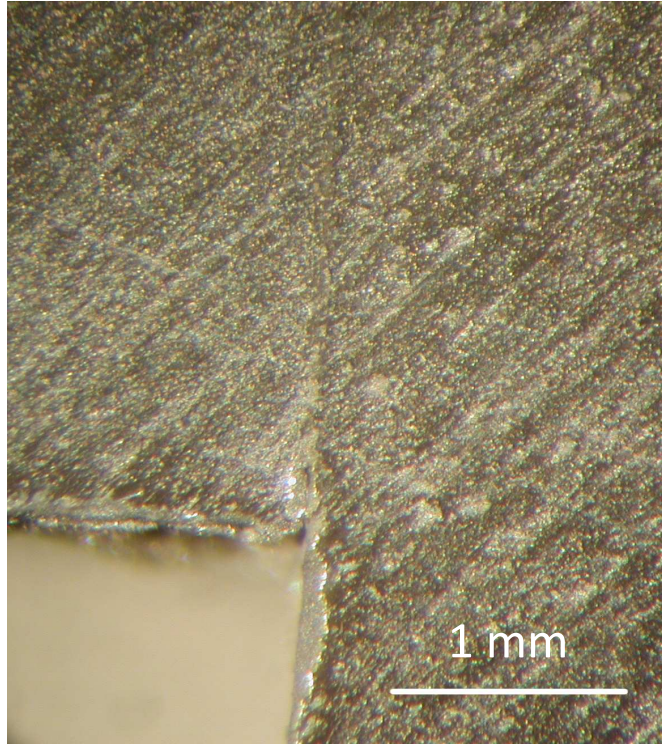


Figure 4.33: Optical image of the joining area between the 2 sialon substrates after heat treatment at 1550°C for 3 h.

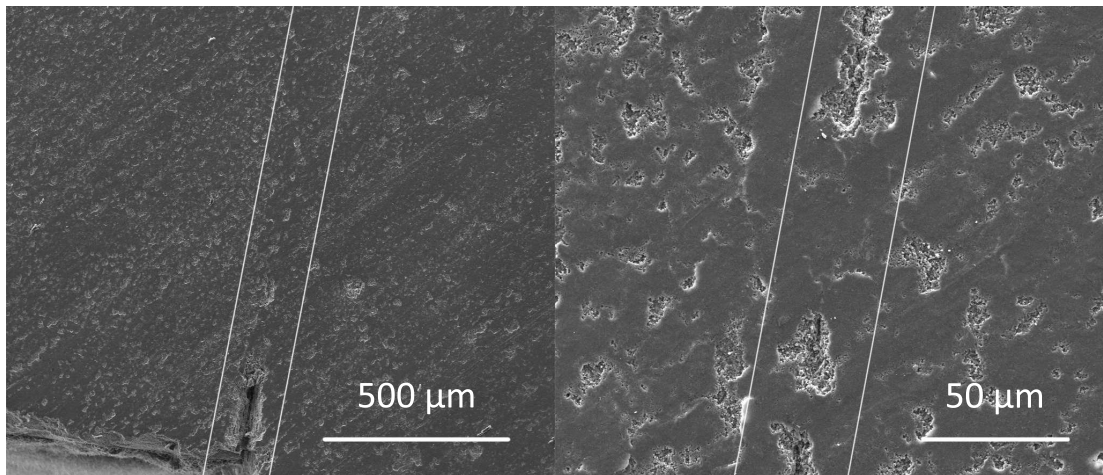


Figure 4.34: SEM image of the joining area between the 2 sialon substrates after heat treatment at 1550°C for 3 h.

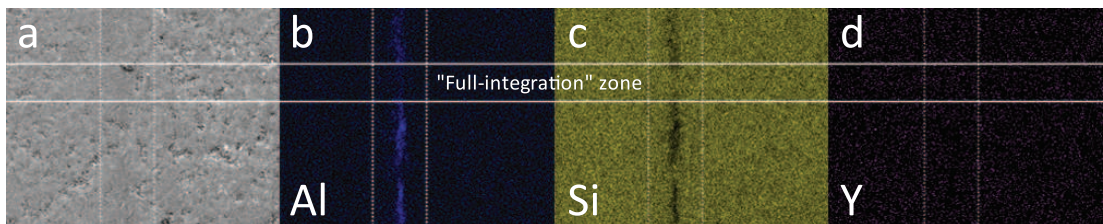


Figure 4.35: Details of the joined region realized by using a polysiloxane/ $\text{Al}_2\text{O}_3$ / $\text{Si}_3\text{N}_4$ / $\text{Y}_2\text{O}_3$  mixture. Heat treated at 1550°C for 180 min in  $\text{N}_2/\text{H}_2$  2%. a) SEM (SE), b) aluminum distribution, c) silicon distribution, d) yttrium distribution.

### 4.4.3 Sialon phosphors

#### Introduction

Light-emitting diodes (LEDs) using semiconductors offer an alternative method of illumination. Compared with conventional lamps, LED-based light sources have superior lifetime, efficiency, and reliability, which promise significant reductions in power consumption.

In general, there are three methods of creating white light in LEDs: (1) using three individual monochromatic LEDs with blue, green, and red colors; (2) combining an ultraviolet (UV) LED with blue, green, and red phosphors; and (3) using a blue LED to pump yellow or green and red phosphors<sup>55</sup>. In the latter two cases, appropriate phosphors are used as downconversion luminescent materials.

The excitation sources used for phosphors in LEDs differ greatly from those of phosphors in conventional lighting. The excitation sources for phosphors in LEDs are UV (360–410 nm) or blue light (420–480 nm). Therefore, the phosphors in LEDs should have high absorption of UV or blue light. In addition, they should also have the following characteristics: (1) high conversion efficiency; (2) high stability against chemical, oxygen, carbon dioxide, and moisture; (3) low thermal quenching; (4) small and uniform particle size (5–20  $\mu\text{m}$ ); and (5) appropriate emission colors<sup>5</sup>.

The phosphor most commonly utilized in bichromatic white LEDs is the yellow-emitting YAG:Ce<sup>3+</sup><sup>56</sup>, as well as other oxide-based materials. However, most oxide-based phosphors have low absorption in the visible-light spectrum, making it impossible for them to be coupled with blue LEDs. On the other hand, sulfide-based phosphors are thermally unstable and very sensitive to moisture, and their luminescence degrades significantly under ambient atmosphere without a protective coating layer. Consequently, to solve these problems and develop high-performance phosphors for LEDs, it is essential to modify existing phosphors or to explore new host crystals for phosphors such as nitrides.

Luminescence in rare-earth-doped III–V group nitrides such as AlN, GaN, InGaN, and AlInGaN has been intensively investigated because of their potential applications in blue-UV optoelectronic and microelectronic devices<sup>57–60</sup>. However, less attention has been paid to the luminescence of silicon-based oxynitride and nitride compounds.

Silicon-based oxynitride and nitride phosphors have received significant attention in recent years because of their encouraging luminescent properties (excitability by blue light, high conversion efficiency, and the possibility of full color emission), as well as their low thermal quenching, high chemical stability, and high potential for use in white LEDs<sup>5</sup>.

Covalent nitrides can be considered as host lattices for phosphors because they have the characteristics of an insulator or semiconductor and wide band gaps, whereas metallic and ionic nitrides are either electrical or ionic conductors and both have narrow band gaps. Furthermore, the covalent chemical bonding in nitrides gives rise to a strong nephelauxetic effect (i.e., electron cloud expansion), reducing the energy of the excited state of the 5d electrons of the activators (e.g., Eu<sup>2+</sup>, Ce<sup>3+</sup>)<sup>61–65</sup>. This results in long excitation/emission wavelengths and low thermal quenching, which cannot be achieved in conventional phosphors.

The ternary, quaternary, and multinary covalent nitride compounds, typically silicon-based nitrides, are interesting because of their unique and rigid crystal structures, availability of suitable crystal sites for activators, and their structural versatility, which enable the doping of rare-earth ions to provide useful photoluminescence<sup>5</sup>. A variety of oxynitride and nitride materials with promising luminescent properties have been discovered recently<sup>61–64,66–69</sup>.

In the following sections, some preliminary results about the possibility of synthesizing

sialon-based phosphors from preceramic polymers filled with nano-particles will be presented, in the light of the extremely promising results on sialon synthesis from polysilazane-based formulations of Section 4.3. These following results, although preliminary, represent probably the first example of sialon phosphors obtained by using preceramic polymers filled with nano-sized fillers, and will be surely the subject of future works.

These results were produced in collaboration with Prof. H. T. Hintzen of the Eindhoven University of Technology (The Netherlands).

### Phosphors preparation

$\beta'$ -sialon composition with low  $z$ -value ( $z=0.4$ ) was selected for the realization of green-emitting phosphors, since the most interesting emission properties have been verified for low  $z$ -values<sup>5</sup>. To obtain the desired  $z$ -value, amorphous  $\text{Si}_3\text{N}_4$  nanopowder was inserted in the starting mixture. Europium atoms were inserted as  $\text{Eu}_2\text{O}_3$  nanoparticles. For PSZ20, a ceramic yield of 70 wt% was considered. The hypothesized reaction is given in Eq. 4.6 and the subsequent formulation is reported in Tab. 4.9.

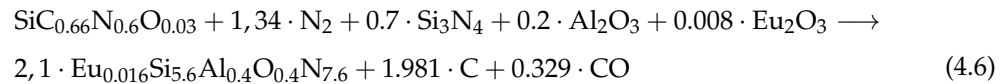


Table 4.9: Formulation for the synthesis of a low  $z$ -value  $\text{Eu}^{2+}$ -doped  $\beta'$ -sialon composition, derived from Eq. 4.6.

Component	Composition (wt%)
PSZ20	64.9
$\text{Al}_2\text{O}_3$	5.9
$\text{Si}_3\text{N}_4$	28.4
$\text{Eu}_2\text{O}_3$	0.8

The dispersion was realized in analogy to the procedure described in Section 4.3.1. Powders obtained were pulverized and heat treated in the 1500–1700°C range for 1 h in  $\text{N}_2/\text{H}_2$  (5%) atmosphere.

### Results

XRD results are reported in Fig. 4.36, while photoluminescence analysis are summarized in Fig. 4.37.

From XRD results, interdependently from the firing temperature,  $\beta'$ -sialon phase with a low  $z$ -value ( $<0.5$ ) is the predominant phase, while an  $\alpha$ -secondary phase is clearly visible, even if with a lower concentration.

The nature of this  $\alpha$ -phase is considered to be of fundamental importance: although is still to be verified, it is believed that at low temperature (1500°C),  $\alpha$  diffraction peaks should be associated with  $\alpha$ - $\text{Si}_3\text{N}_4$ , likely deriving from the crystallization of the extra  $\text{Si}_3\text{N}_4$  amorphous powder inserted in the starting formulation.

At high temperature (1700°C) instead,  $\alpha$  peaks should be probably associated with  $\alpha'$ -sialon, which forms from the reaction of  $\alpha$ - $\text{Si}_3\text{N}_4$  with some  $\text{Al}_2\text{O}_3$  and  $\text{Eu}_2\text{O}_3$ . As a support to this hypothesis,  $\alpha$ - $\text{Si}_3\text{N}_4$  is the low-temperature form of  $\text{Si}_3\text{N}_4$ , while the high-temperature

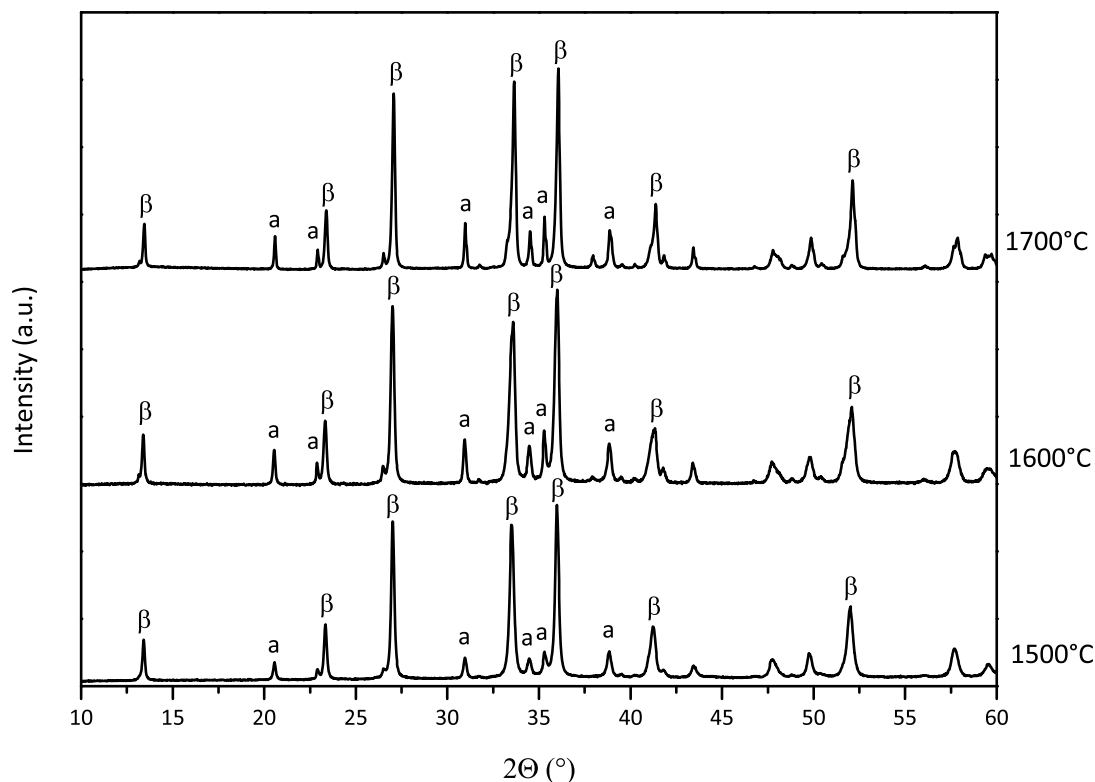


Figure 4.36: XRD patterns of  $\beta'$ -sialon:Eu<sup>2+</sup> powders, treated at 1500, 1600 and 1700°C for 1 h in N<sub>2</sub>/H<sub>2</sub> (5%) atmosphere.  $\beta$ = $\beta'$ -sialon, a= $\alpha$  phase ( $\alpha$ -Si<sub>3</sub>N<sub>4</sub>/ $\alpha'$ -sialon).

form is the  $\beta$ -Si<sub>3</sub>N<sub>4</sub>. For this reason, the  $\alpha$ -peaks should be associated to  $\alpha'$ -sialon.

With regards to the europium cations, some Eu<sup>3+</sup> must be present inside  $\alpha'$ -sialon structure, as a stabilizer of the crystal lattice (necessary to maintain the electro-neutrality of the crystal lattice). Phase pure Eu- $\alpha'$ -sialon are well known to be more difficult to obtain than other  $\alpha'$ -sialons stabilized with other rare-cations (e.g. Ca, Mg, Y, Yb), due to the strong tendency of europium to be in the Eu<sup>2+</sup> configuration rather than in the Eu<sup>3+</sup> configuration<sup>70</sup>. However, in the present formulation, europium is the only cation present that can effectively stabilize the  $\alpha'$ -sialon phase.

A certain fraction of Eu<sup>2+</sup> is believed to be present as well inside  $\alpha$ -sialon phase, since the excitation/emission characteristics of the material fired at 1700°C are more similar to Eu<sup>2+</sup>-doped Ca- $\alpha'$ -sialon than to Eu<sup>2+</sup>-doped  $\beta'$ -sialon<sup>5</sup>, especially with regards to the emission wavelength, which is centered around 580 nm. Also the excitation spectrum seems very similar to the one of Eu<sup>2+</sup> in Ca- $\alpha'$ -sialon<sup>5</sup>.

On the other hand, the emission peak observed at low temperature (423 nm) is difficult to be identified, since it is different from what previously observed in literature for both Eu<sup>2+</sup>-doped Ca- $\alpha'$ -sialon (581 nm) and Eu<sup>2+</sup>-doped  $\beta'$ -sialon (538 nm). Probably, this peak is associated with some other compounds where europium cations are present at low temperature, maybe an intermediate glassy phase that eventually dissolves inside the  $\alpha$ -Si<sub>3</sub>N<sub>4</sub> at higher temperatures to give the formation of Eu- $\alpha'$ -sialon. A clue for this hypothesis could be found in the intermediate temperature 1600°C: the unidentified peak at 423 nm dramatically decreases, and at the same time the peak at 570 nm starts to build up, accordingly to ( $\alpha$ -Si<sub>3</sub>N<sub>4</sub>+Eu-based unknown phase)→ Eu- $\alpha'$ -sialon.

These results could possibly indicate that, in the absence of phase purity, i.e. with a  $\alpha/\beta$  duplex composition (as in our case), the  $\alpha$  phase seems more prone to accept europium

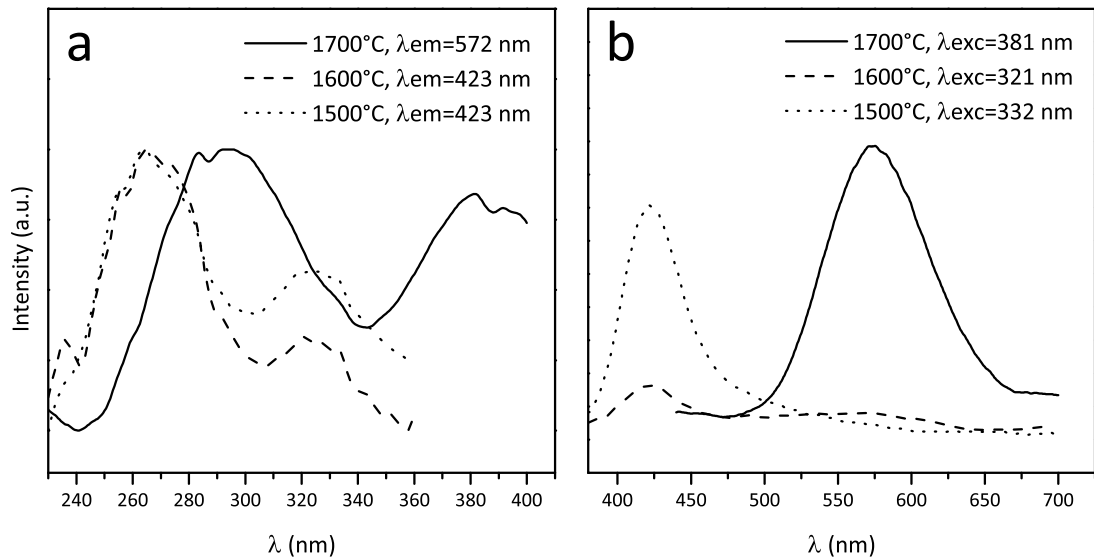


Figure 4.37: Excitation (a) and emission (b) spectra of Eu<sup>2+</sup>-doped β'-sialon formulation treated at 1500, 1600 and 1700°C.

cations inside its crystal structure; β-phase instead does not easily accommodate additional cations inside its lattice. This fact is very well known in literature<sup>10</sup>: additional sintering aids added to β'-sialon powders (e.g. Y<sub>2</sub>O<sub>3</sub>) remain in the intergranular regions as glassy phase (often in combination with SiO<sub>2</sub> and/or Al<sub>2</sub>O<sub>3</sub>), while α'-sialons can easily dissolve a wide range of foreign cations inside their lattice, and a much more limited amount of intergranular phase is generally observed.

## References

- [1] T. Ekstrom and M. Nygren, "SiAlON Ceramics", *J. Am. Ceram. Soc.*, **76** 259—276 (1992).
- [2] Jack, K. H., "Sialon ceramics: retrospect and prospect", *MATERIALS RESEARCH SOCIETY SYMPOSIUM PROCEEDINGS*, **287**, 15 (1993).
- [3] M. I. Jones, H. Hyuga and K. Hirao, "Optical and Mechanical Properties of alpha/beta Composite Sialons", *J. Am. Ceram. Soc.*, **22** 520–522 (2003).
- [4] R. J. Xie, N. Hirosaki, M. Mitomo, K. Uheda, T. Suehiro, X. Xu, Y. Yamamoto and T. Sekiguchi, "Strong green emission from alpha-SiAlON activated by divalent ytterbium under blue light irradiation.", *J. Phys. Chem. B*, **109** [19] 9490–4 (2005).
- [5] R. J. Xie and N. Hirosaki, "Silicon-based oxynitride and nitride phosphors for white LEDs—A review", *Sci. Technol. Adv. Mat.*, **8** [7-8] 588–600 (2007).
- [6] D. P. Thompson, "Innovation in SiAlON Ceramics", *Key Eng. Mat.*, **352** 137–146 (2007).
- [7] Jack, K. H. and Wilson, W. I., *Nature phys. Sci.* **238**, 28 (1972).
- [8] K. H. Jack, "Sialons and related nitrogen ceramics", *J. Mater. Sci.*, **11** [6] 1135–1158 (1976).
- [9] L. J. Gauckler, H. L. Lukas and G. Petzow, "Contribution to the Phase Diagram Si<sub>3</sub>N<sub>4</sub>-AlN-Al<sub>2</sub>O<sub>3</sub>-SiO<sub>2</sub>", *J. Am. Ceram. Soc.*, **58** [7-8] 346–347 (1975).
- [10] H. Mandal, "New Developments in alpha-SiAlON Ceramics", *J. Eur. Ceram. Soc.*, **19** 2349–2357 (1999).
- [11] S. Boskovic, L. J. Gauckler, G. Petzow and T. Y. Tien, "Reaction sintering forming β-Si<sub>3</sub>N<sub>4</sub> solid solutions in the system Si, Al/N, O - Sintering of Si<sub>3</sub>N<sub>4</sub>-AlN-Al<sub>2</sub>O<sub>3</sub> mixtures", *Powder Metall. Int.*, **11** 169 (1979).
- [12] S. Boskovic, L. J. Gauckler, G. Petzow and T. Y. Tien, "Reaction sintering forming β-Si<sub>3</sub>N<sub>4</sub> solid solutions in the system Si, Al/N, O. I- Sintering of SiO<sub>2</sub>-AlN mixtures", *Powder Metall. Int.*, **9** 185–189 (1977).
- [13] T. Ekstrom, Z. j. Shen, K. J. D. Mackenzie, I. W. M. Brown and G. V. White, "alpha-Sialon ceramics synthesised from a clay precursor by carbothermal reduction and nitridation", *J. Mater. Chem.*, **8** [4] 977—983 (1998).
- [14] Q. Qiu, V. Hlavacek and S. Prochazka, "Carbonitridation of Fly Ash. I. Synthesis of SiAlON-Based Materials", *Ind. Eng. Chem. Res.*, **44** [8] 2469–2476 (2005).
- [15] G. D. Soraru, A. Ravagni, R. Campostrini and F. Babonneau, "Synthesis and characterization of beta-SiAlON ceramics from organosilicon polymers", *J. Am. Ceram. Soc.*, **74** [9] 2220–2223 (1991).
- [16] T. Ekstrom, "Sialon Ceramics Sintered with Ytria and Rare Earth Oxides", *Mat. Res. Soc. Symp. Proc.*, **287** 121–132 (1993).
- [17] Z. Shen and M. Nygren, "On the Extension of the alpha-Sialon Phase Area in Yttrium and Rare-Earth Doped Systems", *J. Eur. Ceram. Soc.*, **2219** [96] 1639–1645 (1997).
- [18] K. Niihara, "New design concept of structural ceramics - Ceramic nanocomposites", *J. Ceram. Soc. Jpn.*, **99** [1154] 974–982 (1991).
- [19] J. Binner and B. Vaidhyanathan, "Processing of bulk nanostructured ceramics", *J. Eur. Ceram. Soc.*, **28** [7] 1329–1339 (2008).
- [20] I. W. Chen and X. H. Wang, "Sintering dense nanocrystalline ceramics without final-stage grain growth", *Nature*, **404** [6774] 168–171 (2000).
- [21] M. J. Mayo, "Processing of nanocrystalline ceramics from ultrafine particles", *Int. Mater. Rev.*, **41** [3] 85–115 (1996).

- [22] X. Xu, T. Nishimura, N. Hirosaki, R. J. Xie, Y. Yamamoto and H. Tanaka, "Fabrication of beta-sialon nanoceramics by high-energy mechanical milling and spark plasma sintering", *Nanotechnology*, **16** [9] 1569–1573 (2005).
- [23] M. Mitomo, "Preparation of alpha-Sialon Powders by Carbothermal Reduction and Nitridation", *Ceram. Int.*, **14** 43–48 (1988).
- [24] P. Colombo, G. Mera, R. Riedel and G. D. Soraru, "Polymer-Derived Ceramics: 40 Years of Research and Innovation in Advanced Ceramics", *J. Am. Ceram. Soc.*, **1837** 1805–1837 (2010).
- [25] R. Riedel, G. Mera, R. Hauser and A. Klönczynski, "Silicon-based polymer-derived ceramics: synthesis, properties and applications - a review", *J. Ceram. Soc. Jpn.*, **114** [6] 425–444 (2006).
- [26] M. Peuckert, T. Vaahs and M. Brück, "Ceramics from organometallic polymers", *Adv. Mat.*, **2** [9] 398–404 (1990).
- [27] J. Berakdar and R. Riedel, "Handbook of Ceramic Hard Materials", .
- [28] E. Bernardo, P. Colombo and S. Hampshire, "SiAlON-Based Ceramics from Filled Pre-ceramic Polymers", *J. Am. Ceram. Soc.*, **89** [12] 3839–3842 (2006).
- [29] E. Bernardo, G. Parcianello, P. Colombo, J. H. Adair, A. T. Barnes, J. R. Hellmann, B. H. Jones, J. Kruse and J. J. Swab, "SiAlON ceramics from preceramic polymers and nano-sized fillers: Application in ceramic joining", *J. Eur. Ceram. Soc.*, (2011).
- [30] R. M. Rocha, P. Greil, J. C. Bressiani and A. H. A. Bressiani, "Development and Characterization of Si-Al-ONC Ceramic Composites Obtained from Polysiloxane-Filler Mixtures", *Materials science forum*, **416** 505–511 (2003).
- [31] K. J. D. Mackenzie, R. H. Meinhold, G. V. White, C. M. Sheppard and B. L. Sherriff, "Carbothermal formation of  $\beta$ -sialon from kaolinite and halloysite studied by  $^{29}\text{Si}$  and  $^{27}\text{Al}$  solid state MAS NMR", *J. Mater. Sci.*, **29** [10] 2611–2619 (1994).
- [32] P. C. Silva and J. L. Figueiredo, "Production of SiC and Si<sub>3</sub>N<sub>4</sub> whiskers in C+ SiO<sub>2</sub> solid mixtures", *Mater. Chem. Phys.*, **72** [3] 326–331 (2001).
- [33] C. R. Blanchard and S. T. Schwab, "X-ray diffraction analysis of the pyrolytic conversion of perhydropolysilazane into silicon nitride", *J. Am. Ceram. Soc.*, **77** [7] 1729–1739 (1994).
- [34] M. Scheffler, T. Gambaryan-Roisman, T. Takahashi, J. Kaschta, H. Muenstedt, .. Buhler and P. Greil, "Pyrolytic decomposition of preceramic organo polysiloxanes", *Innovative Processing and Synthesis of Ceramics, Glasses, and Composites IV: Ceramic Transactions*, **115** 239–250 (2000).
- [35] G. D. Soraru, S. Modena, E. Guadagnino, P. Colombo, J. Egan and C. Pantano, "Chemical Durability of Silicon Oxycarbide Glasses", *J. Am. Ceram. Soc.*, **85** [6] 1529–1536 (2002).
- [36] E. Bernardo, P. Colombo, E. Pippel and J. Woltersdorf, "Novel Mullite Synthesis Based on Alumina Nanoparticles and a Pre-ceramic Polymer", *J. Am. Ceram. Soc.*, **89** [5] 1577–1583 (2006).
- [37] R. Riedel, L. Toma, C. Fasel and G. Miehe, "Polymer-derived mullite-SiC-based nanocomposites", *J. Eur. Ceram. Soc.*, **29** [14] 3079–3090 (2009).
- [38] D. H. Filsinger and D. B. Bourrie, "Silica to silicon: key carbothermic reactions and kinetics", *J. Am. Ceram. Soc.*, **73** [6] 1726—1732 (1990).
- [39] J. Zheng and B. Forslund, "Carbothermal Preparation of beta-SiAlON Powder at Elevated Nitrogen Pressures", *J. Eur. Ceram. Soc.*, **19** [2] 175–185 (1999).
- [40] T. Ekstrom, "Effect of composition, phase content and microstructure on the performance of yttrium Si-Al-O-N ceramics", *Mat. Sci. Eng. A*, **109** 341–349 (1989).

- [41] I. Tanaka, G. Pezzotti, Y. Miyamoto and T. Okamoto, "Fracture toughness of Si<sub>3</sub>N<sub>4</sub> and its Si<sub>3</sub>N<sub>4</sub> whiskers composite without sintering aids", *J. Mater. Sci.*, **26** 208—210 (1991).
- [42] Q. Qiu and V. Hlavacek, "Carbonitridation of Fly Ash. III. Effect of Indecomposable Additives", *Ind. Eng. Chem. Res.*, **44** [19] 7352–7358 (2005).
- [43] K. Komeya, T. Ide and T. Meguro, "Synthesis of AlN Powder by Carbothermal Reduction-Nitridation of Various Al<sub>2</sub>O<sub>3</sub> Powders with CaF<sub>2</sub>", *J. Am. Ceram. Soc.*, **82** [11] 2993—2998 (1999).
- [44] J. E. Gilbert and A. Mosset, "Preparation of beta-SiAlON from Fly Ashes", *Mater. Res. Bull.*, **33** [1] 117—123 (1998).
- [45] Y. W. Cho and J. A. Charles, "Synthesis of nitrogen ceramic powders by carbothermal reduction and nitridation - Part 2 Silicon aluminium oxynitride (sialon)", *Mater. Sci. Tech.*, **7** [5] 399—406 (1991).
- [46] E. Kroke, Y. L. Li, C. Konetschny, E. Lecomte, C. Fasel and R. Riedel, "Silazane derived ceramics and related materials", *Mat. Sci. Eng. R*, **26** [4-6] 97–199 (2000).
- [47] Y. L. Li, E. Kroke, R. Riedel, C. Fasel, C. Gervais and F. Babonneau, "Thermal cross-linking and pyrolytic conversion of poly(ureamethylvinyl)silazanes to silicon-based ceramics", *Appl. Organomet. Chem.*, **15** [10] 820–832 (2001).
- [48] C. Vakifahmetoglu, I. Menapace, A. Hirsch, L. Biasetto, R. Hauser, R. Riedel and P. Colombo, "Highly porous macro- and micro-cellular ceramics from a polysilazane precursor", *Ceram. Int.*, **35** [8] 3281–3290 (2009).
- [49] J. S. Ha, C. S. Kim and D. S. Cheong, "Densification and phase formation behavior of alumina infiltrated with polycarbosilane", *J. Ceram. Process. Res.*, **2** [4] 180–183 (2001).
- [50] T. Plachký, Z. Lenčič, A. Hric, P. Šajgalík, P. Baláž, R. Riedel and H. J. Kleebe, "Processing and mechanical properties of Si<sub>3</sub>N<sub>4</sub> composites employing polymer-derived SiAlOC as sintering aid", *J. Eur. Ceram. Soc.*, **30** [3] 759–767 (2010).
- [51] A. C. Ferrari and J. Robertson, "Interpretation of Raman spectra of disordered and amorphous carbon", *Phys. Rev. B*, **61** [20] 95–107 (2000).
- [52] A. Takase and E. Tani, "Infrared and Raman spectroscopic studies of Si<sub>3</sub>N<sub>4</sub>-SiC composites", *Journal of materials science letters*, **8** [6] 684–686 (1989).
- [53] T. Isoda, H. Kaya, H. Nishii, O. Funayama, T. Suzuki and Y. Tashiro, "Perhydropolysilazane precursors to silicon nitride ceramics", *J. Inorg. Organomet. P.*, **2** [1] 151–160 (1992).
- [54] P. Greil, "Polymer Derived Engineering Ceramics", *Adv. Eng. Mater.*, **2** [6] 339–348 (2000).
- [55] U. Kaufmann, M. Kunzer, K. Kohler, H. Obloh, W. Pletschen, P. Schlotter, J. Wagner, A. Ellens, W. Rossner, M. Kobusch, *Phys. Stat. Sol. A* **192** (2002) 246.
- [56] S. Nakamura, G. Fasol, "The Blue Laser Diode: GaN Based Light Emitters and Lasers", Springer, Berlin, 1997.
- [57] A.J. Steckl, R. Birkhahn, *Appl. Phys. Lett.* **73** (1998) 1700.
- [58] A.A. Andreev, *Phys. Solid State* **45** (2003) 419 .
- [59] K.P. O'Donnell, B. Hourahine, *Eur. Phys. J. Appl. Phys.* **36** (2006) 91.
- [60] A.J. Steckl, J.C. Heikenfeld, D.S. Lee, M.J. Garter, C.C. Baker, Y.Q. Wang, R. Jones, *IEEE J. Sel. Topics Quantum Electron.* **8** (2002) 749.
- [61] H.A. Hoppe, H. Lutz, P. Morys, W. Schnick, A. Seilmeier, *J. Phys. Chem. Solids* **61** (2000) 2001.
- [62] J.W.H. van Krevel, H.T. Hintzen, R. Metselaar, A. Meijerink, *J. Alloys Compd.* **268** (1998) 272.

- [63] J.W.H. van Kreveld, J.W.T. van Rutten, H. Mandal, H.T. Hintzen, R. Metselaar, *J. Solid State Chem.* 165 (2002) 19.
- [64] R.-J. Xie, M. Mitomo, K. Uheda, F.F. Xu, Y. Akimune, *J. Am. Ceram. Soc.* 85 (2002) 1229.
- [65] K. Uheda, H. Takizawa, T. Endo, H. Yamane, M. Shimada, C.M. Wang, M. Mitomo, *J. Lumin.* 87–89 (2000) 967.
- [66] R.-J. Xie, N. Hirosaki, M. Mitomo, in: W.M. Yen, S. Shionoya, H. Yamamoto (Eds.), "Phosphor Handbook", second ed, *CRC Press*, Boca Raton, 2007, p. 331.
- [67] R.-J. Xie, N. Hirosaki, M. Mitomo, Y. Yamamoto, T. Suehiro, N. Ohashi, *J. Am. Ceram. Soc.* 87 (2004) 1368.
- [68] Y.Q. Li, A.C.A. Delsing, G. de With, H.T. Hintzen, *Chem. Mater.* 17 (2005) 3242.
- [69] R. Le Toquin, A.K. Cheetham, *Chem. Phys. Lett.* 423 (2006) 352.
- [70] Z. Shen, M. Nygren and U. Halenius, "Absorption spectra of rare-earth-doped alpha-sialon ceramics", *J. Mater. Sci. Lett.*, 6 3–6 (1997).



## **Part III**

# **Summary, conclusions and future perspectives**



The research activity described in the present thesis regarded the synthesis of a wide variety of crystalline ceramics by the controlled pyrolysis of mixtures of preceramic polymers and ceramic fillers. The work was logically divided in 2 macro-areas: the first one regarded the synthesis of various silicates, ranging from relatively simple binary systems (e.g. zircon, wollastonite, Y-silicates) to ternary systems (mullite/ZrO<sub>2</sub>, cordierite). All these ceramics were synthesized in air in the 1000–1500°C range, and polysiloxanes (Silres MK and Silres H62C) were selected as precursors for silica.

Mullite/ZrO<sub>2</sub> nanocomposites, showing extremely interesting mechanical characteristics, were successfully synthesized at relatively low temperatures (1350°C) starting from mixtures of Silres MK, Al<sub>2</sub>O<sub>3</sub> and ZrO<sub>2</sub>. Nano-grains were observed for both the matrix (mullite) and the reinforcing phase (ZrO<sub>2</sub>). A favorable effect of the introduction of ZrO<sub>2</sub> on the mechanical properties was verified: significant improvements of indentation toughness were observed, associated to an effective t-ZrO<sub>2</sub> → m-ZrO<sub>2</sub> transformation during the propagation of cracks ("transformation toughening"). These materials represent promising candidates as high-temperature structural parts or as matrix for CMCs (ceramic matrix composites).

With regards to zircon, the synthesis of this ceramic from polysiloxane/ZrO<sub>2</sub> mixtures was extensively studied, analyzing in particular the influence of the addition of TiO<sub>2</sub> nanopowders and zircon seeds to the formation of zircon phase at high temperatures. While in a pure silicone/ZrO<sub>2</sub> system zircon was virtually absent even at 1500°C, the introduction of TiO<sub>2</sub> (as a sintering aid) and zircon seeds produced a remarkable effect on the zircon nucleation kinetic. Highly pure zircon ceramics were synthesized at temperatures as low as 1200°C. Moreover, the substitution of part of Silres MK with H62C demonstrated to be fundamental for the realization of bulk, crack-free zircon monoliths, with a relative density in the 81–86% range and a biaxial flexural strength of 138 MPa.

High-purity cordierite ceramics were obtained by the pyrolysis of MK/Al<sub>2</sub>O<sub>3</sub>/MgO mixtures. 2 different processing techniques were used for the realization of low-porosity bulk samples (in analogy with the experimental results obtained for zircon ceramics) and high-porosity samples, realized by the introduction of PMMA sacrificial micro-beads. In principle, cordierite ceramics with a tailorable porosity between the maximum value (82%) and the minimum (19%) could be easily achieved with a very simple processing. This methodology could also be, in principle, easily extended to other ceramic system, like most of those studied and described in the present thesis (e.g. mullite-based materials, zircon ceramics).

Porous samples were also realized with a wollastonite composition, starting from mixtures of Silres MK and CaCO<sub>3</sub>. Almost pure wollastonite was effectively synthesized at 900°C by using nano-CaCO<sub>3</sub>, or by using micro-CaCO<sub>3</sub> and a mixing/extrusion process in an extruder, assisted by supercritical CO<sub>2</sub> as solvent. To produce porous samples, an alternative methodology was used: after extrusion, rods produced (that, upon direct pyrolysis, were characterized by poor mechanical consistency) were pulverized, and powders obtained were subsequently warm pressed, or simply poured inside Al containers, with and without the introduction of PMMA sacrificial micro-beads. In both cases, after a heat treatment at 300°C, the coalescence of CO<sub>2</sub> micro-bubbles created a quite homogeneous open porosity, which is of basilar importance for biological applications. Again, results concerning the use of supercritical CO<sub>2</sub> to generate a controllable porosity could be, in principle, also extended to other polymer(s)/filler(s) combinations, and thus to other ceramic systems.

Finally, Y-silicates (both the mono-silicate, Y-MS, and the di-silicate, Y-DS) were synthesized from MK/Y<sub>2</sub>O<sub>3</sub> mixtures. Environmental barrier coatings (EBCs) on Si-SiC (silicon-infiltrated SiC) foams were produced by dip-coating on Y<sub>2</sub>O<sub>3</sub>, polysiloxane, kaolin (added to increase

the stability of the dispersions) and mullite (passive filler) dispersions in isopropyl alcohol. Analogous dispersions ( $ZrO_2$  instead of  $Y_2O_3$ , and zircon instead of mullite) were also produced for the realization of zircon-based coatings. In both cases, relatively thick (100  $\mu m$ ) and homogeneous layers were successfully produced after ceramization treatment. After oxidation test, Y-DS-based coatings seem to have slightly better performances than zircon based coatings. However, the densification of the coatings has still to be improved. Y-MS instead was doped with 5 mol% of  $Eu^{3+}$  (substituting  $Y^{3+}$  cations) for the realization of red-emitting phosphors for LED applications. A strong luminescence at 614 nm (excitation at 400 nm) was observed. This experimentation demonstrates the potentialities of this ceramic as a host phase for rare earths elements, for the realization of thermally stable phosphors with different emission characteristics, depending on the doping cations introduced.

Ceramics in the Si-Al-O-N systems instead represented the second macro-system investigated. The distinctive characteristic of this class of ceramics is represented by the additional presence of nitrogen inside their crystal structure, which make the synthesis of this class of materials not trivial.

First experiments concerned mixtures of a polysiloxane (Silres H44) and  $Al_2O_3$  nanoparticles. After pyrolysis in inert atmosphere, Silres H44 gives a carbon-rich ceramic residue, thanks to the phenyl groups present inside its structure. It was hypothesized that this higher carbon content could provide an efficient reduction of the global oxygen content of the ceramic at high temperatures (through the formation of volatile CO) that, together with a nitrogen intake from the furnace atmosphere, would give the formation of sialon phases. It was verified that, without the addition of additives, it was impossible to achieve high  $\beta'$ -sialon yields. On the contrary, the introduction of additives ( $Y_2O_3$ , extra carbon,  $CaF_2$ ) or the use of slightly reducing atmospheres ( $N_2/H_2$  2%) demonstrated to effectively increase  $\beta'$ -sialon yield. However, from polysiloxane-based formulations, it was not possible to achieve phase purity, and  $Al_2O_3$  was always detected as the principal impurity in the final ceramics.

On the contrary, a systematic study with polysilazane(PSZ20)-based mixtures demonstrated the possibility of obtaining higher  $\beta'$ -sialon yields, thanks to the presence of nitrogen inside the ceramic residue of the preceramic polymer. Phase purity was effectively increased by substituting part of the PSZ20 with a fully inorganic polysilazane (perhydropolysilazane, PPHS), thus eliminating the only impurity present, i.e. SiC nano-crystals.

Both siloxane- and silazane-based mixtures were successfully applied as sintering aid for  $Si_3N_4$  powders. Although similar hardness and toughness values were obtained, siloxane-based mixtures seem to be more promising, because of higher densification rates and an easier handling of the precursors, if compared to polysilazane-based mixtures. Future characterization of these composites will focus on their mechanical properties at high temperatures, with special attention to the potentially high creep resistance that this newly developed highly-crystalline intergranular phase (generated by the evolution of the preceramic polymer-based mixture) could provide. Siloxane-based mixtures were also applied as joining media for the joining of sialon substrates. A good morphological and chemical continuity was found across the joint region, thus indicating the good potentiality of this strategy for the realization of the "perfect" joint by a relatively simple processing. Finally, some preliminary results regarding the realization of  $\beta'$ -sialon phosphors were presented. The purity of the system seems to be a critical factor to achieve the desired photoluminescence characteristics. In the light of these promising results, future works will focus on the synthesis of sialon-based phosphors and silicon-oxynitride phosphors in general, that represent a relatively new and extremely promising class of inorganic compounds for LED applications.

# Appendices



# Appendix A

## Materials

### A.1 Polymeric precursors

#### A.1.1 Silres MK

Silres MK (Wacker-Chemie GmbH, München, Germany) is a solid methyl polysilsequioxane (general chemical formula  $[\text{RSi-O}_{1.5}]_n$ ) powder characterized by a 84 wt%  $\text{SiO}_2$  yield after pyrolysis in oxidative atmosphere. Silres MK has a melting point in the 35-55°C range, is soluble in aromatics, esters, ketones and selected paraffins and chlorinated hydrocarbons. MK can be thermally cross-linked through condensation reactions between the hydroxyl and ethoxy functionalities present inside its molecular structure, with the consequent release of water and other volatile species, i.e. ethanol. Cross-linking reactions could also be enhanced by the addition of appropriate catalysts.

#### A.1.2 Silres H44

Silres H44 is a solid methyl-phenyl polysiloxane. Similarly to Silres MK, H44 could be thermally cross-linked using the hydroxyl and ethoxy functionalities present inside its molecular structure, or by the use of an appropriate catalyst. After complete pyrolysis in oxidative atmosphere, it shows a  $\text{SiO}_2$  yield of approximately 84 wt%.

#### A.1.3 Silres H62C

Silres H62C is a viscous liquid methyl-phenyl-vinyl-hydrogen polysiloxane. If compared to MK and H44, it is characterized by a lower ceramic yield (approximately 58 wt%), but is capable of undergoing thermal crosslinking without the release of gaseous byproducts.

#### A.1.4 HTT 1800 and PSZ20

HTT 1800 (also referred in literature as VL20) and PSZ20 (KiON Defense Technologies Inc., Huntingdon Valley, PA, USA) are liquid polysilazane, characterized by an alternated Si-N backbone with methyl (~80%) and vinyl (~20%) side groups. The presence of vinyl functionalities allows a thermally-activated cross-linking process in the 180-200°C range, or at lower temperature by adding a free radical initiator such as an organic peroxide. Besides the identical chemical composition, PSZ20 is characterized by a lower amount of oligomers than HTT 1800, which implies a slightly higher ceramic yield after pyrolysis (in the 70-80

wt% range). Since the Si-N bond energy is lower than that of Si-O, polysilazane are generally moisture sensitive, and they could readily react with water to give the following reaction:



For this reason, particular attention must be taken during the handling and processing of this class of preceramic polymers.

### A.1.5 NN 120-20

NN 120-20 (Clariant, USA) is a 20 wt% solution of perhydropolysilazane (PHPS) in di-n-butyl-ether. PHPS is a fully inorganic polymer, i.e. does not contain carbon-based moieties. After the evaporation of the solvent in the 20-120°C range, solvent-free PHPS could be cured in the 180-250°C range. Particular precaution should be taken during PHPS handling, since it strongly reacts with water, alcohols, protic solvents and amines with evolution of ammonia and hydrogen gas. In addition, formation of self-igniting silanes is also possible.

## A.2 Inorganic powders

**High specific surface area fumed metal oxides** High specific surface area (SSA) powders (like most of the powders used during the present research activity) are synthesized by processes based on gas-phase reactions. The advantages of this synthesis route are 1) materials of high purity at high yields and with a high throughput can be produced, 2) large volumes of liquids as in wet processes are not involved, 3) process time scales are usually very short and 4) multicomponent or nanophase materials can be produced. The Aerosil® process (patented by Degussa in 1942) is one of the best examples of this type of processes for the realization of extremely fine SiO<sub>2</sub> and other inorganic compounds.

For the production of SiO<sub>2</sub>, the process is based on the following reactions



Silicon tetrachloride is volatilized and fed into an oxygen-hydrogen flame. The water formed by reaction of hydrogen and oxygen serves for the very fast hydrolysis of SiCl<sub>4</sub> at approximately 1000°C. HCl is then separated and recycled, and powders are collected by conventional means (e.g. cyclones) and de-acidified (for more details, see "Synthesis of inorganic materials" by U. Schubert and N. Hüsing).

Other fumed metal oxides nanopowders could be produced by similar processes, as well as other compounds. In the case of Si<sub>3</sub>N<sub>4</sub> nanopowders, reaction between ammonium tetrachloride and ammonia could give highly-pure Si<sub>3</sub>N<sub>4</sub> powders through the following reaction:



In this case, final calcination temperature determines the predominant allotropic form of Si<sub>3</sub>N<sub>4</sub>: α-Si<sub>3</sub>N<sub>4</sub> equiaxed grains are produced at 1420°C, while elongated β-Si<sub>3</sub>N<sub>4</sub> whiskers are synthesized for T>1460°C.

In Tab. A.1 some physical properties of the powders used during the present research work

are summarized.

Table A.1: Description and properties of inorganic powders used during the experimental work.

Commercial name	Chemical composition	SSA (m <sup>2</sup> /g)	Mean particle size (nm)	Purity (%)	Producer
Oxides					
Aeroxide Alu C	Al <sub>2</sub> O <sub>3</sub>	100±15	13	≥99.8	Evonik Industries
Aeroxide TiO <sub>2</sub> P90	TiO <sub>2</sub>	90±20	14	≥99.5	Evonik Industries
ZrO <sub>2</sub> VP PH	ZrO <sub>2</sub>	100±15	13		Evonik Industries
ZrO <sub>2</sub> VP 3-YSZ	ZrO <sub>2</sub> (3 mol% Y <sub>2</sub> O <sub>3</sub> )	100±15	13		Evonik Industries
TiO <sub>2</sub> VP-P90	TiO <sub>2</sub>	90	13		Evonik Industries
ZrO <sub>2</sub> TZ-0	ZrO <sub>2</sub>	14	40		Tosoh
Y <sub>2</sub> O <sub>3</sub> nanopowders	Y <sub>2</sub> O <sub>3</sub>	30-50	30-50	99.95%	Inframat Advanced Materials
MgO nanopowders	MgO	50	30	99.9	Inframat Advanced Materials
Eu <sub>2</sub> O <sub>3</sub> nanopowders	Eu <sub>2</sub> O <sub>3</sub>		45-58	>99.9%	Cometox
Zircon	ZrSiO <sub>4</sub>		10 μm		Industrie Bitossi
Mullite Symulox M72	3Al <sub>2</sub> O <sub>3</sub> · 2SiO <sub>2</sub>		3-5 μm	90-95%	Nabaltec
Nitrides and carbides					
SN-E10	Si <sub>3</sub> N <sub>4</sub> , α-phase >95%	9-13 ±15	500	>98%	UBE Industries
Amorphous Si <sub>3</sub> N <sub>4</sub>	Si <sub>3</sub> N <sub>4</sub>		20		Goodfellow
Inorganic salts					
CaCO <sub>3</sub> micro-powder	CaCO <sub>3</sub>		<10 μm		Industrie Bitossi SpA
CaCO <sub>3</sub> nanopowders	CaCO <sub>3</sub>		90		PlasmaChem
CaF <sub>2</sub> powders	CaF <sub>2</sub>				Carlo Erba



## Appendix B

# Materials characterization

### B.1 X-Ray Diffraction

All XRD analysis were made using Bruker AXS D8 Advance diffractometer (Bruker, Karlsruhe, Germany) using a Cu-K $\alpha$  radiation,  $\theta$ -2 $\theta$  configuration with a 0.05° step size, unless differently specified. Phase identification was performed using Match! software package (Crystal Impact GbR, Bonn, Germany) supported by ICDD PDF-2 Powder Diffraction File (International Center for Diffraction Data, Newtown Square, PA, USA) as the reference database.

Rietveld refinements were performed with the MAUD (Materials Analysis Using Diffraction) program by Luca Lutterotti (University of Trento).

A comprehensive treatise on the Rietveld method could be found in *"The Rietveld Method"* by R. A. Young (Oxford University Press).

### B.2 Raman analysis

Raman spectra were recorded with an Invia Renishaw Raman microspectrometer attached to a confocal microscope (50x objective) using the 633 nm line of a He-Ne laser as the excitation wavelength.

### B.3 Density measurements

Density measurements on bulk samples were made following the ASTM-C 373 ("Standard Test Method for Water Absorption, Bulk Density, Apparent Porosity, and Apparent Specific Gravity of Fired Whiteware Products"). After the determination of the dry mass  $D$ , the saturated mass  $M$  and the mass while suspended in water  $S$ , all density and porosity values were calculated following the formulas reported in Tab. B.1.

Powders density was measured by gas (helium) pycnometry (AccuPyc 1330, Micromeritics, Norcross, GA).

### B.4 SEM - Scanning Electron Microscopy

SEM images were acquired using FEI Quanta 200 FEG, Quanta 200 (FEI Company, The Netherlands) and JEOL JSM-6300F (JEOL, Tokyo, Japan) scanning electron microscopes.

Table B.1: Calculations description for the determination of water absorption, bulk density, apparent porosity and apparent specific gravity for fired product, as reported in ASTM-C 373. In the calculations, water is considered as the buoyant medium, and the assumption is made that 1 cm<sup>3</sup> of water weights 1 g.

Quantity	Formula
Exterior volume	$V = M - S$
Open pores volume	$V_{OP} = M - D$
Impervious portions volume	$V_{IP} = D - S$
Apparent porosity	$P = [(M - D)/V] \cdot 100$
Water absorption	$A = [(M - D)/D] \cdot 100$
Apparent specific gravity	$T = D/(D - S)$
Bulk density	$B = D/V$

## B.5 Mechanical characterization

### B.5.1 Flexural strength

4-point flexural strength measurements were made with an Instron 1121 UTM (Instron, Danvers, MA) with a cross-head speed of 1 mm/min. For this purpose, specimens were cut down to bars of approximately 20 mm×2 mm×2 mm with a diamond wafering blade, and subsequently carefully polished at 5 μm finish and chamfered at the edges, by using abrasive papers and diamond paste. Considering a beam of rectangular section, 4-point flexural strength  $\sigma_f$  could be calculated with the equation

$$\sigma_f = \frac{3F(L - L_i)}{2bd^2}$$

where  $F$  is the load applied,  $L$  is the length of the support span,  $L_i$  is the length of the loading span,  $b$  is the width and  $d$  the thickness of the rectangular section of the beam (See Fig. B.1).

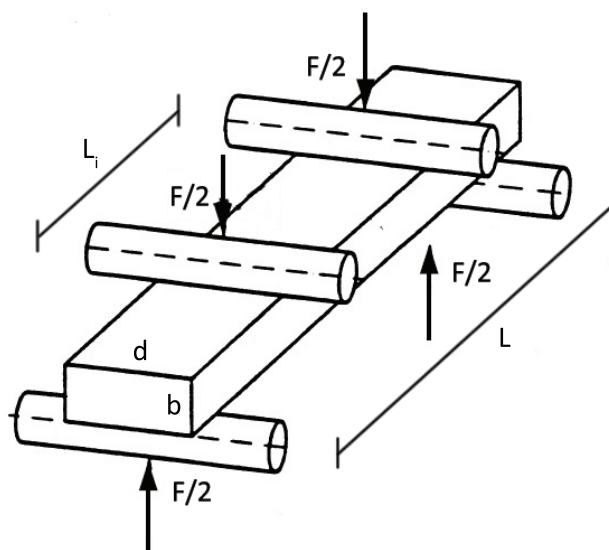


Figure B.1: Schematic representation of 4-point flexural strength test.

Biaxial flexural strength measurements were made with the "Ball on 3-balls" test (*J. Eur. Ceram. Soc.*, **22** [9-10] 1425–1436 2002). A simplified scheme of the loading geometry is reported in Fig. B.2. Based on sample characteristics and on load of rupture, biaxial flexural

strength was determined with the following relationship

$$\sigma_{max} = \frac{3F(1+\nu)}{4\pi t^2} \left[ 1 + 2\ln\left(\frac{r_a}{b}\right) + \frac{1-\nu}{1+\nu} \cdot \left(1 - \frac{b^2}{2r_a^2}\right) \cdot \frac{r_a^2}{r^2} \right] \quad (\text{B.1})$$

where  $F$  is the applied load (N),  $\nu$  is the Poisson's ratio of the specimen,  $t$  is the thickness of the sample (at the center),  $b$  is the contact radius of the of the loading ball (assumed equal to  $\frac{t}{3}$ ),  $r$  is the radius of the specimen and  $r_a$  is the support radius of the supporting balls.

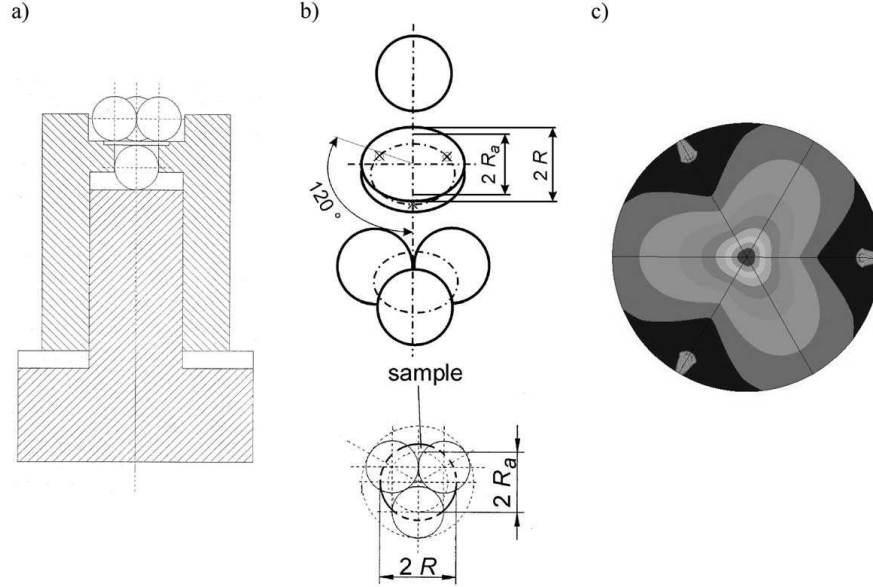


Figure B.2: a) Experimental set-up for the ball on three balls test; b) view of the positioning of the balls relative to the sample; c) example of a stress field at the tensile side of the disc for a typical loading situation.

### B.5.2 Compressive strength

Compressive strength measurements were made with an Instron 1121 UTM (Instron, Danvers, MA) with a cross-head speed of 1 mm/min. Before testing, samples were cut down to an approximate cubic shape with length of the edges of  $\sim 1$  cm. Compressive strength  $\sigma_c$  could be calculated with the relation

$$\sigma_c = \frac{P}{A}$$

where  $P$  is the load applied and  $A$  the surface area where the load is applied.

### B.5.3 Young's modulus

For the determination of the elastic modulus, dynamic Young's modulus measurements on disc-shaped specimens were carried out, according to ASTM-E 1876 ("Standard Test Method for Dynamic Young's Modulus, Shear Modulus, and Poisson's Ratio by Impulse Excitation of Vibration"). This methodology allows to correlate the natural resonant frequencies, the material properties and the specimen dimension through the following equation:

$$f_i = \frac{K_i}{2\pi r^2} \sqrt{\frac{A}{\rho t}}$$

where  $f_i$  is the resonant frequency of interest,  $K_i$  is the geometric factor for that resonant frequency,  $r$  is the radius of the disc,  $A$  is the plate constant ( $A = Et^3/[12(1 - \mu^2)]$ ),  $t$  is the disc thickness,  $\rho$  is the density of the disc,  $E$  is the Young's modulus of elasticity, and  $\mu$  is the Poisson's ratio for the disc material.

After the preparation of the samples following the requirements indicated in the norm, the standard measurement procedure consisted of the following steps:

1. determination of the Poisson's ratio from the experimental values for the first and second natural resonant frequencies, tabulated in the norm text as a function of  $f_1/f_2$  and  $t/r$ .
2. calculation of two independent values for  $E$  using the Poisson's ratio from step 1 and the first natural and second natural resonant frequencies, and then the calculation of  $E$  by the following relations:

$$\begin{aligned} E_1 &= [37.6991f_1^2D^2m(1 - \mu^2)]/(K_1^2t^3) \\ E_2 &= [37.6991f_2^2D^2m(1 - \mu^2)]/(K_2^2t^3) \\ E &= (E_1 + E_2)/2 \end{aligned}$$

where  $D$  is the diameter (mm) of the disc,  $m$  is the mass (g) of the disc, and  $K_1$  and  $K_2$  are the first and second natural geometric factors tabulated in the norm text as a function of  $t/r$  and  $\mu$ .

For each sample, at least 6 specimens were prepared and tested, and the average value was taken as the final Young's modulus.

#### B.5.4 Hardness

Hardness values were determined by Vicker's indentation technique. For each sample, at least 6 impressions were produced, and the average value was taken as the final hardness value.

#### B.5.5 Indentation toughness

Toughness measurements were performed by micro-indentation, following the formula proposed by Anstis et al. (*J. Am. Ceram. Soc.*, **64** [9] 533–538 1981).

$$K_{IC} = \zeta \left( \frac{E}{H} \right)^{0.5} \left( \frac{P}{c^{1.5}} \right) \quad (\text{B.2})$$

where  $K_{IC}$  is the indentation toughness ( $\text{MPa}\cdot\text{m}^{0.5}$ ),  $E$  is the Young's modulus (GPa),  $H$  is the hardness (GPa),  $P$  is the applied load during indentation (N),  $c$  is the crack length (measured from the tips of the impression corners, see Fig. B.3) and  $\zeta$  is a constant. Appropriate loading conditions were selected in order to obtain after indentation a so called "half-penny" crack system (see cross section scheme in Fig. B.3), which the Anstis formula is related to.

When Young's modulus values were not available, indentation toughness measurements were made following the Shetty's relationship:

$$K_{IC} = 0.0889 \left( \frac{HP}{4l} \right)^{0.5} \quad (\text{B.3})$$

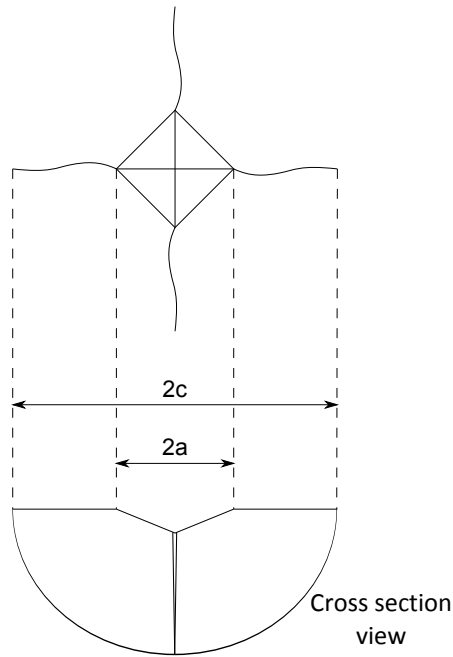


Figure B.3: Crack propagation after indentation with a Vickers indenter.  $c$  is the crack length considered in Eq. B.2. A simplified scheme of the "half-penny" crack system is illustrated in the cross section view.

For each sample at least 6 impressions were produced, and the average value was taken as the final indentation toughness value.

## B.6 Differential Thermal Analysis/Thermogravimetry

Differential thermal and thermogravimetric analysis (DTA/TG) were carried out in air or  $N_2$  or Ar atmospheres, in the  $T_{amb}$ -1500°C range (DTA/TGA, STA409, Netzsch GmbH, Selb, Germany). Temperature increasing rates in the 2-10°/min were used.

## B.7 Photoluminescence

Excitation and photoluminescence spectra were acquired using a Jasco FP6300 spectrofluorimeter. When dispersions of powders were realized, an equal amount of material was dispersed in water in a quartz cuvette (1 cm optical path).



# Curriculum Vitae

## Education

- **Ph.D. Materials Science and Engineering**  
January 2009–December 2011  
University of Padova, Padova, Italy  
Thesis title: *"Advanced ceramics from preceramic polymers and nano-sized fillers"*  
Advisor: Prof. Ing. Paolo Colombo
- **Interchange Research Program**  
September 2010–March 2011  
Penn State University, University Park, PA, USA  
Project title: *"Transparent sialon ceramics for armor applications"*  
Advisor: Prof. Gary L. Messing
- **M.S. Materials Science and Engineering**  
110/110 cum laude  
October 2006–October 2008  
University of Padova, Padova, Italy  
Thesis title: *"Mullite coatings on SiC foams"*
- **Erasmus Interchange Program**  
September 2006–January 2007  
Instituto Superior Técnico, Lisbon, Portugal
- **B.S. Materials Engineering**  
110/110 cum laude  
October 2003–June 2006  
University of Padova, Padova, Italy  
Thesis title: *"Electrodeposition of Nickel/SiO<sub>2</sub> nanoparticles composite coatings"*

## Publications in Journals

- E. Bernardo, G. Parcianello, P. Colombo, *"Wollastonite foams from an extruded preceramic polymer mixed with CaCO<sub>3</sub> micro-particles assisted by super-critical carbon dioxide"*, Adv. Eng. Mater., *submitted*
- E. Bernardo, G. Parcianello, P. Colombo, *"Novel Synthesis and Applications of Yttrium Silicates from a Silicone Resin Containing Oxide Nano-particle Fillers"*, Ceram. Int., *submitted*
- G. Parcianello, E. Bernardo, P. Colombo, *"Optimization of phase purity of β'-sialon ceramics produced from silazanes and nano-sized alumina"*, J. Am. Ceram. Soc., *submitted*
- G. Parcianello, E. Bernardo, P. Colombo, *"Low Temperature Synthesis of Zircon from Silicone Resins and Oxide Nano-sized Particles"*, J. Eur. Ceram. Soc., *accepted*.
- G. Parcianello, E. Bernardo, P. Colombo, *"Mullite/Zirconia nano-composites from a preceramic polymer and nano-sized fillers"*, J. Am. Ceram. Soc., 94 [5] 1357-1362 (2011).
- E. Bernardo, G. Parcianello, P. Colombo, J.H. Adair, A.T. Barnes, J.R. Hellmann, B.H. Jones, J. Kruse, J.J. Swab, *"SiAlON Ceramics from Preceramic Polymers and Nano-sized Fillers: Application in Ceramic Joining"*, J. Eur. Ceram. Soc., *in press*.

- E. Bernardo, G. Parciannello, P. Colombo, J. Adler, D. Boettge, "Mullite Monoliths, Coatings and Composites from a Pre ceramic Polymer Containing Alumina Nano-Sized Particles", *Advances in Polymer Derived Ceramics and Composites*, 51-60 (2010).

## Presentations at Conferences

- **ECerS XII, 12th Conference of the European Ceramic Society**  
Stockholm, Sweden 19–23 June 2011.  
*"Fabrication of 1-1, 2-2, and 3-3 SiAlON Microstructure Composites" and "Multifunctional Silicates from Silicone Resins filled with Oxide Nanoparticles"*.
- **CIMTEC 2010, 12th International Ceramic Congress**  
Montecatini Terme, Italy, 6–11 June 2010.  
*"Development of zirconia-toughened mullite and SiAlON ceramics from a nano-filled pre ceramic polymer"* (oral presentation).
- **3rd International Symposium on SiAlONs and Non-Oxides**  
Cappadocia, Turkey, 1–4 June 2010.  
*"SiAlON Ceramics from Pre ceramic Polymers and Nano-sized Fillers"*.
- **34th International Conference & Exposition on Advanced Ceramics & Composites**  
Daytona Beach, Florida, USA, 24–29 January 2010.  
*"Mullite and SiAlON-based Ceramics from a Silicone Resin and Nano-Fillers"* (oral presentation).
- **9th International Conference on Experimental Techniques and Design in Composite Materials**  
Vicenza, Italy, September 30–October 2 2009.  
*"Development of Zirconia-toughened Mullite matrix composites from a nano-filled pre ceramic polymer"* (oral presentation).